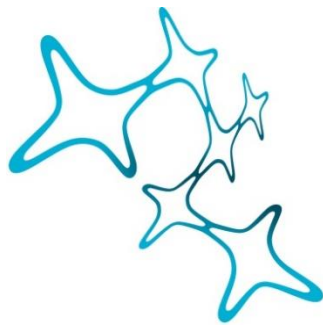

EPIGENETIC REGULATION OF RETINAL DEVELOPMENT

IN VIVO MOUSE AND HUMAN 3D MODELS TO UNRAVEL THE ROLE OF TET3-MEDIATED DNA DEMETHYLATION

Grazia Giorgio



Graduate School of
Systemic Neurosciences

LMU Munich



Dissertation at the
Graduate School of Systemic Neurosciences
Ludwig-Maximilians-Universität München

January, 2023

Supervisor
Prof. Dr Stylianos Michalakis
Department of Ophthalmology
Ludwig-Maximilians-Universität München

First Reviewer: Prof. Dr Stylianos Michalakis
Second Reviewer: Prof. Dr. Silvia Cappello
External Reviewer: Dr. Irina Solovei

Date of Submission: 20/01/2023
Date of Defense: 19/04/2023

“The beginning of knowledge is the discovery
of something we do not understand ”

Frank Herbert

Contents

I	Introduction	15
1	The vertebrate retina: cellular composition	15
2	From progenitors to different retinal populations	16
3	Photoreceptors and phototransduction	19
3.1	Electroretinography	22
4	Cones and colour vision	23
5	Epigenetics	26
5.1	Genomic DNA methylation and demethylation	26
5.2	TET enzymes, variants and function	28
5.3	Localisation and function of oxidated genomic DNA cytosines	29
5.4	Epigenetic regulation of retinal development	31
6	Tools to investigate the role of epigenetics in mammalian retina	32
II	Methods	35
7	Animal experiments	35
7.1	Mouse lines	35
7.2	Genotyping	35
7.3	Anesthesia	36
7.4	Electroretinography	36
7.5	Optical Coherence Tomography (OCT)	37
7.6	Behavioral testing	37
8	Tissue collection and image processing	38
8.1	PFA perfusion and sectioning of brain slices	38
8.2	Retina dissection	38
8.3	Immunohistochemistry	39
8.4	In situ hybridization assay (RNAscope®)	40
8.5	Confocal microscopy	40
8.6	Image processing	40
8.7	Electron Microscopy	42

9	Molecular Biology Techniques	43
9.1	Genomic DNA extraction from tissue or cell pellets	43
9.2	RNA extraction and cDNA synthesis	44
9.3	qRT-PCR and gene expression analysis	44
9.4	Co-Immunoprecipitation (IP)	45
9.5	Western blot	47
9.6	Gibson assembly and bacterial transformation	47
10	Cell culture	48
10.1	HEK293T	48
10.2	induced Pluripotent Stem Cell (iPSC) culture	49
10.3	Human Retinal Organoids (hROs)	49
10.4	Electroporation	50
11	Sequencing	50
11.1	EPIC array	50
11.2	Bulk RNA-seq library preparation and sequencing	52
12	Fluorescent Activated Cell Sorting (FACS) of cone photoreceptors	52
12.1	Retina dissociation	52
12.2	PNA labelling of cone photoreceptors	52
12.3	FACS	53
12.4	Mass spectrometry-based whole proteome analysis of sorted cone photoreceptors	53
13	Other methods	54
13.1	LS-MS/MS measurement of cytosine modifications	54
13.2	LC MS/MS measurement of thyroid hormones	55
III	Results I	57
14	Generation and characterisation of <i>Tet3</i> conditional mutant mouse line	57
14.1	<i>Tet3</i> is expressed in the mouse retina and the short isoform is the most abundant	57
14.2	Generation of a <i>Tet3</i> conditional mutant mouse line	58
14.3	<i>Tet3</i> protein generated in <i>Tet3</i> mutant mice is catalytically inactive	59
14.4	<i>Tet3</i> mutation does not affect retinal lamination and layer formation	61
15	Outer nuclear layer and cone photoreceptors	63
15.1	Cone photoreceptors are increased in their number in <i>Tet3</i> mutant retinae	63
15.2	Different dorso-ventral distribution of S-cones upon <i>Tet3</i> mutation	66

16 Inner nuclear layer	68
16.1 <i>Tet3</i> mutation leads to less cells in the inner nuclear layer	68
17 Retinal light responses are remarkably reduced in <i>Tet3</i> mutant mice	72
18 <i>Tet3</i> in cone sub-type specification	76
18.1 <i>Tet3</i> mutation affects genes involved in photoreceptors versus bipolar cell development and in photoreceptor functional maturation	76
18.2 Thyroid hormones and their receptor <i>Thrb2</i> are not affected by <i>Tet3</i> mutation .	78
18.3 The binding between <i>Tet3</i> and <i>Thrb2</i> is not affected in <i>Tet3</i> mutant mice	79
19 <i>Tet3</i> in cone vs bipolar cell differentiation	81
19.1 Cellular changes in cone and bipolar cells mostly manifest in the late postnatal period	81
19.2 Neither cell death nor proliferation contribute to the altered cell numbers in both ONL and INL	83
19.3 <i>Vsx2</i> and <i>Prm1</i> show differentially methylated loci and enhancers	85
20 <i>Tet3</i> in photoreceptor maturation and metabolism	87
20.1 At later postnatal period, <i>Tet3</i> mutation leads to gene expression dysregulation related to visual perception	87
20.2 Proteomic analysis of cone photoreceptors reveals <i>Tet3</i> involvement in actin filament dynamics for vesicle release and cell-cell contact	92
20.3 Manipulating <i>Tet3</i> affects metabolic pathways in cone photoreceptors	94
IV Results II	98
21 Human retinal organoids: background and scientific reasoning behind the choice of this tool	98
21.1 Susceptibility of different iPSC lines to culture condition aimed at differentiating retinal organoids	98
22 Cellular and molecular characterisation of hROs	102
22.1 Cellular and molecular composition of differentiated human retina organoids mirror <i>in-vivo</i> retinal development	102
22.2 Differentiating human retinal organoids showed dynamic pattern of DNA methylation and demethylation	105
23 Electroporation as tool for gene delivery	105

23.1	<i>In vitro</i> electroporation efficiently targets Müller glial but not photoreceptor precursors in human retinal organoids	105
23.2	<i>In vitro</i> electroporation of differentiated hROs with promoter specific GFP constructs.	109
24	Strategy for TET3 knock down in human retinal organoids	110
V	Discussion	114
25	Tet3 and the generation of distinct retinal cell populations	115
25.1	An imbalance in DNA methylation of key genes controlling photoreceptors vs bipolar cell fate commitment suggests a role of Tet3 in this process	115
25.2	More cone photoreceptors generated during postnatal stages suggest late born neurons as source	117
25.3	The role of Tet3 in cone sub-type specification and cone gradient establishment	118
25.4	Thrb has a key role in cones gradient formation	119
25.5	Rxrg helps Thrb in silencing S-opsin and concurs in cone gradient establishment	120
25.6	Prediction of loss of opposing opsin gradient on colour vision	121
25.7	Tet3 is important for correct cone synaptogenesis and synaptic function	123
25.8	The altered metabolic profile of cone photoreceptors in catalytically impaired Tet3 mice – cause or consequence?	126
26	Human retinal organoids	127
26.1	Limitations of current models in the study of human retinal development, physiology, and disease	127
26.2	Different iPSCs line might react differently to culture conditions	128
26.3	<i>In vitro</i> electroporation is an effective and versatile tool for genetic material transfer in selected retinal cell populations	129
26.4	Future directions	130
27	Appendix I	165
28	Appendix II	166
29	Appendix III	170
30	Appendix IV	173
31	Appendix V	177

List of Figures

1	Structure of the mammalian retina	16
2	Mouse retinogenesis	17
3	Transcription factors in retinogenesis	18
4	Photoreceptor types and subtypes	20
5	Phototransduction	21
6	Bipolar subtypes	22
7	Horizontal cell inhibitory feedback	25
8	Epigenetics	27
9	TET enzymes	28
10	Homologous recombination	32
11	Identification of layer IV in primary visual cortex (V1)	43
12	Schematic representation of bisulfite (BS) and oxidative bisulfite (OX-BS) procedure	51
13	<i>Tet3</i> expression in mouse retina	58
14	Generation of <i>Tet3</i> conditional mutant mouse line	60
15	Cytosine modifications	62
16	<i>Tet3</i> Catalytic activity <i>in vitro</i>	63
17	Optical Coherence Tomography (OCT)	64
18	Cone photoreceptors (<i>Arr3</i>)	65
19	Cone photoreceptors (PNA)	66
20	Rod photoreceptors	67
21	Opsin distribution in flat mount retina	68
22	Opsin distribution in retina cross-sections	69
23	Cell densities in inner nuclear layer	70
24	Bipolar cell sub-types	71
25	Responses to electrical stimulation (ERG)	73
26	Immediate early gene response to visual stimuli	74
27	Behavioural testing	75
28	RNA-seq p4	76
29	RNA-seq p10	77
30	Opsin expression at early post-natal stages	79
31	Canonical thyroid hormone pathway	80
32	<i>Thrb2</i> Co-IP and interaction with <i>Tet3</i>	82
33	Bipolar cell markers	83
34	Bipolar and cone cells specification	84
35	Apoptosis and cell proliferation	86
36	Differential methylation in <i>Tet3</i> mutant mice	88
37	RNA-seq p30	89

38	Synaptic markers ONL	91
39	Fluorescence activated cell sorting (FACS)	93
40	Proteomics of sorted cone photoreceptors	94
41	String analysis of enriched proteins	95
42	Metabolic alteration in <i>Tet3</i> mutant mice	97
43	Human retinal organoids (hROs) differentiation protocols	100
44	Cellular and molecular characterisation of hROs differentiated according to [128]	101
45	Molecular characterisation of hROs differentiated according to [32]	103
46	Cellular characterisation of hROs differentiated according to [32]	104
47	<i>TET3</i> and cytosine modification in differentiating hROs	106
48	Schematics of hROs electroporation	107
49	Electroporation test	108
50	Muller glia morphology in electroporated hROs	109
51	Cellular and molecular characterisation of more mature hROs	111
52	Electroporation of hROs using promoter specific constructs	112
53	Knock down of mKATE2 by mir15b in HEK293T cells	114

List of Tables

2	List of primary antibodies used with mouse tissue	41
3	List of primary antibodies used with human derived tissue	42
4	List of mouse primers for qRT-PCR	45
5	List of human primers for qRT-PCR	46

List of abbreviations

5caC	5-carboxy Cytosine
5fC	5-formyl Cytosine
5hmC	5-hydroxymethyl Cytosine
5mC	5-methyl Cytosine
ACs	Amacrine Cells
BER	Base Excision Repair
bHLH	basic Helix Loop Helix
BPs	Bipolar cells
ChIP	Chromatin Immunoprecipitation
CNS	Central Nervous System
Co-IP	Coimmuno Precipitation
CPs	Cone Photoreceptors
DMS	Differentialy Methylated Sites
DNMT	Dna Methyl Transferases
EM	Electron Microscopy
ERG	Electroretinography
ESCs	Embrionic Stem Cells
GCL	Ganglion cell layer
GMP, GDP, GTP	Guanosine Mono-, Di- and Tri Phosphate
GO	Gene Ontology
HCs	Horizontal Cells
hROs	human Retinal Organoids
IHC	Immunohistochemistry
INL	Inner Nuclear Layer
IPL	Inner Plexiform Layer
iPSCs	induced Pluripotent Stem Cells
IS	Inner Segment
loxP site	locus of crossing (x) over, P1
MGs	Müller Glial cells
NR	Neuronal Retina
OCT	Optical Coherence Tomography
OFF-BPs	OFF Bipolar cells

ON-BPs	ON Bipolar cells
ONL	Outer Nuclear Layer
OPL	Outer Plexiform Layer
OS	Outer Segment
OX-PHOS	Oxidative Phosphorilation
PCR	Polymerase Chain Reaction
PRs	Photoreceptors
qRT-PCR	Quantitative Realtime Polymerase Chain Reaction
RA	Retinoic acid
RBP, CBP	Rod and Cone Bipolar cells
RGCs	Retinal Ganglion Cells
RNA-seq	RNA sequencing
RPCs	Retinal Progenitor Cells
RPE	Retina Pigmented Epithelium
RPs	Rod Photoreceptors
SWS, MWS, LWS	Small, Medium and Long Wavelength Sensitive
TDG	Thymine DNA Glycosylase
TET	Ten Eleven Translocation
TF	Transcription Factor
THRB	Thyroid Hormone Receptor Beta
Tss	Transcription start site
WPE	λ_{\max} Absorpion maxima
λ_{\max}	Absorpion maxima

Abstract

Tet3 is a member of the ten-eleven translocation enzymes, which include also Tet1 and Tet2. Their canonical function is the oxidation of the 5-methylcytosine (5mC) on the DNA into 5-hydroxymethylcytosine (5hmC), and subsequent oxidative states 5-formylcytosine (5fC) and 5-carboxycytosine (5caC), thereby promoting increased gene expression. Although Tet3 is the most abundant member in brain and retina, its role in the latter has not been addressed.

The mammalian retina comprises a variety of cell types which are generated from a common progenitor cell during two waves of differentiation. In mice, retinal ganglion (RGCs), amacrine (ACs), cone photoreceptors (CPs) and horizontal (HCs) cells are born during embryonic times, whereas rod photoreceptors (RPs), bipolar (BPs) and Müller glial (MGs) cells are generated postnatally. Although many more sub-types of each of these main populations have been identified in human retina, the order in which these cells are formed is maintained in the two species.

Tet3 is expressed in the mouse retina from postnatal day 0 (p0) and declines after eye opening (p12), implying its role during the same time window in which retina cells develop and mature. Mutations in TET3 catalytic domain have been previously identified and linked to neurological, but also ophthalmological defects. To better investigate the role of Tet3 in the mouse retina, we generated conditional mutant (*Tet3* cMut) mice lacking part of the catalytic domain in retinal progenitors and in their progeny. The resulting protein is catalytically inactive, as shown by a reduced dioxygenase activity with lower 5hmC both *in vivo* and *in vitro*.

Photoreceptors, cones and rods, are light-sensing cells, responsible for colour and diurnal vision, and dim light vision, respectively. Additionally, cones can be divided in S-cones (blue cones), M-cones (green cones) and L-cones (red cones) depending on the expression of specific light responsive proteins. Mice have only S- and M-cones distributed in opposite dorso-ventral gradient with S-cones more abundant in the ventral side and scarcely represented in the dorsal, whereas M-cones have an opposite gradient. Results show that *Tet3* cMut mice have an increased number of cone photoreceptors and altered cone sub-type distribution with increased numbers of S opsin-positive cones in the dorsal retina therefore abolishing the characteristic dorsal to ventral S-cone gradient. Minor changes are observed for M-cones. The increased cone number is accompanied by a reduction in the total cell number of the several retinal population in the inner nuclear layer (INL) and more specifically ACs, HCs, and mostly BPs, while MGs are unaltered. To assess functionality of the retina we performed *in vivo* electroretinography to record rod and cone mediated responses in whole retina, depending the light stimulus intensity. Results shown here reveal that cone, but not rod, mediated responses are affected. Deeper investigation at the level of outer plexiform layer (OPL) where synaptic contacts are made between photoreceptors and lower layer neurons of the INL, revealed from one side enlarged OPL, and on the other side a lower number of synaptic contacts made between these cells.

Moreover, we show that the altered numbers of cone photoreceptors and other retinal cell populations are not caused by perturbation in either cell death or progenitor proliferation, suggesting re-direction of some retinal progenitors towards cones instead of inner nuclear layer cell types. Genes involved in photoreceptors versus bipolar cell-fate commitment were differentially regulated in *Tet3* mutant mice, and their loci showed differential methylation in line with their affected expression. These results suggest that Tet3 has a role in retinal development and/or lineage specification. Elucidating the mechanisms downstream of Tet3 will improve our understanding of retinal homeostasis under physiological and pathophysiological conditions.

From these observations on cone number and sub-type specification, we questioned whether TET3 might have the same role in other species, specifically humans. For this purpose, human retinal organoids (hROs) were differentiated according to published protocols from several induced pluripotent stem cells (iPSCs) lines of healthy donors. Results show that iPSCs lines are differentially affected by experimental conditions. Nevertheless, differentiating hROs recapitulates retinal development and maturation *in vitro*. Curiously, *TET3* is expressed at increasing levels during differentiation accompanied by an increase in 5hmC. To investigate the specific function of TET3 in cones, from one side knockdown (KD) using a previously identified microRNA (miR15b) will be performed. On the other side, a *TET3* KO iPSC line is currently being generated from which hROs will be differentiated and analysed. Preliminary results show that electroporation of complex 3D models is a versatile and reliable tool for gene delivery of retinal progenitors and Müller glial cells, but it is not for terminally differentiated neurons.

Part I

Introduction

1 The vertebrate retina: cellular composition

The eye is the fundamental organ of the visual system, whose function is to receive and process visual details of an object. Light enters the eye through the pupil, which acts as a diaphragm adjusting the intensity of the luminous stimulus, passes through the lens, whose role is to shape and focus the image to finally converge it onto the retina [140]. The retina (Fig. 1) is a thin layer of tissue located in the back of the eye with the unique task of converting the light stimulus into an elaborated electrical signal, which after processing is conveyed to higher brain regions for cognitive perception of the aforementioned visual stimulus. All this is possible thanks to the presence of highly specialised neurons, called photoreceptors, located in the outermost region of retina and capable of absorbing light stimuli, at various wavelengths (λ), and pass them in the form of electrical signals to lower layer neurons for further processing. The retina is indeed composed of seven major cell populations (six neuronal and one glial type) distributed in three different nuclear layers, where the cell bodies of these cells are located, in turn separated by two plexiform layers where contact between them is established in an interweaving of synaptic processes [155]. Photoreceptors (PRs) residing in the outer nuclear layer (ONL), as mentioned before, are light sensitive cells and are of two types: rods (RPs), for dim-light vision, and cones (CPs), essential for colour vision. Once the incoming photons are converted into an electrical signal, this is propagated to lower layer neurons called bipolar cells (BPs). These further pass on the information to third order neurons or retinal ganglion cells (RGCs) positioned in the ganglion cell layer (GCL), which through their long axons, forming the optic nerve (ON), transport this message out of the retina to cortical regions. In between this longitudinal propagation, the other two neuronal cell types, the horizontal and amacrine cells (HCs and ACs, respectively) further shape and refine the visual output from the retina. HCs face the outer plexiform layer (OPL) and contact PRs and BPs, whereas ACs face the inner plexiform layer (IPL) and contact RGCs. Müller glial (MGs) are glial cells in the neuronal retina (NR) with a role of support in maintaining retinal balance and wellness [33]. Finally, an additional cell type not originating from the NR but still considered part of the retina, is the retinal pigmented epithelium (RPE) located in between the PRs and the blood vessels (choroid) therefore proving PRs with nutrients and metabolites taken up by the choroid. Moreover, thanks to their pigmentation, RPE cells are crucial for blocking the light rays refracted and not absorbed by PRs, preventing collateral damages [246].

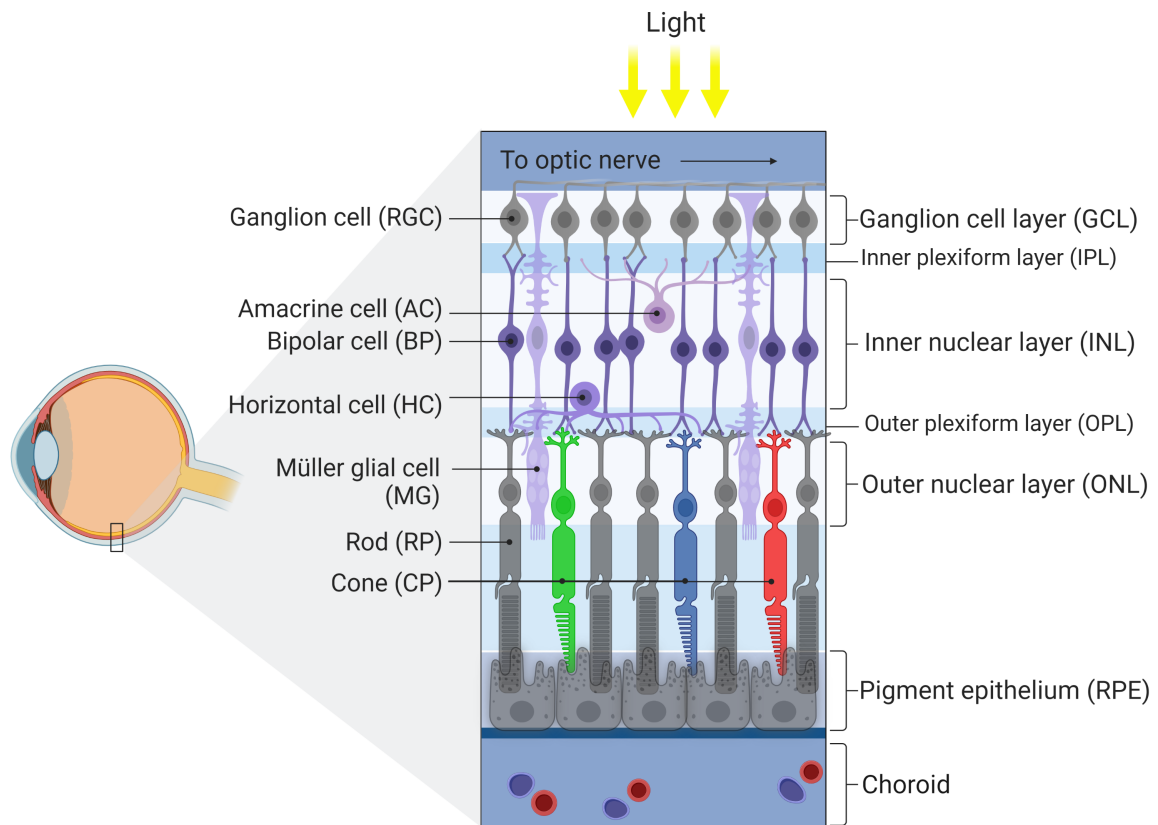


Figure 1: Structure of the mammalian retina
(modified from Biorender)

2 From progenitors to different retinal populations

Before the different cells are born, the NR is constituted of a pool of fast proliferating retinal progenitor cells (RPCs) forming a pseudostratified neuroepithelium layer. This effect is due to a very peculiar phenomenon called interkinetic nuclear migration, typical of many proliferating epithelial cells, where nuclei move along the apicobasal polar axis spanning the entire layer thickness using the cell radial process [13]. Interkinetic nuclear migration is thought to be needed for balancing the neurogenic and proliferative signals on RPCs and ensure the correct progression of retinogenesis. Disruption of this process, either affecting the apicobasal polarity or interfering with known signaling molecules can lead to premature cell cycle exit and differentiation with severe consequences on the retinal composition and structure [49]. During these proliferation events, a small subset of amplifying progenitors becomes postmitotic and start differentiating. RPCs undergo a series of competence state ensuring that the different neuronal populations are born at a given time [268]. In the vertebrate retina indeed, the order in which these cells are generated is maintained (Fig. 2) and sees the RGCs as first born, followed in

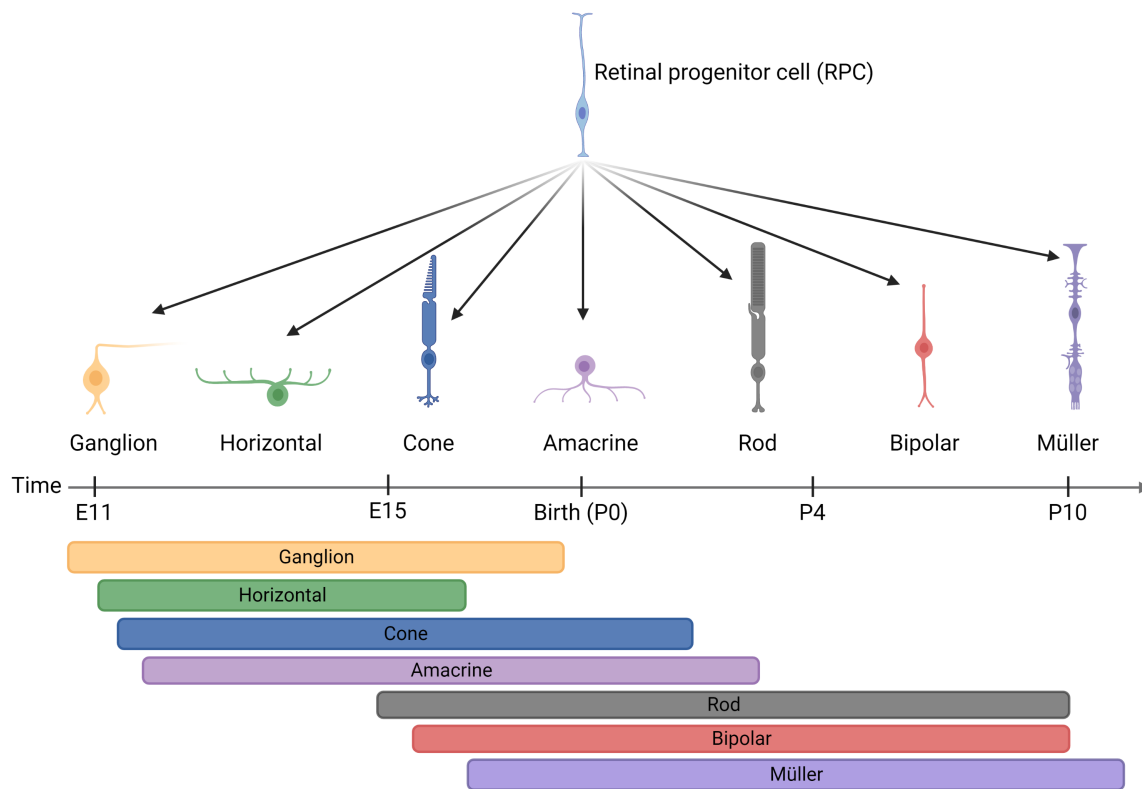


Figure 2: Mouse retinogenesis

this order by cone photoreceptors, HCs and ACs, rod photoreceptors and eventually BPs and MGs [13]. Although many of these events occur simultaneously, it is possible to recognize a spatiotemporal pattern with new neurons originated in a central to peripheral gradient [270] during two main waves of retinogenesis: one embryonic (for RGCs, CPs, HCs and ACs) and one postnatal (RPs, BPs and MGs). Despite the fact that different retinal cells are born during different times, it is nowadays accepted that all of them originate from the same common pool of RPCs which are therefore multipotent. This work was initially demonstrated by Turner, Snyder and Cepko in 1990, by injections of retroviruses encoding for β -galactosidase in embryonic rats at e13 and e14. By measuring the β -galactosidase, this resulted in labelled clones of all seven major retinal cell-classes [268]. In another study of injected postnatal rat retina, they showed that progeny clones were restricted to four different cell types in different combinations [268], therefore suggesting that some of these cell types may arise from a common precursor. Both intrinsic and extrinsic factors have been identified as promoters of these different competence states in RPCs (Fig. 3), ensuring the formation of the appropriate retinal cell in the correct time and number. Many of these intrinsic factors belong to the basic helix loop helix (bHLH) family [122], [27] or homeodomain gene family [192][297] or are nuclear receptors [224], [252], [223]. Regarding the extrinsic factors these are mostly soluble and diffusible signaling molecules like Fgf, Wnt, Shh, Notch, the active form of the thyroid hormones (T3) and retinoic acid (RA) [215], [179], [210], [104]. For example, the orthodenticle homeobox gene OTX2 is a master

regulator of both bipolar cells and photoreceptors, it is expressed in postmitotic precursors and, when deleted, results in a lower number of PRs, BPs and HCs [63][132] and excess of ACs. It can promote other two transcription factors (TFs) involved in bipolar vs photoreceptors cell

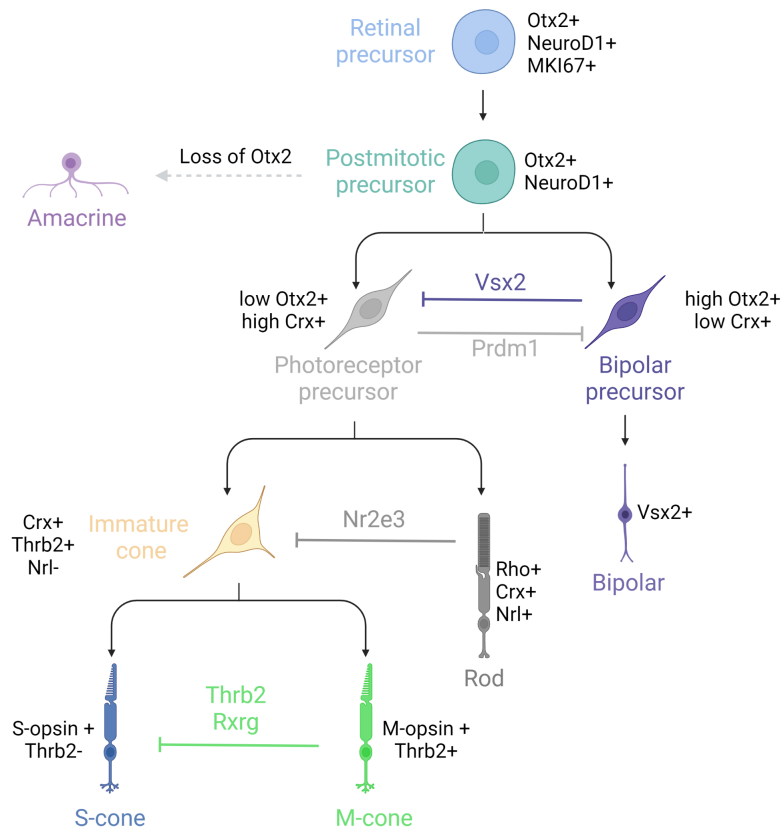


Figure 3: Transcription factors in retinogenesis
 Cascade of transcription factors dictating cell fate commitment in some retinal populations

fate commitment which are VSX2/CHX10 and PRDM1/BLIMP1. These two, downstream to OTX2, compete in retinal precursors for the final commitment of these cells towards bipolar or photoreceptor destiny, respectively [76][156]. The cone-rod homeobox gene (CRX) is vital for photoreceptors development, it is abundant in postmitotic precursors as well as in bipolar cells [295]. CRX is not sufficient alone in promoting retinal precursor differentiation towards photoreceptors since its deletion does not alter photoreceptor cell fate but rather their maturation with downregulation of many phototransduction genes and absence of outer segments (OS) [70]. Neural retina-specific leucine zipper protein (NRL) and photoreceptor cell-specific nuclear receptor (PNR/ also known as NR2E3) are two other TFs, the first is a direct activator of rod genes and rod fate, the second through the suppression of cone genes indirectly further push NRL committed photoreceptors in becoming rods. In both cases, deletion or mutations in these two genes result in no rods and conversion of these precursors to cones (or cone-like cells) with excess expression of S-opsin (S-cones or blue cones) [172][43][36]. Finally, one of the most studied ligand-regulated nuclear receptors in the field of cone maturation and functional specification is the thyroid hormone receptor isoform beta 2 (THR2). In mice, when absent, the

mature cones acquire a S-opsin expressing fate, while M-cones (or green cones) are completely abolished highlighting its role in cone patterning [194]. With the identification of these (and many more) TFs promoting selective transcriptional programs in these cells, a transcriptional dominance model has been proposed where the coordinated actions of these factors in RPCs would determine the particular differentiation outcome [253]. The hunt for the identification of additional key master regulators of retinal cell-fate specification is still open since many are the still unanswered questions in this process.

3 Photoreceptors and phototransduction

Photoreceptors are highly compartmentalised and specialised neurons whose structure allow them to absorb light and convert it into an electrochemical signal propagated to downstream neurons. From a structural point of view, they are composed of the following elements: an outer segment (OS), a connecting cilium, an inner segment (IS), a nuclear compartment and a synaptic process. The OS of rods and cones is a cylindrical or conical structure of plasma membrane with specialised parts called discs that are either enclosed in or a protrusion of the OS, respectively. These discs contain specialised membrane proteins having fundamental role in the phototransduction cascade (see below). The connecting cilium connects the OS and IS and allows the shuttling of proteins to the OS. The IS of both photoreceptors is filled in mitochondria, the energetic power source of a cell, and other organelles [182]. The nuclear region contains the nucleus and is from one side continuous with the IS and from the other side with the synaptic process. This terminates in the synaptic region filled with vesicles and peculiar structures called ribbon synapses, important for tethering and priming synaptic vesicles for their release to lower layer neurons [261]. The OS contains light-sensitive proteins called opsins whose excitation by light promotes the beginning of the phototransduction cascade. Opsins are apoproteins which in their inactive form are bound to their ligand, the 11-cis retinal, through a Schiff base bond to a lysine residue in one of the helices. The vertebrate opsins can be discriminated based on the absorption maxima (λ_{\max}), that is the λ at which the highest light absorption is observed, and whether they respond to bright light (photopsins) expressed in cone cells or dim light (scotopsins) in rod cells (Fig. 4)[242]. Cone opsins are originally of four classes: the short (SWS1 and SWS2), the medium (MWS or Rh2) and the long (LWS) wavelength-sensitive, but during mammalian evolution, e.g., *Mus musculus*, lost the SWS2 and Rh2 therefore they are dichromat. Primates, including humans, are trichromat as in addition to the SWS1 gene later developed two distinct LWS opsin variants, the LWS and the MWS by duplication of the initial LWS gene [103]. Moreover, based on the spectral sensitivity, the short opsin (OPN1SW) range is from an λ_{\max} of 360 nm in mice, in the ultraviolet (UV) range, to 430 nm (blue range) for humans, while the LWS gene shows less variability in the different species ranging from 535 nm (green

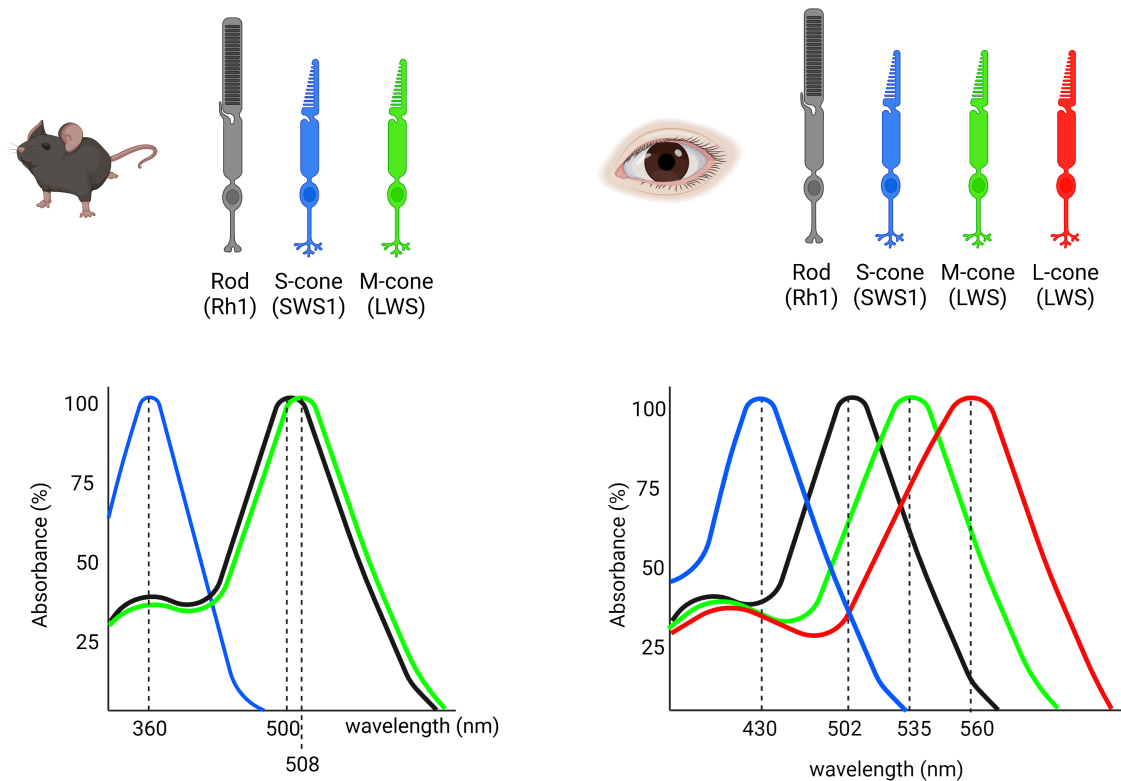


Figure 4: Photoreceptor types and subtypes with corresponding spectrum sensitivity in mouse and human eye

range) for the OPN1MW and 560 nm for the OPN1LW (red range). Mice are the exception since their single LSW gene (called *Opn1mw*) is more blue shifted to 508 nm and, lacking the second LWS gene, they are blind to red light [103]. These different chromatic properties are conferred by the different amino acid sequence of the opsin which in turn provides the perfect environment to the chromophore isomerisation at different λ . Indeed, phototransduction begins in the OS when photons hit and isomerise the 11-cis retinal chromophore component to all-trans retinal (Fig. 5). Since the chromophore and the apoprotein are tightly bound, the isomerisation causes a conformational change in the opsin which passes into its active state catalysing the exchange of GDP to GTP. This in turn determines the activation of the α -subunit of the G-protein (transducin), to which opsins are bound, which detaches from the $\beta\gamma$ complex activating the phosphodiesterase protein (PDE) leading to the hydrolyses of the cyclic guanosine monophosphate (cGMP). Reduction of the cGMP levels results in the closure of cyclic nucleotide gated ion channels (CNG) in the plasma membrane stopping the influx of Na^+ and Ca^{++} ions. The suppression of the positive inward charges flux determines a decrease in the membrane potential of photoreceptors (hyperpolarisation) stopping the release of glutamate at the PR synapses. The phototransduction cascade is returned to its inactive state for a termination of the signal at multiple levels. The natural hydrolase activity of transducin α -subunit restores the GDP from GTP therefore leading to its inactivation. Consequently, the PDE is returned to its inactive state and

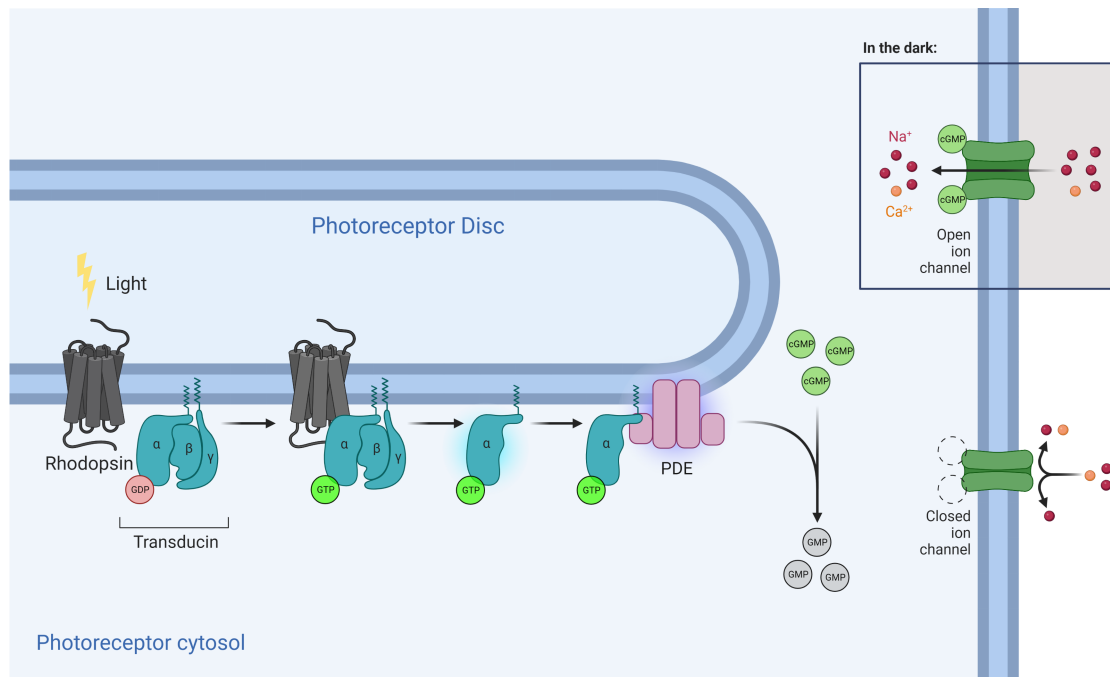


Figure 5: Phototransduction

Phototransduction cascade is started upon light excitation of the specific opsin protein, in this example rhodopsin (modified from Biorender)

cGMP levels are also restored through activation of the guanylate cyclase causing the opening of the CNG channel and the influx of Na^+ and Ca^{++} ions which depolarises the membrane for glutamate release. Moreover, the opsin protein is phosphorylated by protein kinases and inhibited by the binding of arrestin proteins returning to its inactive state. Finally, the all trans retinal is converted back to 11-cis retinal by a series of chemical reactions in an exchange between the RPE and the PR, and its binding to the apoprotein closes the circle [182]. Once light hits on the PR, the light stimulus is converted into an electrochemical response that is forwarded to the inner retina. PR are in direct contact with BPs, contacts between rod-to-BP and cone-to-BP are different depending on the type of BP cell and the PR they are connected to. So far, a total of 15 different types of BP have been identified in the mouse retina [282][239][94] [89] [71] which can be distinguished depending on the light-evoked responses and the cell type they are preferentially connected to. Some of these BPs are depolarised in the presence of a light stimulation, therefore they are called ON-bipolar cells (ON-BPs); on the other hand, bipolar cells which hyperpolarise following a light signal are of the OFF type (OFF-BPs). These two broad classes are also distinguished based on their lamination pattern, that is ON-BPs send their basal axonal processes to layer 3-5 of the inner plexiform layer (IPL), whereas the OFF-BPs have shorted dendrites culminating in the first two layers of the IPL connecting to other time on ON and OFF retinal neurons, respectively [66]. Moreover, different bipolar subtypes are connected to either rods or cones, therefore they can be distinguished in rod- and cone-bipolar cells (RBC and CBC), respectively. Up to today, 15 different CBCs have been identified: type 1a, 1b, 2, 3a, 3b, 4, are OFF-CBCs and 5a, 5b, 5c, 5d, 6, 7, 8, 9 are instead ON-CBCs, whereas so far

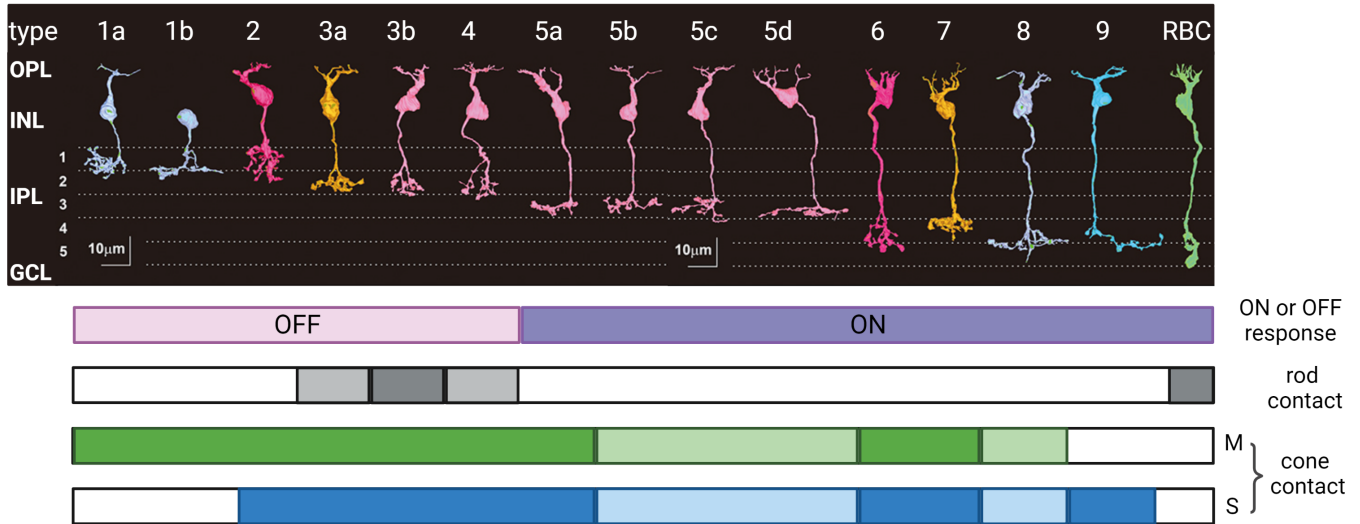


Figure 6: Bipolar subtypes

Identified subtypes of bipolar cells with corresponding morphology of dendritic endings in IPL. Electrical responses as well as rod and cone contacts are illustrated. Image adapted from [267] and [65]

only one type of RBC is known which is of the ON-type (Fig. 6) [285]. Each RBC simultaneously connects with two to three rods in their receptive field, while cones are contacted by a single dendrite of each CBC sub-type (therefore received contacts from multiple CBCs), but cone pedicles are innervated by single axons of single CBC territorially arranged without overlap [267][282]. In addition to receiving glutamatergic drive from PRs, BPs signal is also shaped by lateral GABA-mediated inhibition by HC and, on the opposite extremity, by ACs before the information is passed onto RGCs. This also means that BPs output always reflect ACs activity [274].

3.1 Electrophysiology

All these cell-to-cell communication and responses are translated into electrical signals, which can be measured by a non-invasive technique called electroretinography (ERG) and used to assess retinal functionality in both physiological and pathophysiological conditions. In the full-field-ERG, light stimulation yields a transient evoked response which is the result of the collective activity of the different retinal populations. Normally after an initial dark-adapted (scotopic) evaluation, that enables rod-driven activity to be studied, the eye is light-adapted (photopic) to obtain cone-mediated responses [190]. Light stimulation usually results in a first inward negative wave, called a-wave, which is PR-driven and the result of stopping the dark-current flow, followed by a positive deflection which corresponds to the b-wave and is the result of the inner retina response after its stimulation [212]. Rods that are active in dim light conditions are the PR type mainly driving the scotopic a-wave, whereas cones are responsible for photopic vision and the corresponding a-wave. These responses are followed by an outward current with different

responses in either scotopic or photopic conditions. In general, the positive current is the result of mainly ON-BP cells both CBCs and RBCs, and only to a minor extent OFF-BP responses [257]. In scotopic evaluations, light stimuli of increasing intensities ranges from very low to brighter luminance. While in low luminance conditions, rods are the only PR type driving the b-wave because of their higher sensitivity, at brighter values a contribution of cone-to-bipolar driven response is to be expected (in the so-called mesopic conditions). On the opposite hand, in photopic examinations, the resulting b-wave has been shown to be mainly, if not exclusively, mediated by cone-to-CBC responses. Indeed, before the evaluation, the eyes are initially exposed to constant bright light illumination for a certain time, at high enough luminance able to saturate rods even in the case such rods were desensitised and therefore “immune” to such saturation. Measurements in *Cnga3* knock out mice, affecting specifically CPs, gave overlapping responses to wild type (WT) animals suggesting that, under these conditions, the responses are entirely cone-driven [190].

4 Cones and colour vision

As mentioned before, among the five different classes of vertebrate opsins Rh1, Rh2, SWS1, SWS2 and LWS, mammals lost the Rh2 and SWS2 therefore possessing only two types of cone opsins: SWS1 and LWS and being dichromats. Later on, by duplication of the LWS gene, a new MWS gene was created conferring trichromat properties to primates [260]. When referring to mammals, the cones that possess the SWS1 are generally called S-cones or blue cones, while the ones with the LWS pigment are the M-cones or green cones. Finally, primates with a third cone sub-type, still of the LWS class, are called L-cones or red cones because of the spectral absorbance falling in the red range [103]. Mouse and humans vary not only because of the type of pigment that their cones express, but also in terms of arrangement. In fact, despite having only two types of pigments, mice have three different cone subtypes due to the fact that they do not only have single clones (S-cones or M-cones), but they also have double or hybrid cones (S/M-cones). Humans have three cones as well, but each of them expresses only one pigment type [90]. Moreover, in mouse and human retina, cones are arranged differently: in mice single M-cones are mostly found in the dorsal region (or lower visual field), true S-cones are instead less abundant but mainly enriched in the ventral region (or upper visual field), whereas hybrid cones are the majority in particular in the centre-to-ventral periphery [226]. In primates, the distribution of the cones and the ratio between rods and cones changes depending on the distance from the region with the highest visual acuity, a pit-like depression called fovea. In the fovea there are only M- and L-cones randomly distributed and in different numbers among individuals. This area is completely depleted of rods and S-cones [22]. Moving out from the fovea, S-cones increase in number, and they appear distributed in a regular and non-random array [227]. Rods outnumber cones in more peripheral regions [116].

Thomas Young advanced the first theory of colour vision, according to which the different species are able to discriminate colours based on the asset of pigments their cones express [258]. At the same time, this theory does not explain why species with theoretically two or three different pigments are actually able to discriminate a broader spectrum of light, for example by combination of these pigments in a single cone cell. Another important property of photoreceptors is the so-called theory of univariance, which says that the response of a cone photoreceptor does not depend on the associated λ (of that specific opsin), but it is rather the number of acquired photons. Therefore, if the number of photons for the two wavelengths is adjusted, the light-evoked responses will be indistinguishable [15]. The second theory of colour vision was proposed by Hering and hypothesised that perception of colours is based on the establishment of colour-opponency pathways where for example the red colour would be cancelled by its green opponent creating red-green responses (the same principle applied to blue-yellow and white-black for luminance/contrast) [152]. How and where this colour opponency arises in the retina is still under investigation and seems to vary among species; nevertheless, there are some common rules. For example, HCs through their negative feedback are known to create an antagonistic action on a given cone when their wide dendritic harbour is stimulated by other surrounding cones (Fig. 7). Indeed, light stimulation a given cone will evoke an hyperpolarising response in the centre of this stimulated cone. At the same time, the activation of surrounding cones and consequent hyperpolarisation of HCs causes a change in the inhibitory feedback from the HC to the central CP and consequent depolarisation response in that cone. This centre-surround receptive field is then passed on a cone-BP and in turn to ganglion cells. This arrangement has the advantage of removing redundant information about luminance and chromaticity, therefore enhancing the signal efficiency [14]. The same principle of negative feedback is applied and has been demonstrated to exist also in rods [259]. Two types of HCs have been identified so far: the A-, where the A stands for axonless, and the B- for axon-bearing, types. The equivalent in primate retina are the H2 and H1 types, respectively, while mice lack the A-type and only have the B-type [206]. Nevertheless, in mammals HCs never showed colour opponency following light stimulation, although they may still play a role in the appearance of colour opponency in both rodents and primates. For example, the H2 type in primates has been shown to receive colour opponent information from surrounding L+ M cones (yellow) contrasting the centre S-cone (blue) response through a negative feedback mechanism (Fig. 7) [145]. In mice, the same mechanism has been proposed as neuronal circuit supporting colour vision, at least in the upper visual field (ventral retina), where the genuine S-cones (blue) may receive negative feedback by HC received from neighbouring S+M cones [254]. Among the different BPs described in the previous paragraph, the majority receive inputs from both S- and M-cones, therefore opponent blue versus green signal are thought to be missing in the mouse retina. The two exceptions are the type 1 and type 9 that received inputs specifically from M- and S- cones, respectively, and may therefore provide the basis for dichromatic colour vision (M-OFF/S-ON), in particular in the dorsal retina where the majority are M-cones interspersed with blue cones

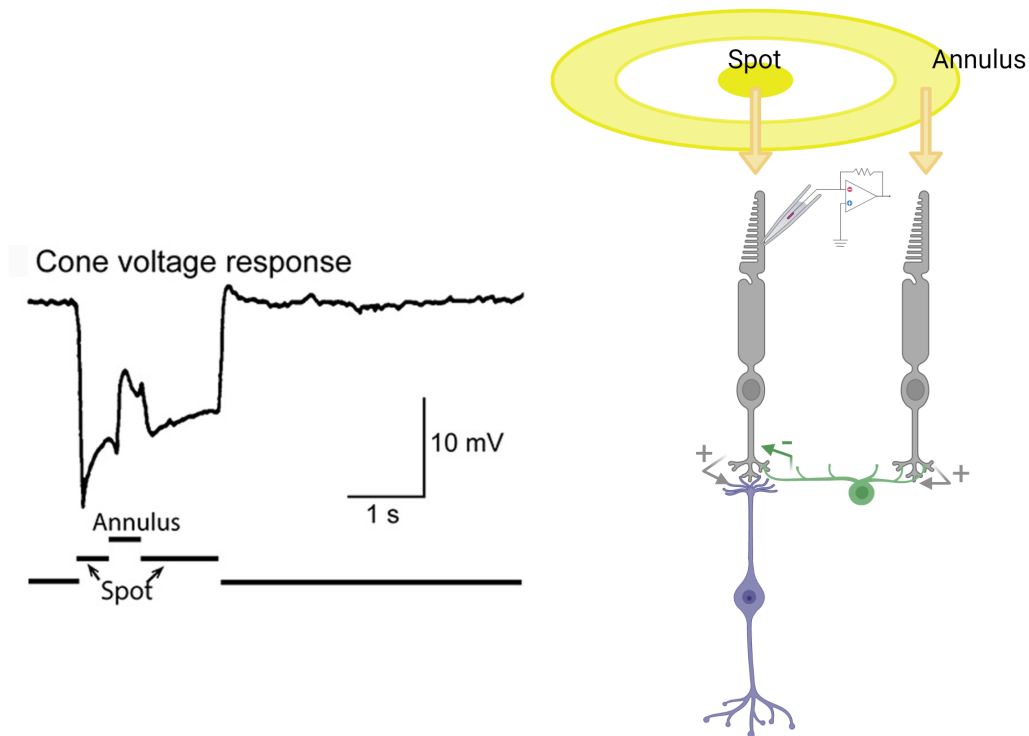


Figure 7: Horizontal cell inhibitory feedback

Schematics of inhibitory feedback from horizontal cell to cone photoreceptors. Recording from a cone receiving a spot of light illumination elicits an initial hyperpolarized response, followed by a depolarisation when an annulus is applied which stimulate surrounding cones and in turn HC inhibiting the initial cone response (adapted from [260])

[?]. This might not be the only retinal circuitry underlying colour opponency in the mouse inner retina because of the newly identified RGCs showing M-OFF/S-ON responses which do not rely on OFF type 1 BP [248]. However, so far clear colour opponency has not been detected in either bipolar cell sub-type in the rodent retina. On the other hand, primates have a defined separation in the colour opponent pathways for both blue-yellow and red-green mediated opponency. The former is achieved by a dedicated S-cone circuitry involving both centred S-ON and S-OFF bipolars [131][203], while the latter is established by unique centre contacts made by either M- or L-cones on ON or OFF mid-gate bipolar cells [47]. Finally, also ganglion cells show colour opponency in mostly S-cones mediated circuitry. Of these, some RGCs have a S-ON/M-OFF response, where the S-ON is mediated by the ON type 9 BP cells that exclusively contact blue cones, while the M-OFF surround seems to result from inhibitory feedback of amacrine cells receiving from M-cones, acting on type 6 and 8 ON-BPs [248]. These have been found in both dorsal and ventral periphery of the mouse retina, with reduced chromatic opponency in the ventral retina (consistent with the reduced M-opsin expression) [298]. The S versus M opponent RGCs is the functional counterpart of small bistratified RGCs observed in the primate retina and responsible for the blue-yellow colour opponency mediated by S-ON/L+M-OFF evoked responses [208]. In the transition zone, where the majority of cones are hybrid, a group of gan-

glion cells have been described to have both M-ON/S-OFF or S-ON/M-OFF, where both ON and OFF responses seems to be mediated by ON-BP cells with ACs lateral inhibition feedback on the M-OFF component [?]. This recently described mechanism of blue-green opponency is reminiscent of the red-green opponent circuit described for midget RGCs in the primate retina [204], where colour opponency is achieved by selective centre and diffuse surround taking advantage of the disperse and random distribution of the L and M cones [119] (similarly to the hybrid opsin expression in mouse cones). Lastly, mice also have a population of colour opponent RGCs consisting of S-OFF centre with a surround more sensitive to middle λ which has been attributed to rods [115].

5 Epigenetics

The term epigenetics was first coined by Waddington in describing how specialised structures are defined coming from a general precursor to a differentiated cell, how their cell-fate is acquired and where genetics comes into this scenario [276]. During the years epigenetics has been associated to the inherited tracts that determine gene expression and cellular memory, for example in the context of the chromosome X inactivation, where DNA methylation has been proposed to the mechanism mediating this process [97]. Genomic DNA methylation has then been linked to changes in transcription, extending the meaning of epigenetics to any DNA signatures generated in response to stimuli affecting the transcriptional output. The chromatin is composed of both DNA and associated proteins called histones which, through specific signature molecules or epigenetic marks, guarantee the correct assembly and packaging of the DNA into such complex structure preventing DNA damage and guaranteeing transcriptional regulation. Epigenetic marks can occur on either histone proteins, at different positions, or on the “naked” DNA. I will only focus on genomic DNA methylation, but for more extensive reads on histones and histones modifications, I recommend the following interesting reviews: [307] [144] , and [44] for more details in the retina context.

5.1 Genomic DNA methylation and demethylation

General DNA modifications are methylation on cytosines at position 5 (5mC) [101] and its oxidative states which include hydroxymethylation (5hmC) [255], formylcytosine (5fC) and carboxylcytosine (5caC) [106] (Fig. 8). Addition of the methyl group on the cytosine at position 5 is catalysed by a group of enzymes called DNA methyltransferases (DNMT), among which we can discriminate four members: DNMT1, 2, 3a and 3b. DNMT1 copies the methylation pattern from a mother to a daughter cell ensuring that the genetic information is preserved during cell division with a strong preference towards CpGs on hemimethylated DNA. [95]. DNMT3a/b are de novo methyltransferases whose role is to establish new methylation pattern on both hemimethylated and unmethylated DNA during differentiation and adulthood [74]. The effect of methylation

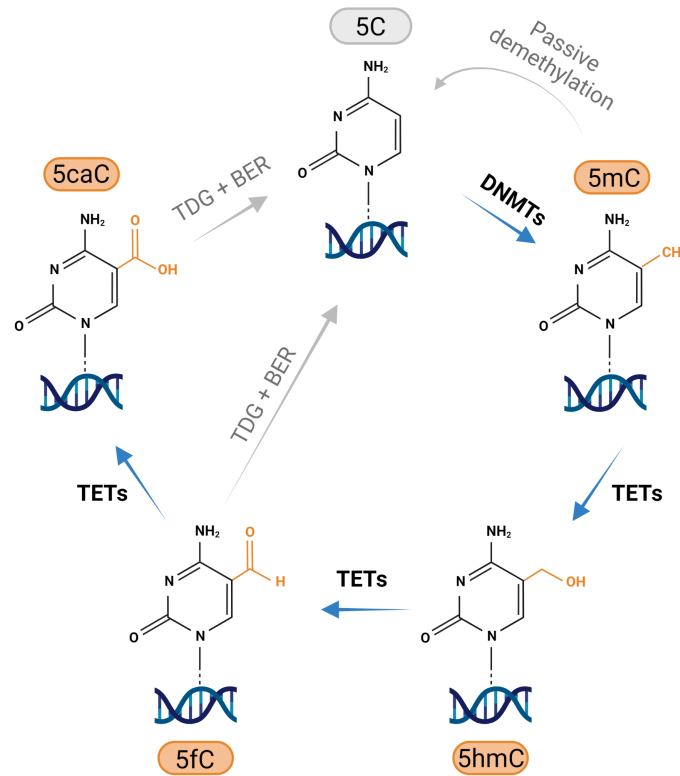


Figure 8: Epigenetics

Schematics of methylation and demethylation pathways with corresponding enzymes

on gene transcription depends on the number of these deposited epigenetic marks as well as the location in a gene at which these are observed. For example, accumulation of 5mC near the transcription start side (TSS) and enhancers regions has been inversely correlated with gene transcription, whereas its presence in the gene body positively influence this process [117], although methylation in the first intron has been consistently negatively linked with gene transcription independently from the tissue and the species [6]. Moreover, methylation is not only associated with variation in gene expression, but also to other processes such as splicing [11], in fact, the presence of methylgroups in intergenic region can promote exon skipping or alternative promoter usage, suggesting that the role of intergenic methylation depends on the context and probably also on the cell identity [170]. Further oxidative states of mC are catalysed by a group of enzymes called ten eleven translocation (TET) dioxygenases of which three members are so far known: TET1, 2 and 3 [255]. These enzymes oxidise 5mC into 5hmC and further into 5fC and 5caC, a process that is called active demethylation, opposite to passive demethylation that is observed during replication. During the demethylation process, 5fC and 5caC are quickly removed by thymine DNA glycosylase (TDG) [91], [168] and the resulting abasic site is removed by base excision repair (BER) mechanism reprimating the unmethylated cytosine [235] (Fig. 8). Conversely, 5hmC is a stable DNA modification accumulating in adult neuronal cells mostly in transcribed regions since its deposition in particular at the level of promoter and enhancer region has been positively associated with gene transcription [86] [209] [42].

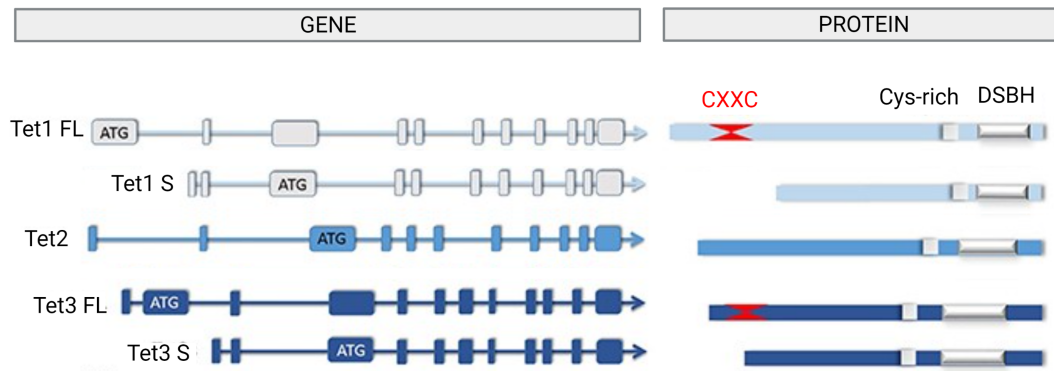


Figure 9: TET enzymes

TET isoforms and corresponding proteins with main domains illustrated. Image modified from [173]

5.2 TET enzymes, variants and function

The TET enzyme family are 2-oxoglutarate (2OG) dependent dioxygenases which require also Fe^{2+} and molecular oxygen (O_2) to support their reaction [134]. As mentioned before, the TET family includes three members. TET1 is mostly expressed in embryonic stem cells (ESCs), where it plays a major role in maintenance of pluripotency and downregulates during cell differentiation, TET2 is also expressed in ESCs and has also been linked with haematopoiesis and tumorigenesis; finally, TET3 is the only member expressed after fertilisation where it was shown to mediate mass demethylation of the paternal pronucleus [80], but more recent studies suggest that its deletion or inhibition affect the level of 5hmC at zygote level without affecting the 5mC erasure of the paternal pronucleus [5]. Subsequently, TET3 is expressed in differentiating cells, in particular in neurons [154] [173]. TET1 exists in three isoforms generated by alternative promoter usage which gives origin to three different isoforms: a long isoform which includes a CXXC domain, a short and a truncated protein (Fig. 9). TET2 is encoded by a single transcript which lacks the CXXC domain, although it seems that the same function is carried out by a neighbouring gene encoding for a CXXC4 protein originally thought to belong to TET2 before chromosomal arrangement (Fig. 9). Finally, TET3 exists in two main isoforms, a long isoform (full length, TET3 FL) which includes a CXXC domain for DNA binding, and a short isoform (TET3 S) generated by alternative promoter usage [154]. As for TET2, the short TET3 isoform, which lacks the CXXC domain, also appears to be associated with a CXXC4, that might direct the binding to the DNA. Alternatively, the same isoform has been shown to be recruited by other protein, e.g., REST, for TET3 mediated demethylation and activation of target genes [209] (Fig. 9). The major role of the CXXC domain/protein is to bind to unmethylated cytosine, to probably avoid aberrant methylation of these sites during cell differentiation. Moreover, TET3-CXXC domain has high affinity for 5caC, in particular it has been found close to promoter regions of selective neuronal genes where it may function as recruiter for proteins involved in BER mechanism [114]. All the members exert their function through a conserved catalytic domain which consists of a double-stranded β -helix and a cysteine-rich domain. The binding of the substrate

and the cofactors triggers the reaction: the O₂ oxidises Fe²⁺, the oxidation of the substrate, the decarboxylation of 2OG in succinate + CO₂, while the cysteine domain tightens the interaction between these factors [290]. Since TETs activity depends on these different cofactors, their function and kinetics can also be regulated by their availability and this may vary in pathological scenarios [151] [143] [296]. Moreover, both post-transcriptional and post-translational modifications have been identified, among these various microRNAs (miRNAs) are involved in TET transcript downregulation like miR15b [166], miR22 [245], whereas at protein level ubiquitylation, phosphorylation and acetylation of conserved residues have been described [188] [54] [12]. The mechanism of TET recruitment to targeted genetic loci has been investigated but it so far poorly understood, what is clear is that both protein-dependent and protein-independent (e.g., interaction with other proteins or transcription factors) seem to be involved. Because of the CXXC domain in both TET1 and 3 and its affinity to unmethylated or methylated cytosine, this has been used to partially explain the binding preference of these enzymes. Chromatin immunoprecipitation (ChIP) followed by sequencing suggested that Tet1 is enriched at CpG islands of promoters and enhancers and loci that are marked with open chromatin accessibility (e.g., H3K4me3) [288] [293]. Curiously, the short Tet1 isoform localises to similar genomic regions although the lack of the CXXC domain suggesting that other TET-independent mechanisms must be in place to direct its binding to these loci. In order to overcome the technical limitation of the lack of ChIP grade TET2 antibodies, Rasmussen and co-workers have used a CRISPR homology directed repair to insert a flag tag in the Tet2 locus of murine ESCs and showed that Tet2, similarly to Tet1, binds to CpG islands, promoter and enhancer region influencing the binding of TF and methylation readers [218]. The same method could in principle be applied to TET3 to unravel its genomic localisation which so far remain unknown [219]. As mentioned before, other factors have been shown to recruit the TETs to targeted genetic loci for active demethylation. Of note, in the mouse retina REST has been identified as TET3 interactor partner for targeted demethylation with positive regulation of gene expression [209], likewise the thyroid hormone T3 recruits TET3 to discrete genomic regions followed by gene expression [217] and TET3 has also been shown to interact with the thyroid hormone receptors (THR) and stabilise their association to chromatin [81]. Considering that TETs and TDG are tightly coupled in the context of DNA demethylation, it is also not surprising that TDG is similarly distributed to TET1 at enhancers and promoters [193] [50].

5.3 Localisation and function of oxidated genomic DNA cytosines

About the distribution of the different oxidised genomic cytosines, hydroxymethylation is the most abundant, especially in the central nervous system (CNS) and neurons, where the amount is five to ten times higher than in any other tissues [284]. This suggests that 5hmC is either only an intermediate of the demethylation process, serving to keep the methylation turnover high, or that its accumulation in certain tissue might exert its own function. 5fC and 5caC are less

abundant, either because the TDG is a very efficient machinery at removing these marks or because the kinetics of the conversion from 5hmC is less efficient. In agreement with the efficient TDG removal, studies focused on depleting this mechanism showed an increase in the amount of both DNA oxidated cytosines [240]. Differently from the TETs, in ESCs 5hmC is not enriched at promoter regions with high CpG content, which normally bear other pro-transcription marks for example H3K4me3 [244] [20]. Curiously, 5hmC is enriched at bivalent promoters, those promoters that are repressed in ESCs but are active during differentiation, suggesting that the localisation of 5hmC is strictly dependent on the tissue, the genetic and chromatin context [288] [293] [20]. Differently from the ESC, in neurons, 5hmC is completely absent from the TSS, independently from the CpG context, but is mainly observed at upstream and downstream positions from the TSS [150] [174]. In gene bodies, the amount of 5hmC increases from TSS to the end of transcription, pointing to a role of hydroxymethylation in transcriptional elongation [113]. On the same line, loss of intragenic 5hmC catalysed by Tet3 on highly expressed genes in smooth muscle cells resulted in aberrant transcription with accumulation of these transcripts and activation of pro-inflammatory pathways, suggesting a role for hydroxymethylation in regulating the entry of RNA polymerase II and transcription [287]. Finally, this epigenetic mark is also observed at exon-intron boundaries, therefore as for methylation, 5hmC might have a role in exon skipping and alternative promoter usage. [284] [125]. Due to higher 5hmC abundance in particular in neurons, unravelling the connection between DNA demethylation and neuronal function has become of high interest. On this regard, Tet1 deficiency in hippocampal neurons affects progenitor proliferation impairing learning and memory accompanied by a downregulation of multiple genes involved in neuronal plasticity [306] [228]. Moreover, Tet1 has critical role in neuronal cell death since its depletion increased the number of apoptotic cells following oxidative stress damage [292]. Ablation of Tet3 in mouse adult mature neurons results in increase anxiety-like behaviour [7], while its specific depletion from a subgroup of hippocampal neurons involved in feeding behaviour revealed a critical role in appetite and energy metabolism [291]. Furthermore, specifically in the context of the retina, hydroxymethylation has been shown to increase during retinal development and differentiation *in vivo* [209], and impairments of this TET-mediated DNA demethylation process during retinogenesis mostly affects terminal morphogenesis of retinal neurons [238]. Less is known on the other two oxidative intermediates: 5fC and 5caC. For example, both 5fC and 5caC transiently accumulate in undifferentiated cells, with 5fC relatively abundant at both poised and active enhancers [244] linking this mark to epigenetic priming, and 5caC mainly at tissue specific promoters, suggesting a role in lineage specification [286]. Their level is higher at early embryonic stages while they are basically undetectable in most of the adult brain cells [286]; the accumulation of 5fC in mouse ESCs positively correlates with enhanced gene transcription through its increased nucleosome occupancy at tissue specific enhancers [216]. Moreover, 5caC transiently accumulates in neuronal stem cells at promoters during both neuronal and glial differentiation possibly linking DNA demethylation to terminal differentiation and lineage specification [286]. The genomic localisation of 5fC and

5hmC strongly overlap although at single base level this overlap decreases suggesting that 5fC might have a different role [20]. In many studies on DNA stability, it has been shown that 5fC has an effect on local DNA structure and nucleosome stability due to higher DNA flexibility [196]. In mammalian cells 5fC delays the RNA polymerase II [123] and associates with many transcriptional regulators as well as with enzymes involved in DNA repair machinery suggesting a role for this epigenetic mark in transcription and DNA damage [107].

5.4 Epigenetic regulation of retinal development

The presence of DNMTs in the mammalian retina suggests a role for methylation in regulating gene expression during retinal development. Different studies have deciphered the importance of these enzymes in particular for photoreceptor and RPE maturation. Mutations in *Dnmt1* affect photoreceptor terminal differentiation with ectopic cell soma and aberrant dendritic morphologies, without altering cell fate commitment considering that all the major retinal cell types are formed [221]. On the same line, conditional knockout of *Dnmt1* in the embryonic retina did not cause lamination defect or altered retinal cell fate except for cone photoreceptors, in fact in these mice not only the total number of cones was reduced, but also the expression of S-opsin was impaired [225]. Moreover, photoreceptors did not have outer segments, which was attributed to aberrant polarity and malfunctioning of RPE cells [225]. The relationship between methylation and gene expression has been studied, and curiously, it has emerged that the many retinal cell types have different methylation status, for example, rhodopsin gene (*Rho*) is hypomethylated in rods around the TSS, but the same gene is hypermethylated in cone photoreceptors and cells in the inner retina [176]. This has made genomewide analysis of DNA methylation in whole retina difficult to interpret since a low correlation between methylation and gene expression has been observed, a phenomenon which could be partially explained when taking into account the multiple retinal populations and their contribution to the final methylation status [4]. Methylation accumulation at promoter regions is associated with silencing of gene transcription as for genes involved in pluripotency that are normally hypomethylated to keep their expression high but become hypermethylation upon cell differentiation [127] [142]. On the other hand, genes important for photoreceptor function and differentiation are highly methylated in retinal progenitor cells but hypomethylated or unmethylated in photoreceptors [59]. In the retina, Tet3 regulates DNA methylation status by binding at unmethylated promoter regions through its CXXC domain, therefore preventing aberrant DNA methylation and silencing of key gene promoters (*Pax6* and *Rx*) during eye formation [294]. In Tet2 and Tet3 double knockout studies in the zebrafish retina, a critical role of demethylation in terminal morphogenesis of differentiated neurons has emerged, where first born RGCs were less affected in their number but many failed to form and extend a neuronal axon and the few photoreceptors failed to form outer segments [238]. Finally, methylation and demethylation could have an impact on TFs binding to restricted chromatin regions and their interaction with epigenetic modifiers might help to ensure

stringent transcriptional regulation during retinal development. For example, CRX was shown to bind a methylated DNA motif different from its canonical one [102], as well as the histone acetyltransferases CBP and p300 for histone three (H3) acetylation at opsin promoter promoting transcription [207]. Analogously, Nr2e3 was shown to interact with polycomb repressive complex 1 (PRC1) for gene-selective repression of S-opsin expression in rod photoreceptors [201], whereas the repressive TF Rest was shown to recruit Tet3 to its binding sites for DNA demethylation and positive regulation of gene transcription [209].

6 Tools to investigate the role of epigenetics in mammalian retina

Genetic engineering is a process applied to alter the genetic (and epigenetic) context on an organism in order to directly manipulate the activity and/or function of one or more genes to address their physiological tasks. In this study two approaches have been employed to address the effects of DNA demethylation on retinal development and function. In the first approach, specifically the role of Tet3 in retinal development and function has been investigated using a genetically modified mouse line generated using the Cre recombinase technology (Fig. 10). The

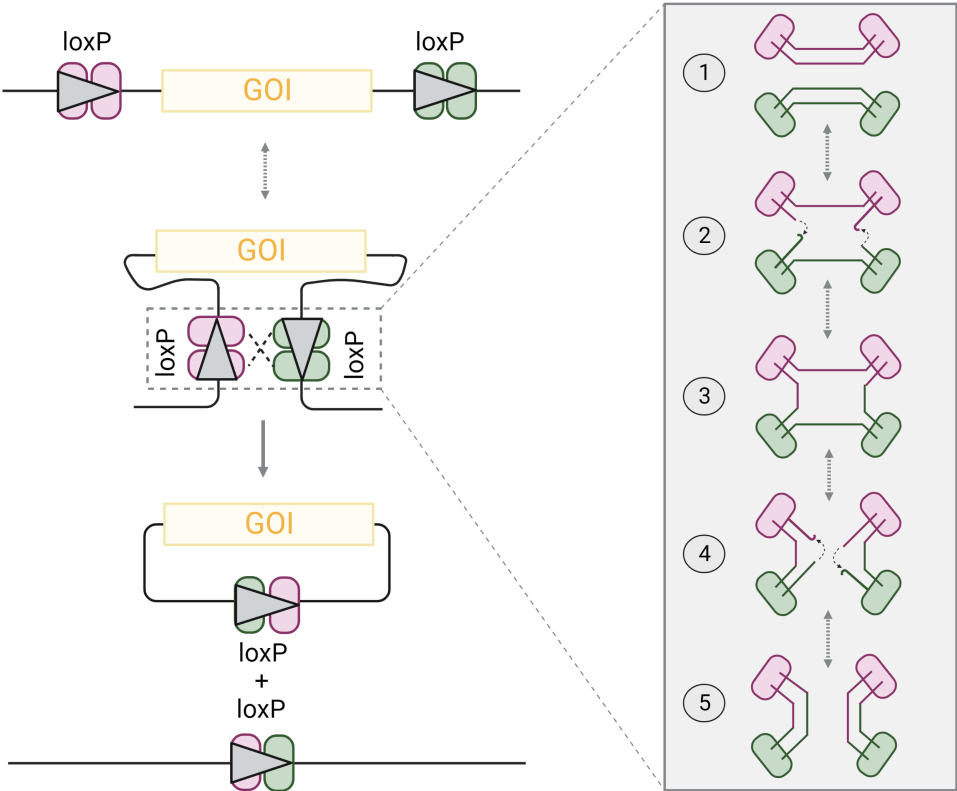


Figure 10: Homologous recombination

Schematics of the Cre-mediated homologous recombination. When the two loxP sites have the same orientation, the final product is the excision of the gene of interest (GOI)

Cre recombinase was first discovered in 1981 by Sternberg and Hamilton who found out that the bacteriophage P1 had site recombination properties by recognition of so-called loxP sites (locus of crossing (x) over, P1) [250]. The loxP sites consist of 34 base pair (bp) of two 13 bp palindromic sequences separated by a spacer of 8 bp. The orientation of the two loxP site is important for the Cre activity, when the loxP sites have the same orientation, the activity of Cre recombinase results in the excision of the genetic material in between the two loxP (the gene flanked by the two loxP sites is also referred to as “floxed”). In this study a floxed Tet3 mouse line and a Rx-Cre expressing mouse line were used to generate a conditional mutant Tet3 mouse line. The floxed Tet3 mouse line has the exon 7 and 8 floxed by two loxP sites inserted in the same orientation. These exons encode for part of the catalytic domain of Tet3 protein [5]. The Rx-Cre mouse line instead, expresses the Cre recombinase under the control of the Rx promoter, which is an important transcription factor for eye and retina development [130]. The crossing of these mouse lines results in the recognition of the two loxP sites by the Cre recombinase, a site directed recombination and final excision of the two floxed exons from the *Tet3* locus. In the second approach, a 3D model of human retinal organoids (hROs or simply ROs) derived from wild type (WT or control) human induced pluripotent stem cells (iPSCs) has been employed to address more general epigenetic questions. Retinal organoids are a simplistic but versatile tool to study basic biological questions *in vitro*, since they recapitulate the histoarchitecture of a vertebrate retina and contain all the major retinal cell populations [32] [46]. Initially, ROs are mostly aggregates of proliferating stem cells that in defined medium conditions soon acquire a retinal fate commitment recapitulating early neurogenic steps of optic cup formation. In ROs the temporal birth sequences of the major retinal cell types is preserved starting with RGCs and ending with photoreceptors and Müller cells, including RPE cells. [138] [164] [46]. The later stages of their *in vitro* differentiation are accompanied by morphological and structural maturation, with extension of bristles-like structures reminiscent of photoreceptors inner and outer segment formation [32], and establishment of functional synaptic connections among the different layers [46] as shown by recorded electrical activity following light-stimulation [87] [309]. With respect to mouse models, hROs are an attractive tool to investigate retinal development and related disorders in a context more representative of the human physiology. Recently, a mechanism involving retinoic acid (RA) has been described to define the spatiotemporal pattern of green and red cones in a model of hROs, which could not be previously investigated in mice because of their dichromatic vision [84]. On the other hand, the model presents known limitations, represented by the high variability in size and shape among several batches obtained from same and different iPSC lines [175], or the fact that the RPE that forms in ROs is never juxtaposed to the photoreceptor layer but usually finds place posteriorly to the neural retina [60]. Moreover, ROs lack blood vessels which are of mesodermal origin, supporting the maintenance of the system in the long-term, therefore early born cells like RGCs, facing the inside structure, are the first to die due to lack of nutrients and supplies, one reason of the lack of axonal ex-

tension and optic nerve formation [46]. Retinal organoids also lack microglia and even though recent protocols have allowed to reach a better cone to rod ratio [128], these structures still miss a macula. Despite these downsides, organoids have proven to be a versatile and easy to manipulate model for the elucidation of novel developmental mechanisms in health and disease in genetic [120] [211] [273] as well as epigenetic [163] [111] studies.

Part II

Methods

7 Animal experiments

7.1 Mouse lines

All animal experiments were conducted after approval by the competent authorities (Regierung von Oberbayern) in agreement with the German Animal Welfare and Institutional guidelines. Animals were kept in a 12h light-dark cycle and were provided with food and water *ad libitum*. Tet3 floxed mice [5] were obtained from Prof. Petra Hajkova (Institute of Clinical Sciences, Imperial College, London) under an MTA agreement with Dr. Koseki (Laboratory for Developmental Genetics, RIKEN Institute, Japan). Tet3 floxed mice bear two loxP sites between the exons 7 and 8 of *Tet3* locus, in the following referred to as control mouse line.

The Bl6.Cg-Tg(Rax-cre)1Zcoz/Ph mouse line, hereafter referred as Rx-Cre, was generated according to [130] and obtained under an MTA agreement from the Institute of Molecular Genetics of the ASCR, Prague, Czech Republic. The two mouse lines were crossed to generate a conditional *Tet3* mutant mouse line, hereafter referred as *Tet3* mutant, Tet3 cMut or simply mutants. As a result of the Cre recombinase activity, the Tet3 cMut line harbors a homozygous deletion of the exons 7 and 8 in the *Tet3* locus. Mice were analyzed independently from their gender and in experiments involving retinal dissection, the left and/or the right eye were sampled randomly or pooled together. The day of birth is counted as p0 throughout the entire study and all *in vivo* experimental procedures were performed on p30 young adult mice.

7.2 Genotyping

gDNA isolation

Ear or tail biopsies were collected in 1.5 mL tubes and used to isolate gDNA for gene region specific amplification by polymerase chain reaction (PCR). The resulting product was visualized on 2% agarose gels. In details, the gDNA was isolated by boiling the tissue in 300 μ L of 50 mM NaOH at 95°C for 10 min on a heating block. The solution was neutralized with 26 μ L of 1M Tris-HCl (pH 8) and vortexed. The samples were then centrifuged for 6 min at max speed (> 10 000 rcf) at RT. The resulting gDNA in the supernatant was used for amplification by PCR.

Polymerase chain reaction (PCR)

Master mix for the PCR reaction was prepared according to manufacturer instructions using GoTaq® as polymerase (Promega, #M3001). Annealing temperature was adjusted according

to specific set of primers used in the reaction. PCRs were run in a ProFlex™ 3x32- well PCR System (Applied Biosystems, Thermo Fisher Scientific). The resulting product was run on a 2% agarose gel and visualized under UV light (Gel Doc 2000, Biorad, Hercules, CA, USA). In the case of *Tet3*, a band at 206 bp is identified as wild type, while the floxed band appears at 280 bp. The presence of the Cre recombinase was confirmed by a band at 320 bp. Primers used for genotyping (in direction 5' – 3') and corresponding annealing temperatures are reported below:

Tet3 Fw: TGAGTAAGAGCAGGCAGGGAG

Tet3 Rev: CTAGCACCTCAGTCTGGGACC

Annealing temperature 60°C

Cre Fw: AGCACCAAAGCTCCAGTTACC

Cre Rev: CGTTGCATCGACCGGTAATGCA

Annealing temperature 60°C

7.3 Anesthesia

Prior to *in vivo* experiments mice were anesthetized by intraperitoneal injection of a combination of ketamine (40 mg/kg body weight; Medistar GmbH, Ascheberg, Germany) and Xylazine (20 mg/kg body weight, Xylarium®; Ecuphar GmbH, Greifswald, Germany), diluted in 0.9 % sodium chloride (NaCl 0.9 %, B. Braun, Melsungen, Germany). Deep sleep stage is confirmed by absence of reflexes (tail and pedal) and decrease in respiratory rate.

7.4 Electroretinography

Mice were anesthetized as described above and, after immobilization, drops of 0.5% tropicamide (Mydriadicum Stulln) were applied to dilate the pupils. Full-field electroretinography (ERG) responses were recorded using a Celeris apparatus (Diagnosys LLC). Light guide electrodes which are embedded in the stimulators were placed on each eye. The mice were evaluated under both scotopic and photopic conditions. For scotopic conditions, mice were dark adapted 24h prior the real experiment was performed. The photopic investigation was performed immediately after, following a 10-minute light adaptation step with 9 cd/m² background illumination. Electrodes were applied on each eye and, as one eye was recorded, the other eye served as reference. Sequential light stimuli of differential intensity were applied and recorded. For single-flash measurements under scotopic condition, 8 different stimuli at 0.003, 0.01, 0.03, 0.1, 0.3, 1, 3 and 10 cd.s / m² were used and for photopic evaluation 0.3, 1, 3 and 10 cd.s/m² with constant 9 cd/m² background illumination. One result was generated by averaging 5-10 sweeps, respectively. 50 ms were recorded prior to one sweep, while post-trigger time was 300 ms. Mice were kept warm for the entire duration of the experiment and to avoid dryness of eyes, mice received ointment (Bepanthen®, Bayer) after the procedure. Mice were moved back to their cage, positioned on

a warm surface kept at 37°C, given time to awake. Data was analyzed by the Espion software (Diagnosys LLC) and plot using graphpad.

7.5 Optical Coherence Tomography (OCT)

Mice were anesthetized as before, and the pupils dilated. During the scanning procedure, mice were placed on a rotating platform to ensure alignment and correct placement of the camera in front of the mouse eye. Custom-made contact lenses in combination with hydroxyl-propyl methylcellulose (Methocel 2%; OmniVision, Puchheim, Germany) kept the eye moist and avoided the refractive power of the interface between air and cornea. The ophthalmic examinations of mouse retinas were performed using a modified Spectralis HRA + OCT system (Heidelberg Engineering, Dossenheim, Germany) as described in [236]. Images were recorded in high resolution mode with the scanner set to 30° field of view. Data was analyzed via the Heidelberg Eye explorer software (Heidelberg Engineering).

7.6 Behavioral testing

Ligh-dark test

The light dark test apparatus is a box consisting of a light compartment for 2/3 of the space, exposed to the ambient or experimental light condition and the other 1/3 is a dark compartment completely in the darkness. The awake mouse was placed in the light chamber and left free to move in the experimental area for the following 5 min, time of the duration of the experiment. During this time, the movements of the mouse were recorded by a camera from above and monitored using the VideoMot2 software by TSE Systems. The test was performed under bright light conditions (82.8 cd/m²). After the experiment the mouse was returned to its cage. The box is thoroughly cleaned with ethanol and water after each run to prevent misbehaviors of next mice due to odorants. Mice were recorded once and mice excluded from the analysis, either because they did not move for the entire procedure or spent >90% of time in the light chamber) were not remeasured.

Optomotor test (qOMR)

Visual acuity measurements were carried out using the PhenoSys qOMR device [135]. The device consists of a PVC box (W/H/D: 53 x 54 x 40 cm) with four interconnected monitors attached to the inside working as single screen. The mouse was placed on a platform in the middle of the box and left for 5 minutes to adapt to the environment. An upper and a lower mirror create the illusion of infinite depth, preventing the mouse from jumping out of the platform. A contrast plate was inserted to improve the mouse tracking. Jumps off the platform may occur, if this happened during the experimental procedure, the mouse was gently repositioned on the platform. For the actual test, the mouse is presented with moving bars of different frequencies

at fixed contrast of 1 (100% contrast). The visual stimulus pattern consists of black and white squared stripes moving at frequency of 0.025, 0.05, 0.1, 0.15, 0.2, 0.25, 0.3, 0.35, 0.4, 0.425 and 0.45 cyc/° at the speed of 12°/s. Each trial was presented for 60 s and the direction of the moving bars was changed every 60° (5 seconds) to keep the attention of the mouse high. The sequential stimuli were shuffled in a random order and spaced by 5 seconds of gray screen to catch mouse attention. Head movements of the mice were recorded by an automated tracking, part of the OMRstudio software. Measurements were obtained on the average of three tests per animal performed on different experimental days. If one mouse was hyperactive or jumped often off the platform, it was remeasured at the end. All measurements were performed under photopic condition at a nominal brightness of 300 cd/m². After their performance mice were returned to their cage and the apparatus wiped with ethanol before the next mouse was measured. Mice were not kept in the chamber for more than 30 min each.

8 Tissue collection and image processing

8.1 PFA perfusion and sectioning of brain slices

p30 mice were anesthetized by intraperitoneal injection of a combination of ketamine (40 mg/kg body weight; Medistar GmbH, Ascheberg, Germany) and Xylazine (20 mg kg⁻¹ body weight, Xylarium®; Eucuphar GmbH, Greifswald, Germany), diluted in 0.9 % sodium chloride (NaCl 0.9 %, B. Braun, Melsungen, Germany). Deep sleep stage was confirmed by an absence of the reflexes (tail and pedal) and decrease in respiratory rate. Anesthetised mice were positioned under a chemical wood for cardiac exposure. A 21G cannula connected to a pump was used to perforate the left ventricle and flow PBS solution for 5 min at 0.72 mL/min. Upon bleaching of the liver, a small cut was made at the right atrium and at this point the solution was switched to 4% PFA/PBS for 20 min. Brains were dissected at the end of the procedure and transferred in 4% PFA/PBS overnight (O.N.) and kept at 4°C in PBS up to one week before processing. After this time brains were cut along the midline in two equal halves and embedded in a 2% Agarose solution in milliQ H₂O for cutting. Sagittal sections were cut at 60µm thickness at vibratome (VT1200S, Leica). Slices were stored in a 24-well plate (surrounded by parafilm) in 600 µL storing solution (30 % glycerol, 30 % ethylene glycol, 10 % PO₄ buffer 0.25 M pH 7.2 - 7.4 in water) at -20°C

8.2 Retina dissection

For the procedure deep anesthesia was induced with isoflurane at a flowing rate of 5% of the total chamber volume per minute, and the animal was sacrificed by cervical dislocation. Before eye enucleation, the temporal side was marked with a burn mark and tail biopsies were collected for confirmatory genotyping. The left and the right eye were enucleated and placed in a petri

dish filled with PBS under a stereomicroscope. If the tissue was intended for nucleic acid isolation, the anterior part of the eye was removed cutting below the ora serrata in order to break the connection between the retina and the ciliary body and facilitate removal of tissue. The retina was transferred in a 2mL safe lock Eppendorf tube (#K197151K) and snap frozen in liquid nitrogen. The frozen tissue was kept at -80°C for long term storage or immediately processed. In case of tissue sectioning, the eye was punctured with a 21G cannula (Sterican, B. Braun) and transferred to 4% PFA/PBS for 5 min on ice. A small cut towards the posterior side was made to keep track of the temporal burn mark. The anterior part was dissected cutting above the ora serrata to preserve the retinal integrity and cornea, vitreous and lens were manually removed. The remaining optic cup was transferred to 4% PFA/PBS for tissue fixation for 45 min on ice, then transferred to 30% sucrose in PBS solution for cryopreservation O.N. at 4°C . Finally, the eyecup was embedded in tissue freezing medium (Tissue-Tek® O.C.T.TM Compound, Sakura FinetekTM), frozen on dry ice, and stored at -80°C until use. For flat mounts preparations, four deep incisions were made on the optic cup to flatten it out. The retina was detached from the adjacent RPE, lifted and transferred to 4% PFA/PBS for 30 min at RT in agitation for fixation before immunohistochemistry. The tissue was immediately processed for immunohistochemistry. In case of dorso-ventral separation, isolated optic cups were cut in two halves from the temporal to nasal side, the RPE was removed, and the two areas were snap frozen and kept at -80°C until further use.

8.3 Immunohistochemistry

The procedure was performed as follow with slight modifications depending on the tissue to be analysed. Retinal sections of mouse tissue or retinal organoids were collected ($14\ \mu\text{m}$) sequentially at a cryostat (Leica CM1950) and stored at -80°C for long term storage or immediately used. Frozen sections were rehydrated for 20 min with PBS at RT and then section borders were delimited using a pap-pen. Sections were post-fixed with 4% PFA in PBS for 10 min at RT and rinsed three times with PBS before the blocking step. Blocking was performed with 2% BSA + 0.5% Triton-X 100 in PBS for 1 hour at RT, after which primary antibody diluted in blocking solution according to the table 2 and 3 and incubated O.N. at 4°C . The day after, sections were washed three times with PBS and incubated for 2 hours at RT in a secondary antibody solution diluted in blocking solution. Sections were washed three times with PBS and counterstained with DAPI (1:2000, D1306, Thermo Fisher) in PBS for 5 min at RT. Finally, sections were washed two times and mounted with a glass cover slide (18606-5, Aqua-Poly/Mount).

For flat mount staining and free floating sagittal brain sections, the tissue was immediately incubated in blocking solution (2% BSA/PBS + 2% Triton X-100) O.N. at 4°C rotating (in case of flat mounts) or shaking (free floating sections) and then incubated with primary antibodies diluted in blocking solution for two nights at 4°C . Retinae and brain sections were washed three times with PBS before incubation with secondary antibody solution diluted in 2% BSA/PBS +

0.5% Triton X-100 for 1h at RT. Retinae were mounted with the photoreceptor side facing the glass cover slide, brain sections were transferred to a glass slide, unfolded using a brush and mounted with a glass cover slide (18606-5, Aqua-Poly/Mount).

8.4 In situ hybridization assay (RNAscope®)

Retina cryosections were collected as previously described, but sections were dried at -20°C for 120min to retain tissue adherence before storage at -80°C. The RNAscope® Multiplex fluorescent v2 assay was performed according to manufacture instructions for fixed frozen tissue samples with minor modifications. Briefly, slides were washed several times with PBS and then baked at 60°C for 45 min, post-fixed in 4% PFA in PBS for 30 min at 4°C and dehydrated in increasing EtOH solutions (50%, 70%, 100%). For protease III treatment, the slides were baked for 10 min only at 40°C in the HybEZ™ oven and then washed several times with double distilled H2O (ddH2O). The mouse *Tet3* probe (ACD bio, #505491-C3) was diluted 1:50 in probe diluent (ACD bio, #300041) and hybridized for 2 hours at 40°C. Amplification steps were performed as described in the manual instruction (#323100-USM). For signal development of the C3 channel, Opal™ 570 (FP1488001KT, Akoya Biosciences) was diluted 1:1500 in TSA buffer provided in the RNAscope® Multiplex Fluorescent Reagent Kit v2 (#323100) and the slides baked at 40°C for 30 min. Nuclei were counterstained with DAPI (1:1000, D1306, Thermo Fisher) and mounted with a glass coverslip in Aqua-Poly/Mount. Positive and negative control sections were always included in each experiment.

8.5 Confocal microscopy

Laser scanning confocal microscope images were obtained using an inverted Leica SP8 confocal system (Leica) equipped with the following lasers: 405, 488, 552 and 638nm and with 20x or 40x objectives. Images, consisting of many z-stacks each of height 1 µm, with at least 1024 x 1024 pixels resolution, were acquired using the LAS X software (Leica) Images were saved as .lif file format to contain the metadata for the subsequent image analysis conducted via the Fiji ImageJ software.

8.6 Image processing

Image analysis was done in Fiji [233] collapsing the many acquired z-stacks into a maximum projection image and adjusting the brightness and contrast. When necessary, a Gaussian blur filter was applied with a sigma of 0.5 to 1 to smoothen the image and images were always background corrected. Maximum intensity projection images of a defined area (250µm x 250 µm) were used for manual cell count using the manual cell counter plugin. For cone image representation orthogonal projection of single stack image was used using the corresponding plugin. For flat mount preparation the entire size of the image was used for manual outer segment

Target protein	Host species	Company	Reference number	dilution
Arr3	Rabbit	Kindly provided	NA	1:200
AP2a	Mouse	Kindly provided	NA	1:500
Cacna1s	Mouse	Merck Millipore	MAB427	1:500
Calbindin (D-28K)	Mouse	Sigma-Aldrich	9848	1:500
cFos	Rabbit	Cell Signaling Technology	2250	1:1500
Ctbp2	Mouse	Kindly provided	NA	1:500
GS	Rabbit	Abcam	AB49873	1:500
GS	Mouse	Invitrogen	MA5-27749	1:500
Islet1	Goat	SantaCruz	sc-390793	1:100
Mki67	Rabbit	Thermo Fisher Scientific	MA514520	1:500
MYC	Mouse	Cell Signaling	9B11	1:500
M-Opsin	Rabbit	Merck	AB5405	1:500
S-Opsin	Rabbit	Merck	AB5407	1:500
S-Opsin	Goat	SantaCruz	sc-14365	1:1000
Pcp2	Mouse (IgG2b)	SantaCruz	137064	1:500
PKC-a	Mouse (IgG2a)	Leinco Technologies	P108	1:500
Lectin PNA-488	<i>Arachis- ipogaea</i>	Thermo Fisher Scientific	L21409	1:200
PSD95	Mouse	Merck	P246	1:500
Rho	Mouse	Merck	MAB5356	1:1000
Sox2	Rabbit	Abcam	AB97959	1:500
Tet3	Rabbit	Custom made	NA	1:500
TUNEL (Kit)	NA	Merck	11684795910	NA
vGlut1	Guinea Pig	SYSY	135318	1:500
Vsx2	Sheep	Exalpa	X1179P	1:500

Table 2: List of primary antibodies used with mouse tissue

Target protein	Host species	Company	Reference number	dilution
ARR3	Goat	Novus Biologicals	NBP1-37003	1:250
CRALBP	Mouse	Abcam	AB15051	1:200
CRX	Mouse	Abnova	H00001406-M02	1:200
GFP	Chicken	Aves Labs	GFP-1020	1:1000
GNGT2	Rabbit	Proteintech	11988-1-AP	1:200
M-OPSIN	Rabbit	Merck	AB5405	1:500
NRL	Goat	R&D Systems	AF2945-SP	1:500
OTX2	Goat	R&D Systems	AF1979-SP	1:500
RCVRN	Rabbit	Merck Millipore	AB5585	1:500
RHO	Mouse	Merck	MAB5356	1:1000
RPE65	Mouse	Novus Biologicals	NBP100-355SS	1:500
RXRG	Rabbit	Proteintech	11129-1-AP	1:200
S-OPSIN	Rabbit	Merck	AB5407	1:500
VSX2	Sheep	Exalpha	X1179P	1:500

Table 3: List of primary antibodies used with human derived tissue

counting using the same manual cell counter plugin. Synaptic markers (VGlut1, PSD95 and Cacna1s) positive areas were defined using the region of interest (ROI) manager in Fiji and the resulting area displayed in μm^2 . For sagittal brain sections and quantification of immediate early gene response (cFos), the number of cFos⁺ cells were quantified manually in layer IV of primary visual cortex identified by DAPI counterstaining as denser region as shown in the example in Fig. 11. The selected area was saved using the ROI manager in Fiji.

8.7 Electron Microscopy

Sample preparation

Eyes were enucleated and the optic cup isolated as previously described. The posterior part of the eye was fixed in 0.1M cacodylate buffer (sodium cacodylate trihydrate > 98% diluted in milliQ H₂O, Sigma, #C0250) containing 4% sucrose and 2% glutaraldehyde added freshly before fixation (50% stock aqueous solution, Electron Microscopy Sciences, #16320) for 3h at RT covered and protected from light. The optic cup was cut into dorsal and ventral halves directly in the fixative and then washed for three times in 0.15M cacodylate buffer. The halves were transferred in 2 mL safe lock Eppendorf tubes and kept at 4°C until further use.

Staining procedure

The procedure was carried out by Dr. Silke Haverkamp at CAESAR in Bonn according to [26] using the ROTO (reduced osmium-thiocarbohydrazide-osmium) en bloc staining protocol previously described (Briggman et al., 2011). 1 x 1 mm² pieces of fixed mouse retinas were rinsed

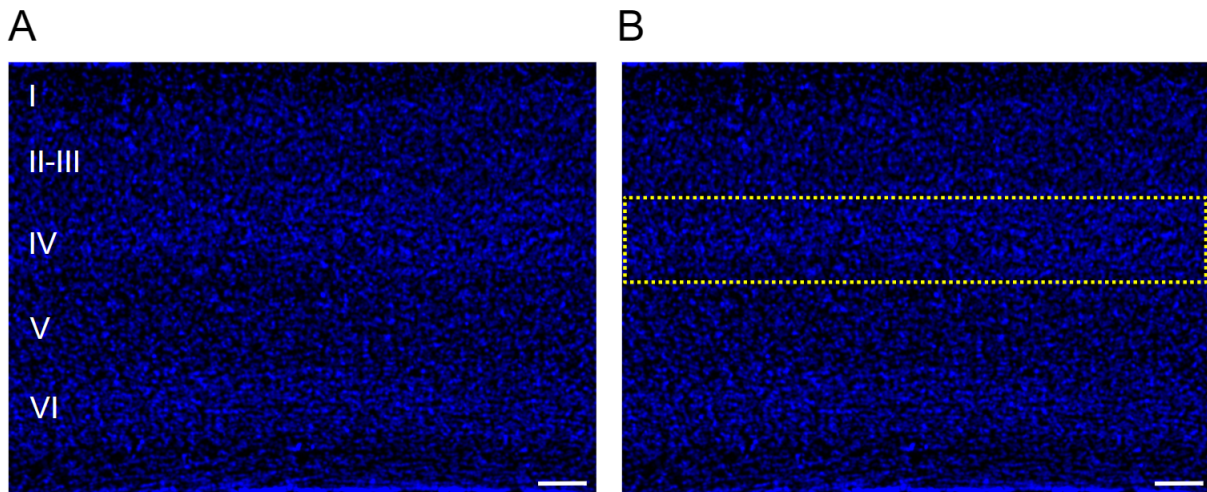


Figure 11: Identification of layer IV in primary visual cortex (V1)

Confocal micrographs of sagittal brain slice stained with DAPI for nuclei identification. Note the denser layer IV compared to layer II-III and V. Regions of interest (ROI) (yellow rectangle) were saved in ROI manager and used for manual quantification of immediate early gene response positive nuclei (not shown in the example). Scale bar= 200 μ m

in 150 mM CB with 1M CaCl₂ prior to EM staining. Samples were then stained in a solution containing 2% osmium tetroxide, 1.5% potassium ferrocyanide, and 150 mM CB for 2 hr at room temperature. The osmium stain was amplified with 1% aqueous thiocarbohydrazide (1 hr at 45°C), and then 2% aqueous osmium tetroxide (1 hr at room temperature). The samples were then stained with 1% aqueous uranyl acetate for 6 hr at 45°C and lead aspartate for 6 hr at 45°C. The tissue was dehydrated through an 70%–100% ethanol series, transferred to propylene oxide, infiltrated with 50%/50% propylene oxide/Epon middle hard, and then 100% Epon middle hard. The blocks were cured at 70°C for 48 hr. Ultrathin sections (45-70 nm) were cut from block faces and imaged on a Supra55 (Zeiss).

9 Molecular Biology Techniques

9.1 Genomic DNA extraction from tissue or cell pellets

For tissue or cell pellet lysis, 350 μ L lysis buffer consisting of RLT plus (provided in the RNeasy® Plus Mini kit, Qiagen, #74134) + 1% 2-Mercaptoethanol (Sigma, #M6250) was added. In order to homogenize the material, one stainless bead was added to the samples, and they were sheared for 1 min at 30 Hz. After removing the magnetic beads, the homogenous samples were centrifuged 5 min at 21 000 g at RT to remove the foam. During this time, Zymo-Spin™ IIC-XL columns (Zymo research, #C1102-50) were prepared by transferring the columns into de-capped 2mL Eppendorf tubes. After centrifugation the 350 μ L were transferred to the columns at 1500g for 4 min at RT and then 1 min at 10 000g. The flow-through contains the RNA to be used in the following RNA extraction procedure and can be either used immediately or stored at -80°C

for long term storage. In the meantime, RNase wash buffer was prepared diluting RNase A (Qiagen, #19101) at a final concentration of 0.4 mg/mL in Genomic Lysis Buffer (Zymo research, #D3004-1-250). After addition of 400 μ L per columns of RNase wash buffer, samples were incubated for 15 min and then centrifuged 2 min at 10 000g at RT. Samples were washed once with 400 μ L of gDNA Pre-Wash Buffer (Zymo research, #D3004-5-250), centrifuged for 1 min at 10000g and then twice with 600 μ L gDNA Wash Buffer (Zymo research, #D3004-2-250) and centrifuged 2 min at 10 000g. In each of the centrifugation step, the flow-through was discarded pipetting. The columns were placed in a fresh de-capped 2mL Eppendorf tubes and centrifuged again at 10 000g for 1 min to further empty and dry the tubes. For the elution, columns were transferred in a new 1.5 mL Eppendorf tube adding 100 μ L of MilliQ H₂O and incubating for 15min before centrifugation at 10 000g for 2 min at RT. The DNA concentration was measured using a NanoDrop 2000c spectrophotometer (Thermo Fisher Scientific). Good quality gDNA showed 260/280 and 260/230 ratios around 1.80-1.9 and >2 respectively. Samples were stored at -80°C until further use.

9.2 RNA extraction and cDNA synthesis

The extraction of the total RNA was performed using the RNeasy™ Plus Mini kit (Qiagen, #74134), according to manufacturer's protocol with minor modifications. Tissue or cell pellet lysis and homogenization were performed as described in the previous paragraph or, in case gDNA isolation was performed first, the first flow-through was used for the RNA extraction. The lysates were loaded were then processed as in the original provided protocol and the elution was performed with 30 μ L of RNase free H₂O. The RNA concentration was measured using a NanoDrop 2000c spectrophotometer (Thermo Fisher Scientific). RNA samples were processed immediately for cDNA synthesis and the left over frozen and stored at -80°C until further use.

First strand cDNA from RNA templates were synthesized using 100 ng of isolated RNA according the the manual protocol of the RevertAid First Strand cDNA Synthesis Kit (Thermo Ficher Scientific, #K1621). For the actual synthesis step a ProFlex™ 3x32- well PCR System (Applied Biosystems, Thermo Fisher Scientific) was used. The hybrid DNA-RNA product was diluted 1:100 in RNase, DNase free H₂O and stored at -20°C.

9.3 qRT-PCR and gene expression analysis

Quantitative Realtime Polymerase Chain Reaction (qRT-PCR) was performed on the StepOne-Plus Real-Time PCR system (Applied Biosystems, Thermo Fisher Scientific) using PowerUp SYBR™ Green qPCR Master Mix (Applied Biosystems, Thermo Fisher Scientific, #A25742) for quantification of the PCR product. All primers (table 4 and 5) were designed using Primer-BLAST with annealing temperatures between 58-62°C and with max difference of 3°C between the primer pairs. The primers were then ordered and synthesized by Eurofins as lyophilized pow-

Gene	Forward (Fw)	Reverse (Rev)
<i>Dio2</i>	TTGGGGTAGGGAATGTTGGC	TCCGTTTCCTCTTTCCGGTG
<i>Dio3</i>	GCTCGAAACAGCGCCTAAAG	TGGTCTCGAAGTCCATCCCT
<i>Isl1</i>	CTGCAAATGGCAGCCGAAC	TTCTCGTTGAGCACAGTCCG
<i>Lhx4</i>	GATCTCGGTAGACTGCGACTT	CACACTGGGGAATCTGTTGCAT
<i>Opn1mw</i>	TCCCACTCAGCATCATCGTG	GAGGCAGTATGCGAAGACCA
<i>Opn1sw</i>	GAGCCCCTCGAAACGAAGAA	GCTCCTTCTCACAGCTACGG
<i>Otx2</i>	TGAGGGAAGAGGTGGCACTGAA	GCCTCACTTTGTTCTGACCTCC
<i>Prdm1</i>	GTGGGTACGACCTTGGCTG	TTCAAACCTCGGCCTCTGTCC
<i>Prdm8</i>	TCCGCAGGATTGCCAAAGAT	GTAAGGAGACGACCCGTTCA
<i>Rxrg</i>	TGATTACTGACAGGCACCAGC	GCCCTCTGGGATTAGTCAGG
<i>Tet1</i>	TGAAGCTCAAACATCAAGCA	GTACCTCCATCACAGTCAC
<i>Tet2</i>	AGCGGAGCCCAAGAAAGCCA	GCAAAGCTGCGGTTGTGCTGT
<i>Tet3 FL</i>	ATCGTCGCACACACCAGATC	TCCTTCACGAGCAATTATTTCCA
<i>Tet3 total (FL + S)</i>	GAGCACGCCAGAGAAGATCAA	CAGGCTTTGCTGGGACAATC
<i>Thrb</i>	GTGTTTTCCCTCTCGTCCATCA	CTGTACTGGCATTCCCTCTGAC
<i>Vsx2</i>	CAAGAAGCGTAAGAAGCGGC	AGACATCTGGGTAGTGGGCT
<i>Gapdh</i>	AATGGTGAAGGTCGGTGTGAA	GCAACAATCTCCACTTTGCCA

Table 4: List of mouse primers for qRT-PCR

der which was resuspended according to the provided instructions using RNase, DNase free H₂O to 100 μ M final concentration. Primers were further diluted in a 10 μ M working concentration. Reaction mixtures consisting of 8 μ L Master Mix solution (1X SYBR green, 0.5 μ M primers in H₂O) and 2 μ L DNA solution (100ng diluted 1:10 in H₂O) were pipetted in MicroAmp Fast 96-well reaction plates (Applied Biosystems, Thermo Fisher Scientific, #4346907) and 1 μ L of previously diluted cDNA was used in a 10 μ L final reaction volume. All reaction plates were run in the Standard-Mode and comparative CT mode and then analyzed using by the StepOne™ Software (Applied Biosystems, Thermo Fisher Scientific). An $n \geq 3$ run in at least technical duplicates with Gapdh as housekeeping gene were used. Data were plotted using GraphPad.

9.4 Co-Immunoprecipitation (IP)

450 000 HEK294T cells were seeded in a 10 cm petri dish in 10% FBS (Bio and Sell, #FBS.S 0615) in DMEM (Gibco, #61965-026) w/o antibiotics. The day after cells were transfected with 20 μ g of single plasmid DNA, or 10 μ g each in case of co-transfection, using the Xfect™ Transfection Reagent Protocol (Clontech Laboratories, #631317). For GFP encoding plasmids, the GFP fluorescence was checked 24h after transfection. Cells were washed once with cold DPBS (Gibco, #14190-094), harvested by scraping and centrifuged at 300g for 5 min at RT. The

Gene	Forward (Fw)	Reverse (Rev)
<i>ARR3</i>	TCTCTCCCCAGAAAAGGCTC	GTCCCGTTTCCCCAGGTAGA
<i>CRX</i>	CTTTCTGAAGGCCCCCTGAC	ATCCACACTGGGGCCACTTA
<i>GLUL (GS)</i>	ATGCTGGAGTCAAGATTGCG	TCATTGAGAAGACACGTGCG
<i>OPNIMW</i>	CGTCATCGCCAGCACTATCA	TGTGATCCCACACAGGGAGA
<i>OPNISW</i>	GTCGCCAGCTGTAACGGATA	AACCAGACCTGCTACAGTGC
<i>RCVRN</i>	AGCTGCAGCTGAACACCAAG	TCGTCTGGAAGGAGCTTCAC
<i>RLBP1 (CRALBP)</i>	AGTCACAACCTGGCCCTGAC	AGTCACAACCTGGCCCTGAC
<i>RX</i>	GCGTTCGAGAAGTCCCCTA	GTTCTGGAACCACACCTGGA
<i>RHO</i>	TGGATACTTCGTCTTCGGGC	ACAGGGCAATTCACCGCC
<i>TET3</i>	TGGATACTTCGTCTTCGGGC	CCTCGTTGGTCACCTGGTTC
<i>VSX2</i>	CGGCGACACAGGACAATCTT	GGGTAGTGGGCTTCGTTGAA

Table 5: List of human primers for qRT-PCR

supernatant was removed and the cell pellet snap frozen in liquid nitrogen. Cells were either processed immediately or stored at -80°C. Cells were lysed in lysis buffer (20 mM Tris HCl pH 8.0 (Sigma, #T2194), 140 mM NaCl (Sigma, #59222C), 1% Igepal (Sigma-Aldrich, #I8996) and 2mM EDTA (Invitrogen, #15575-038) in PBS added of fresh protease inhibitor (cOmplete™, Roche, #04693132001)) and incubated for 2h on a tube rotator at 4°C to ensure full lysis. Then, the lysates were centrifuged at 10 000g for 10min at 4°C to remove the debris (the pellet) and the supernatant containing the proteins was transferred to a new tube. Meanwhile, Dynabeads Protein G (Thermo Fischer Scientific, #10004D) were washed three times with IP wash buffer (same as lysis buffer but w/o Igepal and protease inhibitor) and incubated with 1.5 µg of anti-Myc antibody (Cell Signaling, mouse mAB (clone 9B11), #2276S) or with 1.5 µg of Normal Mouse IgG (Santa Cruz, #sc-2025) for the IgG control. The mixture was incubated for 1.5 hours at 4°C on a tube rotator and then washed three times with IP wash buffer.

Protein concentration was determined using Qubit4 (Thermo Fischer Scientific) and Qubit Protein Assay-Kit (Thermo Fischer Scientific, #Q33211). 250 ug of protein lysates were used for the IP and IgG contro, and diluted in 200 µL of ice cold PBS. After incubation the beads-Ab mix was incubated with the lysates for 1h at 4°C on a tube rotator. Afterwards, the beads with the bound proteins were washed three times with 500 µL of IP wash buffer. Proteins were eluted in two rounds, first adding 25 µL of 1x SDS loading buffer (50mM Tris-HCl pH 6.8, 100 mM DTT, 2% SDS, 10%Glycerol, 0.1/ bromophenol blue), and incubating at 70°C for 10 min and then adding 8 µL and boiling at 95°C for 10 min. The two eluates were pooled together and loaded on SDS-PAGE precast gel (4–20% Mini-PROTEAN® TGX™ Precast Protein Gels, Biorad, #4561096). For input material, 10% of the protein lysates were used and mixed with 5x SDS loading buffer and incubated at 95°C for 10 min.

9.5 Western blot

The eluates and a PageRuler™ Plus Prestained Protein Ladder (Thermo Fisher Scientific) were loaded onto the precast gel and the SDS-PAGE was run at 100V and RT for 10 min and 140V for 1 h in 1x Electrophoresis buffer (10X stock 250mM Tris, 1.92M Glycin, 1% SDS). The run proteins were then blotted to a PVDF membrane (Roche, #03010040001) in cold 1x Blotting buffer w/ 20% methanol (10x stock 250 mM Tris, 1.92M Glycin, 0.38% SDS) and run at 25V at 4°C overnight. Afterwards the membrane was blocked with 5% non-fat milk powder (AppliChem) in 1x TBS-T buffer (10x stock 200 mM Tris pH7.5, 1.5M NaCl + 0.1% Tween-20) and incubated agitating at RT for 1h. The membrane was cut in two pieces between 100 and 70 kDa bands. The upper half was incubated with anti-GFP antibody (Clontech, #632381), while the lower half was incubated with the same anti-Myc antibody used for IP, both at 1:1000 in 2.5% milk in TBS-T. The membranes with the primary antibodies were incubated on an orbital shaker for 1h at RT. Membranes were washed three times with TBS-T to remove the excess of antibodies and then incubated with secondary antibody solutions for 1h at RT. The upper half containing the GFP-Tet3 protein band (≈ 250 kDa) was incubated with anti-mouse HRP antibody diluted 1:2000 in 1% milk in TBS-T (Santa Cruz, sc-2005), while the lower half, with the Thrb2-myc tagged band (≈ 60 kDa), was incubated with VeriBlot® for IP (Abcam, #131366) 1:5000 in 1% milk in TBS-T. After washing the membrane three more times in TBS-T buffer and rinsing it with TBS, the western blot was developed by applying Immobilon® Forte Western HRP substrate (Millipore, #WBLUF0100) according to the manufacturer's instructions. The signal was detected using the ChemiDoc™ MP Imaging System (Bio-Rad).

9.6 Gibson assembly and bacterial transformation

For cloning, Gibson Assembly (GA) (Gibson et al., 2009) was used. Backbone plasmids were enzymatically digested and dephosphorylated to avoid re-ligation. Primers were designed using the NEBuilder Assembly tool (nebuilder.neb.com) with at least 20 bp overlap to the corresponding insertion region and manufactured as cloning oligos by Eurofins Genomics. Primers were used to PCR amplify the region of interest. PCR products and linearized vectors which were subsequently run on an 0.7-2% agarose gel and excised for DNA purification according to QIAquick Gel Extraction kit (Qiagen, #28704) protocol. For the actual GA procedure, all the purified vectors and inserts were mixed in equimolar ratios of 1:3 or 1:5 calculated using the open source software NEBioCalculator (New England Biolabs). These were mixed with a self-made Gibson assembly mix containing a 5' exonuclease, a DNA polymerase and a ligase for 1 h at 50 °C. 5 μ L of the GA mix was used to transform chemically competent 10-beta Escherichia coli K12 bacteria (New England Biolabs). In brief, bacteria cells were thawed approx. 30 min prior the procedure, as well as agar plates were warmed up at RT. 5 μ L of the GA mix were added to 50 μ L of competent cell mix and the tube was tapped at the bottom gently to mix. The cell-DNA mixture was incubated on ice for 30 min and then heat shocked for 30-45 s at 42°C in

a dry bath. This allows small pores to form on the membrane of the bacterial cell and facilitates the penetration of the ligated plasmid in the cell. After the brief thermal shock, the cells were transferred again on ice for 2 min to ensure the closure of the pores. For Kanamycin resistant plasmid, 300 μ L of LB+ medium was added to the tube and the bacteria were shaken for 1h at 37°C. After this time, the solution was transferred and distributed on the agar plate and left growing O.N. at 37°C in an incubator (Heraeus, Thermo Fisher Scientific). Plates were checked for colonies and either stored at 4°C sealed with parafilm or picked the same day for bacterial growth. For small-scale production 5 mL of LB+ medium were supplemented with 100 μ g/ml ampicillin or 150 μ g/ml kanamycin, inoculated with one colony and incubated at 37 °C in a shaking incubator (Certomat IS, B. Braun Biotech International) at 225 rpm overnight. The plasmid DNA was extracted using an alkaline lysis-based protocol. For medium scale production 100 mL of LB+ medium was used, and the plasmid DNA was isolated from the bacteria using the PureLink™ HiPure Plasmid Midiprep kit (Invitrogen, Thermo Fisher Scientific). Before use all the plasmids interest were checked with sequencing performed by Eurofins Genomics.

10 Cell culture

10.1 HEK293T

Culture

Cells were maintained in T-75 flasks in complete medium containing DMEM + Glutamax and high glucose (Gibco, #61965-026) supplemented with 10% FBS and 1% P/S, and passaged at 90% of their confluency. For splitting, the media was removed, the flask washed once with DPBS (-Ca⁺⁺, -Mg⁺⁺) and after addition of 0.05 % Trypsin-EDTA (Gibco, #25300-054), the flask was incubated for 5 min at 37°C. Cells were counted with 0.4% Trypan Blue (Thermo Fischer Scientific, #T10282) and the Countess 3 FL Automated Cell Counter (Thermo Fisher) before seeding at the desired density in a new recipient flask. For cryopreservation, the cells were detached as described, collected in a 50 mL falcon tube and centrifuged at 300g for 5 min. The media was removed, the cell pellet resuspended in freezing medium (DMEM + Glutamax, +20% FBS and 10%DMSO (Sigma Aldrich, #C6295)) and preserved in liquid nitrogen.

Transfection

At 90% of their confluency cells were passaged and seeded in the desired density in either 6-well plates or 10 cm dishes in warm medium w/o antibiotics. The day after seeding cells were transfected using the Xfect™ Transfection Reagent Protocol (Clontech Laboratories, #631317) according to manufacturer's instructions. For 6-well plates, 3 μ g of total DNA plasmid were used (1.5 μ g each in case of co-transfection), while for 10 cm dishes 20 μ g of total DNA plasmid

were given (10 µg each in case of co-transfection). A maximum of two plasmids were transfected at the same time. Cells were harvested or fixed for immunohistochemistry after 24 hours.

10.2 induced Pluripotent Stem Cell (iPSC) culture

01F49i-N-B7 (short name: B7) clone [45], PGP#1 and CRTD, were grown on 6-well plates (#Corning, #3516) coated with human embryonic stem cells Matrigel coated plates (Corning, #354277) at 37°C and 5% CO₂ in mTESR1 medium (Stem Cell Technologies). For the coating, a Matrigel aliquot, thawed at 4°C O.N., was diluted 1:100 in X-vivo medium (Lonza#be-04-380q), distributed in 6-well plates and plates incubated for at least 4h at 37°C. Cells were grown until 80% confluence at which point, they were split adding 600µL of 0.5 mM EDTA (Invitrogen, #15575020) or TrypLE express (Thermo Fischer, #12604013, according to manufacturer instructions) in sterile DPBS and incubating 3 min at 37°C. The EDTA solution was removed, and cells were washed with 1 mL mTESR1 media minimizing the pipetting enough to break the colonies into small pieces. Cells were transferred to a new Matrigel coated plate at 1:3 – 1:6 ratio. Media was exchanged every day and double fed on weekends. For B7 cryopreservation, cells were detached as described and, centrifuged at 300g for 5 min and resuspended in CryoStor (Stem Cell Technologies, #07930). Cells were preserved in cryovials and stored in liquid nitrogen until further use. PGP#1 and CRTD were cryopreserved in 10% DMSO molecular grade solution/media. Cells were transferred at -80°C for the first 24h and then to liquid N₂ for long term storage. When bringing the cells into culture, warm media was supplemented with 10 µM ROCK inhibitor (Y27632, Stem Cell Technologies, #72302) or Revita cell (Thermo Fischer, #A2644501) for the first 24 hours

10.3 Human Retinal Organoids (hROs)

Differentiation protocol

Retinal organoids were differentiated from PGP#1, CRTD and B7 cells according to the following protocols [38] [32] [128] when iPSCs reached 90% of their confluency. [32] was followed with minor modifications. In brief, colony bonds were weakened with Dispase 1U/mL (Stem Cell Technologies, #07923) and incubated for 7 min at 37°C. The well was washed three times with warm media to dilute the Dispase and then 2 mL of warm mTESR1 media was added. Afterwards, the colonies were detached using a cell scraper and transferred into 35 mm dish (Stem Cell Technologies, #38069). This is referred as d0 of the culture. Cells formed embryoid bodies (EBs) within 24h and media was slowly transitioned into neuronal induction medium (NIM) consisting of DMEM/F12 + Glutamax (Gibco, #31331-028), 1% MEM-NEAA (Gibco, #11140-035), 1% N-2 supplement (Gibco, #17502048). On d1 media was changed in 75% mTESR1 and 25% NIM, on d2 in 50% mTESR1 and 50% NIM, on d3 in 25% mTESR1 and 75% NIM and from d4 to 100% NIM. Media was changed every day until d6. On d6 1 35mm

dish with mature EBs was transferred on 3 wells of a 6-well Matrigel coated plate, where they attached after 24h. The adherent culture was kept in NIM media until d15 with media change every other day. Afterwards, media was changed in Retinal Differentiation Media (RDM-A) containing DMEM + Glutamax mixed with F12 + Glutamax (Gibco, #31765-027) in a ratio 3:1, supplemented with 1% MEM-NEAA, 2% B27 w/o vitamin A (Gibco, #A3353501) and 1% Anti-mycotic/Anti-biotic (A/A). During this time cells spontaneously differentiate and optic vesicles (OVs), containing neuronal retina and dark pigmented epithelium are formed. Between d25 and d30, time when OVs are well formed, the adherent culture is roughly broken with a p200 tip with zig-zag movement at 0° and 90° plate orientation. The pieces are transferred to TPP® culture dishes (#Z707651) and cultured as suspension culture from this point on in RDM-A media until d41, changing media every other day. During the suspension culture, organoids self-assemble and from d40 retinal vesicles are clearly visible. On d42, the media was changed to Retinal Maturation Media 1 (RMM1) consisting of RDM-A supplemented with 10% FBS, 100 µM taurine (Sigma, #T8691) until d69, with media change every other day. On day 70, 10 µM retinoic acid was added to the RMM1, decreased to 5 µM on d100 and completely removed from d130 to favor outer segments formation. At this time point, the media was switched to RMM-2 where 2% B27 w/o vitamin A was replaced by 1% N-2 supplement. From d70 the media was changed twice per week and organoids kept until the point of analysis.

10.4 Electroporation

ROs were kept in RMM1 or 2 without A/A for better electroporation efficiency and plasmid expression. The organoids were placed in a petri dish filled with warm media and plasmids at a concentration of 1 µg/µL, supplemented with fast green (0.1%; Sigma) for visualization, were either injected into retinal vesicles cavities or solution drops dispersed in the media facing the outer side of the retinal vesicle. Electroporation was performed with the BTX Gemini X2 electroporation device (Harvard Apparatus) and Platinum Tweezer Electrodes (3mm, #BTX450487) by subjecting the organoids to a 1 second interval with 5 pulses of 50 ms duration at 80V. Medium was changed to antibiotic containing RMM1 or 2 on the next day and kept for 2 weeks before fixation and embedding (as described for retinal tissue in section 8.3)

11 Sequencing

11.1 EPIC array

The procedure was carried out by Dr. Gilles Gasparoni from Prof. Dr. Jorn Walter's research group at Saarland University in Saarbrücken.

Per sample 2,000 – 2,500 ng were used with the TrueMethyl oxBS Module (Tecan, #0414-32) according to the manufacturer's protocol to achieve bisulfite conversion (BS) and oxidative

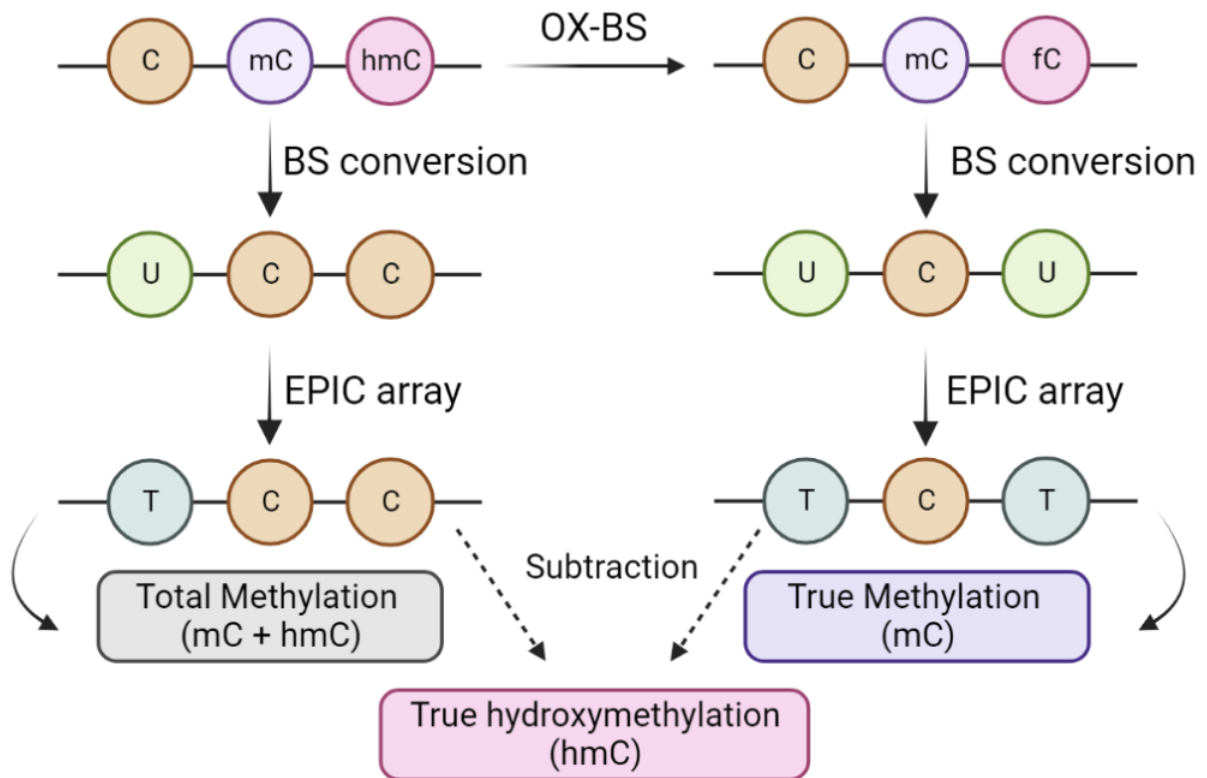


Figure 12: Schematic representation of bisulfite (BS) and oxidative bisulfite (OX-BS) procedure

bisulfite (OX-BS) conversion, respectively. The converted DNAs (bisulfite converted and oxidative bisulfite converted) were then hybridized to the Infinium Mouse Methylation BeadChip (Illumina) using the manufacturer's recommendations. The bead arrays were scanned on an Illumina HiScan. The raw data files were processed with RnBeads (v2.16.0, [137] [185] [9]) using dazen normalization (no background subtraction). The obtained methylation values were then further analyzed in R, where the values obtained from the oxidative bisulfite converted DNA was considered as true 5mC signal (mC) (Fig. 12) and values obtained from the bisulfite converted DNA was considered as a combined 5mC plus 5hmC signal (mC + hmC) (Fig. 12). Accordingly, 5hmC values were calculated by subtraction of OX-BS values from BS values (Fig. 12). By this mathematical operation we obtained both positive and negative values across the entire set of CpGs. Only those CpGs which exhibited a positive value for each of the three biological replicates (control or mutated) were considered as a true 5hmC signal. Differential analyses were performed separately on 5mC and 5hmC levels using Student's T-tests. Further evaluation of differential CpGs (ranking) was relying on CombinedRank metrics as implemented in RnBeads. Briefly, CombinedRank is based on the average of the two rankings based on p-values (T-Test) and the average delta between two groups.

11.2 Bulk RNA-seq library preparation and sequencing

RNA sequencing was carried out by Dr. Gilles Gasparoni from Prof. Dr. Jorn Walter's research group at Saarland University in Saarbrücken.

RNAseq libraries were prepared using 100 ng of total RNA per sample with the NEBnext Ultra II Directional RNA library kit for Illumina (New England Biolabs) according to the manufacturer's recommendations. Libraries were quantified with the NEBnext library quant kit for Illumina (NEB) and then sequenced for 100 nt using a V3 single read flow cell on a HiSeq 2500 (Illumina). After QC with FastQC Version 0.11.2 (<http://www.bioinformatics.bbsrc.ac.uk/projects/fastqc/>), reads were adaptor-trimmed ($Q < 20$) with Cutadapt (Version 1.4.132) using Trim Galore! (Version 0.3.3) (https://www.bioinformatics.babraham.ac.uk/projects/trim_galore/). Reads were aligned to mm10 assembly with the grape-nf pipeline (<https://github.com/guigolab/grape-nf> wrapping STAR (Version 2.4.0j33, [55]) and RSEM (Version 1.2.2134, [146]). Differential analysis was performed in R using the DESeq2 package [158].

12 Fluorescent Activated Cell Sorting (FACS) of cone photoreceptors

12.1 Retina dissociation

Two retinæ were pooled from one animal for dissociation which was performed according to [67], using the Papain Dissociation System (Worthington Biochemical Corporation link) with minor modifications. Briefly, retinæ were minced into smaller pieces and incubated in a mixture of papain and DNaseI at 37°C on a dry bath for 45 minutes and 650 rpm. Dissociation was monitored and stopped when pieces were no longer visible. To stop the digestion action of papain, a neutralizing solution containing DNaseI/BSA/Ovomucoid in EBSS was then added, followed by BSA/Ovomucoid and more pipetting, until no more retinal pieces were visible. In general pipetting was minimized to ensure survival of the cells and stopped when tissue pieces were no longer visible. The cell suspension was then centrifuged at 300 g for 5 min at 4°C and the supernatant discarded. The cell pellet was resuspended in FACS buffer (5% FBS and 2 mM EDTA in DPBS) for the labeling procedure.

12.2 PNA labelling of cone photoreceptors

From the cell suspension, 10 μ L were used as unstained control and diluted in 500 μ L of FACS buffer ready for sorting. For the staining procedure, 1:50 PNA-488 label was added to the cell suspension and incubated for 20 min. Then, the stained suspension was centrifuged at 300g for 5 min, and the pellet washed once with FACS buffer, centrifuged again at 600g for 5 min and

resuspended in 500 μ L of FACS buffer for sorting.

12.3 FACS

FACS was carried out by Pardis Khosravani at the Core Facility Flow Cytometry at the Biomedical Center, LMU Munich.

Cell sorting was performed using a FACS AriaIIIu (Becton Dickinson) on BD FACSDiva software v8.0.1 using a 70 μ m Nozzle. To this end, cells were filtered through a PluriStrainer Mini 40 μ m (PluriSelect, #43-10040-60) right before sorting. Gates were adjusted according to forward (FSC) and side scatter (SSC) behavior to identify cells based on their size, granularity and complexity. The events with very low FSC and SSC, representing debris and cell fragments, are eliminated. Afterwards, clumps (with increased area relative to the height) were identified and gated out. The remaining single cells were gated based on their 488-channel emission and PNA⁺ cones were sorted in PBS. Samples were centrifuged at 500g for 10 min, the supernatant removed and the snapped frozen pellet stored at -80°C until use.

12.4 Mass spectrometry-based whole proteome analysis of sorted cone photoreceptors

The MS samples were prepared using the filter-aided sample preparation (FASP) protocol. The cells were lysed using 100 μ L of 8 M urea in 100 mM Tris/HCl pH 8.5. The reduction and alkylation was done by 10 mM TCEP (tris(2-carboxyethyl)phosphine) and 40 mM CAA (2-chloroacetamide) at 95 °C for 5 min. Subsequently, the lysates were cleared by centrifugation at 14,000 g for 5 min. The supernatant was transferred onto 30 kDa cut-off column (Microcon - 30, Centrifugal filters, Merck Millipore). The samples were topped with 200 μ L of 8 M urea in 100 mM Tris/HCl pH 8.5 and spin down at 14,000 g for 15 min. The proteins were subsequently washed twice with 100 μ L ABC buffer (50 mM NH₄HCO₃ in water). The protein digest was performed in 100 μ L of ABC buffer with trypsin (1 μ g, Promega, V5113). Before incubation overnight at 37 °C the columns were mixed at 600 rpm for 1 min. After the digest the peptides were eluted by spin down at 14,000 g for 15 min into a new 1.5 mL eppendorf tube. The filters were washed twice with 40 μ L of ABC buffer and acidified using 1 μ L of formic acid. The peptides were concentrated on SpeedVac to volume of 30 μ L.

MS measurements were performed on Orbitrap Eclipse Tribrid Mass Spectrometer (Thermo Fisher Scientific) coupled to UltiMate 3000 Nano-HPLC (Thermo Fisher Scientific) via an EASY-Spray source (Thermo Fisher Scientific) and FAIMS interface (Thermo Fisher Scientific). First, peptides were loaded on an Acclaim PepMap 100 μ -precolum cartridge (5 μ m, 100 Å, 300 μ m ID x 5 mm, Thermo Fisher Scientific). Then, peptides were separated at 40 °C on a PicoTip emitter (noncoated, 15 cm, 75 μ m ID, 8 μ m tip, New Objective) that was packed in house with Reprosil-Pur 120 C18-AQ material (1.9 μ m, 150 Å, Dr. A. Maisch GmbH). The

long gradient was run from 4-35.2% acetonitrile supplemented with 0.1% formic acid during a 150 min method (0-5 min 4%, 5-6 min to 7%, 7-105 min to 24.8%, 105-126 min to 35.2%, 126-140 min 80%, 140-150 min 4%) at a flow rate of 300 nL/min. The short gradient was run from 4-35.2% acetonitrile supplemented with 0.1% formic acid during a 60 min method (0-5 min 4%, 5-6 min to 7%, 7-36 min to 24.8%, 37-41 min to 35.2%, 42-46 min 80%, 47-60 min 4%) at a flow rate of 300 nL/min. FAIMS was performed with two alternating CVs including -50 V and -70 V. The Orbitrap Eclipse Tribrid Mass Spectrometer was operated in dd-MS2 mode with following settings: Polarity: positive; MS1 resolution: 240k; MS1 AGC target: standard; MS1 maximum injection time: 50 ms; MS1 scan range: m/z 375-1500; MS2 ion trap scan rate: rapid; MS2 AGC target: standard; MS2 maximum injection time: 35 ms; MS2 cycle time: 1.7 s; MS2 isolation window: m/z 1.2; HCD stepped normalised collision energy: 30%; intensity threshold: 1.0e4 counts; included charge states: 2-6; dynamic exclusion: 60 s.

GO term and interaction analysis using String.db

STRING database was used to perform Network Analysis of enriched proteins identified Tet3 cMut sorted cone photoreceptor cells. Network nodes represent the enriched proteins. Network edges represent protein-protein interaction. Thickness of the network edges was chosen to indicate edge confidence, meaning strength of the data support for the shown interaction. Minimum required interaction score was set to 0.400. Functional enrichments in each network were considered significant in case of a false discovery rate FDR < 0.05.

13 Other methods

13.1 LS-MS/MS measurement of cytosine modifications

The procedure was carried out by Dr. Franziska Traube at the Institute of Chemical Epigenetics Munich (ICE-M) according to a previously described [263].

In brief, quantification of cytosine modifications was carried out using an ultra-high-performance liquid chromatography tandem mass spectrometry (UHPLC-MS/MS) system and analysing three technical replicates per biological replicate. For each technical replicate, 3 µg of genomic DNA in 35 µL water were digested (depending on the amount and sort of original sample). In detail, 7.5 µL of a 480 µM ZnSO₄ aqueous solution, containing 18.4 U nuclease S1 (*Aspergillus oryzae*, Sigma-Aldrich), 5 U Antarctic phosphatase (New England BioLabs) and labelled internal standards ([¹⁵N₂]-5caC 0.04301 pmol, [¹⁵N₂,D₂]-5hmC 7.7 pmol, [D₃]-5mC 51.0 pmol, [¹⁵N₅]-8-oxo-dG 0.109 pmol, [¹⁵N₂]-5fC 0.04557 pmol) were mixed with the sample DNA. Afterwards, the mixture was incubated at 37 °C for 3 h. Then, 7.5 µL of a 520 µM [Na]₂-EDTA solution, containing 0.2 U snake venom phosphodiesterase I (*Crotalus adamanteus*, USB corporation) were added. The mixture was incubated again for 3 h at 37 °C and then stored at -20 °C.

Before using for UHPLC-MS/MS analysis, samples were filtered using an AcroPrep Advance 96 filter plate 0.2 μm Supor (Pall Life Sciences). Quantitative UHPLC-MS/MS analysis was performed using an Agilent 1290 UHPLC system equipped with a UV detector and an Agilent 6490 triple quadrupole mass spectrometer. Natural nucleosides were quantified with the stable isotope dilution technique, which allowed the concurrent analysis of all nucleosides in one single analytical run. The following source-dependent parameters were set: gas temperature 80 $^{\circ}\text{C}$, gas flow 15 L/min (N₂), nebulizer 30 psi, sheath gas heater 275 $^{\circ}\text{C}$, sheath gas flow 15 L/min (N₂), capillary voltage 2,500 V in the positive ion mode, capillary voltage 2,250 V in the negative ion mode, nozzle voltage 500 V, fragmentor voltage 380 V/ 250 V and for the positive mode Delta EMV 500 V. Chromatography was performed by a Poroshell 120 SB-C8 column (Agilent, 2.7 μm , 2.1 mm \times 150 mm) at 35 $^{\circ}\text{C}$ using a gradient of water and MeCN, each containing 0.0085 % (v/v) formic acid, at a flow rate of 0.35 mL/min: 0 \rightarrow 4 min; 0 \rightarrow 3.5% (v/v) MeCN; 4 \rightarrow 6.9 min; 3.5 \rightarrow 5 % MeCN; 6.9 \rightarrow 7.2 min; 5 \rightarrow 80 % MeCN; 7.2 \rightarrow 10.5 min; 80 % MeCN; 10.5 \rightarrow 11.3 min; 80 \rightarrow 0 % MeCN; 11.3 \rightarrow 14 min; 0 % MeCN. The effluent before 1.5 min and after 9 min was diverted to waste by a Valco valve. The autosampler was cooled to 4 $^{\circ}\text{C}$. The injection volume was 39 μL .

13.2 LC MS/MS measurement of thyroid hormones

Sample preparation

Dorso-ventral retinae at different time points (p4, p10 and p30) were isolated and snap frozen. A total of 9, 7 and 4 mice (2x retinae each) were pooled together for the above indicated time points, respectively. Measurements were carried out by Andrea Bertolini at the Department of Surgical, Medical and Molecular Pathology and Critical Care Medicine of the University of Pisa.

Retinae, kept at -80°C , were quickly transferred to 2ml homogenizing PRECELLYS® tubes (Bertin Technologies) and weighted. Then, each sample was suspended in 1 mL of a solution made of 840 μL of acetonitrile and 150 μL of pure water added with 10 μL of an internal standard mixture (10 ng/mL of 13C6-T3 and 13C6-T4). After being vortexed, samples were sonicated for 15 minutes and then homogenized using a Precellys®24-Dual Homogenizer (Bertin Technologies). Afterwards, homogenized samples were sonicated again for 15 minutes and then centrifuged for 15 minutes at 14000 rpm. Supernatants were transferred to new 2mL Eppendorf® tubes and washed three times using 1ml of hexane to remove the phospholipid excess. The lower phase was then dried under a gentle stream of nitrogen, in a thermostated block set at 40 $^{\circ}\text{C}$. Before injection, samples were eventually reconstituted using 100 μL of H₂O: MeOH 70:30 (v/v), vortexed for 10 minutes to guarantee a full resuspension and centrifuged for 15 minutes at 14000 rpm. Volumes were then transferred to a 96-well collection plate and injected in the LC-MS/MS system. The quantification of analytes was performed using standard T3 and T4 calibration curves built from 0.025 ng/mL to 5 ng/mL. All reagents used for the extraction

and analysis procedure were LC-MS grade and purchased via Sigma Aldrich-Merck.

HPLC-MS/MS analysis

The instrumental layout consisted in an Agilent 1290 UHPLC system, including a binary pump, a column oven set at 20°C and a thermostatic autosampler, coupled to an AB-Sciex QTRAP 6500+ mass spectrometer working as a triple quadrupole, equipped with an IonDrive™ Turbo V source. Chromatographic separation was achieved by using a 110 Å, 2x50 mm, 3µm particle size, Gemini C18 column, protected by a C18 Security Guard Cartridge and using (A) MeOH/ACN (20/80 by volume) added with 0.1% FA and (B) water containing 0.1% FA as mobile phases. The integrated switching valve was used to discard both head and tail of the HPLC runs. Gradient elution (400 µL/min flow rate) was performed as follows: 0.1-3 min (A) 5%, 8.5 min (A) 65%, 9.0-11.0 min (A) 100%, 11.50-13.50 (A) 5%, while injection volume was set at 20 µL. System control, data acquisition and analyses were performed using an ABSciex Analyst® version 1.7 software. A mass spectrometry selected reaction monitoring (SRM) method operated in positive ion mode. For each compound, after the optimization of declustering potential (DP), collision energy (CE) and collision exit potential (CxP), three transitions were considered in the analysis. Based on the highest signal/noise ratios, one of them was used as quantifier (Q) and the other two as qualifiers (q) as reported in Table 1. Further operative parameters were gas source 1 (GS1), 60 arbitrary units; gas source 2 (GS2), 45 arbitrary units; ion spray voltage (ISV), 5.5 kV; source temperature (TEM), 650°C; entrance potential (EP), 10V; Curtain gas (CUR), 20 arbitrary units; collision gas (CAD) N2, operative pressure with CAD gas on, 2 mPa.

Part III

Results I

14 Generation and characterisation of *Tet3* conditional mutant mouse line

14.1 *Tet3* is expressed in the mouse retina and the short isoform is the most abundant

Commonly, genomic DNA methylation has been associated with silencing of gene transcription, in particular when this occurs at the level of promoter and enhancer regions [117]. The majority of the CpG islands on the mammalian genome are methylated on the position 5 of the cytosines (5mC) [147]. Indeed, accumulation of 5mC can be found when big regions of the DNA, such as transposons and imprinted genes, need to be transcriptionally silenced [97]. Since the discovery of TET enzymes and the notion that 5hmC accumulates in differentiating cells, particularly in neurons [154], more attention has been moved to elucidating the meaning of the demethylation process and its involvement in gene transcription [154], [173]. For instance, this mechanism might be involved in regulating the correct onset of specific developmental programs by silencing those genes whose expression is not (or no longer) required. However, despite the increasing interest in this topic, less light has been shed on Tet3 and its role in the CNS, especially in the retina. Tet3 exists in two isoforms, the long or full length (FL) isoform contains a CXXC domain through which Tet3 binds to the DNA, whereas the short isoform (S) lacks this domain and is generated by an alternative promoter usage [173]; binding of this isoform to the DNA is likely mediated by other enzyme/complexes [209]. In order to evaluate the expression at the transcript level, retina cross-sections of 4 weeks old WT mice were analysed by RNA fluorescent in-situ hybridization using a specific *Tet3* probe that binds the common exon2, and therefore recognises both long and the short isoform transcripts. As shown in the Fig. 13A *Tet3* is quite uniformly expressed across the entire retina, since its signal is detected in all the retinal layers, as well as plexiform layers and inner segments, whereas, as expected in negative control, no signal was detected via *DapB* (bacterial transcript) specific probe (Fig. 13B). To determine the contribution of the two isoforms, qRT-PCR was performed from retinal tissue isolated at different time points and using two different set of primers, one set of primer is specific for the long isoform, while the second set amplifies both isoforms. Since *Tet3* long isoform resulted in very low levels of expression at all time points considered (light green points in Fig. 13C), the major contributor to the total *Tet3* expression (dark green dots in Fig. 13C) could be exclusively attributed to the short isoform. Of notice, total *Tet3* peaked at p12, corresponding to the time of eye opening in mice.

Taken together, these results show a broad expression of *Tet3* across all retinal layers and, seemingly, all cell populations, with a higher expression of the short isoform over time.

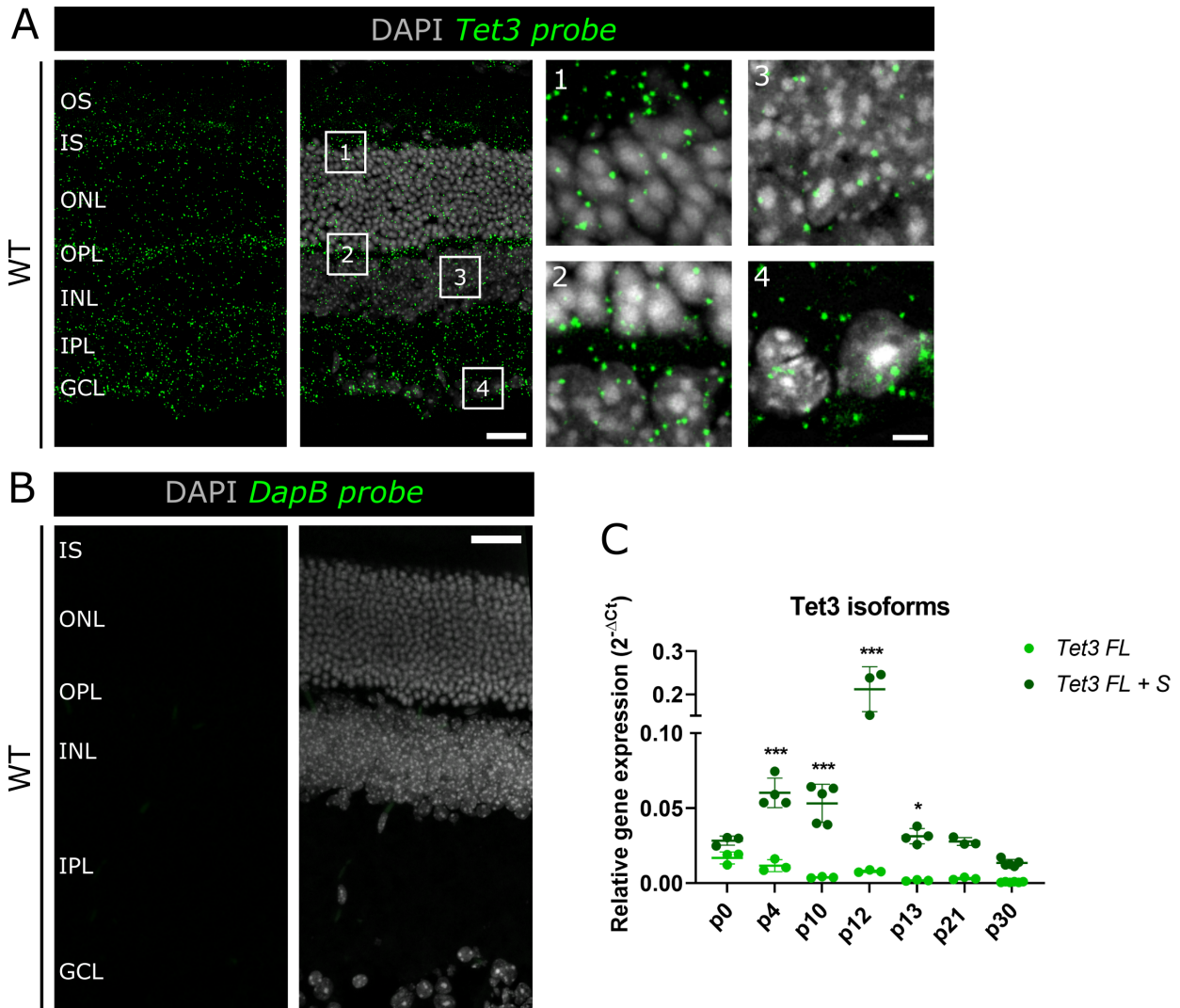


Figure 13: *Tet3* expression in mouse retina

(A-B) Confocal images of retina cross-sections of BL6 WT mice labelled with *Tet3* or *DapB* probe, the latter as negative control (green dots) and counterstained with DAPI (grey). The four quadrants in A are selected magnifications of the ONL and IS (1), OPL (2), INL (3) and GCL (4). Scale bar= 20 μ m (5 μ m for the magnifications) (C) quantitative PCR of *Tet3* transcripts recognising the *Tet3* full length (FL) isoform (light green) or FL and short (S) isoform (dark green). Every dot indicates an experimental value (n). Error bars indicate \pm SD. Two-way ANOVA with Bonferroni's post-hoc test in B. * $p < 0.05$, ** $p < 0.01$, *** $p < 0.001$

OS, IS= outer and inner segments; ONL, INL, GCL = outer, inner and ganglion cell layers; OPL, IPL= outer and inner plexiform layers

14.2 Generation of a *Tet3* conditional mutant mouse line

Maternal ablation of *Tet3* is known to affect embryos morphology and viability rate [80] [110] [264]. To overcome this problem, we generated a conditional mouse model lacking only part of

Tet3 sequence via Cre recombinase approach, by crossing two selected mouse lines. In the first, *Tet3* locus bears the insertion of two lox-P sites between exons 7 and 8, a region encoding part of the catalytic domain of the protein [5]. This mouse line, without Cre construct is referred in the text as Control. In the second mouse line, Rx-Cre [130], the sequence encoding Cre recombinase is under the control of Rx promoter. Thus, the resulting mouse line is a conditional mutant of Tet3 catalytic domain (hereby referred to as *Tet3* mutant, Tet3 cMut or mutant), as a consequence of the excision of exons 7 and 8 only in Rx-expressing cells (Fig. 14A). Importantly, since the mutation is in-frame, the truncated protein is likely to be produced. As mentioned, Cre expression is controlled by Rx (Retinal homeobox protein) promoter, which is normally active in all retinal cells starting from embryonic day 8 (e8) [130]. At this developmental stage, the retina is a very thin layer containing only amplifying retinal progenitor cells (RPCs). Since all the retinal cells are generated from the same common pool of RPCs [268] and considering the early expression of Cre recombinase in our mouse model, all retinal cells generated after e8 are likely to inherit the *Tet3* mutation.

In order to further investigate the effects of the excision, Tet3 expression was verified in control and mutant retinæ at both transcript and protein levels. At transcript level, two set of primers were used to amplify regions before and after the deleted area via quantitative reverse transcriptase PCR (qRT-PCR). In both cases, levels of the corresponding amplicon sequence observed in *Tet3* mutant mice were comparable to control mice (Fig. 14B, C). This suggests that the generated transcripts might be stable enough to escape non-sense mediated RNA decay and be successfully translated. Accordingly, at protein level, Tet3 immunostaining of retinal cross-sections of control and Tet3 mutant mice, showed a similar distribution pattern. While signal in the inner and ganglion cell layer (INL, GCL) was nuclear, as expected for its demethylase function, it appeared perinuclear and more enriched in the apical region of the outer nuclear layer (ONL), where normally cone photoreceptors cell bodies are located (Fig. 14D). These results confirm not only that Tet3 is expressed by all different cell types in the retina, seemingly without exceptions, but also that, even in *Tet3* mutant mice, a protein can still be produced.

14.3 Tet3 protein generated in *Tet3* mutant mice is catalytically inactive

As previously mentioned, despite the deletion of exons 7 and 8, *Tet3* mutant mice still produce Tet3 protein. Since these exons encode for the first of the two dioxygenase domains, which are part of the catalytic domain of the protein, we speculated that Tet3 function could be altered. Therefore, we quantified *ex vivo* the absolute amount of 5mC, 5hmC and 5fC, the substrate and the products of Tet-mediated demethylation [255], as readout of Tet3 catalytic activity (Fig. 15A).

The two genotypes showed no significant difference in the level of 5mC at any of the analysed time points (Fig. 15B). Nevertheless, by p30 the levels of 5mC showed a tendential reduction compared to the other time points. This slow reduction in methylation was accompanied

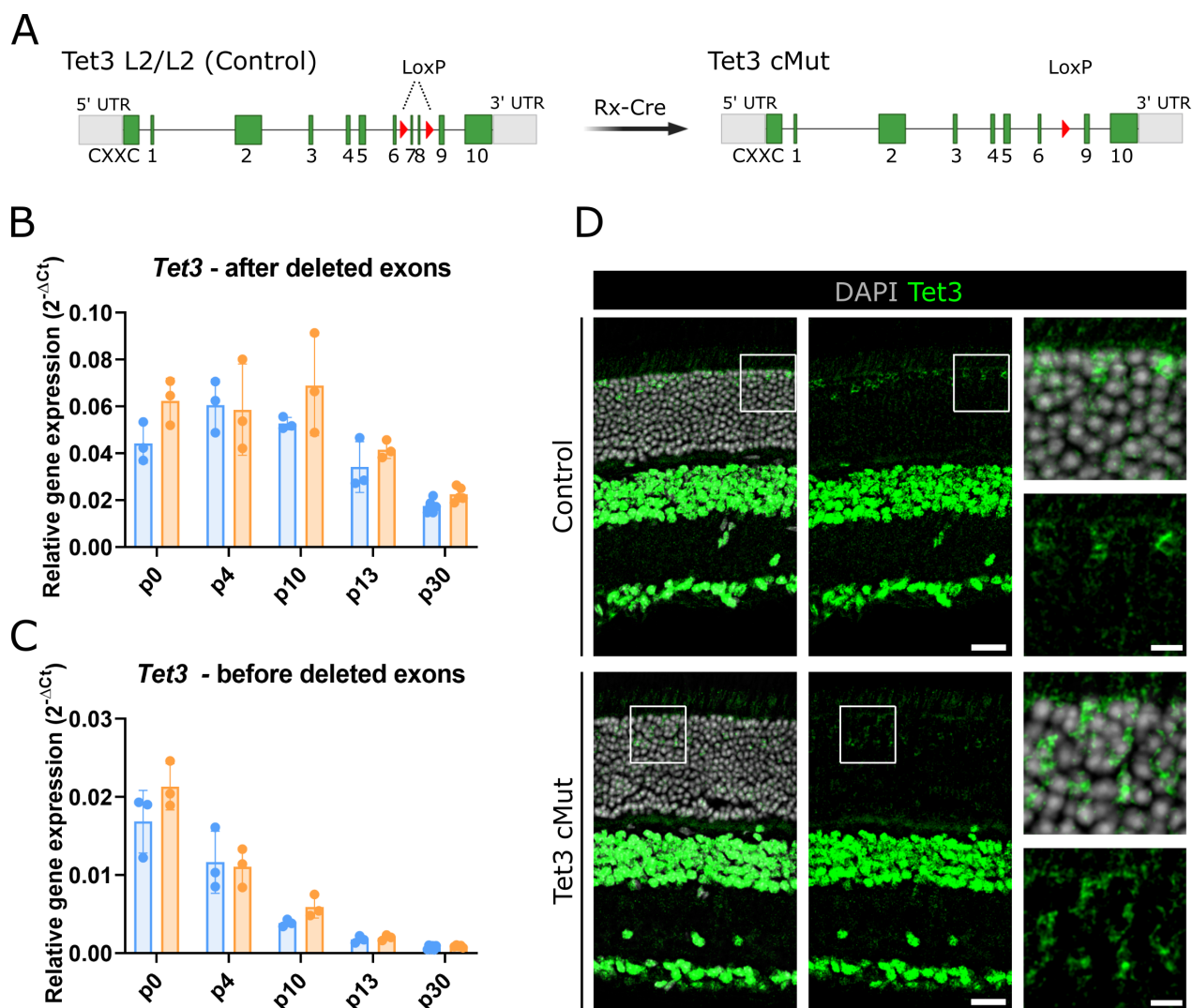


Figure 14: Generation of *Tet3* conditional mutant mouse line

(A) Schematic representation of the modified *Tet3* locus with insertion of two lox-P sites between the exons 7 and 8 and resulting *Tet3* cMut mouse with the deleted region (B-C). qRT-PCR analysis of *Tet3* transcripts amplified with primers binding before and after the deleted region. Two-way ANOVA test. Error bars indicate \pm SD. (D) Confocal images of retina cross-sections labelled for *Tet3* (green). Quadrants are zoomed-in areas of the ONL (1) and INL (2). Scale bar= 20 μ m (5 μ m for the zoomed-in images).

by a gradual increase over time in the level of 5hmC, which in control mice showed the highest level between p21 and p30. 5hmC was also detected in *Tet3* mutant retinæ, although this was significantly lower than the levels reached by control mice (Fig. 15C). The detection of 5hmC in mutant mice is not surprising when considering that the two other members of the TET family, namely *Tet1* and *Tet2*, may also play a role in this process. Indeed, an upregulation of one or both these members could perhaps partially compensate to the absence of *Tet3* (or at least its catalytic function). In order to rule out this possibility, the total *Tet1* and *Tet2* transcript levels were quantified by qRT-PCR. Not only was the expression of these two isoforms significantly lower than *Tet3*, but also the levels of both *Tet1* and *Tet2* transcripts remained constant overtime (Fig. 15E). However, this does not exclude that the endogenous basal level of either *Tet1* or

Tet2, or both, might still contribute to the observed levels of 5hmC. Strikingly, 5hmC levels never reached the control values, at any of the analysed time points. Presumably, this difference between control and mutant, is likely to reflect the impairment in the catalytic activity solely mediated by Tet3. 5fC is the subsequent intermediate step of the demethylation pathway and, in general, is much less abundant than 5mC or 5hmC [209]. In our model system, 5fC showed an opposite trend to 5hmC, declining over time until p13. From p21, the levels of 5fC were undetectable also in control retinae (Fig. 15D). In *Tet3* mutant mice, 5fC levels were below the limit of detection and therefore undetectable at any of the analysed time points (Fig. 15D). This significant difference may indicate that 1) Tet3 is the main, if not the only, player in subsequent steps of DNA demethylation, or that 2) the demethylation process is somehow faster in the absence of Tet3.

To further investigate Tet3 functionality, the same experiment was performed *in vitro*, as more unbiased and simplified system. To this end, plasmids encoding the mouse either the short Tet3^{wt} or short Tet3^{ΔEx7/8} (in which exons 7 and 8 were removed to mirror the *in vivo* mutation) fused to GFP (Fig. 16A) were transfected in HEK293T cells and cytosine modifications used as readout of Tet3 activity. Immortalized cell lines do not show detectable levels of 5hmC, as well as measurable levels of any of the TET enzymes (data not shown). 24h after transfection, cells were harvested, and 5mC, 5hmC, 5fC, 5caC, were quantified by mass spectrometry. Of all conditions, 5mC showed the highest abundance (Fig. 16B-E). Tet3^{wt} revealed a significant reduction in 5mC levels compared to the other two conditions, whereas levels in Tet3^{ΔEx7/8} were comparable to GFP control condition (Fig. 16B). The lower amount of 5mC observed in Tet3^{wt} was accompanied by a significant increase in the amount of 5hmC. Once again, Tet3^{ΔEx7/8} exhibited no significant difference when compared to GFP control condition (fig. 4C). A similar scenario described 5fC and 5caC levels, the latter being last step in the DNA demethylation process, quantifiable only in Tet3^{wt} condition (Fig. 16D,E).

Therefore, we can conclude that Tet3 catalytic activity is affected by the deletion of exons 7 and 8, encoding for one of the dioxygenase domains. *In vivo*, the loss of a catalytically active Tet3 is followed by a reduction in the levels of 5hmC, which neither Tet1 nor Tet2 are able to efficiently compensate. Strikingly, while Tet1 and Tet2 are likely to influence 5mC and 5hmC levels, the complete absence of 5fC in mutant mice, as well as in the complementary study performed in HEK293T cells, strongly prompt Tet3 as the sole enzyme responsible for the regulation of the demethylation process during cell differentiation in the retina. Further investigation is required to pinpoint the mechanisms underlying these unprecedented results.

14.4 *Tet3* mutation does not affect retinal lamination and layer formation

In order to investigate how *Tet3* mutation and its catalytic impairment affect retinal architecture, animals were imaged using optical coherence tomography (OCT) at 4 weeks of age. At this stage, retinal cell identities are defined, and the different cell types are correctly integrated in

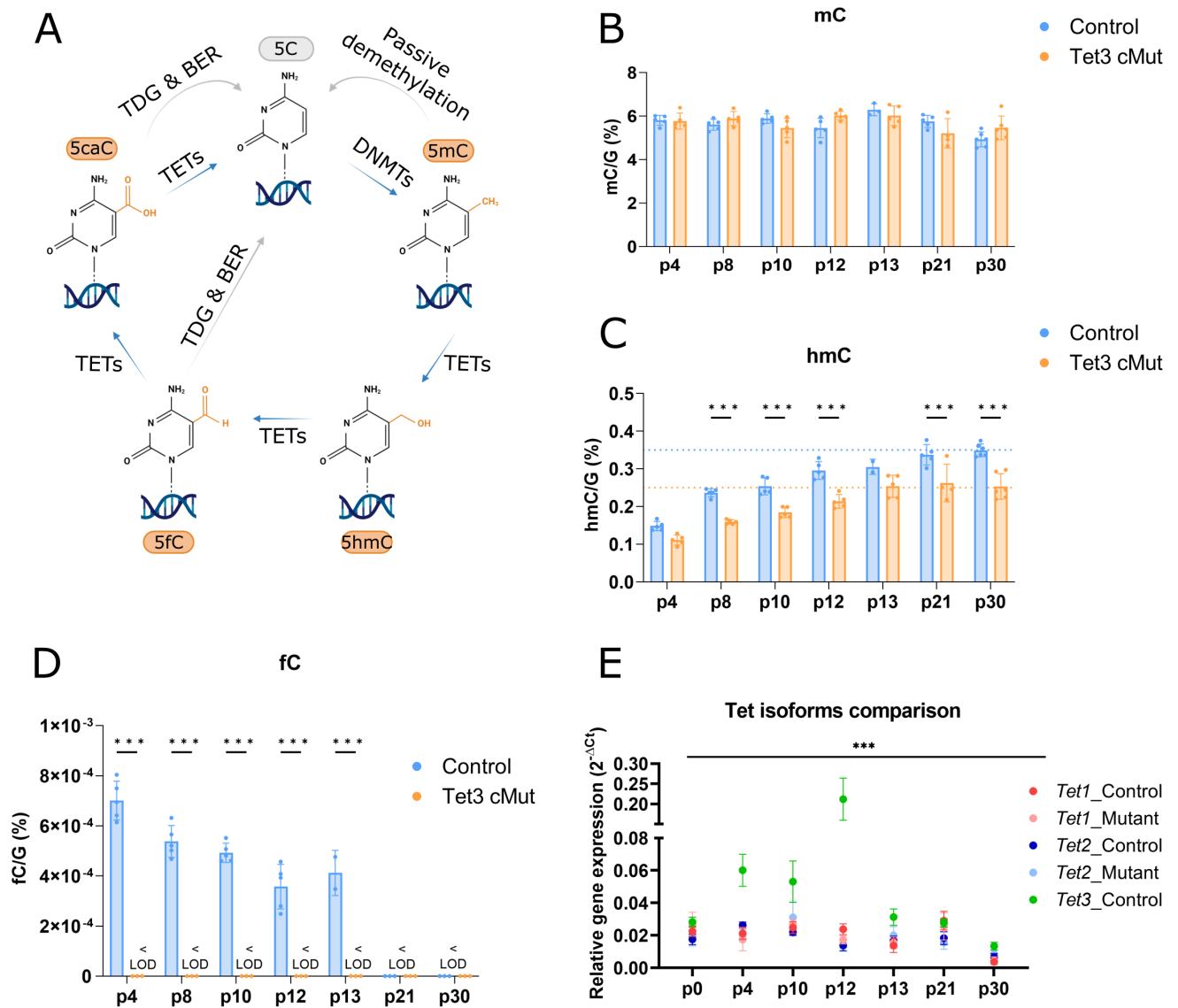


Figure 15: Cytosine modifications

(A) Schematics of the demethylation pathway. Cytosine (C) is methylated by DNMTs and actively demethylated by the TETs in 5hmC, 5fC, 5caC. Alternatively, 5mC can restore C in passive demethylation (proliferation). (B-D) 5mC, 5hmC, 5fC levels measured by mass spectrometry. Each dot in an experimental value (n). < LOD (below limit of detection). Two-way ANOVA with Bonferroni's post-hoc test. Asterisks indicate significance: * $p < 0.05$, ** $p < 0.01$, *** $p < 0.001$. (E) qRT-PCR of all the Tet enzymes at different developmental points in the two genotypes. $n \geq 3$ per time point and condition. Two-way ANOVA comparison, *** $p < 0.001$. Error bars in (B-E) are \pm SD

their final location. At first glance, no major differences could be observed between the two conditions. The retina appeared integral and correctly formed, with its distinctive layers and gross organization (Fig. 17A,B). Next, the thickness of both inner and outer nuclear layer was analysed and, despite the retinal macro structure being largely unaffected by *Tet3* mutation, both layers appeared thinner in *Tet3* mutant retinæ (Fig. 17C). These results indicate potential

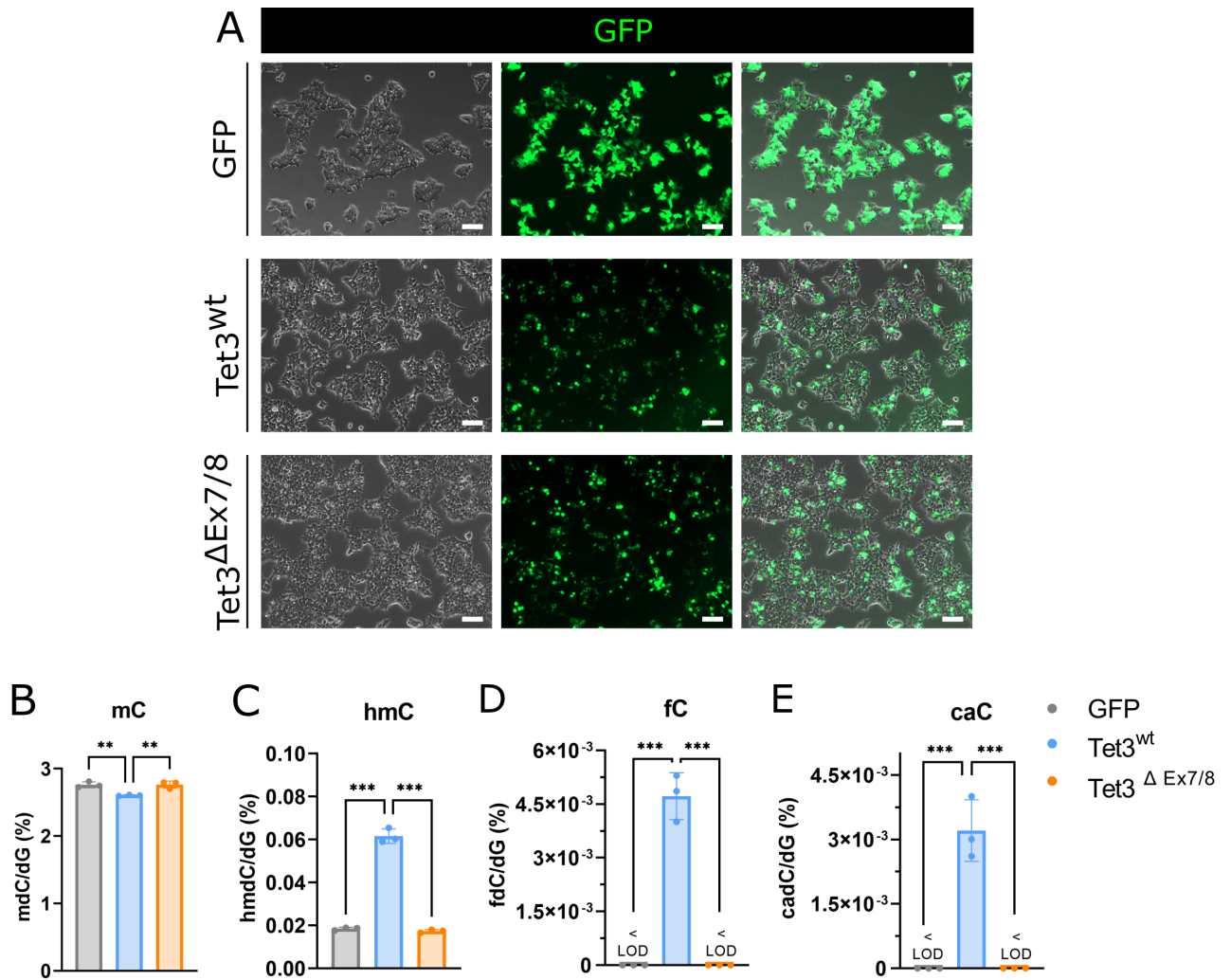


Figure 16: Tet3 Catalytic activity *in vitro*

(A) Brightfield and epifluorescent images of HEK293T collected 24h after transfection. Scale bar= 50 μ m. (B-E) mC, hmC, fC, caC levels quantified by mass spectrometry. n=3 per condition. < LOD (below limit of detection). One-way ANOVA with Tuckey's post-hoc test. ** p<0.01, *** p<0.001. Error bars are \pm SD

alterations in the two most populated retinal layers, thus prompting deeper analysis of the cellular composition of each individual layer.

15 Outer nuclear layer and cone photoreceptors

15.1 Cone photoreceptors are increased in their number in *Tet3* mutant retinae

The ONL is populated by rod and cone photoreceptors (Fig. 18A)[202], essential for dim light and colour vision, respectively. As mice are nocturnal animals, their retina is rod dominated, indeed rods represent more than 90% of the total cell number, while cones are less abundant

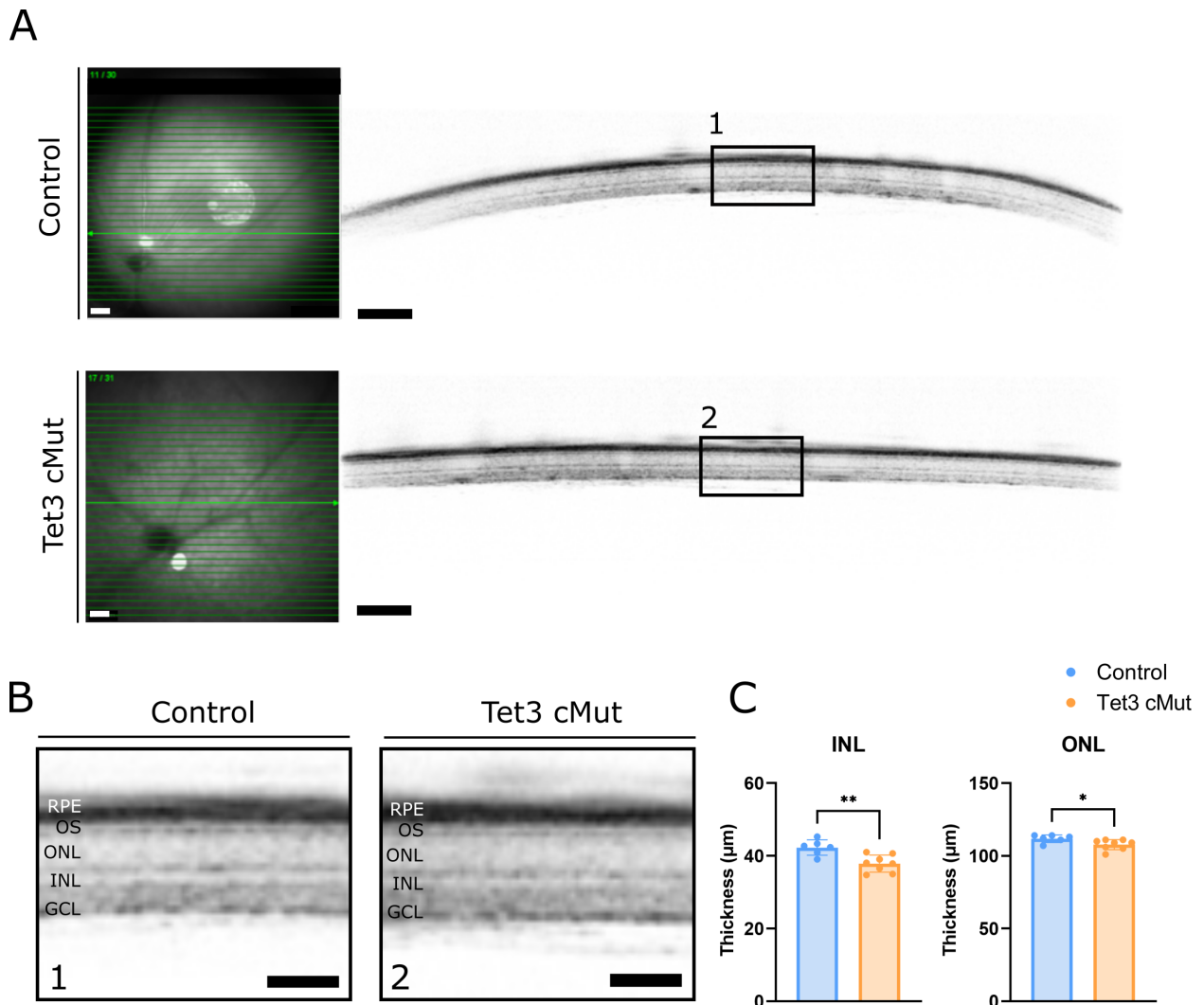


Figure 17: Optical Coherence Tomography (OCT)

(A) OCT images of control and Tet3 mutant eyes. Scale bar= 500 µm. Quadrants are shown magnified in B (B) Magnified images of both genotypes Scale bar= 200 µm (C) Bar plots of INL and ONL thickness. The n is indicated in the graph per condition. Error bars represent ±SD. Unpaired student t-test *p<0.05, ** p< 0.01

RPE= retinal pigmented epithelium; OS= outer segments; ONL, INL, GCL = outer, inner and ganglion

and reach only a 3-5% [202]. Surprisingly, upon mutation of *Tet3*, mice showed an increase in the number of cone photoreceptors labelled with Arr3, a general known marker for these cells. Remarkably, the percentage of cone photoreceptor raised from roughly 4% to 6.1% (~ 50% increase) (Fig 18B, C). Additionally, the morphology of Arr3⁺ cells appeared to be different. In fact, in control mice Arr3 labelling was confined to the inner and outer segments of cone photoreceptors and their synaptic pedicle, while cell bodies were faintly labelled. In *Tet3* mutant mice, instead, Arr3 protein was distributed along the entire cell length, thereby equally labelling these different compartments. Interestingly, the increase in cone number could also be observed within the OPL, where the cone pedicle is located. While in control mice pedicles nicely distribute next to each other in a single row, the synaptic layer of mutant mice appeared to have a

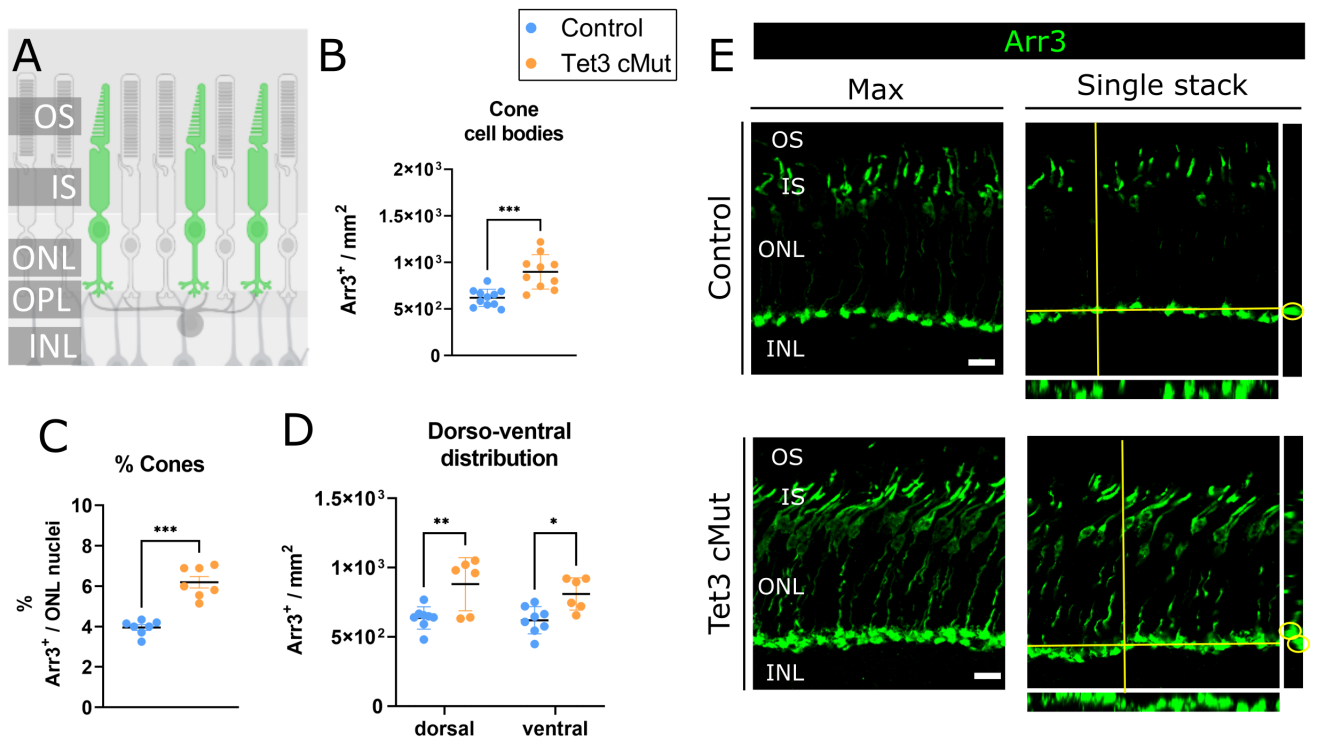


Figure 18: Cone photoreceptors (Arr3)

(A) Schematic representation of the localisation of cone photoreceptors (green) in the retina. (B-C) Scatter plots of specified quantifications in control (blue) and mutant (orange) mice. Error bar is \pm SD. Unpaired t-test *** $p < 0.001$ (D) Number of cones per dorsal or ventral area (mm^2). Two-way ANOVA with Tuckey's post-hoc test. * $p < 0.05$, ** $p < 0.01$, *** $p < 0.001$. (E) Confocal images of retina cross sections labelled with Arr3 (green) for cones. Left: maximum projection of 10 single stack images; right: single stack and related orthogonal projection. Yellow vertical and horizontal lines represent the location of the orthogonally projected image. Yellow circle in the vertical projection indicates selected for cone pedicles. Scalebar = $20 \mu\text{m}$

higher density of cone pedicles no longer able to appear aligned in a single row (Fig. 18E).

Next, we investigated whether this increase in the number of cone photoreceptors was ubiquitously present in the retina of these mice, by looking at two different areas along the dorso-ventral axis. As expected, no differences were observed along this axis in control retinæ, whereas *Tet3* mutant mice showed a significant increase in both areas compared to the controls, but no significant difference between the two positions (Fig. 18D).

Similar results were obtained labelling cone photoreceptors with peanut agglutinin (PNA), another well-known cone marker that recognizes galactose-galactosamine disaccharide residues [19] expressed on the surface membranes of outer and inner segments, as well as cone pedicles (Fig 19A). Also in this case, cone photoreceptors appeared to be increased in their number and percentage (~45% increase) (Fig 19B, C) and the same effects were equally observed in both dorsal and ventral retina, therefore corroborating the previous results (Fig. 19D).

An indirect measurement, performed subtracting the number of Arr3⁺ cones from the total

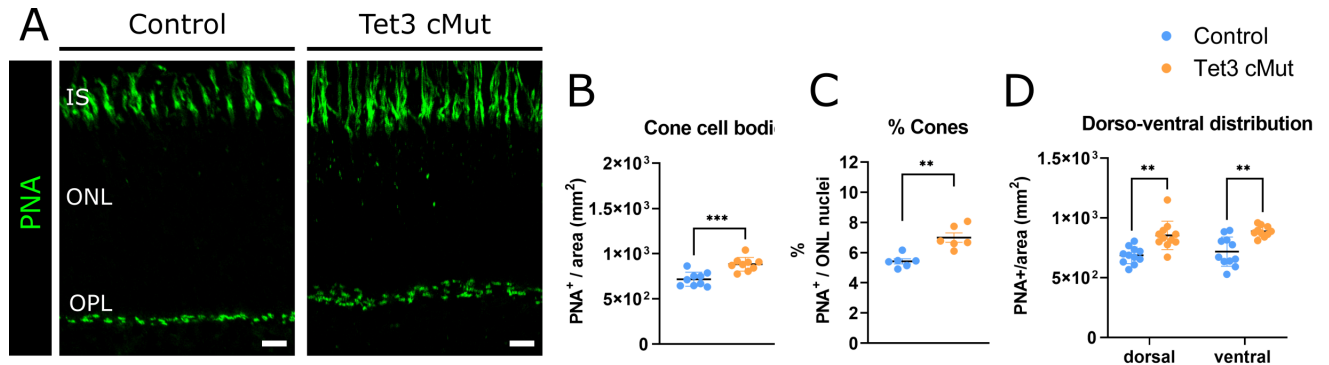


Figure 19: Cone photoreceptors (PNA)

(A) Maximum intensity projection of several stacks of confocal images, in which cone photoreceptors have been labelled with PNA (green). Scalebar= 20 μm (B-C) Scatter plots of specified quantifications in control (blue) and mutant (orange) mice. Unpaired Student t-test (D) Number of PNA cones per dorsal or ventral area (mm^2). Two-way ANOVA with Bonferroni's post-hoc test. * $p < 0.05$, ** $p < 0.01$, *** $p < 0.001$. Error bars in (B-D) are $\pm\text{SD}$

number of nuclei counterstained with DAPI, indicated no alterations in the number of rod photoreceptors (Fig. 20). All in all, these results showed that impairing Tet3 leads to an altered number of cone photoreceptors across the entire retina. Conversely, no alteration in the number of rod photoreceptors could be assessed, though the elevated abundance of this cell population in the retina makes detecting subtle changes challenging.

15.2 Different dorso-ventral distribution of S-cones upon *Tet3* mutation

Based on the previous results on the altered cone number, we next investigated whether cone sub-types were also affected by *Tet3* mutation. In mice, only two types of cones are present and can be distinguished based on opsin expression. The blue cones are short (S) wavelength sensitive cones, and express the S-opsin pigment, while the green or medium (M) cones express the M-opsin chromo protein [103]. A second classification is made based on their expression pattern: cones can be divided into “pure” if they express only one chromophore (the S- or M-opsin only), or “hybrid” if they express both (Fig. 21A, B) [8]. These cones have also distinct distribution patterns in the retina, with the highest variability along the dorso-ventral axis. Most cones in wild type BL6J mice are hybrid and uniformly distributed, in particular in the central part of the retina. Moreover, pure S-cones are very scarcely represented in the dorsal side and more abundant in the ventral side of the retina [90]. Because of this different dorso-ventral distribution of cones expressing S-opsin, the majority of cones in the dorsal side of the retina are actually pure M-cones [202]. These decrease towards the ventral side, although this gradient is less marked than for S-cones [202].

With this in mind, we checked in retinal flat mount preparations whether the opsin expression pattern changed as a consequence of the higher number of cone photoreceptors. Surprisingly,

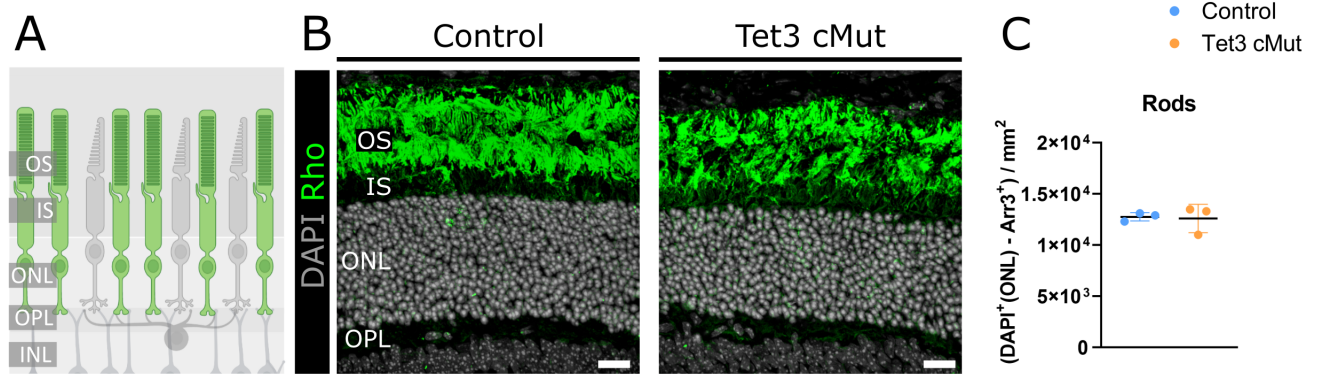


Figure 20: Rod photoreceptors

(A) Schematic representation of rod photoreceptors (green) in the retina. (B) Confocal images of retina cross-sections stained for rhodopsin (Rho in green) and counterstained with DAPI (grey, showed as insert). Scalebar= 5 μm for DAPI images and 20 μm for Rho. (C) Bar plot of rod photoreceptors density (cells per mm^2). This number was calculated as an indirect measurement, subtracting the number of Arr3^+ cones from the total DAPI nuclei in the ONL. Unpaired Student t-test. Error bars are $\pm\text{SD}$

Tet3 mutant mice showed a different gradient distribution of both S- and M-opsin expressing cones. S-cones, which are scarcely represented in the dorsal retina, increased significantly and almost reached values comparable to the ventral region. Numbers resulted tendentially increased also in the latter. However, due to the normally higher abundance in the ventral region, the increase was overall not significant (Fig. 21C, E). The opposite situation could be observed for M-cones, with significant increase in the ventral side (where these cones are generally less represented) compared to the smaller non-significant increase in the dorsal side (Fig. 21D, F).

Next, I evaluated the co-expression of the two photopigments in retinal cross-sections, making use of PNA to identify all cone photoreceptors (Fig. 22A). In agreement with the previous results in flat mount preparations, both S- and M-cones showed the highest increase in the number of S-cones in the dorsal part of the retina (Fig. 22B, C). Co-labelling with PNA confirmed a perturbation of the distribution of S-opsin expressing-cones, as almost 100% of the cones in the dorsal retina was S-opsin⁺, compared to just roughly 50% in the same region of control retinae (Fig. 22D). Remarkably, S-pure cones (indicated by white arrowheads in Fig. 22A), located for the most part in the ventral half of the retina [90], were not affected and did not show any difference between the two conditions (Fig. 22F). Conversely, the overall gradient distribution of M-opsin⁺ cones did not change, showing lower percentage of M-cones in the ventral side compared to the dorsal side in both *Tet3* mutant and control littermates, despite an appreciable increase in both dorsal and ventral part of the retina (Fig. 22C, E). As a consequence of the altered S-cone distribution and their increase in number, most of the cones expressed both photopigments, even in the dorsal retina (Fig. 22G).

Taken together, these results demonstrate the importance of *Tet3* in the determination of cone sub-types. All cones acquired a hybrid identity by expressing both S- and M- pigment, possibly as a consequence of the altered pattern of S-cones, which, differently from the control retinae,

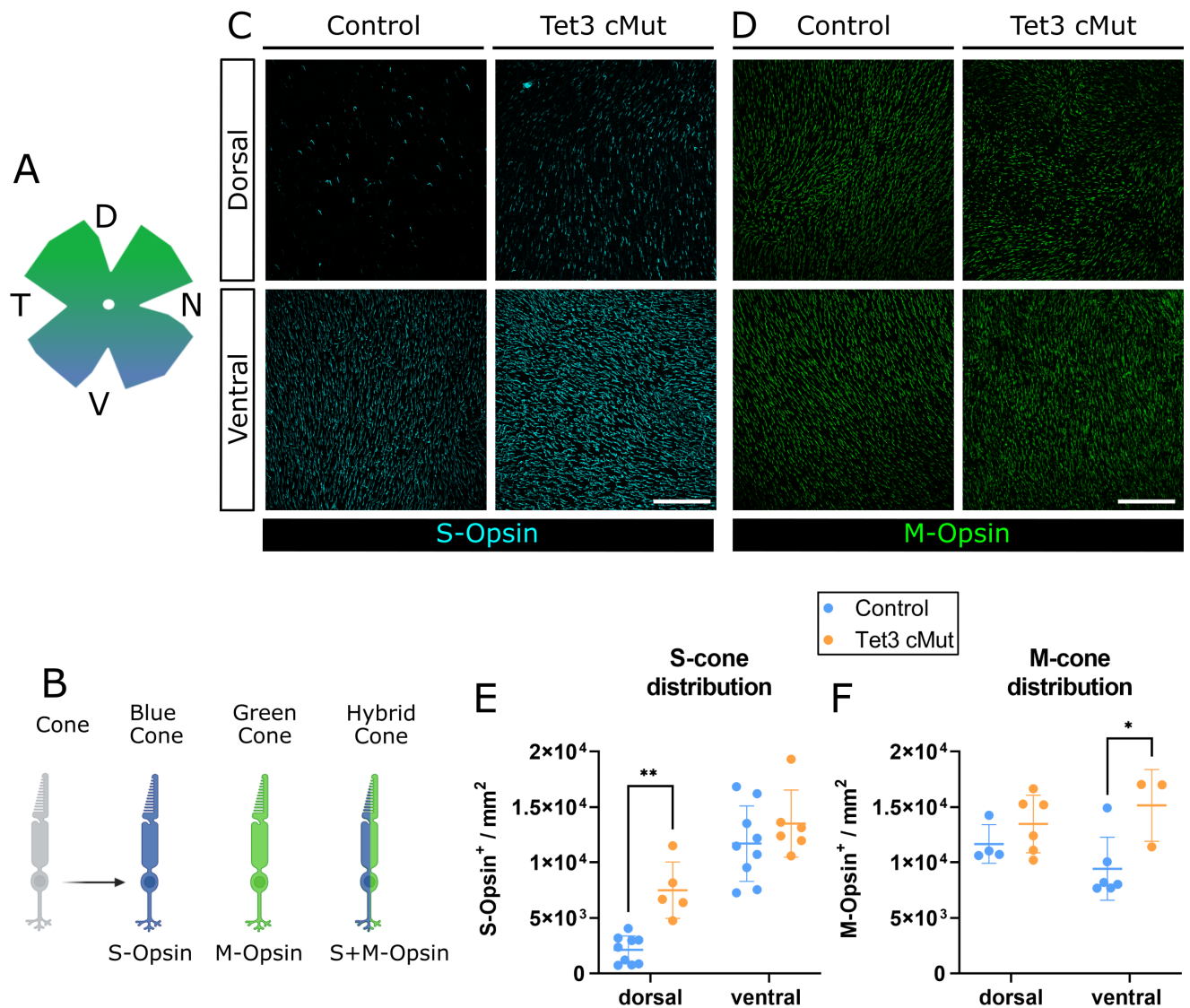


Figure 21: Opsin distribution in flat mount retina

(A) Schematics of the different cone types in the mouse retina and their gradient distribution (B). (C-D) Confocal images of retina flat mount preparations where outer segments of cones have been labelled with antibodies against S- or M- opsin. Scale bar= 100 μm (E-F) Scatter plot of the number of blue and green cones and their dorsal and ventral distribution. Error bars are $\pm\text{SD}$, two-way ANOVA with Bonferroni's post-hoc test. Asterisks represent significance: * $p < 0.05$, ** $p < 0.01$, *** $p < 0.001$

showed equal distribution across the dorso-ventral axis of *Tet3* mutant retina.

16 Inner nuclear layer

16.1 *Tet3* mutation leads to less cells in the inner nuclear layer

Having observed that the inner nuclear layer thickness was significantly reduced in OCT measurements (Fig. 17B, C), I next focused on the characterization of the cellular composition of this layer. For this purpose, I have immunolabeled cells for specific known markers in retinal

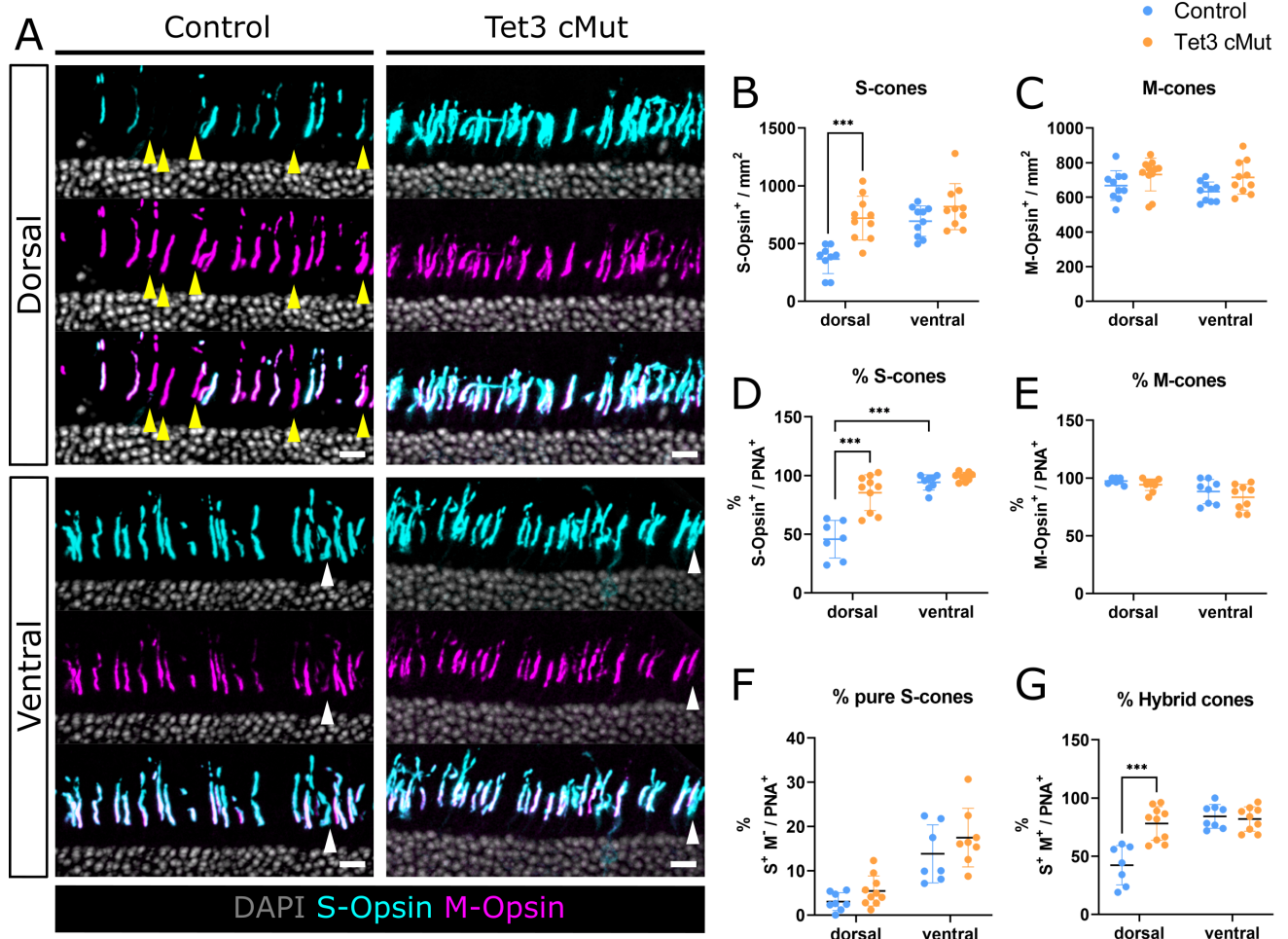


Figure 22: Opsin distribution in retina cross-sections

(A) Confocal images of retina cross-sections stained with S- (cyan) and M-Opsin (Magenta) and counterstained with DAPI (grey) Yellow arrowheads indicate pure M-cones while white arrowheads point to pure S-cones. Scale bars= 20 μm (B-G) Scatter plots of the number and distribution of S- and M-cones along the dorso-ventral axis. Error bars are $\pm\text{SD}$, two-way ANOVA with Bonferroni's post-hoc test. * $p < 0.05$, ** $p < 0.01$, *** $p < 0.001$

cross-sections. With the only exception of Müller cells, all the other cells residing in this layer showed a tendential decrease, significant in case of the bipolar cells, when compared to control littermates (Fig. 23A-D), suggesting that more than one cell type could contribute to the thinning of the inner nuclear layer.

Given the significant reduction in the number of bipolar cells, these cells were additionally immunolabelled with specific sub-type markers, to further investigate whether specific sub-populations are affected more than others. Bipolar cells can be distinguished in ON and OFF based on their response to glutamate release by photoreceptor cells, with which they are directly in contact. Moreover, bipolar cells can be divided into cone or rod bipolar cells depending on the cell type they are in connection to. There are in total 15 diverse types of bipolar cells identified so far [94] [239] [282]. Of these, types 1 to 4 are cone OFF bipolar cells, since they

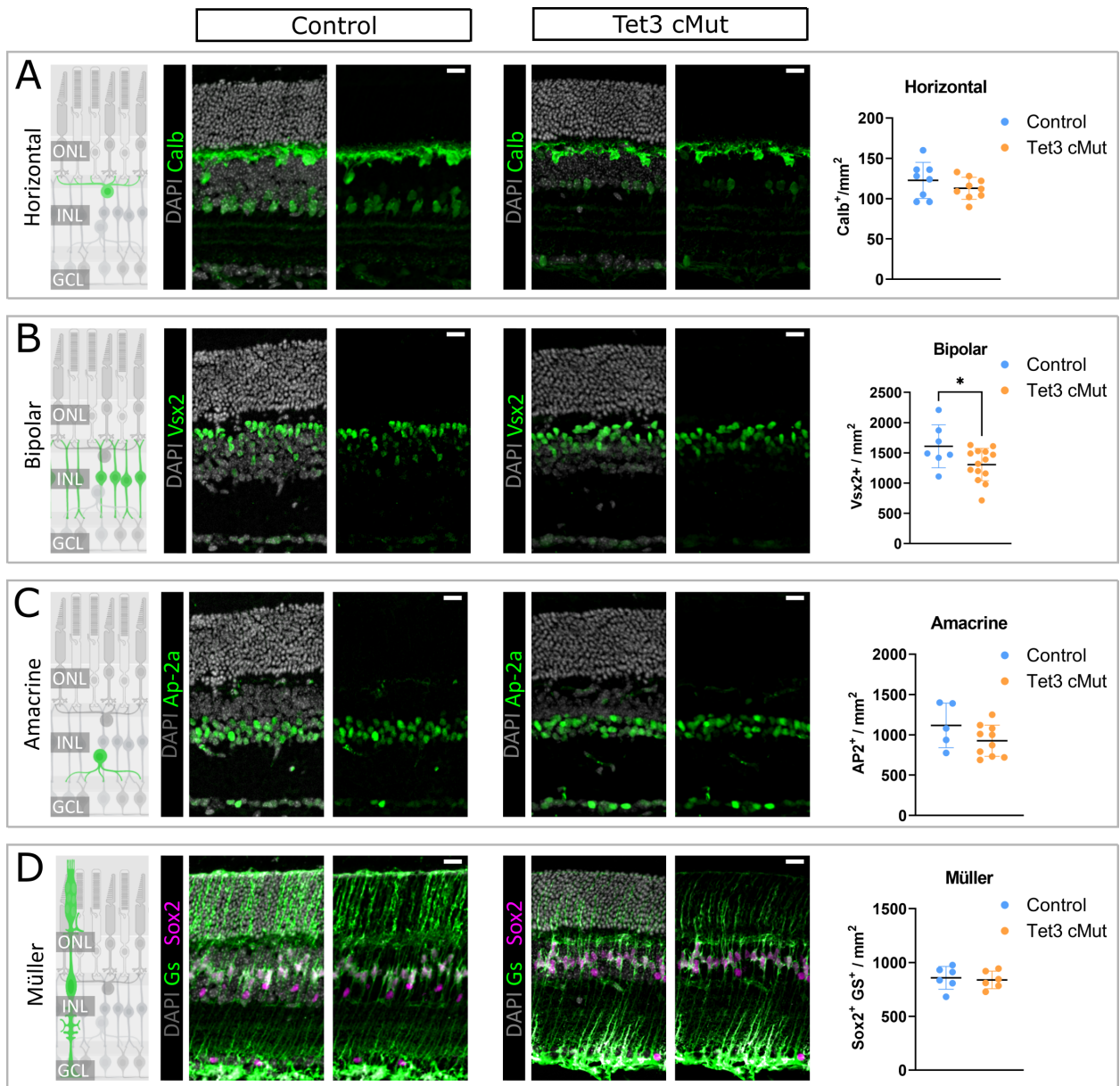


Figure 23: Cell densities in inner nuclear layer

(A-D) From left to right each block contains a schematic of the retina in cross-section and the localisation of the respective cell type (green) in the INL. Confocal micrographs of retina cross-sections stained with markers identifying the different cell population and counterstained with DAPI (grey). Scale bars = 20 μm . Right scatter plot quantifications of the stained sections. Error bars are $\pm\text{SD}$, n is indicated on the graph; unpaired t-test. Asterisks represent significance: * $p < 0.05$

receive inputs from cone photoreceptors. All other types are cone ON bipolar cells (type 9 is pure S-cones-specific), with the only exception of rod bipolar cells (Fig. 6).

ON-bipolar cells were immunostained for two different markers, Isl-1 and Pcp2 (Fig. 24A and D) labelling both rod and cone ON-bipolar cells. In both cases, ON-bipolar cells showed tendential reduction (Fig. 24B and E), albeit not significant, in the total number of these cells. Rod bipolar cells are also of the ON type, and they can be specifically stained with PKC- α . Results showed no difference in rod bipolar cells number between the two genotypes (Fig. 24C),

therefore indicating a stronger impact on cone ON bipolar in this mouse model. Of note, in both PKC- α and Pcp2 images, fewer and less elaborated bipolar axonal harbors were immunolabelled in *Tet3* mutant mice at the IPL, suggesting an effect on axogenesis and neuronal maturation in these mice.

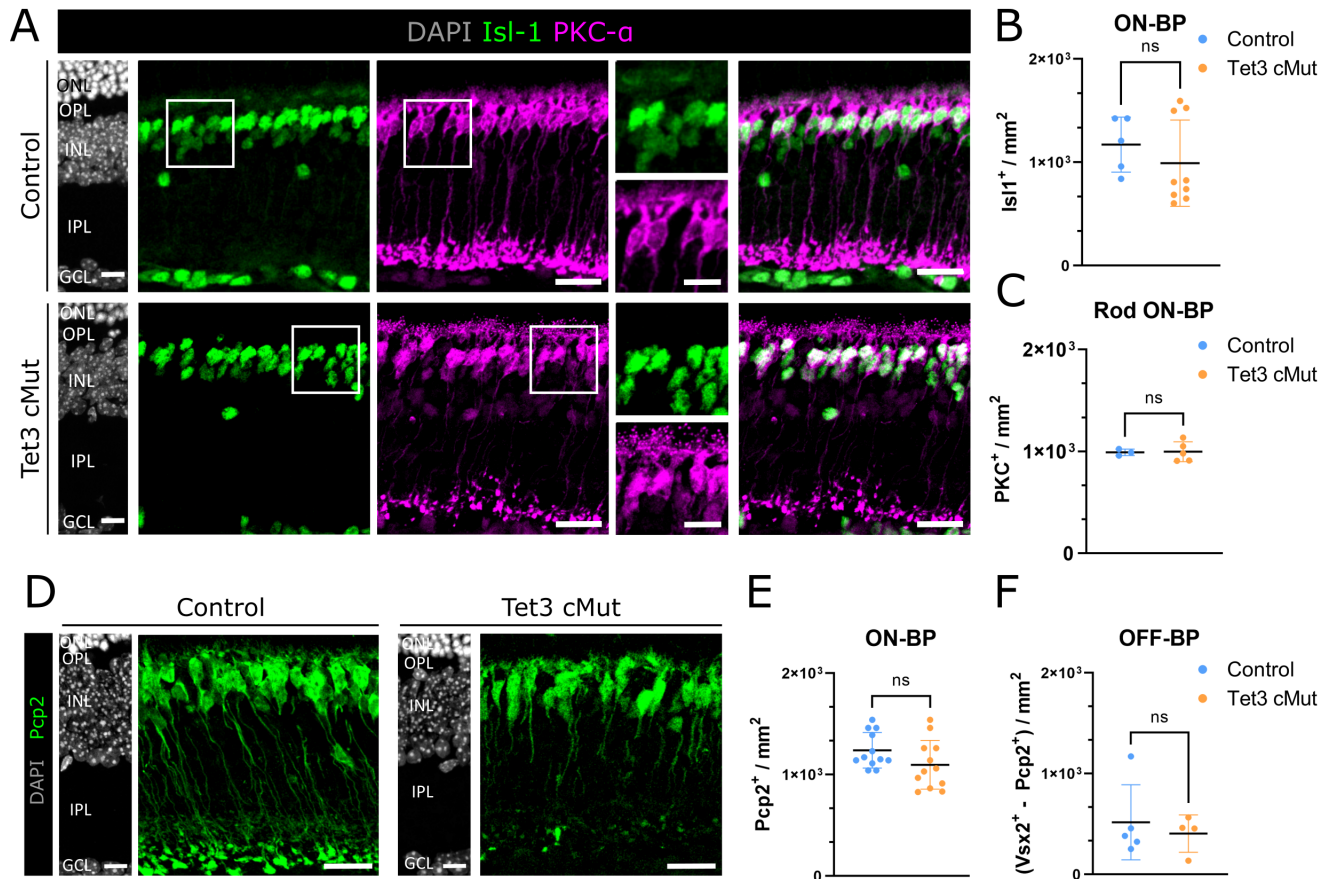


Figure 24: Bipolar cell sub-types

(A) Confocal micrographs of retina cross-sections stained with Isl-1 (green), identifying ON-bipolar cells (BP), and PKC- α (magenta) for rod ON-BP. Nuclei were counterstained with DAPI (grey). Scale bars DAPI and zoomed-in quadrants = 10 μ m, other images = 20 μ m. (B-C) Quantifications of experiments in A, showing a tendential reduction in the number of ON-BP but no effects on rod ON-BP. (D) Confocal micrographs of retina cross-sections stained with Pcp2 (green) another pan marker of ON-bipolar cells (BP). (E) Quantification of D. (F) OFF-bipolar cell indirectly quantified as difference between $Vsx2^+$ (all bipolar) and $Pcp2^+$ (ON bipolar) cells.

Error bars in B, C, E are \pm SD, dots are single n values; unpaired Student t-test.

Given the lack of specific antibodies ubiquitously labelling OFF-bipolar cells, I performed an indirect quantification, by subtracting the number of ON-Bipolar cells ($Pcp2^+$) from the number of all bipolar cells ($Vsx2^+$). Mutant retinæ showed a non-significant reduction in cell number also for OFF-bipolar cells (Fig. 24F). Thus, cone ON- and OFF-bipolar cells together seem to contribute to the significant reduction observed for the total bipolar cells population ($Vsx2^+$ Fig. 23B) Overall, these results support an important role for Tet3 in the specification of bipolar cells and, possibly, horizontal and amacrine cells. Moreover, *Tet3* mutation seems to selectively

affect the number of cone bipolar cells, but not rod ON-bipolar cells.

17 Retinal light responses are remarkably reduced in *Tet3* mutant mice

As seen in previous paragraphs, all analyses pointed towards a light alteration in the composition of retinal cell populations. For this reason, we next asked how these unbalanced amounts reflect on the functionality of this system, specifically in terms of efficiency of light stimulus propagation. Photoreceptors are light-sensitive cells; as such, they convert light into an electrical signal, which is subsequently propagated onto lower layer neurons of the INL [182]. This event induces a response in these neurons and the resulting signal is further converged on retinal ganglion cells (RGCs), whose axons represent the real output of the retina [182]. All these electrical stimulations can be easily recorded via electroretinography (ERG), allowing the investigation of the retinal function in a non-invasive manner [190]. For this reason, mice were subjected to both scotopic and photopic ERG examinations aimed at studying the activity of rod and cone mediated responses (Fig. 25A, D). No differences were detected in the amplitude of both scotopic a-(photoreceptor-related) and b-(lower layer neurons-related) waves when comparing *Tet3* mutant mice to control ones (Fig. 25B, C), thereby corroborating the previous observations that neither rod photoreceptors nor rod bipolar cells seem to be affected by mutations in *Tet3* (Fig. 24C). As cone photoreceptors represent only a small minority of photoreceptor cells (3-5%) [202], photopic a-waves are, instead, small in amplitude and very difficult to measure in mice. For this reason, photopic investigation was focused on the determination and quantification of photopic b-waves only. Notably, the photopic b-wave appeared reduced in amplitude in *Tet3* mutated mice at all tested intensities of single flashes illumination (Fig. 25E). This result was in line with the previous cellular characterization of the INL, showing reduced number of many cell populations and, significantly, of bipolar cells (Fig. 23B).

Next, the expression of immediate early gene (like c-Fos) in layer 4 of the primary visual cortex of these mice was quantified, as an indirect measurement of responses triggered by any visual stimulus (Fig. 26A,B). A significantly smaller number of c-Fos⁺ cells could be detected in mutant mice, suggesting reduced activation of this immediate early gene following naturally occurring visual exposure (Fig. 26C). Surprisingly, the lower c-Fos signal was not limited to cortical layer 4, but rather affected all layers homogeneously (Fig. 26A). Potentially explaining this observation, cortical neurons form a complex meshwork with neurons in other layers, ultimately transferring inter- or extra-cortical information. Moreover, neurons in layer 2/3 can also primarily respond to neuronal activity triggered by visuomotor learning [167]. All together, these results indicate an altered propagation of cone-mediated light stimuli as well as a lower immediate early gene response following visual stimulation and neuronal activity.

Based on these observations, we next investigated vision in these mice by performing two

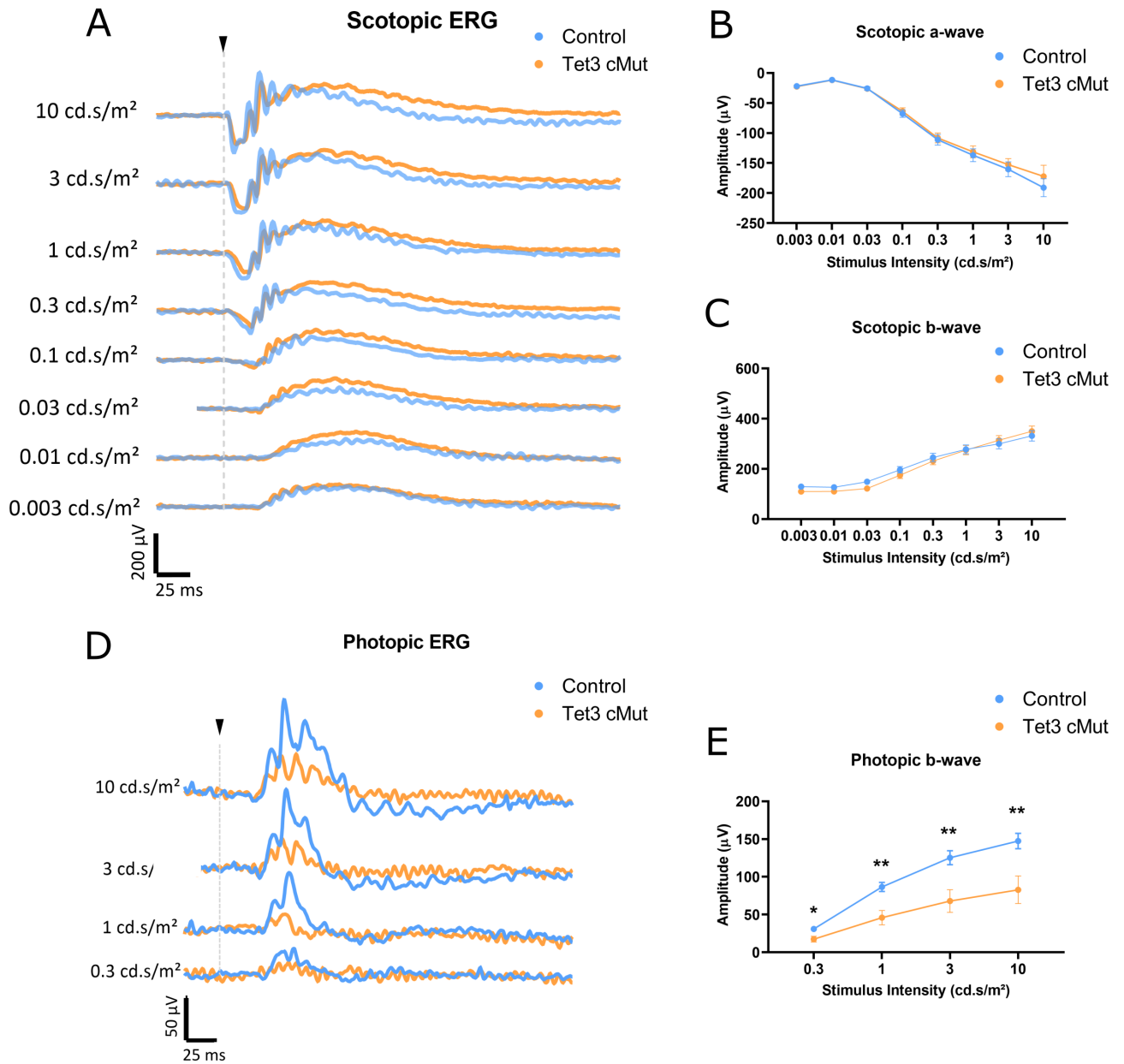


Figure 25: Responses to electrical stimulation (ERG)

(A) Electoretinographic traces of scotopic measurements. Grey dashed line and black arrowhead indicate the onset of the stimulation. Light stimulus propagation in cd.s/m^2 indicated on the left (B-C) Quantification of a- and b-wave, respectively, from experiments in A. ($n=10$ and $n=9$ mice for control and Tet3 cMut respectively). (D) Photopic ERG measurements. Grey dashed line and arrowhead indicate beginning of the stimulation. Intensities of light stimuli on the left. (E) Quantification of photopic b-waves recorded in B ($n=9$ and $n=10$ mice for control and Tet3 cMut, respectively). Error bars in B, C, E are \pm s.e.m, Multiple unpaired t-test with Benjamini's correction. * $p<0.05$, ** $p<0.01$

well-known behavioural tests, namely light-dark [256] and optomotor test (OMR) [135]. The first is based on natural aversion of mice to light and, although it is most commonly used to assess anxiety-like behaviour, it is also an indirect assessment of vision [256]. The optomotor test, instead measures visual acuity i.e., the ability of the eye to distinguish details and shape of an object [135]. In the light-dark test, a light and a dark compartment are separated by a small

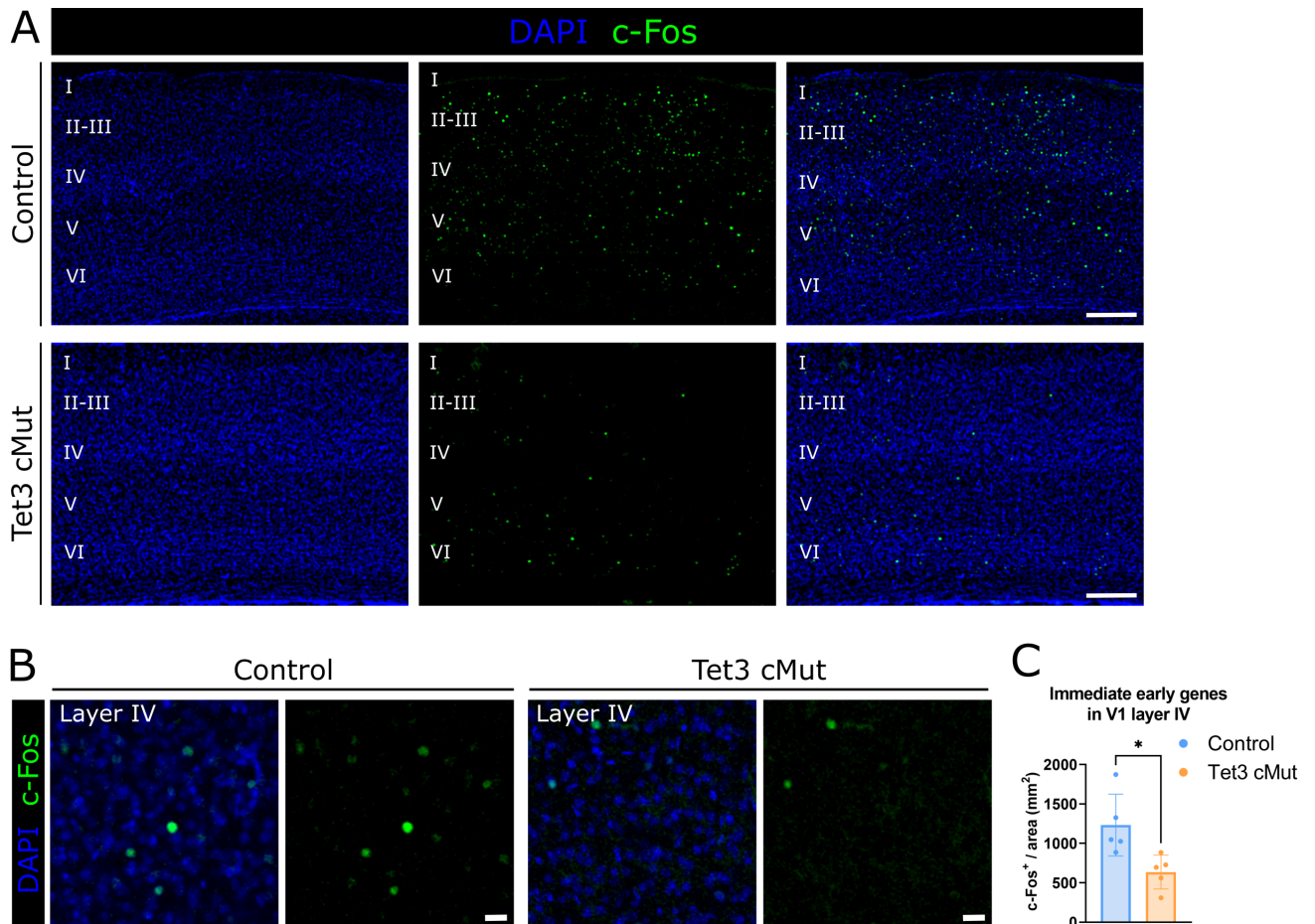


Figure 26: Immediate early gene response to visual stimuli

(A-B) Confocal micrographs of mouse coronal sections imaged at the primary visual cortex for immediate early gene *c-Fos* (green) and counterstained with DAPI (blue). Scale bars in A= 200 μm , and 20 μm in B. (C) Quantification of the experiment in A showing significantly reduced *c-Fos* labelled cells in mutant mice. Error bars represent $\pm\text{SD}$, unpaired t-test. Asterisk indicates significance * $p < 0.05$

opening; at the beginning of the experiment the mouse is placed in the light chamber and can move freely between the two areas (Fig. 27A). *Tet3* mutant mice not only spent longer time in the dark compartment (Fig. 27B), but they also required more time (longer latency) (Fig. 27C) to identify the opening to access the dark chamber. No difference was observed in the total path length as well as in the speed of these mice, indicating no pre-existing motor deficits (Fig. 27D,E). Further experiments will be necessary to investigate whether the increased aversion to light is to be attributed to visual defects or change in anxiety-like behaviour in these mice. In the OMR, the mouse is placed on an elevated platform, surrounded by four continuous screens, and is presented with visual stimuli (rotating bars) at different spatial frequency. No difference was observed between the two conditions when visual functions were evaluated via analysis of the optomotor response (Fig. 27F,G).

These results suggest that despite the significant differences observed in the cellular composition, as well as in ERG recordings and neuronal activity, no obvious change could be detected

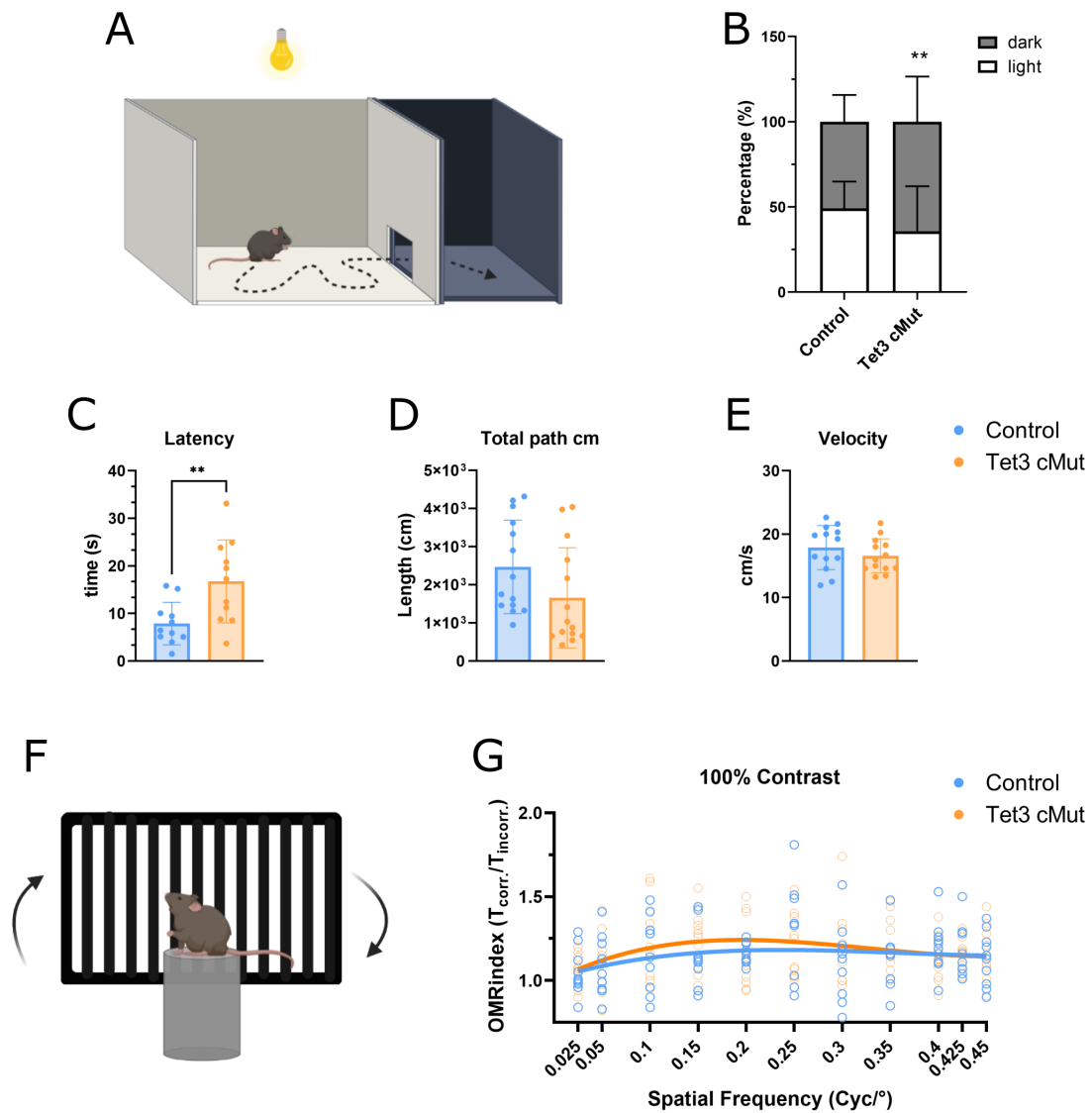


Figure 27: Behavioural testing

(A) Schematic representation of the light-dark experimental setup. (B) Percentage of time spent in each chamber per condition. Error bars are \pm SD. Results compared in 2 way-ANOVA with Tukey post-hoc test. ($n=10$ for controls and $n=11$ for *Tet3* mutant mice), $** p < 0.01$. (C-E) Other parameters of experiment in A. Error bars are \pm SD. Student t-test, $** p < 0.01$. (F) Graphical description of the optomotor test for visual assessment. (G) Polynomial fit curves of quantification based on test in F, showing no difference in visual perception between the two genotypes. 2-way ANOVA statistical test

in the behaviour of these mice in visual perception.

18 Tet3 in cone sub-type specification

18.1 *Tet3* mutation affects genes involved in photoreceptors versus bipolar cell development and in photoreceptor functional maturation

In order to gain more mechanistic insight and uncover any transcriptional differences, RNA-sequencing (RNAseq) was performed at different stages of retinal development, namely p4, p10 and p30. In this section, only the results obtained at p4 and p10 will be presented, while results from the p30 time point will be addressed in a separate section. Fragments per million mapped fragments were generated based on the mapped files and used to assess differences in gene expression among the two genotypes. Statistical analysis revealed that at p4 only a minor set of genes was differentially regulated (Fig. 28A). Specifically, 15 genes were downregulated, and 5 genes were upregulated in *Tet3* mutant mice (Fig. 28B). Because of these small differences, gene ontology could not be efficiently performed. Nevertheless, it is worth noticing that the second most downregulated gene is *Vsx1* (Fig. 28C), paralog of *Vsx2*, a gene whose role has been associated with cone OFF-bipolar cells differentiation [41].

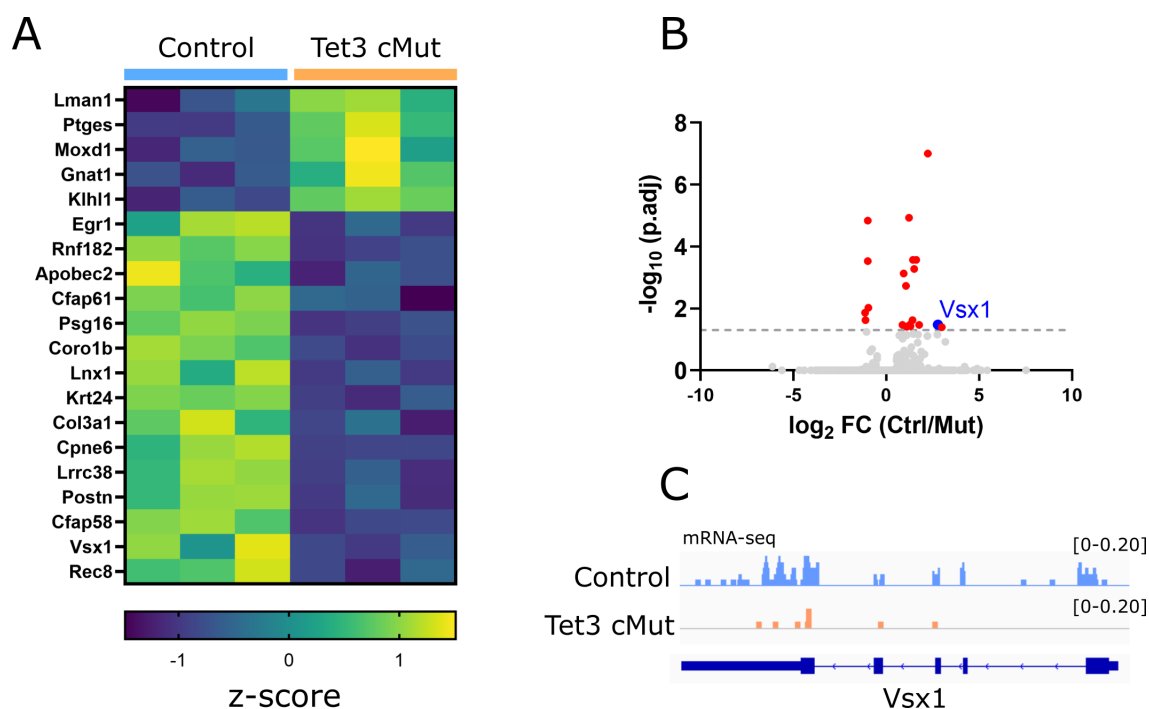


Figure 28: RNA-seq p4

(A) Fragments per million mapped fragments displayed as heatmap of significant differentially expressed genes at p4 represented as z-score. (B) Volcano plot of all the mapped genes showed minor changes in terms of significant differentially expressed genes. Of these, *Vsx1* is the second most downregulated gene in *Tet3* mutant mice. (C) Representative IGV traces of control (light blue) and *Tet3* mutants at *Vsx1* locus showing marked downregulation of this gene in *Tet3* mice.

Conversely, compared to control, p10 *Tet3* mutant mice showed 360 and 102 genes significantly up- and downregulated, respectively (Fig. 29A). Gene ontology (GO) analysis re-

vealed that a subset of downregulated genes plays a role in phototransduction (*Opn1mw*, *Cabp4*, *Guca1b*, *Rho*) of both rod and cone mediated pathways, and retinal rod cell development (*Trpm1* and *Bhlhe23*). Of note, *Trpm1* and *Bhlhe23* have also been associated with differentiation and functional maturation of ON- and OFF-bipolar cells [56] [183] [133]. A great majority of genes are involved in ion transport, neurotransmitter release and synapse assembly, all processes of high relevance in terms of phototransduction mediated responses. Importantly, *Dio2* and *Thrb* are of relevance for cone sub-type (S- versus M- cones) specification (Fig. 29C). Among the genes found upregulated, a subset is associated with cell fate commitment, e.g., *Otx2* and *Prdm1* [278]. These two genes have long been studied and linked to photoreceptors versus bipolar cells generation (Fig. 29D) [278] [76]. Moreover, other upregulated genes outside of any GO term were of particular interest, in light of the cellular characterization of *Tet3* mutant mice. These included *Opn1sw*, *Gngt2* and *Cngb3*, whose related proteins localise in cone outer segment and are implicated in the cone-mediated visual cascade.

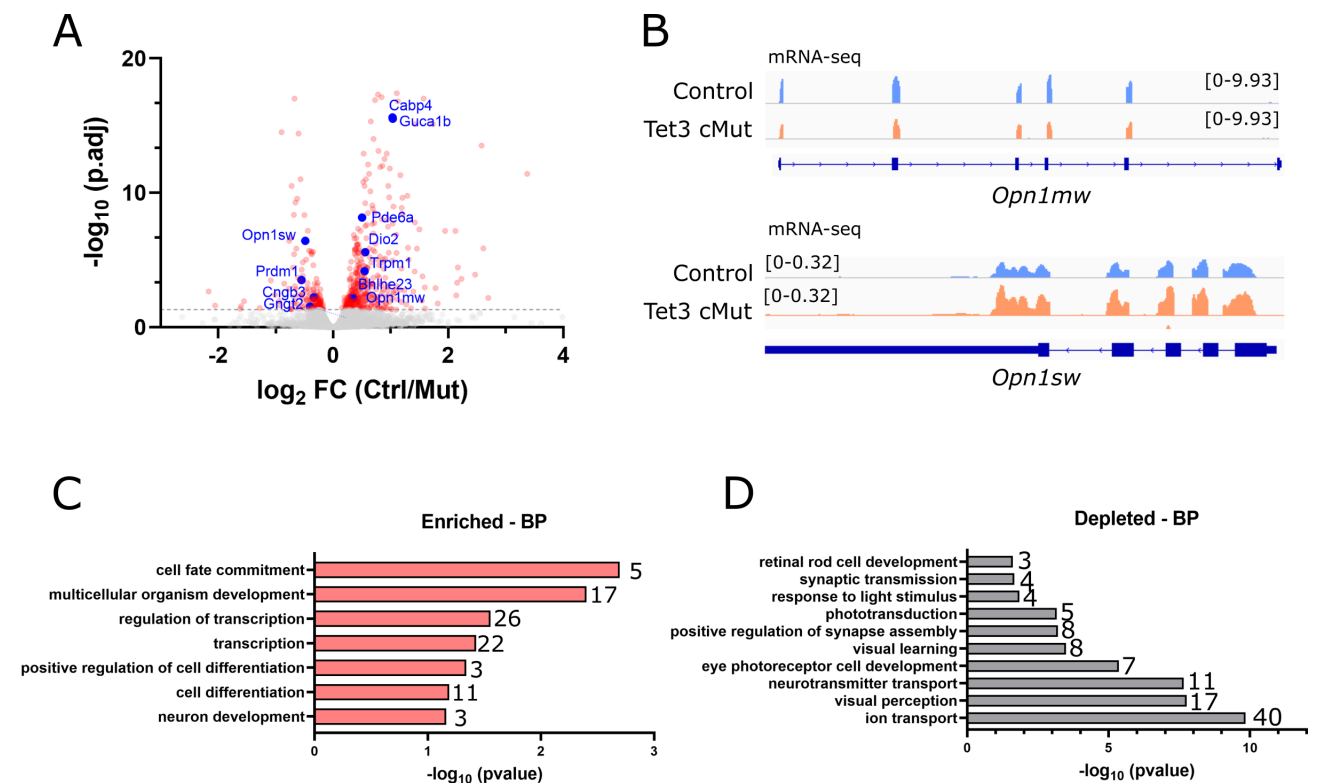


Figure 29: RNA-seq p10

A) Volcano plot of all mapped genes at p10 showed several changes in terms of significant differentially expressed genes. (B) Representative IGV traces of control (light blue) and *Tet3* mutants at *Opn1mw* (above) and *Opn1sw* (below) loci showing marked downregulation and upregulation, respectively, of these genes in *Tet3* mice. (C,D) GO term analysis of differentially enriched (red) and depleted genes (grey) performed using DAVID database and displayed based on significance value. The number of dysregulated genes is indicated next to the respective bar

Overall, these expression studies highlight the importance of *Tet3* in maintaining normal gene expression during retinal development and link for the first time *Tet3* in the context of

retinal cell fate differentiation and functional maturation of these cells.

18.2 Thyroid hormones and their receptor *Thrb2* are not affected by *Tet3* mutation

As observed in previous experiments, *Tet3* mutation significantly affects the expression of S-cones at adult stages, while showing little influence on M-cones levels (Fig. 22). However, RNAseq performed at earlier time points, time at which the cone sub-types are specified, indicated a clear transcriptional regulation of both S- and M-opsin genes (Fig. 28 and 29). Thus, the expression of S- and M-opsins at both transcript and protein levels was checked via qRT-PCR and immunohistochemistry, respectively, focusing on several time points: p4, p10, p13 and p30. At transcript level, *Opn1mw* showed a reduced expression at p4, tendency that was maintained also at p10 in accordance with the RNAseq data. On the contrary, *Opn1sw* showed a small significant increase at p13 (Fig. 30A, B). Because of the differential gene expression of the two opsin transcripts, retina sections were stained at p10, i.e., when outer segments start to form, and opsin proteins localise in this subcellular compartment. At this stage, the cone gradient is not expected to be established yet [224]. In agreement with qRT-PCR results, S-cones appeared to be normal (Fig. 30C,D), whereas M-opsin showed a reduced expression (Fig. 30C), representative of significantly fewer cone cells having M-opsin⁺ outer segments in both the dorsal and the ventral side of the retina (Fig. 30E). Moreover, cells bodies appeared to be misplaced, with many still in the lower half of the ONL (yellow arrowheads).

Being thyroid hormone (TH) and its receptors the most investigated factors in opsin specification field [73] [194] [160], different transcripts involved in this pathway were analysed by qRT-PCR at different developmental stages. Both transcripts for *Thrb* and *Rxrg*, the latter being a receptor able to bind *Thrb* to promote gene expression [24] (Fig. 31A), showed no differential expression at any of the investigated time points (Fig. 31B, C). Next, the two enzymes involved in the metabolic process of thyroid hormone, namely *Dio2* and *Dio3* were analysed. In particular, *Dio2* converts the inactive secreted thyroid hormone T4 in the active form T3, while *Dio3* inactivates T3 and converts it into reverse T3 (rT3) (Fig. 31D) [21]. *Dio2* transcript showed downregulation at p10, in agreement with RNAseq data, and at p30 (fig. 29E), while *Dio3* showed significant downregulation at p13 (Fig. 31F). Since the two *Dio* isoforms act immediately upstream and downstream T3, both dysregulations are likely to affect the availability of active T3 in the cells. To confirm this finding, we next measured the amounts of T4 and T3 in retina samples of these mice. Moreover, considering the opposite dorso-ventral gradients of S- and M-cones, we divided the retina into dorsal and ventral. Surprisingly, for both T3 and T4 there were no differences detected between the two genotypes at all time points analysed (Fig. 31G, H). On the one hand, the simultaneous reduction of both *Dio2* and *Dio3* expression could be seen as a possible explanation to these results, in which the overall levels of T3 are kept equal in the two conditions. On the other hand, we cannot exclude that although both transcripts

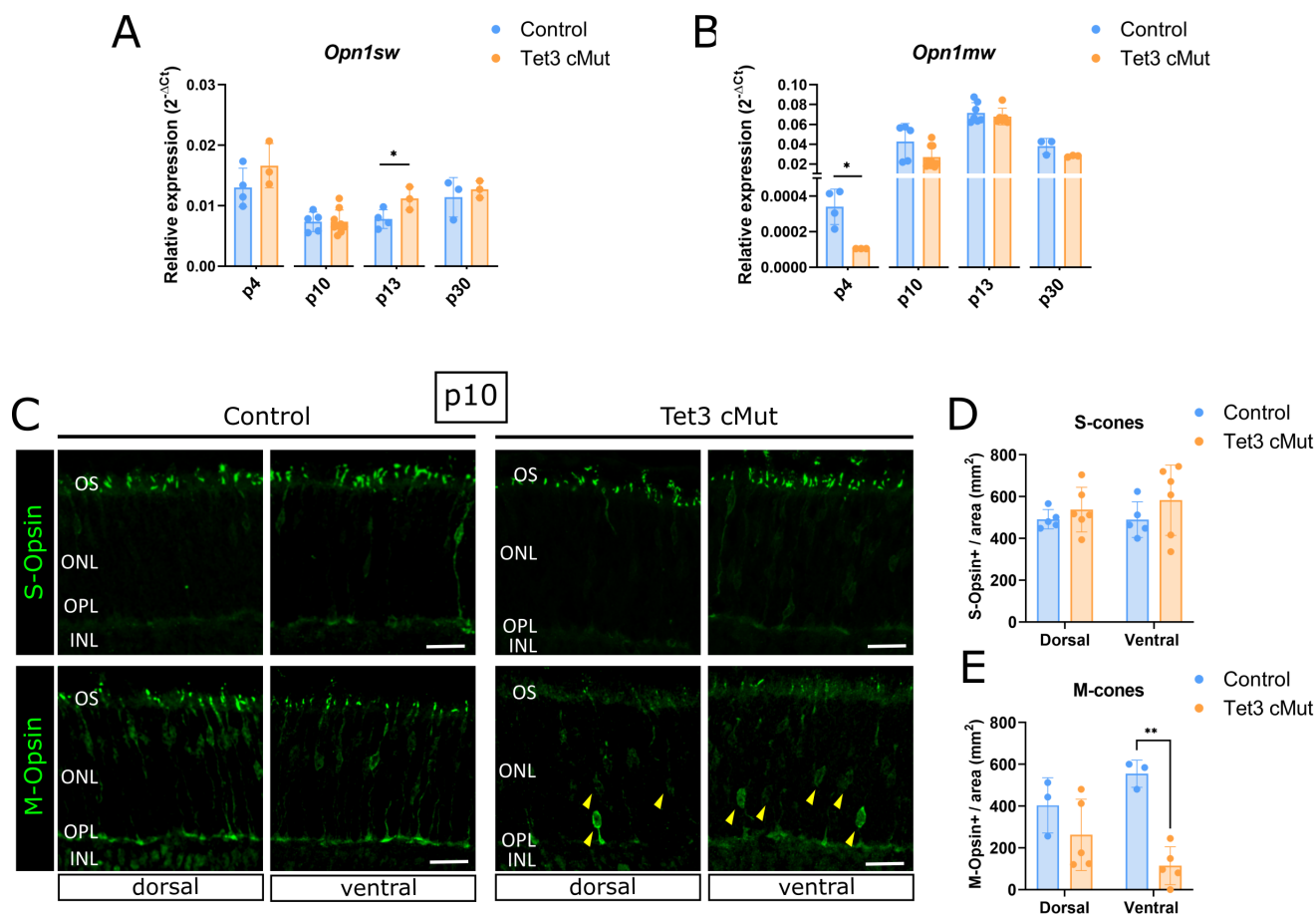


Figure 30: Opsin expression at early post-natal stages

(A-B) Relative gene expression of *Opn1mw* and *Opn1sw* at different developmental stages of mouse retina. Error bars show mean \pm SD, two-way ANOVA with Bonferroni's post-hoc test; * $p < 0.05$ (C) Confocal micrographs of mouse coronal sections imaged at p10 for S- or M-opsin (green) in dorsal and ventral retinae. Scale bars 20 μ m in B. (D-E) Quantification of the experiment in C showing significantly reduced M-Opsin⁺ outer segments. Error bars are \pm SD. Two-way ANOVA with Bonferroni post-hoc test, * $p < 0.05$, ** $p < 0.01$

showed differential expression, the translated proteins are seemingly affected.

All in all, these data suggest that altering the expression levels of key players involved in the canonical thyroid hormone pathway is not sufficient to induce molecular changes in the levels of thyroid hormones. Thus, their expression levels might not be the cause of the cone phenotype associated to *Tet3* mutation.

18.3 The binding between Tet3 and Thrb2 is not affected in *Tet3* mutant mice

Previously it was shown that T3 is able to induce Tet3-dependent DNA demethylation at specific loci and that this occurs via interaction and stabilisation of the Thrb on chromatin [81]. For this reason, we next asked whether Tet3 mutation affects Thrb activity, in turn mediating the observed

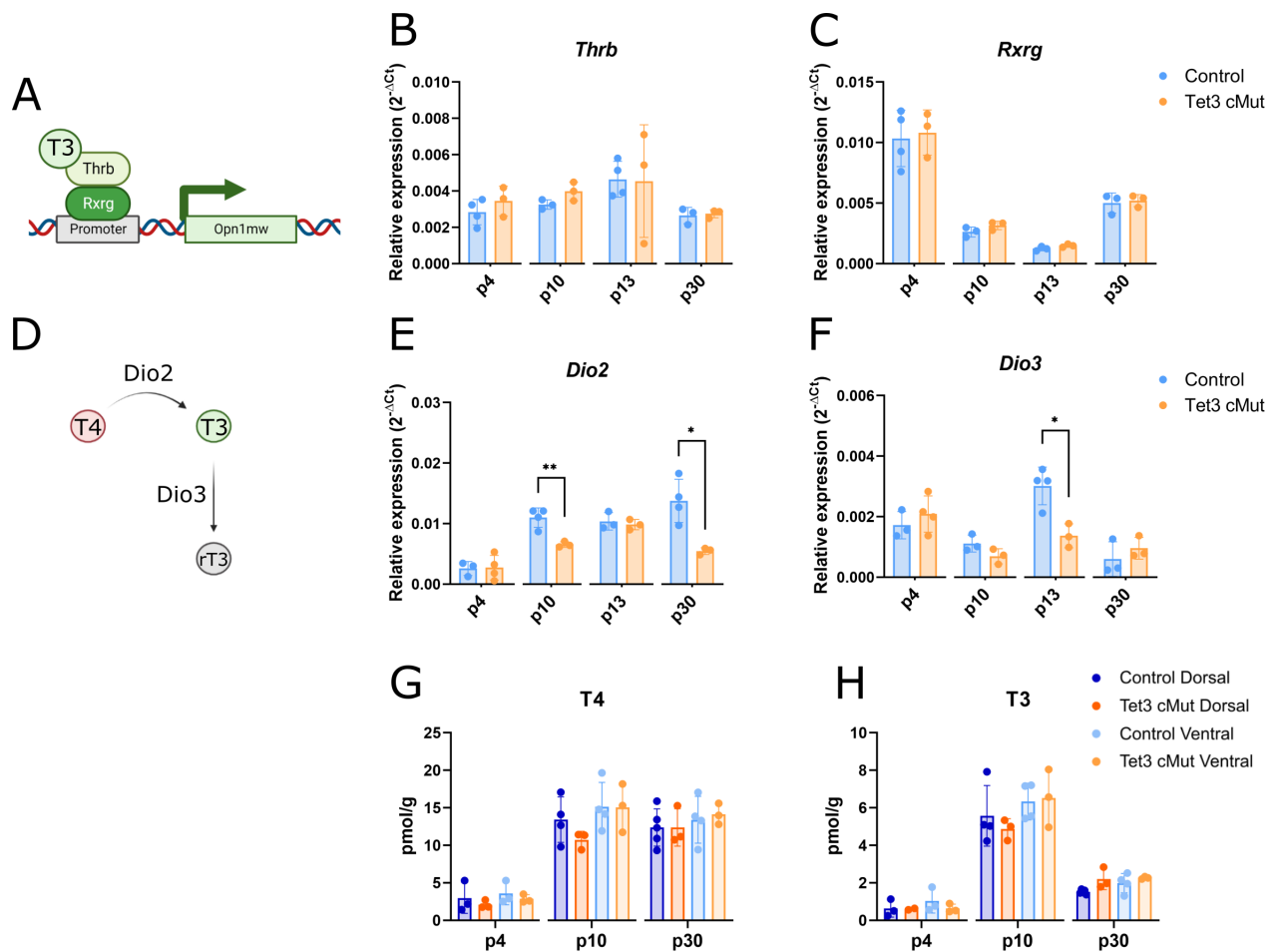


Figure 31: Canonical thyroid hormone pathway

(A) Graphics showing the heterodimer complex formed by *Thrb* and *Rxrg* receptors and their positive regulation on gene transcription (e.g., on *Opn1mw* gene) (B-C) Relative gene expression of *Thrb* and *Rxrg* at different developmental stages of mouse retina. Error bars show \pm SD, two-way ANOVA with Bonferroni's post-hoc test (D) Schematic representation of the thyroid hormone metabolic pathway (E-F) Relative gene expression of *Dio2* and *Dio3* at different developmental stages of the mouse retina. Error bars show \pm SD, Student t-test each time point comparison. * $p < 0.05$, ** $p < 0.01$, *** $p < 0.001$ (G-H) Quantification of total T4 and T3 in dorsal and ventral halves of the mouse retina in control and mutant mice. Two-way ANOVA with Bonferroni's post-hoc test

delay in M-opsin expression in cone photoreceptors. Therefore, plasmids encoding either the wildtype mouse short Tet3 isoform (Tet3^{wt}) or its mutated version (Tet3 ^{Δ Ex7/8}), lacking the same exons 7 and 8 as in the *in vivo* mouse model, fused with GFP were generated. With these, HEK293T cells were co-transfected with a construct encoding the mouse *Thrb2*, myc tagged at the carboxy terminal end (mThrb2-MYC). After successfully assessing co-transfection via immunolabeling for both GFP⁺ and MYC⁺ cells (Fig. 32A), we investigated protein-protein interaction by co-immunoprecipitation, pooling down the *Thrb2* with an anti-MYC antibody and proceeding to detect the two proteins via Western blot. In agreement with previously published data [81], the deletion of exons 7 and 8 in the catalytic domain of Tet3 did not affect its ability to bind *Thrb2* (Fig. 32B). Moreover, as a more indirect validation of the interaction between Tet3

and thyroid hormone receptor, the different cytosine modifications (namely 5mC, 5hmC, 5fC and 5caC) were measured using HPLC coupled with tandem mass spectrometry (MS/MS) (Fig. 32C-F). The analysis revealed that the presence of *Thrb2* boosted the demethylase activity of *Tet3*^{wt}, resulting in a significant increase in the levels of 5hmC, 5fC and 5caC (Fig. 32D-F). As expected, this synergistic effect was absent in hmC when expressing the catalytically inactive form of *Tet3* (light and dark orange bars in Fig. 32D). Thus, with these experiments we could confirm the interaction between *Tet3* and *Thrb2*. Moreover, that impairing part of *Tet3* catalytic domain does not interfere with binding to *Thrb2*, and that the latter potentiates *Tet3*-dependent demethylation activity.

19 Tet3 in cone vs bipolar cell differentiation

19.1 Cellular changes in cone and bipolar cells mostly manifest in the late postnatal period

Having observed that many genes involved in bipolar cell fate determination (*Otx2*, *Vsx2* and *Prdm1*) are differentially expressed in the RNAseq data at both p4 and p10 (Fig. 28 and 29), the expression level of these and other genes (*Isl1*, *Lhx4* and *Prdm8*) implicated in this process (Fig. 33A) were analysed by qRT-PCR at three different time points. *Isl1*, *Lhx4* and in turn *Prdm8* are downstream genes activated by *Vsx2* for bipolar cell sub-type specification (Fig. 33A, [56]). All three genes showed a significantly decreased expression at p4, which in case of *Prdm8* was also observed at p10 (Fig. 33B-D). Accordingly, their upstream regulators *Otx2* and *Vsx2* showed a similar trend (Fig. 33F,G), while *Prdm1* was the only gene showing upregulation at p10, confirming the previous data (Fig. 33H).

Of these genes, the triad *Otx2*, *Vsx2*, *Prdm1* has been linked to photoreceptor vs bipolar cell fate decision. *Otx2* is expressed by both photoreceptor and bipolar cell precursors and is able to regulate the expression of both *Vsx2* and *Prdm1*[132], thus acting as a master regulator. As such, it is necessary factor to induce the specification of these two cell types [277]. Following *Otx2* activity, *Vsx2* and *Prdm1* compete at the precursor stage, by inhibiting each other and pushing the differentiation towards bipolar (*Vsx2*) or photoreceptor (*Prdm1*) cell fate [75] [76] [157] [277]. Considering the downregulation of *Otx2* and *Vsx2* and the upregulation of *Prdm1*, we raised the question of whether the altered number of cone photoreceptors in ONL and bipolar cells in the INL is caused by a shift in the differentiation of the two retinal cell populations. Cone photoreceptors and bipolar cells are specified during two different waves of retinogenesis, one embryonic and the other postnatal, respectively (Fig. 34A) [268]. The excess of cones observed in *Tet3* mutant could be determined in either of the two developmental periods, or both. In case it takes place embryonically, when most cone photoreceptors are generated, quantifications of this cell type at selected postnatal stages should show no alteration in number. Indeed, the total number of cone photoreceptors (*Arr3*⁺) did not differ over time in control mice, with the

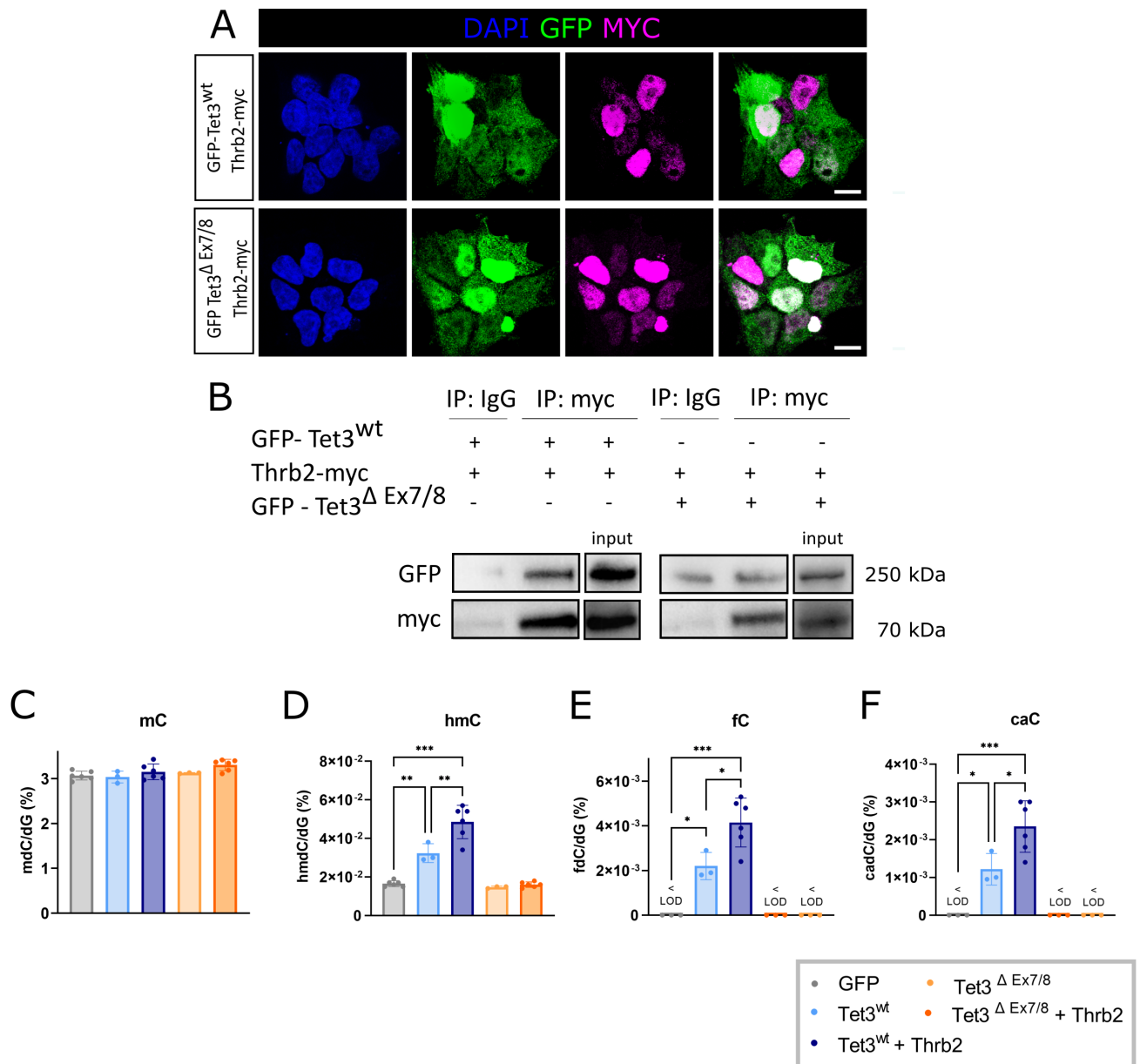


Figure 32: Thrb2 Co-IP and interaction with Tet3

(A) Confocal images of transfected HEK294T cells immunostained for GFP (green) and MYC (magenta) and counterstained with DAPI (blue). In both conditions the staining revealed successful transfection and nuclear localisation. Scale bar= 5 μ m. (B) Co-immunoprecipitation using anti-myc antibody to pool down Thrb2 interactors revealed an interaction between Tet3 and Thrb2 despite the mutated Tet3 (Δ Ex7/8). Input 2% of the lysate material (C-F) HPLC-MS/MS measurements of the different cytosine modifications in HEK293T cells transfected with Tet3^{wt} or catalytically inactive Tet3, with or without Thrb2, showing synergistic effects of Thrb2 and Tet3^{wt}. Error bars represent mean \pm SD; two-way ANOVA with Bonferroni's post-hoc test. * $p < 0.05$, ** $p < 0.01$, *** $p < 0.001$

exception of a modest decrease at p30, probably due to selective cell death following synaptic maturation [23]. However, in *Tet3* mutant mice, this number was tendentially higher at p13 and differed significantly from the number of cones observed at p30 in control mice (Fig. 34B). The opposite trend could be observed for ON-bipolar cells, where the number of Pcp2⁺ cells

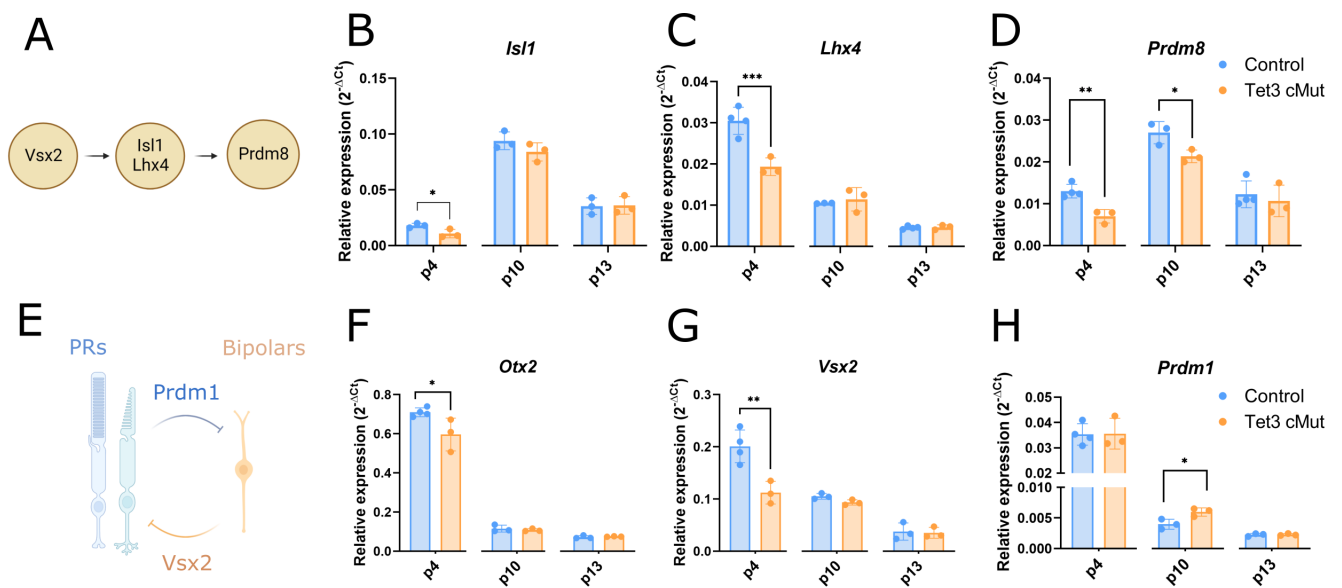


Figure 33: Bipolar cell markers

(A) Schematics of the sequential pattern of gene expression involved in bipolar cell specification. (B-D, F-H) Relative expression of indicated genes quantified by qRT-PCR at different developmental stages. Error bars represent \pm SD; Student t-test * $p < 0.05$, *** $p < 0.001$. (E) Image showing the competing effect between Prdm1 and Vsx2 in photoreceptors vs bipolar cell differentiation

increased in control mice from p10 and p13 to p30, but remained constant over time in *Tet3* mutant mice (Fig. 34C). Being ON-bipolars a sub-population of total bipolar cells, the possibility persists that these numbers are an underestimation of the real decrease of total bipolar number. Thus, these results show that the increase in the number of cone photoreceptors is seemingly taking place at postnatal stages, when bipolar cell generation and maturation occurs.

Strikingly, some misplaced *Arr3*⁺ cones could be occasionally spotted within the INL in proximity of *Pcp2*⁺ cells at both p10 and p13 (white arrowheads in Fig. 34D, F), although to lesser extent in the latter time point, and the two markers never co-localised. If, like these observations would imply, new cones were generated in the INL from former bipolar precursors, these newly formed cells would still need to migrate towards and across the ONL to reach their final location. Along the same line, and as for the M- Opsin⁺ cones (fig. 30), some *Arr3*⁺ cell bodies were often located more basally, in the lower half of the ONL.

19.2 Neither cell death nor proliferation contribute to the altered cell numbers in both ONL and INL

Next, in order to exclude that the observed cellular differences were the result of altered cell survival or proliferation, retina sections were stained via TUNEL assay or with Mki67, to check for apoptosis and cell replication, respectively. No differences in the number of TUNEL⁺ cells could be observed at any of the time points in both INL and ONL, thereby excluding a role for cell death in shaping retinal cells number at p10 and p13 (Fig. 35A, B). In terms of prolifera-

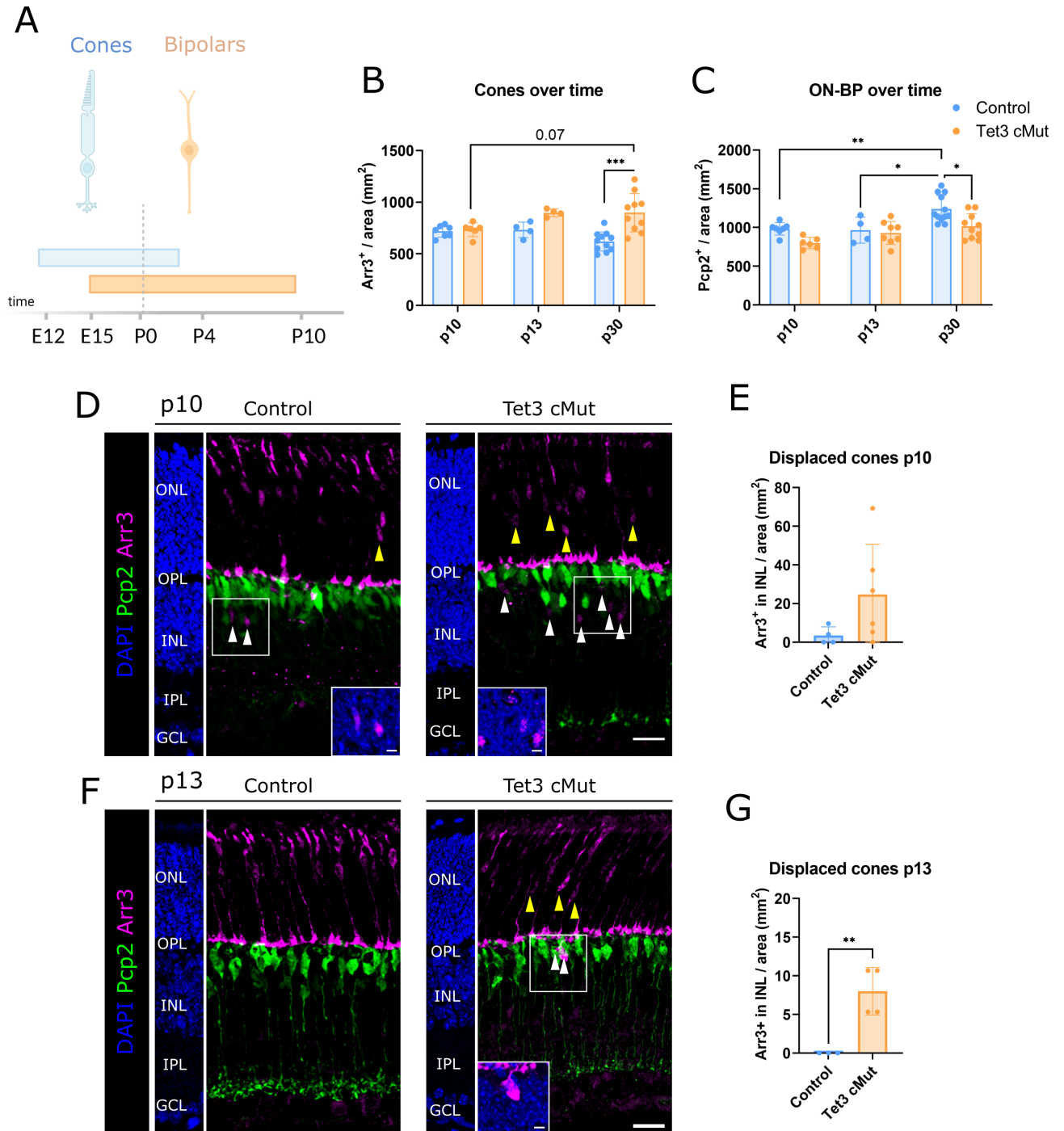


Figure 34: Bipolar and cone cells specification

(A) Schematics of the developmental time of cone photoreceptors and bipolar cells. (B-C) Quantification of Arr3⁺ cones and Pcp2⁺ ON-bipolar cells at the developmental stages indicated. Error bars show mean \pm SD, two-way ANOVA with Tukey's post-hoc test. * $p < 0.05$, ** $p < 0.01$, *** $p < 0.001$. (D and F) Confocal micrographs of retinal cross-sections imaged at p10 (D) and p13 (F) for Pcp2 (green) and cone arrestin (magenta) counterstained with DAPI (blue shown as insert). White arrowheads point at displaced Arr3⁺ signal in the INL, while yellow arrowhead point to Arr3⁺ cell bodies at lower migration rate. Scale bars= 20 μ m and 5 μ m for magnified images. (E and G) Quantification of displaced Arr3⁺ cells in the INL from experiments in D and F. Error bars are SD. Unpaired Student t-test ** $p < 0.01$

tion, the last retina progenitors are known to become postmitotic around birth [302], therefore at p4 very few cells are expected to be strongly immunopositive for Mki67 at the apical side (photoreceptor side), although some protein signal can faintly still label cells in the more basal regions (ganglion side). This was indeed true for control mice, but also for *Tet3* mutant retinæ (Fig. 35C) as the number of apical Mki67⁺ cells did not show any difference between the two genotypes (Fig. 35D). Notably, some of these proliferating apical cells were also Vsx2⁺. One likely explanation is that these Mki67⁺/Vsx2⁺ double positive cells are bipolar cell precursors, which after completing the last round of cell division, started expressing the pan bipolar marker Vsx2 while descending basally (shown by arrowheads in Fig. 35C and magnifications). Their quantification revealed again no difference between controls and *Tet3* mutants (Fig. 35E). During the first postnatal week, retinal precursors (postmitotic) acquire their cell identity and start differentiating [302]. Thus, it is conceivable that all cells are Mki67 negative. As expected, no sign of proliferation could be detected at this stage (not shown). Taken together these results revealed that both cell survival and proliferation are unaffected by our *Tet3* mutation and, therefore, cannot explain the differences in cell composition, particularly in terms of number of bipolar and cone cells. Moreover, although transcripts appeared dysregulated at earlier stages (p4 and p10), the observed alterations in cell number seem to occur only at later postnatal days (between p13 and p30), suggesting that affected cells might require time to fully mature and reach their final location.

19.3 *Vsx2* and *Prm1* show differentially methylated loci and enhancers

In order to gain a better understanding of the regulatory mechanisms of key genes involved in photoreceptor and bipolar cell development, we performed Illumina methylation EPIC arrays to assess the methylation status of genomic loci of p30 mice, based on the assumption that at this stage events driving fate specification of these cells are stabilised together with DNA signature marks. Differential analysis in *Tet3* mutant vs control mice of true methylation (5mC) and hydroxymethylation (5hmC) revealed many differentially methylated sites (DMSs) (Fig.36A,B). Visualisation of top one thousand DMSs (as well as top ten thousand DMSs (data not shown) revealed more hypermethylated and hyperhydroxymethylated regions in *Tet3* mutant mice (Fig. 36A,B), the latter being a rather unexpected result considering the global lower hmC detected in mutant mice (Fig. 15C). Moreover, in terms of position, methylation and demethylation showed a similar trend with the epigenetic marks represented at promoter regions (shown as regions 200 bp upstream the transcription start site (Tss)), farther regions from Tss (indicating enhancers), and at gene body (Fig. 36C,D) suggesting an active role in transcription in agreement with previous studies [174] [117] [113] [150]. GO-term analysis of these DMSs using the database for annotation, visualization and integrated discovery (DAVID) revealed the presence of these epigenetic marks at genes involved in axon guidance (e.g., *Robo2*, *Sema5b*, *Gsk3b*, *Ephb2*, *Ephb1*, *Sema6b*, *Prkca*, *Sema6c*), thyroid hormone signalling pathway (e.g., *Thrb*, *Notch1*, *Thra*, *Rxra*,

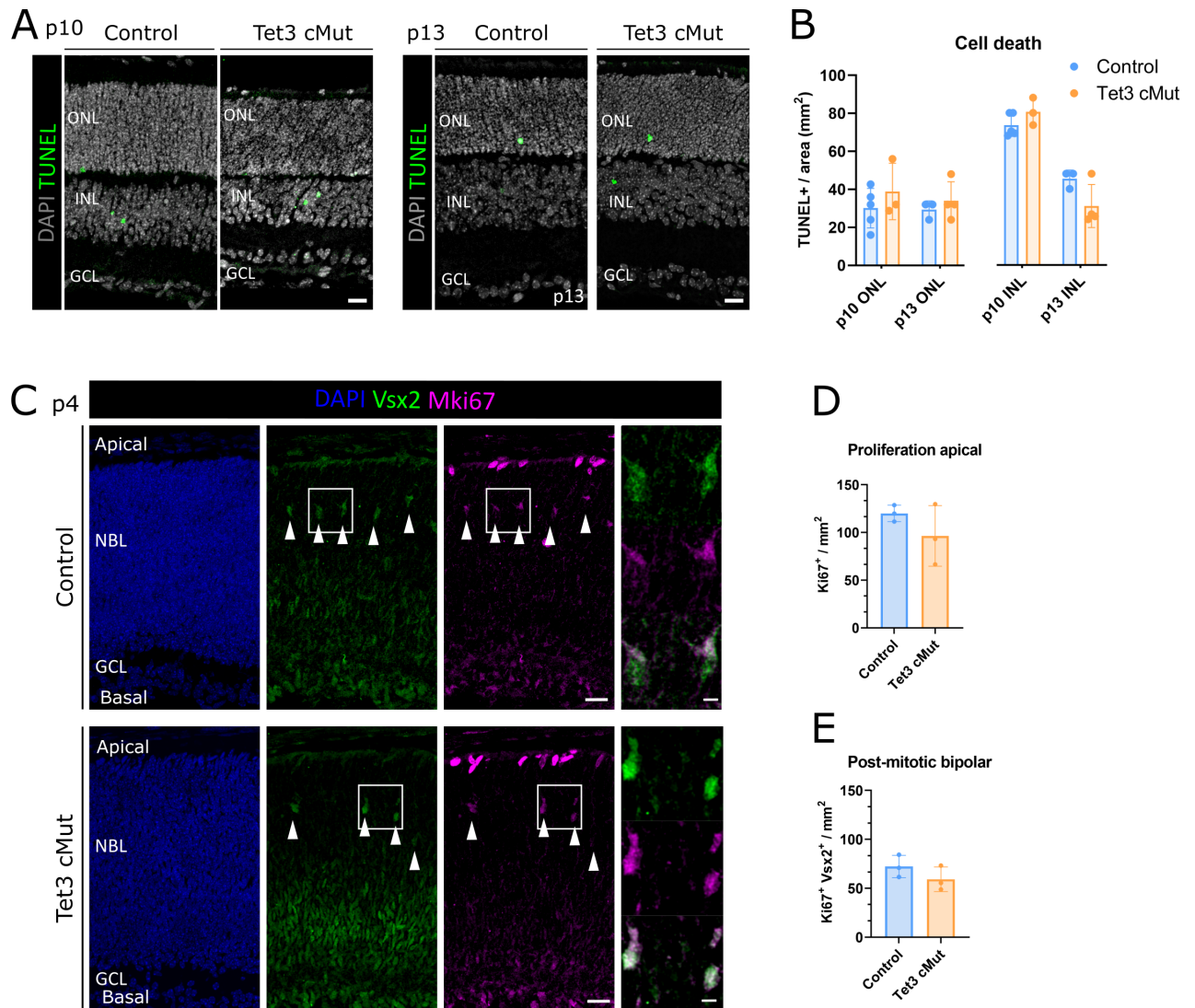


Figure 35: Apoptosis and cell proliferation

(A) Retina cross-sections stained for TUNEL as marker of apoptosis. Scale bar= 20 μ m (B) Quantification of experiments in A showing no difference in apoptotic events between genotypes. Error bars show \pm SD, two-way ANOVA with Bonferroni's post-hoc test. (C) Confocal micrographs of retinal cross-sections imaged at p4 for Mki67 (magenta) as proliferation marker and Vsx2 (green) for committed bipolar cells. Scale bar= 20 μ m and 5 μ m for quadrants, (D, F) Quantification of the stainings in C showing no significant difference in the number of proliferating cells. Error bars are \pm SD. Unpaired Student t-test

ONL, INL: outer and inner nuclear layers; NBL: neuroblast layer; GCL: ganglion cell layer

Slc2a1, *Slc16a2*) and synthesis (e.g., *Prkca*, *Tshr*, *Atf4*, *Creb1*) as well as genes important for the establishments of tight (e.g., *Actb*, *Tjap1*, *Runx1*, *Tjp1*, *Tjp2*, *Tuba1c*, *Jam2*), gap (e.g., *Gucy1b2*, *Adcy3*, *Adcy1*, *Tuba4a*, *Adcy6*, *Tuba1c*, *Egfr*, *Tubb5*) and adherent (e.g., *Actb*, *Cdc42*, *Ctnna1*, *Ctnna2*, *Ctnna3*, *Nectin1*, *Nectin2*) junctions (Fig. 37E,F) (highlighted genes are common to gained 5mC and 5hmC). The fact that same genes appeared to bear both a gain in methylation (5mC) and hydroxymethylation (5hmC) suggest that the position at which these occur is as important as the type of modification, and coupled investigations at transcriptional and pro-

tein levels are required to further assess the outcome in specific cases. Since *Vsx2* and *Prdm1*, the two genes involved in the specification of bipolar and photoreceptor cells, respectively, appeared to be differentially expressed during early postnatal stages (p4 and p10 in our dataset), we had a closer look at the methylation and demethylation patterns of these two genes. Notably, *Vsx2* locus showed gained 5mC (42.9%) in both regions upstream and downstream the Tss, as well as in the gene body, including methylation in the first intron recently showed to negatively correlate with transcription independently from tissue and species [6]. Around 28% of sites showing methylation in control mice were lost in *Tet3* mutants and of these, only 9.5% showed 5hmC mark. Accordingly, 19% of 5hmC marks present in control mice were lost in mutants because these positions were hypermethylated (Fig. 36G). Among these, a recently described super enhancer (SE) regulatory element of *Vsx2* gene (yellow rectangle in Fig. 36G). Deletion of *Vsx2*-SE causes reduction in the number of bipolar cells and increase in the number of photoreceptors, including cones [18]. Overall, the accumulation of 5mC observed at *Vsx2* locus, as well as at regulatory regions, is a conceivable explanation for the reduced expression at transcript level. Opposite to *Vsx2*, *Prdm1* locus showed more gain in 5hmC marks (31.2%), many of which (34.4.%) were generally methylated in control mice, than gain in 5mC (18.7%) (Fig. 36H). Notably, a previously identified enhancer region (En) (yellow rectangle in Fig 36H) close to the Tss of *Prdm1* gene locus, previously shown to influence *Prdm1* expression [181] [277], lost methylation in *Tet3* mutant mice, thus suggesting a plausible positive regulation of expression, corroborating previous data (Fig. 29A and 33H). Taken together these results reveal several differentially methylated sites in *Tet3* mutant mice mostly occurring in gene bodies in agreement with a role of these epigenetic marks in regulation of gene transcription. Moreover, the dysregulation of same pathways harbouring opposite DNA marks (gained 5mC and gained 5hmC) suggest a more complex molecular regulation in part explained by marks position (as for the *Vsx2* and *Prdm1*).

20 *Tet3* in photoreceptor maturation and metabolism

20.1 At later postnatal period, *Tet3* mutation leads to gene expression dysregulation related to visual perception

To address which changes in gene expression might underlie the differences in cell composition observed at later time point, we performed RNA sequencing at p30. Among all 80 significantly dysregulated genes, only 46 resulted significant in the analysis at p10 (Fig. 37A). Notably, none of these genes were related to bipolar or photoreceptor differentiation as well as cone specification. This result is in agreement with the fact that at this stage cells have already migrated, acquired their final identity and integrated in the expected location [249].

Principal component analysis (PCA) showed a clear separation between the two conditions (Fig. 37B), indicative of a strong variability in gene expression levels. This was further high-

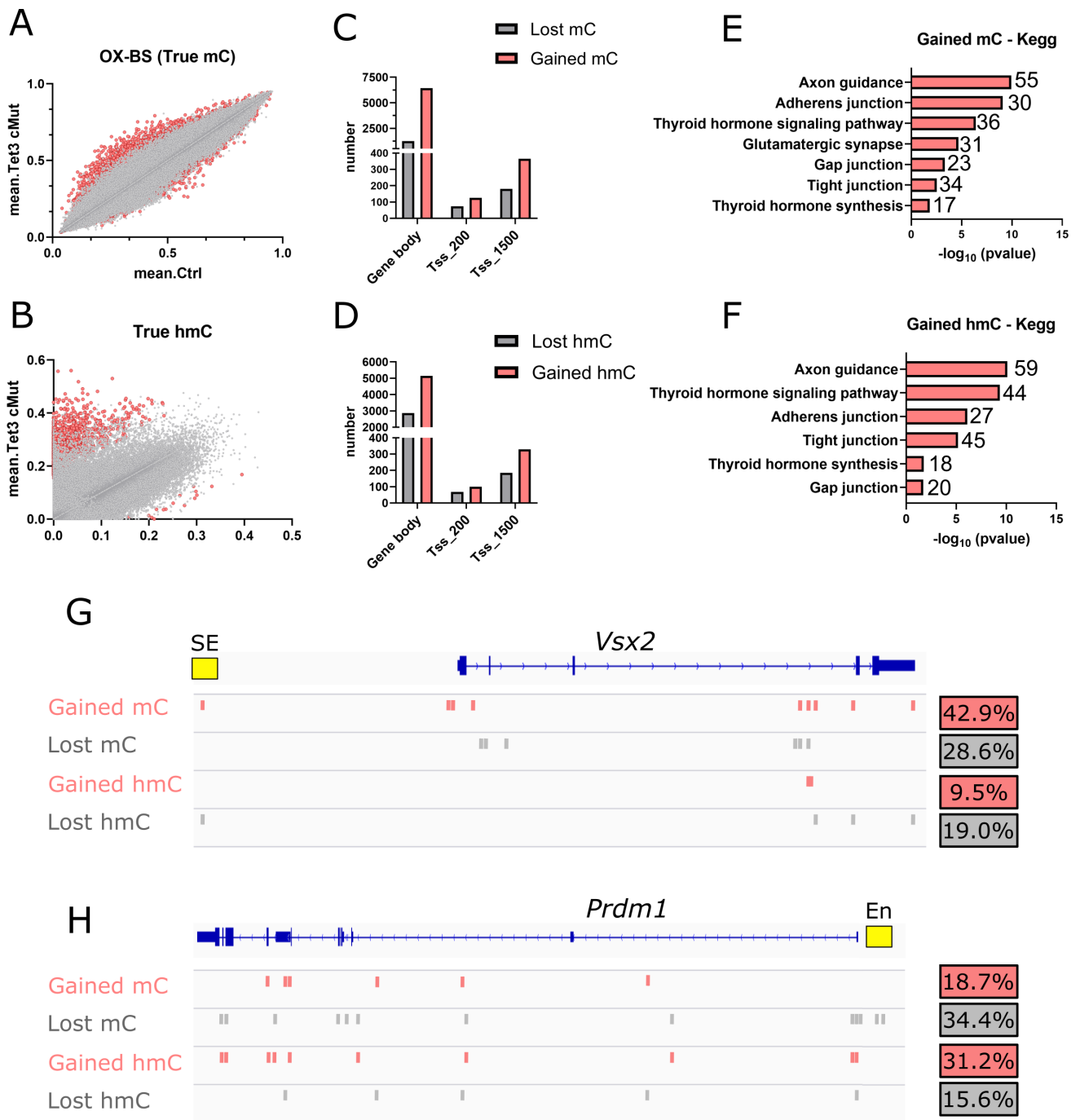


Figure 36: Differential methylation in *Tet3* mutant mice

(A,B) Distribution of differentially methylated sites (DMSs) in *Tet3* mutant and control mice. Top one thousand DMSs are shown with red dots just for visualization purposes. (C,D) Regional position of top ten thousand DMSs (gain and loss of mC and hmC) in gene body, promoters (Tss_200) and enhancer (Tss_1500) regions. (E,F) Kegg pathways of implicated genes showing gained mC and hmC. Number of affected genes are indicated next to the corresponding bar. (G,H) Representative IGV traces showing gained mC and hmC (in red) and lost mC and hmC (in grey). Each bar corresponds to a differential mark in the comparison *Tet3* mutant vs control, percentage indicated on the right. In blue reference *Vsx2* and *Prdm1* gene locus. Yellow rectangles indicate part of a super enhancer (SE) recently described in *Vsx2* locus in [18] (G) and an enhancer region (En) regulating *Prdm1* gene expression (H) [278]

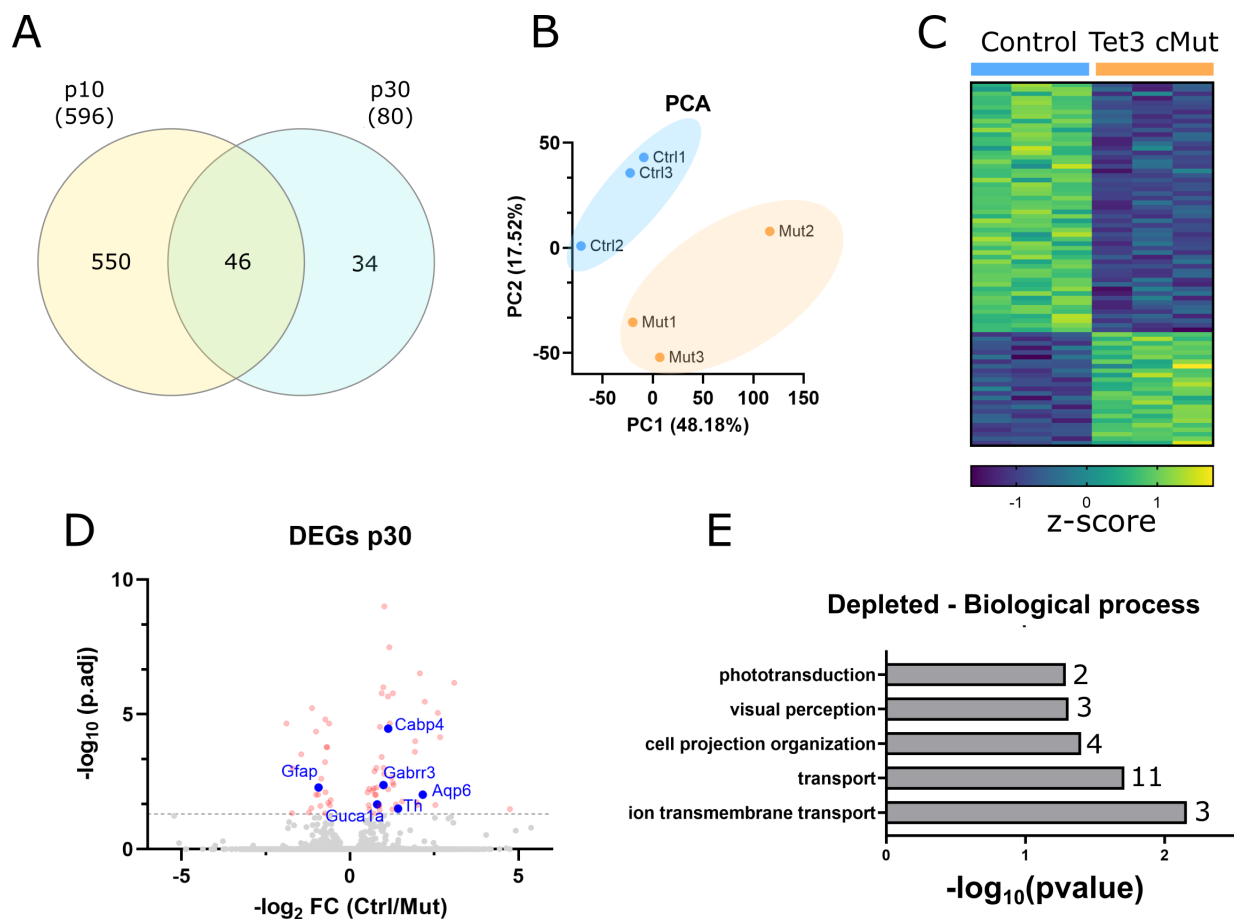


Figure 37: RNA-seq p30

(A) Venn diagram of differentially expressed genes at p10 and p30, showing minor overlap between these two time points. (B) Principal component analysis showing two separate clusters of control and Tet3 mutant mice. (C) Heat map of the significant differentially expressed genes (DEGs). (D) Volcano plot of DEGs. Red dots represent significant genes, grey dots are not significant, and the dashed line represent significance threshold. (E) GO term analysis of depleted genes in Tet3 mutant mice performed with DAVID database

lighted by comparison between the two genotypes, which resulted in 55 down- and 25 upregulated genes (fig. 37C and D). GO term analysis of downregulated genes (fig. 37E) indicated an enrichment of terms related to visual perception and phototransduction (*Th*, *Cabp4* and *Guca1a*) and signal transduction (*Cabp4*, *Gabrr3*, and *Grm8*). Some of the involved genes showed the same trend also at earlier postnatal stage (p10), suggesting that these changes occur much earlier than the time when post-synaptic elements invaginate to form a pre-synaptic ribbon [197], even before eye opening. The encoded proteins locate either in the outer segment or at the synaptic termini of photoreceptors and are, therefore, fundamental to ensure a proper and efficient elaboration of light stimuli and their propagation to lower layer neurons. As such, the observed molecular alterations might contribute to the reduced photopic b-wave, previously shown in this study (Fig. 25), of *Tet3* mutant mice.

Driven by these observations, retina cross-sections from p30 mice were labelled with dif-

ferent synaptic markers, e.g., vGlut1 and PSD95, two general pre- and postsynaptic markers, respectively (Fig. 38A, B). Notably, both vGlut1- and PSD95-covered areas of the outer plexiform layer (OPL) were larger in *Tet3* mutant mice compared to the control (Fig. 38C, D). One explanation for the higher degree of coverage might be attributed to the increase in number of cone photoreceptors observed in the ONL and, consequently, of their pedicles, which make the OPL area more crowded and, therefore, thicker (Fig. 18). Next, we looked more specifically at synaptic termini and synapses established between photoreceptors and bipolar cells using two known antibodies, namely Cacna1s and Ctbp2. Immunostaining with Cacna1s, labelling bipolar dendrites at the synapse with photoreceptors (Fig. 38E), revealed that the total area occupied by this marker was increased (Fig. 38F), same as for vGlut1 and PSD95. Conversely, the number of Cacna1s puncta, corresponding to each individual synaptic bouton, showed a tendency to decrease, despite the overall increase in the number of cone photoreceptors (Fig. 38G).

Finally, synaptic ribbons in both rod and cone photoreceptors were labelled with Ctbp2. The different ribbon synapses formed by the two types of photoreceptors can be easily distinguished based on their morphology. In fact, while cone synapses lay at the base of the pedicle, closer to the INL and more organized into an array-like structure, rod ribbon synapses appear more arcuate in their shape [220]. Some of these array-like structures were consistently observed in control cone pedicles (yellow arrowheads). However, some pedicles in *Tet3* mutant mice were signal deprived (white dashed line), meaning that their ribbon synapses were anatomically and functionally disrupted (Fig. 38H). Since this phenomenon affected only one part of all cones, it is conceivable that specifically newly generated cones do not manage to integrate in the pre-existing circuitry and, thus, do not participate in the established network activity. Overall, from these results we concluded that in *Tet3* mutant mice, cone photoreceptors and lower layer neurons do not establish proper synaptic contacts which results in incomplete maturation of these synapses and improper integration of related cells in retinal circuitry.

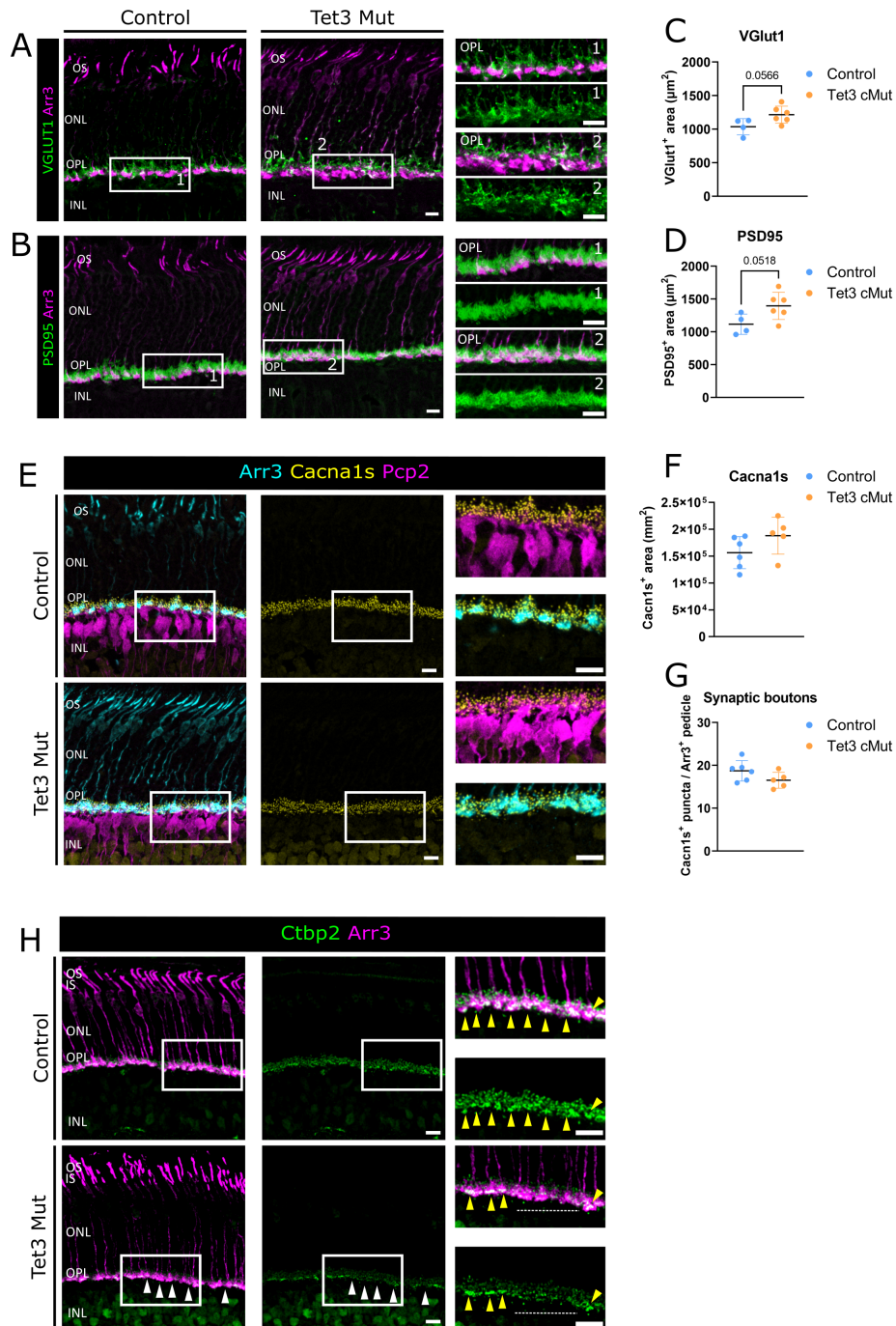


Figure 38: Synaptic markers ONL

(A,B) Immunohistochemistry of retinal cross-sections labelled for vGlut1 and PSD95 (green) as synaptic markers and Arr3 (magenta) for cone photoreceptors. Scale bar= 20 μm and 10 μm for the magnified in quadrants. (C,D) Quantification of sections in A and B showing increased thickness of synaptic layer. Error bars are $\pm\text{SD}$, unpaired Student t-test with corresponding p-value indicated. (E) Retinal cross-sections stained for Arr3 (cyan) for cones, Pcp2 (magenta) for ON bipolar cells and Cacna1s (yellow) to label synaptic boutons. Scale bar= 20 μm and 10 μm for zoomed in images. (F,G) Quantification of the experiments in E. Despite the increase in thickness of Cacna1s labelled OPL, less synapses are formed between ON bipolar and photoreceptors. Error bars= $\pm\text{SD}$, unpaired Student t-test comparison. (H) Confocal micrographs of retina cross-sections immunolabelled for Ctbp2 (green) for ribbon synapses and Arr3 (magenta) for cones. White arrowheads point to regions where ribbon synapses are absent on cone pedicles. Yellow arrowheads are intact cone ribbon synapses. Scale bar in H is 20 μm for lower magnification and 10 μm for high magnification.

20.2 Proteomic analysis of cone photoreceptors reveals Tet3 involvement in actin filament dynamics for vesicle release and cell-cell contact

To gain a deeper insight into the mechanism underlying the observed molecular, cellular and functional phenotype in *Tet3* mutant mice, we performed proteomic analysis on isolated cones at p30. Since cones represent a small minority of cells among photoreceptors, we first enriched this cell population by fluorescence-activated cell sorting (FACS) before proceeding with protein extraction and subsequent analysis. Due to the lack of good surface markers enabling specific isolation of this cell type and because of the general fragility of photoreceptors, in particular at the level of the cilium connecting outer and inner segments, previous attempts at cell selection have proven rather unsuccessful. For this approach, cone photoreceptors were labelled with PNA, already used in my previous immunohistochemistry analyses to identify this cell population. The procedure is schematically represented in Fig. 39A. Cells were gated based on the forward and the side scatter (FSC and SSC, respectively), to exclude debris and duplets, the remaining single cells were sorted on positivity to the corresponding channel (PNA⁺) (Fig. 39B). For both control and *Tet3* mutant samples, a similar amount of cone photoreceptors could be sorted from dissociated retinæ (Fig. 39C). In order to confirm the identity of sorted cells, qRT-PCR was performed checking the expression for both cone opsins (*Opn1sw* and *Opn1mw*), as well as Rhodopsin (*Rho*) to ascertain the degree of rod contamination. Compared to rod population, PNA⁺ sorted cones showed higher transcript expression for both opsins, while *Rho* expression was remarkably lower than in rod pure population (Fig. 39D). *Rho* is highly expressed in rods, therefore, detection in this cell population is expected, whereas the absence of this transcript in PNA⁺ sorted cones, indicates good purity of isolated cells. These results show that PNA can be reliably used for the isolation of cone photoreceptors by FACS.

After successfully performing FACS and confirming cell identities of isolated populations, sorted cones were subjected to proteomic analysis. As additional purity control, we checked for the intensity detection (LFQ) of proteins specifically expressed in either cone or rod photoreceptors in sorted cones versus unsorted retinæ of control mice. In fact, while there was a significant difference in the measured intensities of *Rho*, *Opn1mw* and *Gngt2* (another protein expressed in cones) in unsorted dissociated retina of WT mice, no differences were detected in the intensities of these proteins measured in PNA⁺ sorted cones (Fig. 40A). Therefore, PNA labelling ensures a good and selective enrichment of cone photoreceptors.

Quantitative proteomic analysis revealed dysregulation at protein level in *Tet3* mutant mice with a total of 142 protein found upregulated and 48 proteins downregulated (Fig. 40B). Several identified upregulated proteins play a role in synaptic vesicle transport, priming and transmission (e.g., *Sv2b*, *Synj1*) (Fig. 40C). On the other side, many downregulated proteins are associated with actin filament and actin cytoskeleton organization (*Wdr1*, *Actn1* and *Cdc42*) (Fig. 40E). Kegg pathway analysis also revealed that many upregulated proteins are connected to metabolic pathways (Fig. 40D), while a subset of downregulated proteins was implicated in formation of

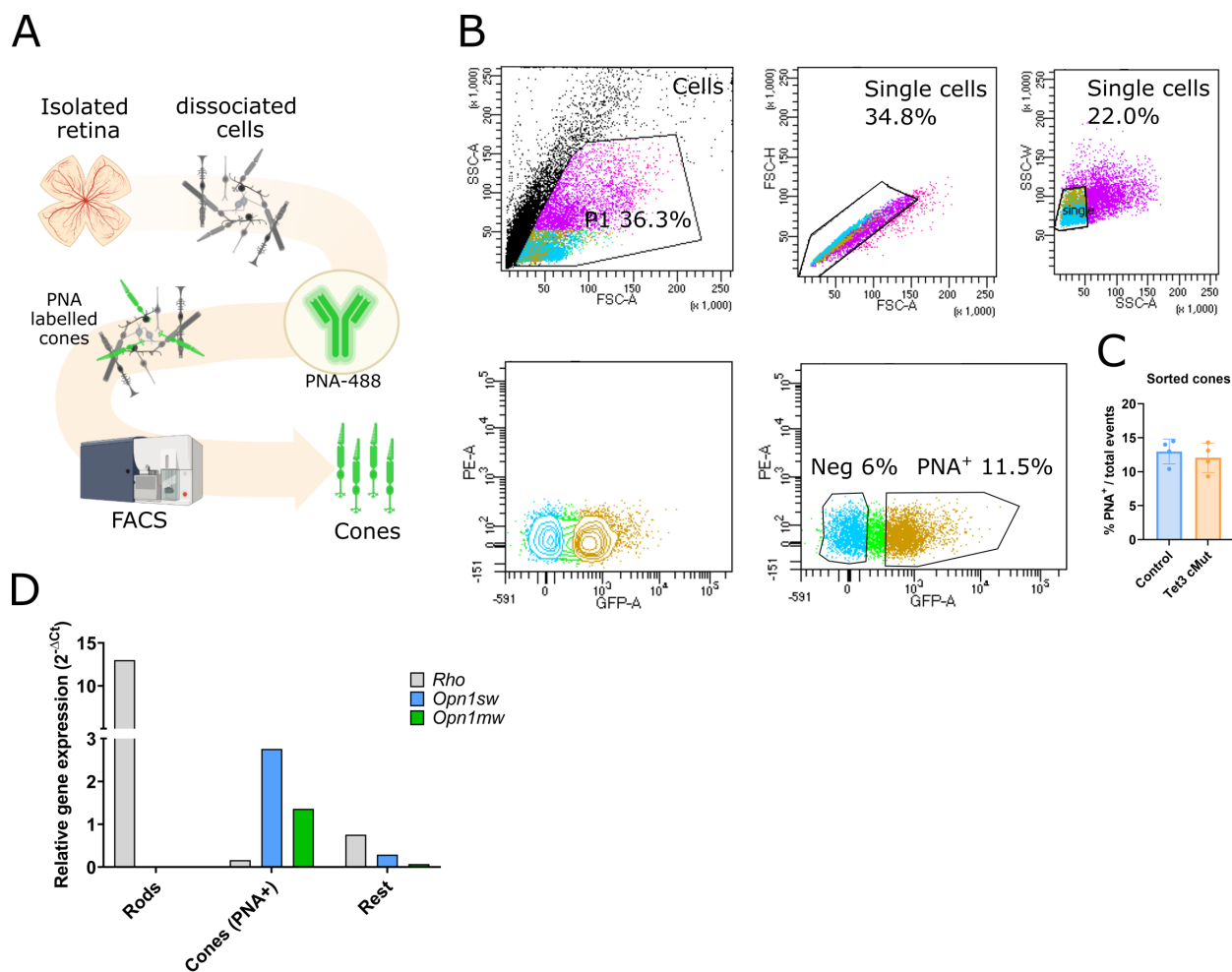


Figure 39: Fluorescence activated cell sorting (FACS)

(A) Schematic representation of FACS procedure to isolate cone photoreceptors from dissected via PNA-488 labelling (modified from [186]). (B) Representative FACS plots showing the sequential gating strategy to first select single cells and viable cells, on which PNA (GFP in the plot) gate is applied. (C) Scatter plot showing the percentage of PNA⁺ events over the total number of cells/events observed. Similar cone numbers were isolated for both control and Tet3 mice. Error bars are \pm SD. Unpaired Student t-test (D) Relative gene expression of rods (Rho, in grey) and cones (Opn1sw, in blue and Opn1mw in green) specific markers in a pure rod population, PNA⁺ sorted cones and negative population. N=1

cell junctions (Fig. 40F). Proteins important for the integrity of tight, adherent and gap junctions were downregulated in *Tet3* mutant mice.

Taken together, these results associate Tet3 to the organization of both actin filaments and bundles, which are key elements of processes such as vesicle priming and fusion as well as cell-cell contact. Moreover, the observed reduction in junctional proteins, essential for a proper crosstalk between cones and rods, is a further indication of poor integration of cones into the retinal network. In the context of light stimulus propagation, perturbations in cone pedicle components would strengthen at sub-cellular and molecular level the previous ERG data indicating and altered electro-chemical signal.

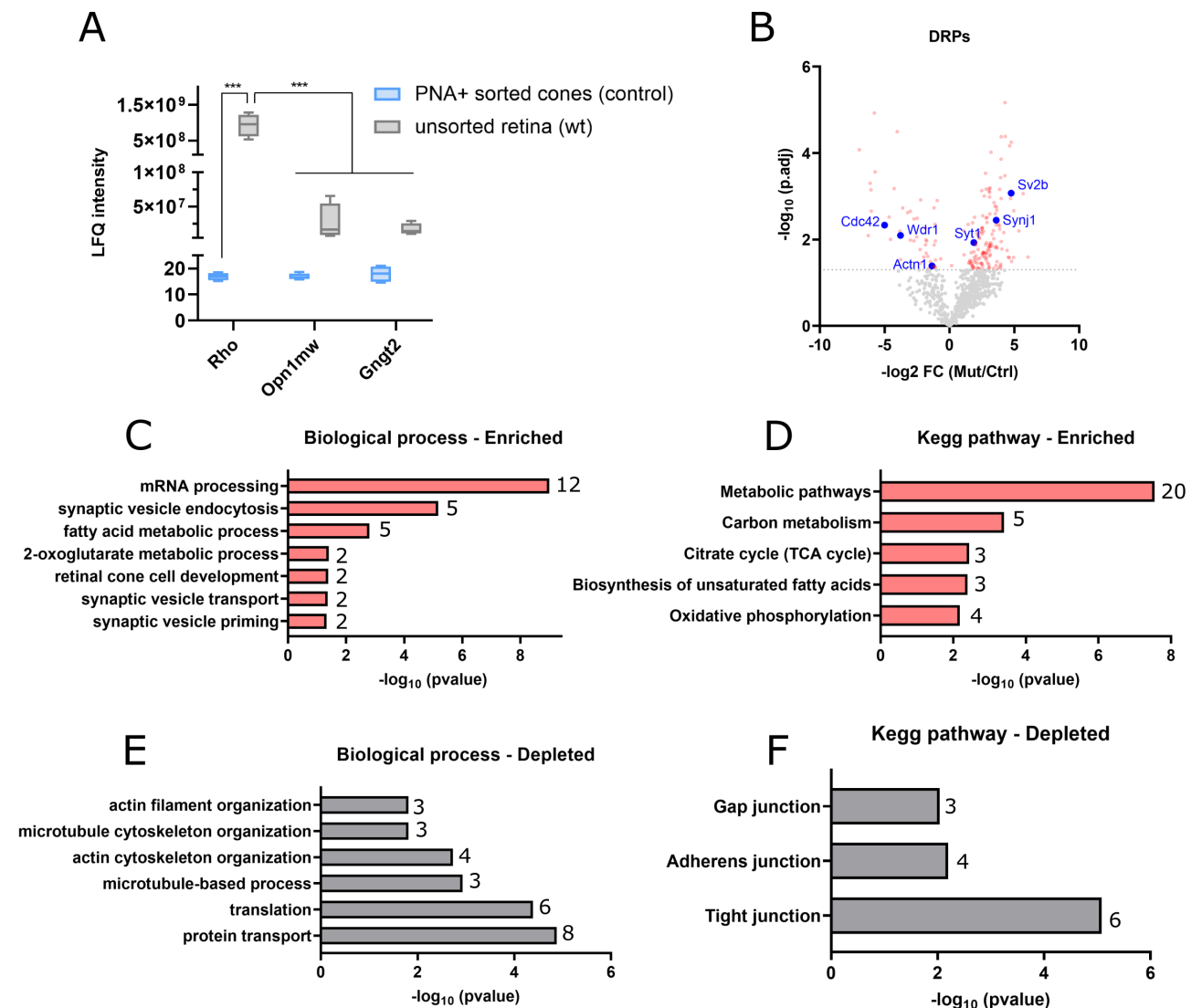


Figure 40: Proteomics of sorted cone photoreceptors

(A) Interleaved box plot showing comparison between two set of proteomics data in control retiniae for indicated proteins (Rho, Opn1mw, Gngt2). Sorted cones (blue boxes) have comparable expression levels of these proteins, whereas these differ significantly in unsorted bulk retina (grey boxes). Boxes show mean and \pm SD; $n=4$ per condition. Two-way ANOVA with Tukey's post-hoc test; *** $p<0.001$. (B) Volcano plot showing the identified proteins in *Tet3* mutant vs control comparison. Dashed grey line represent significance level, grey and red dots are not significant and significant proteins, respectively. Relevant proteins mentioned in the text are highlighted in blue. (C-F) Interleaved horizontal bars representing GO term analysis (performed on DAVID) for biological processes and Kegg pathway, based on enriched and depleted proteins. Numbers next to the bars indicate the number of proteins in my dataset that are found in the reported term.

20.3 Manipulating *Tet3* affects metabolic pathways in cone photoreceptors

As from our proteomic analysis a vast majority of upregulated proteins were allocated to metabolic functions, protein-protein interaction was further investigated using String.db, which utilises experimental knowledge or inference by association to unravel potential relationship in a given list

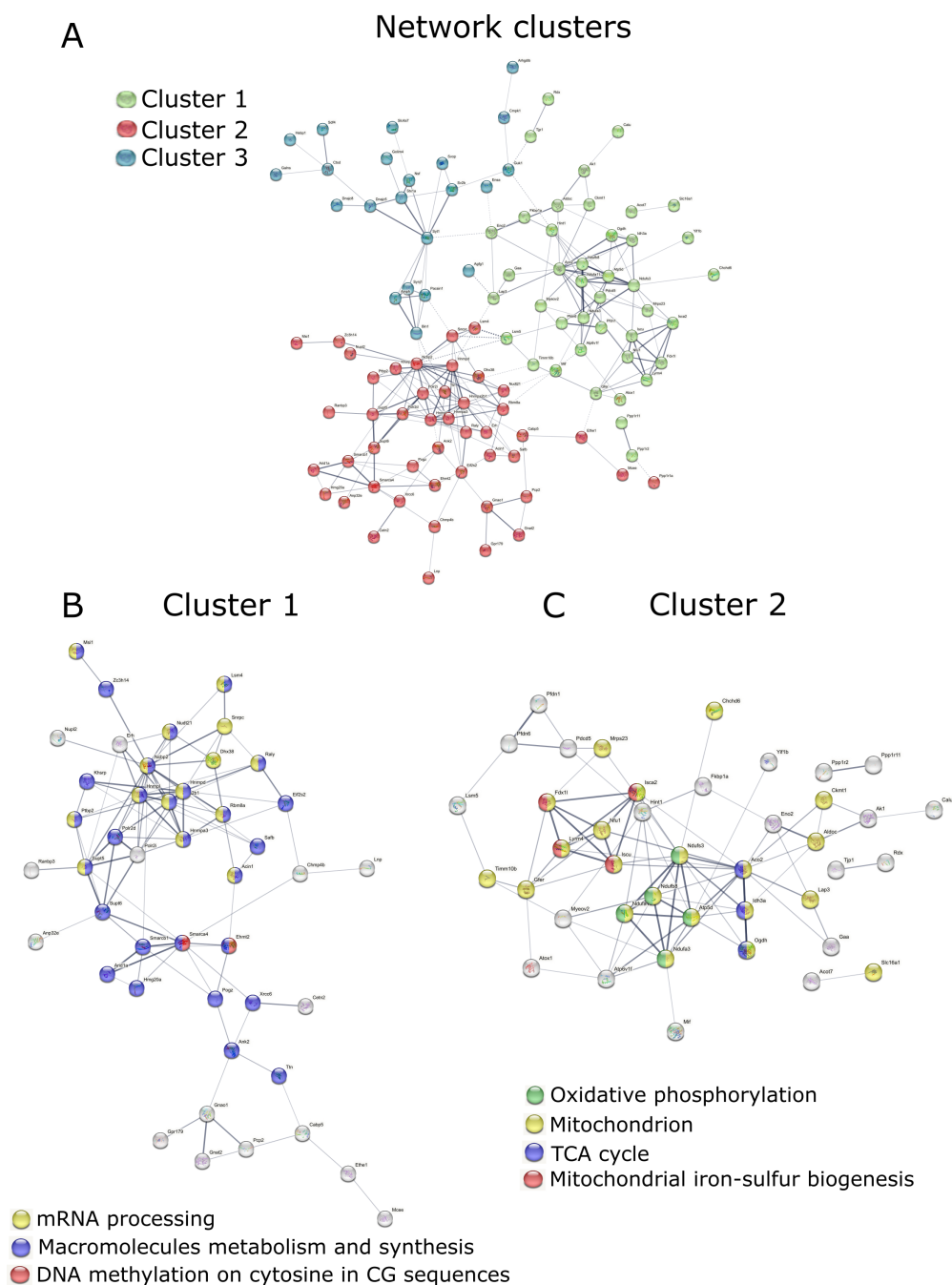


Figure 41: String analysis of enriched proteins

Network analysis of upregulated proteins and protein-protein interaction using STRING.db (A) k-means cluster analysis (number of pre-set clusters =3) labelled by colour coding. Continuous grey lines represent interactions between proteins in the same cluster and the thickness is confidence for that interaction (higher confidence = thicker connecting line). Dashed grey lines are connection points between clusters. (B) Network of cluster 1 colour-coded according to the corresponding GO term. Cluster 1 includes proteins involved in mRNA processing and macromolecules synthesis. (C) Network of cluster 2 coloured based on the corresponding GO term. Proteins involved in mitochondrial metabolic processes belong to this cluster. Proteins that are not assigned to any GO term indicated appear in grey.

of proteins, which are then visualised as tight intermingled networks. (Fig. 41A). When applying a user-specified cluster analysis (k-means method, n=3 number of clusters) and per-

forming GO term enrichment on the resulting clusters, we could observe that cluster1 included proteins of relevance in nucleosome assembly, positive regulation of gene transcription including proteins implicated in the glucose signalling pathway and synthesis of other macromolecules (Fig. 41B). Cluster2 instead, comprised proteins with an active role in tricarboxylic acid cycle (TCA cycle), aerobic respiration and oxidative phosphorylation (OX-PHOS) (Fig. 41C). These results are in agreement with the nature of these cells, as it is well known that most neuronal populations rely on glucose and OX-PHOS for their energy production [308]. However, photoreceptors are very peculiar cells in this regard, mostly relying on the production of lactate and, therefore, aerobic glycolysis for their metabolic needs [272]. As such, this String output might indicate a deviation from the preferred metabolic pathway, which has been previously linked to photoreceptor degeneration and worsening of degenerative conditions like retinitis pigmentosa [3].

Finally, cluster3 contained the upregulated synaptic proteins discussed in the previous paragraph (e.g., *Sv2b*, *Synj1*). Notably, cluster1 and cluster2 had more contact points (represented by the dashed lines) between each other than with cluster3, suggesting an interaction at several protein levels. Moreover, the thicker these lines the stronger the interaction at these connecting points, possibly indicating that the switch in the metabolic program of cones trigger a positive regulation of gene transcription and an enrichment of proteins involved in catabolism of glucose. All in all, these results link *Tet3* to the maintenance of cone metabolic profile, which is crucial to meet the energy need of these cells.

In light of these observations, we imaged retina cross-sections using electron microscopy (EM) at the OPL where synaptic contacts between photoreceptors and lower layer neurons are established, to address the morphology and number of both photoreceptor pedicles and mitochondria. Rod pedicles (green in magnifications of Fig. 42A) can be easily distinguished from cone pedicles (magenta in magnification of Fig. 42A) based on their smaller size and on the fact that they contain a single big mitochondrion adjacent to the ribbon synapse. Instead, cones have generally bigger pedicles that contain more and bigger mitochondria. Remarkably, despite the very thin nature of sections used for EM, the number of cone pedicles in *Tet3* mutant retinae was significantly higher than in control retina (yellow asterisks in Fig. 42A and quantification in Fig. 42B), while the number of rod pedicles was the same in both genotypes (Fig. 42C). We observed no difference in number and size of rod mitochondria (Fig. 42C), whilst cone mitochondria in *Tet3* mutants were significantly more in number, and they also appeared tendentially smaller compared to controls (Fig. 42B). These features are consistent with an increased rate of mitochondrial fission, i.e., the process leading to separation of this organelle into smaller parts, and OX-PHOS, as indicated by the upregulation of proteins implicated in this phenomenon in our proteomic data. Thus, *Tet3* mutation results in the differential levels of proteins involved in the physiological metabolic requirements of cone photoreceptors, which manifests with changes in mitochondrial number and size, and suggests a higher rate of mitochondrial fission events.

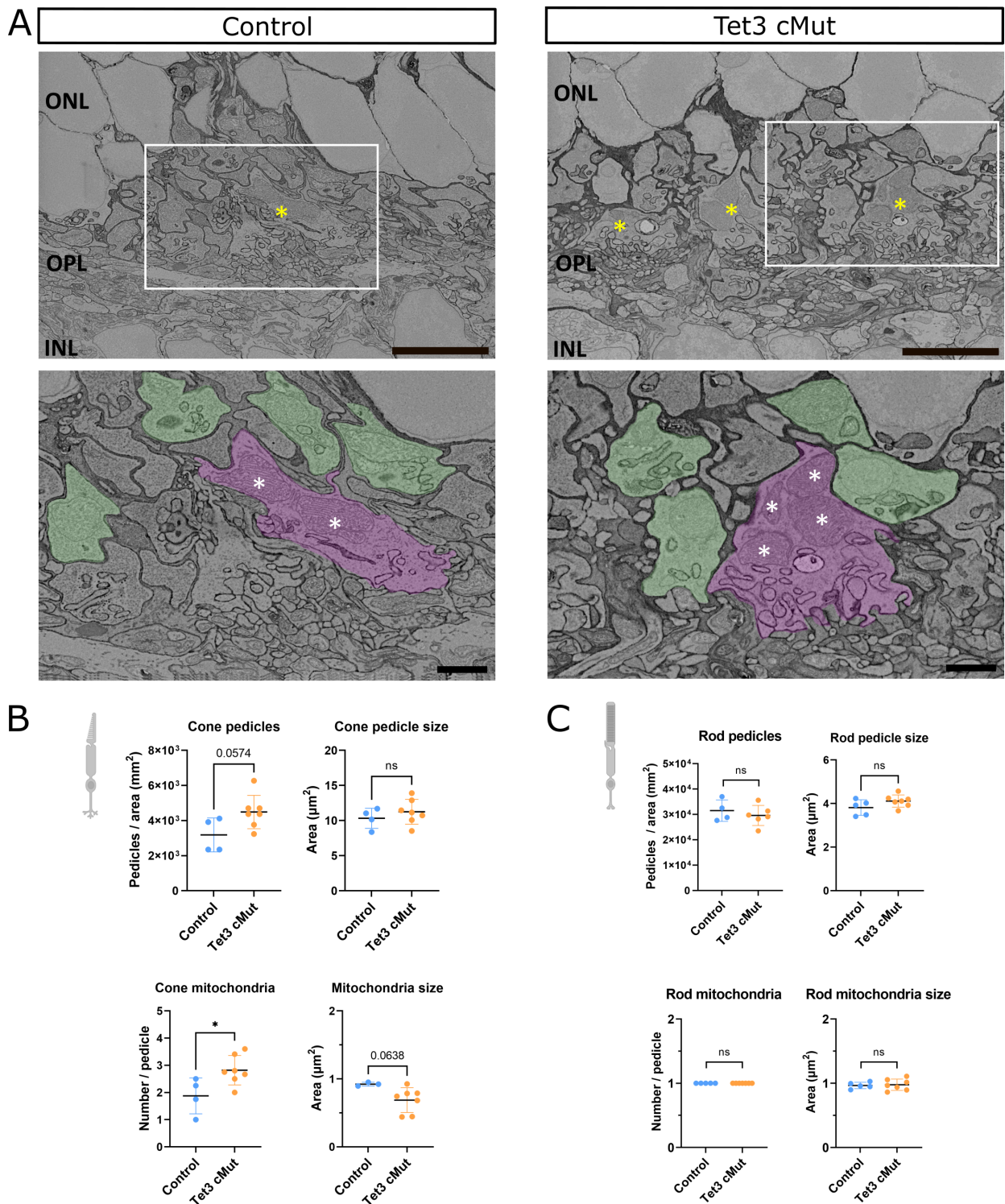


Figure 42: Metabolic alteration in *Tet3* mutant mice

(A) Example image of electron microscopy micrographs of the outer plexiform layer (OPL) from control and *Tet3* mutant mice. The yellow asterisks indicate cone pedicles. Area in the rectangles is shown magnified in the inset below. Cone pedicles in magenta, rod pedicles in green and white asterisks indicate mitochondria in cone pedicle. Error bars: 5 μm upper images, 200 μm lower images (B, C) Quantification of different parameters from images in A, showing increased number of cone pedicles and mitochondria, as well as mitochondria size. No effects detected in rods. Error bars are $\pm\text{SD}$, unpaired Student t-test: * $p < 0.05$

Part IV

Results II

21 Human retinal organoids: background and scientific reasoning behind the choice of this tool

When studying cone photoreceptors, it is worth remembering that, while mice have only two types of cones, expressing S- and the M-opsin, humans have additionally red cones, expressing the L-opsin pigment. Thus, the results obtained in the first part of this study, and specifically the effects of Tet3 catalytic impairment on cone sub-type identity in mice, raise the question on whether Tet3 has a pivotal role also in L-cone identity. Moreover, since Tet3 mutation in mice resulted in more cone photoreceptors and an overall lower cell density in the inner nuclear layer, it would be interesting to know if the same phenotypic observations can be recapitulated in human retina. For this reason, in the second part of this study I will present the results of the differentiation of human retinal organoids from human induced pluripotent stem cells (hiPSCs) of healthy donors, used as a human model to investigate the role of TET3 and epigenetics in retinal development.

21.1 Susceptibility of different iPSC lines to culture condition aimed at differentiating retinal organoids

Human retinal organoids (hROs) were differentiated from three different iPSCs lines, hereafter called PGP#1, (kind courtesy of Prof. Volker Busskamp, University of Bonn), CRTD (iPSCs core facility, CRTD, Dresden) and B7 (kind courtesy of Prof. Botond Roska, Institute of Molecular and Clinical Ophthalmology Basel (IOB)). Since the first published protocol on the differentiation of optic cup-like structures from mouse embryonic stem cells [60], the world of retinal organoids has come a long way and several protocols are now available for the generation of such model system. In order to find the strategy gaining the highest yield, I tested three differentiation protocols [38] [128] [32], whose differences are illustrated in the Fig. 43. In all protocols, the first step includes the formation of so-called embryoid bodies (EBs), 3D aggregates of pluripotent cells which recapitulate early developmental stages *in vitro* and could potentially differentiate in all three germ layers, namely ectoderm, endoderm and mesoderm. Through differential and sequential media exchange, these aggregates are directed towards neuroectoderm differentiation which culminate in optic vesicle-like structures composed of both neuronal retina and RPE. While in [39], aggregates are cultivated in suspension through the entire differentiation (Fig. 43A), both [128], and [32] have an intermediate step where EBs are reattached as adherent culture to the plate for self-differentiation (Fig. 43B,C). After this

time, immature organoids are detached and grown in suspension either shaking as in [128] or in static culture condition [32]. Both PGP#1 and CRTD failed to form embryoid bodies (EBs) 24h after plating cells according to [38] although media was supplemented with RevitaCell, a rho-associated protein kinase (ROCK) inhibitor shown to improve cell survival after single cell dissociation [64]. Despite being more selective than the traditionally used Y-27632, this new supplement contains antioxidants and free-radical scavenger molecules, whose effects on the differentiation process are unknown. Therefore, this protocol was not further pursued for the production of hROs.

One of the biggest problems in 3D culture methods is the formation of a necrotic core in the centre of organoids, caused by dying cells over time [79]. This is probably due to the fact that these cells, as organoid dimensions increase, are less exposed to medium and nutrients necessary for their survival. One way to counteract this complication, is to incubate floating organoids in rotating bioreactors or orbital shakers, as in the [128] (Fig. 43B). Thus, after detachment, retinal organoids were either kept in agitation (according to [128]) or grown in suspension, but in a static culture in normal bacteriological petri dishes, according to [32]. Organoids that occasionally attached to the plate were scratched away and discarded. Surprisingly, retinal organoids maintained in agitation culture failed to express key markers, e.g., recoverin (RCVRN) for all photoreceptors (Fig. 44A'', B'') and arrestin 3 (ARR3) for cone photoreceptors (Fig. 44A''', B''') at d180 of differentiation. In order to investigate whether this lack in expression was caused by a failed differentiation of the organoids into retinal fate, qRT-PCR analysis was performed for selected markers. The results showed that, at earlier steps of differentiation, d14, d21 and d70, where most cells are at the progenitor state, organoids obtained following [128] expressed markers of retinal cell fate like *RX*, *VSX2* and *CRX* (Fig. 44C). The latter is mostly expressed in postmitotic photoreceptor precursors, which appear around two months of differentiation according to other published protocols [32]. Therefore, its lower abundance in organoids at d14 and d21 of differentiation is in agreement with these studies. Around two months after differentiation, organoids expressed other cone specific markers (*ARR3*, *OPN1SW* and *OPN1MW*) as well as *RHO* for rod photoreceptors (Fig. 44D). The lower expression of *OPN1MW* compared to *OPN1SW* at this step of retinal differentiation can be attributed to the fact that, as for mouse development, also in humans M-cones are specified at later time points, after the establishment of the S-cone subtypes. These data suggested that the lack of proteins characteristic of photoreceptor precursors in organoids is not caused by a failure in the differentiation into retinal specific fate, since transcripts of these markers could be detected.

An additional difference in shaking versus static culture (described in more detail in the next section) was the lack of the so-called “halo” on the surface of retina-like organoid structures (Fig. 44E, F). In fact, while organoids grown in static condition form a kind of brush, whose bristles have been defined as emerging outer segments [16] [32] [161] (Fig. 44E', F'), retinal organoids cultivated on the orbital shaker do not, possibly due to shear stress exerted by the medium on the hRO surface during repetitive movement [96]. Altogether, these results indicate that although

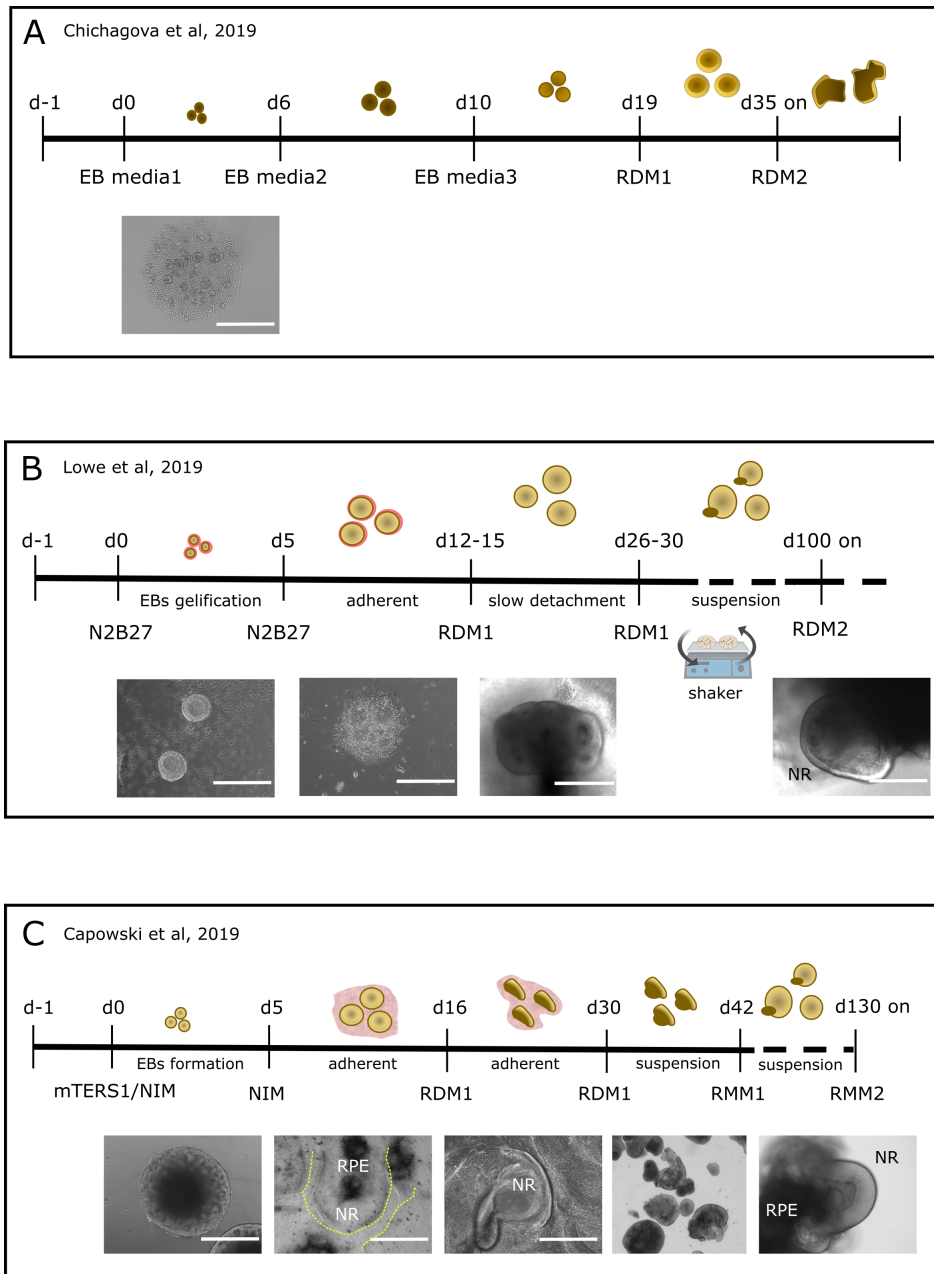


Figure 43: Human retinal organoids (hROs) differentiation protocols

Schematic representation of the three differentiation protocols tested for the generation of hROs. Media composition is described in the method section. The yellow dashed line represents borders between organoids. Scale bars in the BF images are 400 μ m.

EB= embryoid bodies; RDM1,2= retinal differentiation medium 1 and 2; RMM1,2= retinal maturation medium 1 and 2; RPE= retinal pigmented epithelium, NR= neural retina

iPSCs can be successfully differentiated into hROs using either [128] or [32], keeping organoids in agitation as in [128] prevents both molecular and morphological properties typical of photoreceptor differentiation in vitro. Therefore for all the next experiments, hROs were differentiated according to [32].

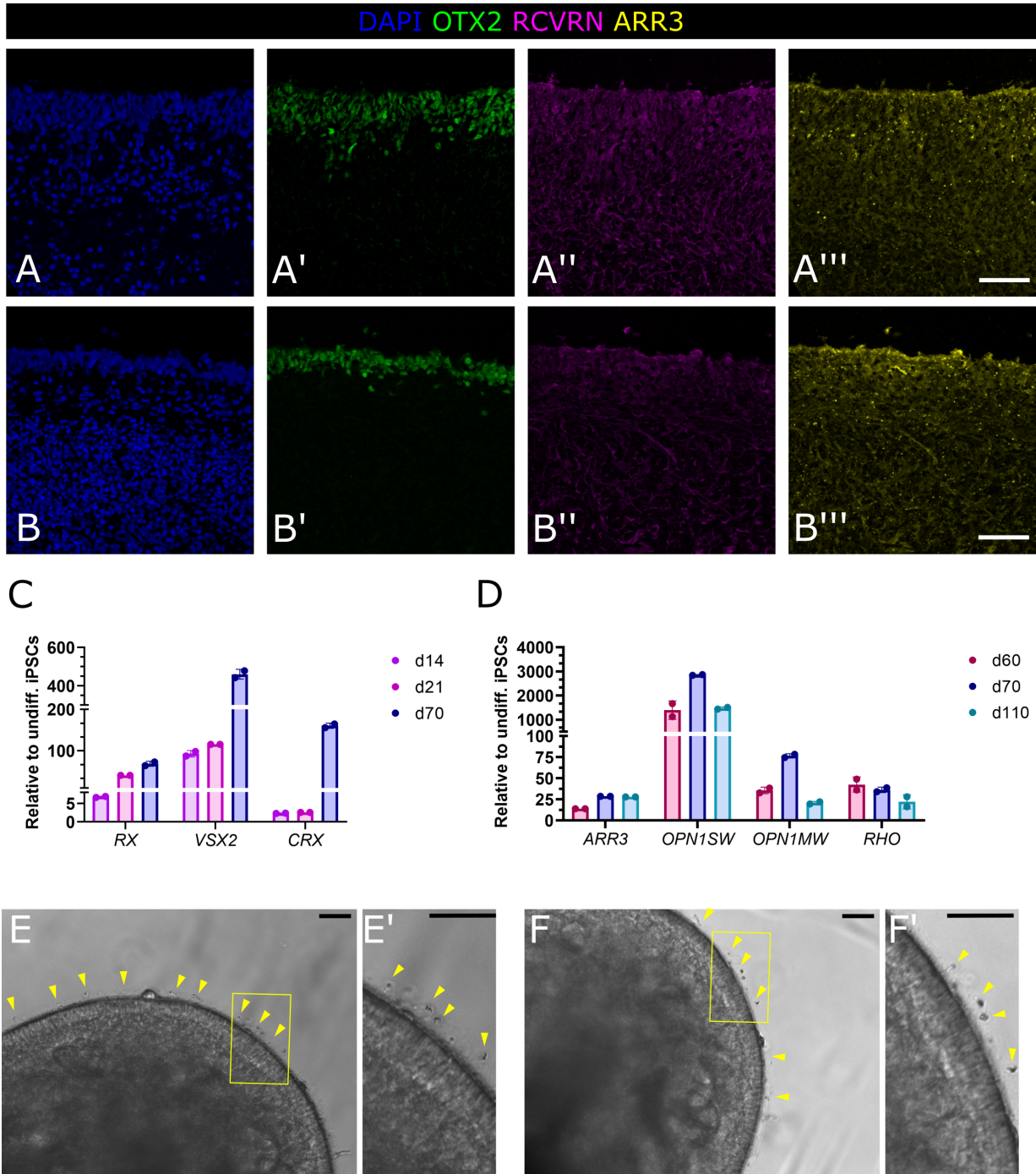


Figure 44: Cellular and molecular characterisation of hROs differentiated according to [128] (A-B''') Confocal micrographs of retinal organoids cross-sections immunostained for OTX2 (green) as general marker of retinal cell fate, RCVRN (magenta) and ARR3 (yellow) for photoreceptors and cones counterstained with DAPI (blue). Images show lack of photoreceptors specific marker expression. Scale bars= 50 μ m. (C, D) qRT-PCR of retinogenesis-related and mature photoreceptor markers at different age of organoid differentiation showed increased expression of these genes and therefore successful retinal specification. Fold change relative to undifferentiated iPSCs. Values are technical replicates, error bars are \pm SD. For each time point, n=3 organoids were pooled together, for differentiation >d40 n=1 organoid per replicate (E, F) Bright field images of retinal organoids at d140 of differentiation (differentiated according to [32]) showing bristle-like structures (yellow arrowheads) protruding from the outer surface. Scale bars are 50 μ m.

22 Cellular and molecular characterisation of hROs

22.1 Cellular and molecular composition of differentiated human retina organoids mirror *in-vivo* retinal development

Retinal cells are sequentially generated from a common pool of retinal progenitor cells [268], which, in human as in mice, starts with retinal ganglion cells and ends with rod photoreceptor and bipolar cells (Fig 45A, [34]). To better characterize hROs differentiated according to [32], qRT-PCR was performed at different stages of their development to analyse specific markers of retinal fate (Fig. 45A). These included *RX* and *VSX2*, two generic early markers of retinogenesis, *OTX2*, *CRX* and *RCVRN* for photoreceptors precursors, and *RLBP1* for Müller glial (MG) cells (Fig. 45A). During early differentiation stages, retinal organoids expressed increasing levels of *RX* and *VSX2* transcripts (Fig. 45B,C) in agreement with expansion of the progenitor pool and growth of organoids at these stages. Additional analysis for *CRX*, *OTX2* and *RCVRN* confirmed the presence of photoreceptor precursors or immature photoreceptors (Fig. 45D-F). Finally, the expression of *RLBP1* transcript at later differentiation stages pointed out to the presence of differentiated MGs (Fig. 45G). Thus, these results highlight how changes in transcriptional profile of human retinal organoids resemble the expression profile seen in mammalian eye development.

Next, to determine the identity and the cellular composition of retinal organoids, immunohistochemistry (IHC) on cross-sections at distinct differentiation stages was performed. At early developmental stages (d40), retinal organoids were shown to express *VSX2* protein spanning the entire retinal-like structure, representing a neural retinal progenitor cell population (Fig. 46A). Interestingly, at later stages (d130), the localisation of *VSX2*⁺ cells moved more internally and below the overlaying photoreceptor layer (see *OTX2*, *CRX*, *RCVRN* staining), giving rise to an area seemingly bipolar cell precursors-restricted (Fig. 46B). Furthermore, *OTX2*⁺ cells could also be sporadically observed below this outer mantle, again resembling *OTX2*⁺ bipolar precursors in the INL. *OTX2*⁺ and *CRX*⁺ signal at the outer and apical side of retinal organoid additionally indicated the presence of photoreceptor precursors cells (Fig. 46A, B). *RCVRN*⁺ cells also confirmed the identity of photoreceptor cells in the outer retinal layer (Fig. 46A, B). Notably, the number of *RCVRN*⁺ cells increased from d90 to d130, indicating stronger photoreceptor cell fate specification over time. Furthermore, the morphology of *RCVRN*⁺ population changed, and cells acquired hair-like structures protruding the outer nuclear layer, which bore resemblance to the inner and/or outer segment formation of mammalian photoreceptors (Fig. 46B). The same aspect was also noticed labelling cells for the gamma subunit of transducin 2 protein (*GNGT2*), selectively expressed by cone photoreceptors and localised in cone outer segments, playing a crucial role in cone phototransduction cascade (Fig. 46B). Of note, the majority of retinal organoids showed appearance of pigmentation around d50, resembling retinal pigmented epithelium (RPE). In order to validate these observations, organoids cross-sections

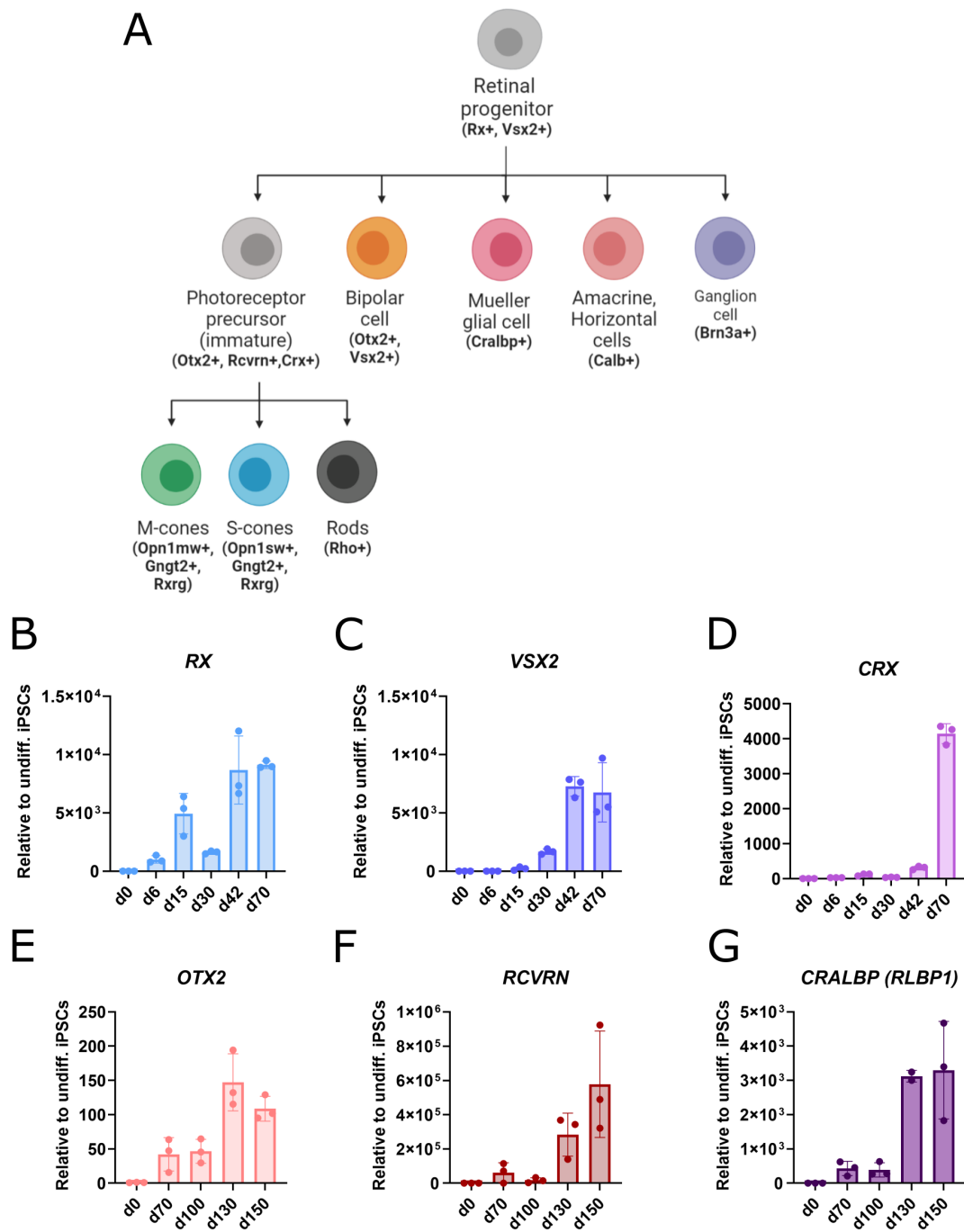


Figure 45: Molecular characterisation of hROs differentiated according to [32] (A) Schematic representation of retinal cell differentiation. Starting from retinal progenitors, several populations acquire their identity and express selective markers. (B, C) qRT-PCR of retinogenesis and mature photoreceptors markers at different age of organoid differentiation showing increased expression of these genes over time and therefore successful retinal specification. Fold change relative to undifferentiated iPSCs. Values are biological replicates and error bars are \pm SD. For each time point, $n=3$ organoids were pooled together, for differentiation $>d40$ $n=1$ organoid per replicate.

were immunostained for RPE65, which is selectively expressed by this cell population. As expected, only the pigmented area contained RPE65⁺ cells, therefore confirming their identity as

RPE cells (Fig. 46C). Interestingly, pigmentation was never observed juxtaposed to the corresponding neural retina, as it is observed at the end vertebrate development, but always laterally or posteriorly to it. This position rather reminds the regionalisation of the optic vesicle at very early developmental stages before the invagination of the eye which brings the neural retina in contact with the RPE [92] [78]. All in all, these data suggest that human retinal organoids differentiated *in vitro* mirror the temporal cell fate acquisition in mammals at both transcriptional and protein levels.

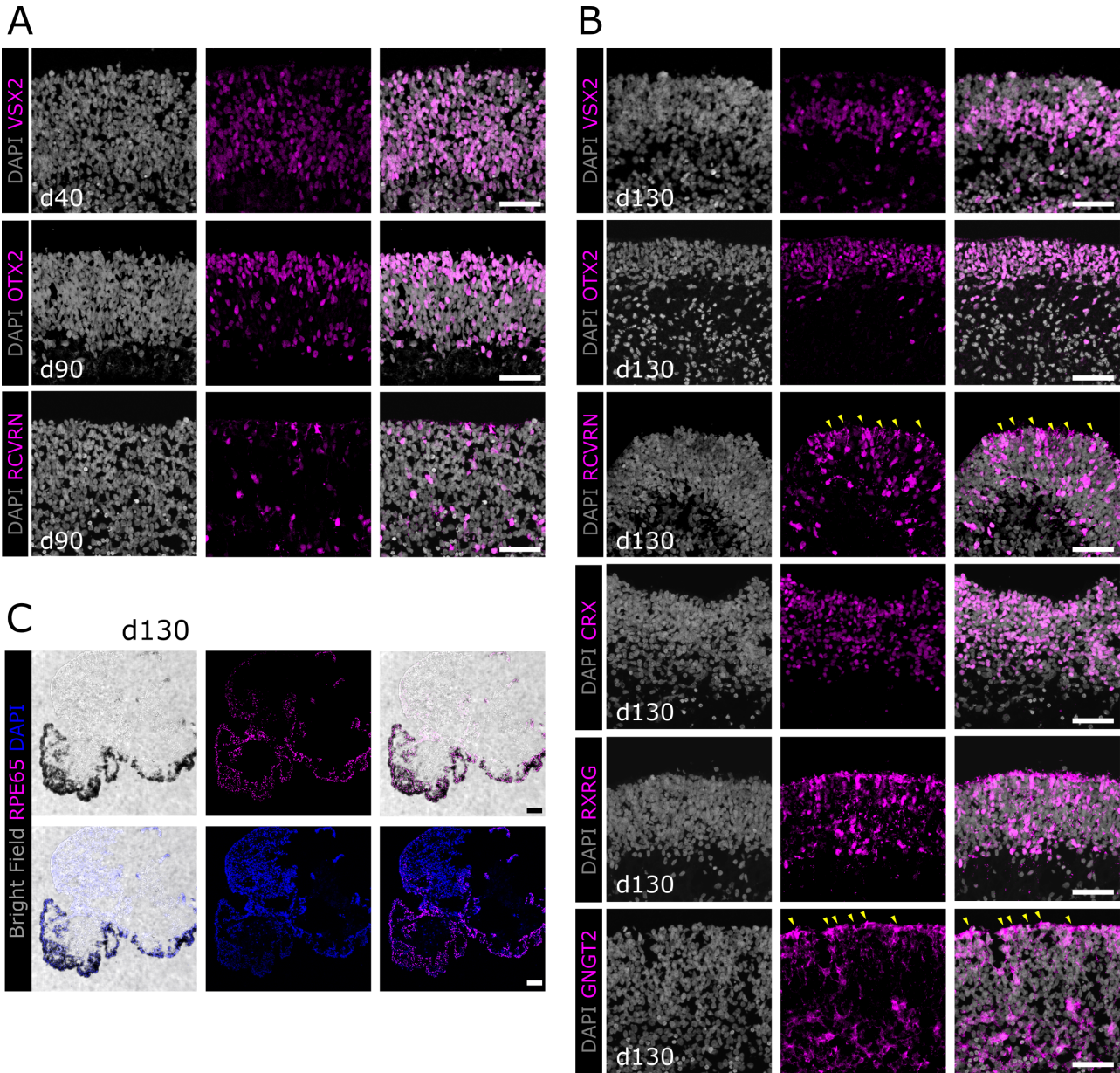


Figure 46: Cellular characterisation of hROs differentiated according to [32] (A-C) Representative confocal micrographs of retinal organoids cross-sections immunostained for several retinal selective markers at different stages of *in vitro* differentiation (indicated in each image). Nuclei are counterstained with DAPI in grey (A, B) and blue (C). Scale bars in A, B = 50 μ m; in C= 100 μ m. Yellow arrowheads point at bristle-like structures reminiscent of photoreceptor inner or outer segments.

22.2 Differentiating human retinal organoids showed dynamic pattern of DNA methylation and demethylation

In order to evaluate whether *TET3* is expressed in retinal organoids, qRT-PCR analysis was performed coupled with mass spectrometry for DNA methylation and demethylation quantification of epigenetic marks at different steps of differentiation. A summary of the protocol used in this study is reported in Fig. 47A [32] with indicated sample collection at key differentiation steps for molecular investigation. Under these differentiation conditions, *TET3* levels increased significantly and progressively over time during *in vitro* differentiation to suddenly drop at d100, when retinoic acid (RA) treatment is stopped to favour outer segment formation (Fig. 47B). Previously, RA has been shown to act as TET modulator, promoting transcriptional activation of *TET3*, a process necessary for massive DNA demethylation and establishment of naïve pluripotency [99]. Thus, a reduction in *TET3* transcript levels at this stage is conceivable by the removal of RA from the medium. On the same line, a significant and stable reduction in 5mC was observed from d30 (Fig. 47C), accompanied by an increase in 5hmC levels from d70, significant at d150, indicating active demethylation catalysed by TET3 (Fig. 47D). At initial steps of differentiation, passive demethylation might also contribute to the observed 5mC reduction since cells at these stages (between p30 and p70) are mostly proliferating progenitors [5] [32] [264]. Curiously, 5hmC showed an initial significant reduction when compared to undifferentiated iPSCs, before increasing progressively at later differentiation steps when several neuronal populations start to appear [305]. This initial reduction reminds the massive demethylation events occurring in a replication-dependent manner in dividing cells at early stages of *in vivo* development [289]. 5fC was nearly detectable in retinal organoids, present only at very early stages of differentiation, pointing to a minor role of this epigenetic mark in this process (Fig. 47E). These results suggest that *TET3* is expressed during differentiation of retinal organoids and its expression might be modulated by RA supplementation to the medium. Moreover, TET3 might participate in active DNA demethylation of as shown by reduction of 5mC followed by increase in 5hmC in differentiating neurons. Whether the other TET enzymes contribute to any of these processes remains to be elucidated.

23 Electroporation as tool for gene delivery

23.1 *In vitro* electroporation efficiently targets Müller glial but not photoreceptor precursors in human retinal organoids

Many different methods are nowadays utilised for gene delivery, which can be distinguished in two broad categories: viral and non-viral. On the one hand, viral carriers, e.g. AAVs and lentiviral particles, offer the possibility to fine-tune the specificity and selectivity to target specific cell populations. On the other hand, non-viral methods offer some advantages in terms of costs,

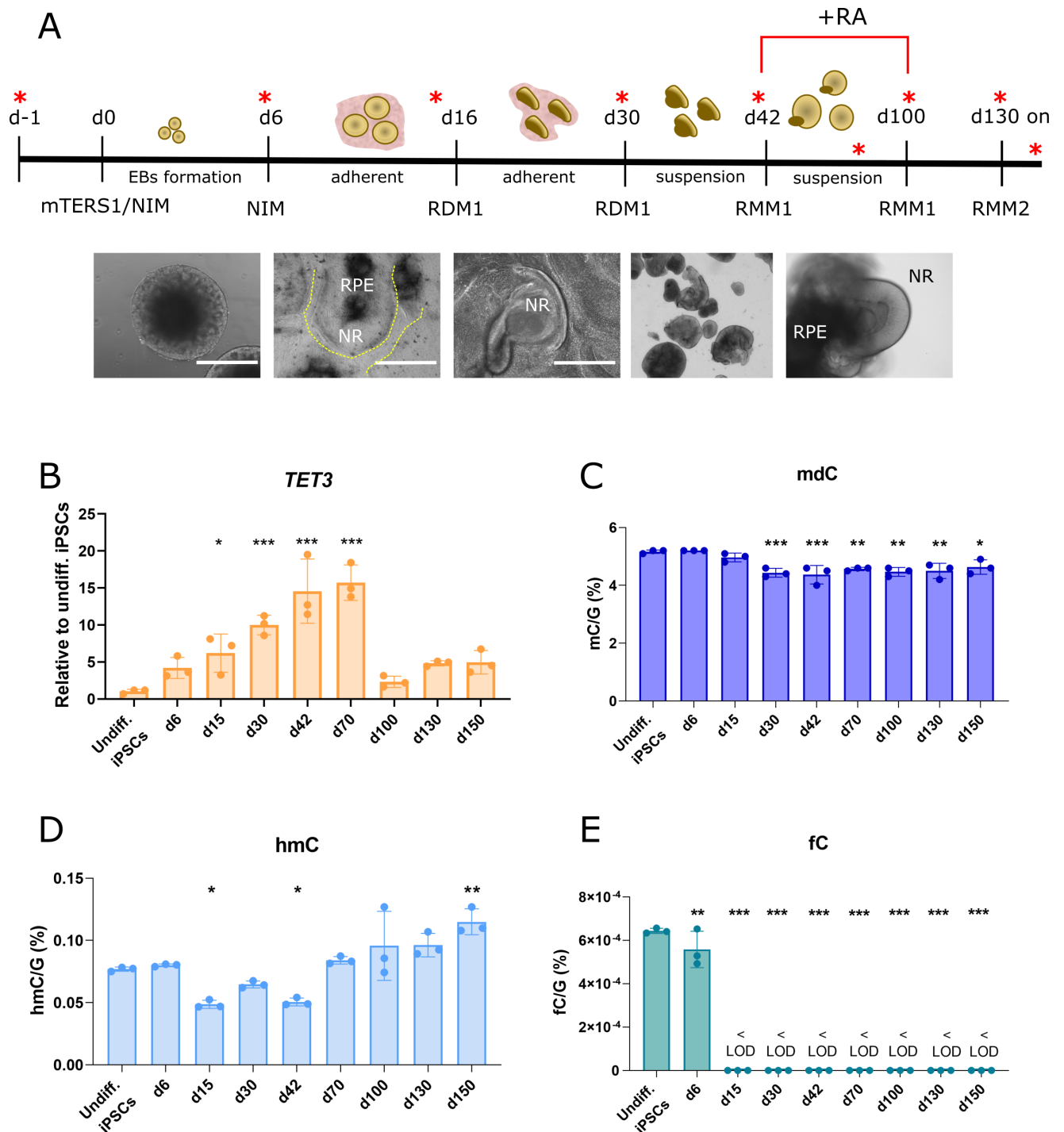


Figure 47: *TET3* and cytosine modification in differentiating hROs

(A) Schematic representation of the differentiation protocol [32] and corresponding brightfield images. Red asterisks indicate sample collection at key differentiation steps used in the next analysis. (B) qRT-PCR analysis of *TET3* at different stages of retinal organoids differentiation. One-way ANOVA comparison relative to undiff. iPSCs. (C-E) LS MS/MS quantification of cytosine modification in differentiating retinal organoids. <LOD= below the limit of detection. One-way ANOVA comparison relative to undiff. iPSCs. * $p < 0.05$, ** $p < 0.01$, *** $p < 0.001$.

NR= neuronal retina, RPE=retinal pigmented epithelium

simple production, reduced pathogenicity, and no loading limitation. As a proof of principle of gene supplementation in hROs, in this study I exploited *in vitro* electroporation as a tool for delivering naked DNA plasmid – a technique that has been already utilised in both organoids [30] [52] and organs (*ex vivo*) [169]. The principle is illustrated in (Fig. 48).

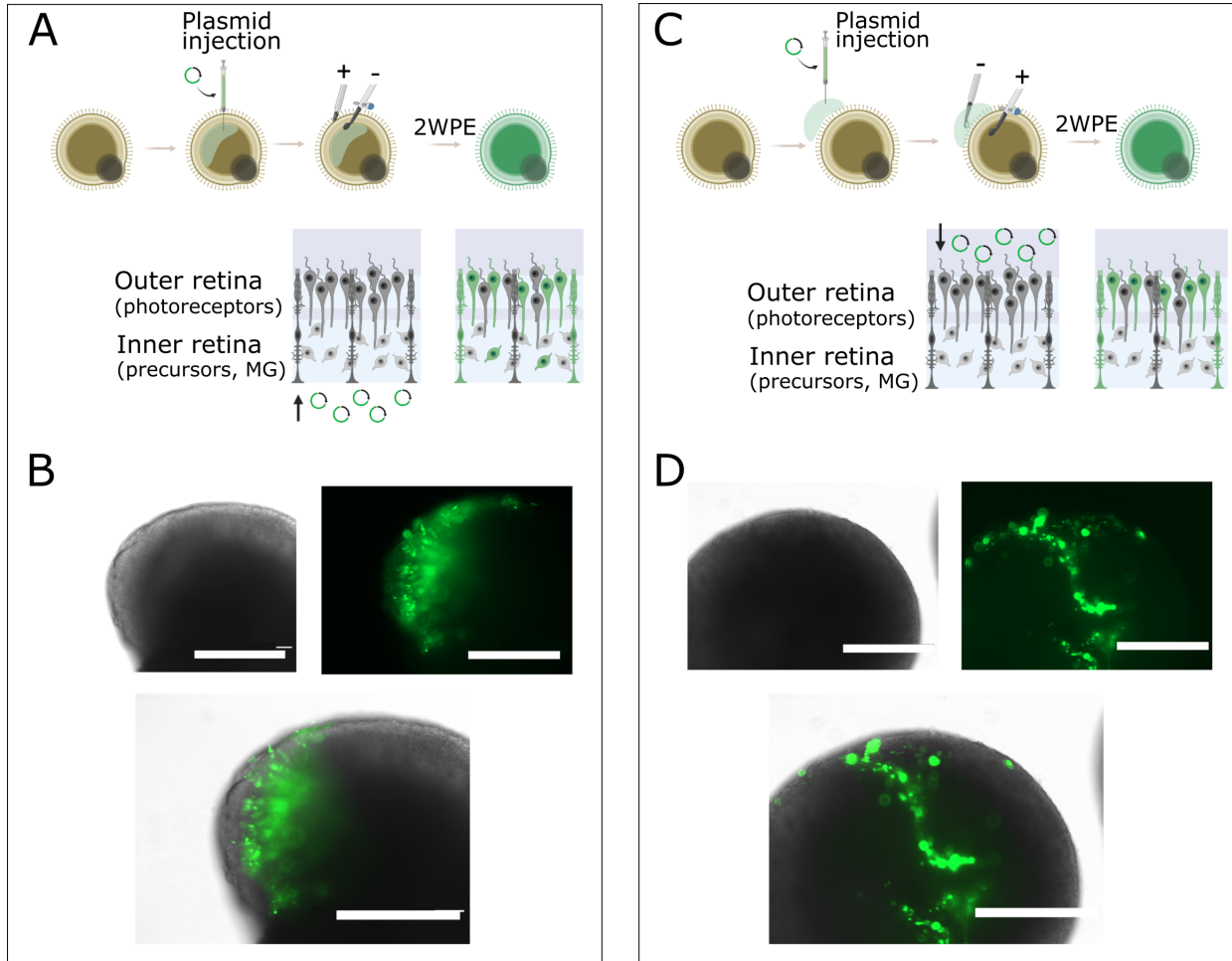


Figure 48: Schematics of hROs electroporation

(A,C) Graphical representation of *in vitro* electroporation for gene transfer in differentiating retinal organoids. (B,D) Representative bright field and fluorescent images of the electroporated organoids, according to the corresponding scheme, imaged 2 weeks post electroporation (2WPE). GFP (green) was used as readout of successful gene administration. Organoids were electroporated at d120. Scale bars = 400 μ m

In brief, depending on the differentiation age and the target cell population, plasmids can either be injected in the internal lumen of the optic vesicle (inner retina side) (Fig. 48A) or dispersed in the media in close proximity to the organoid surface (photoreceptors side) (Fig. 48C). Depending on the orientation of the tweezer electrodes, plasmids can be driven to the desired cell population and checked 24h after for gene expression. As a proof of principle, I injected and electroporated d120 retinal organoids relying on either one of the two paradigms, using a CAG-GFP plasmid to induce the expression of GFP in any cell population. Both methods resulted in successful electroporation of retinal organoids with GFP⁺ cells spanning the total

thickness of the retinal structure (Fig. 48B, D).

In order to investigate the nature and identity of GFP⁺ cells, I fixed organoids at two weeks post electroporation (2WPE) and immunolabelled cross-sections with several markers. Surprisingly, none of the electroporated cells was co-labelled with OTX2, RCVRN, CRX, RXRG or GNGT2 (Fig. 49A-E), thus ruling out the possibility of these being photoreceptor precursors or committed cones.

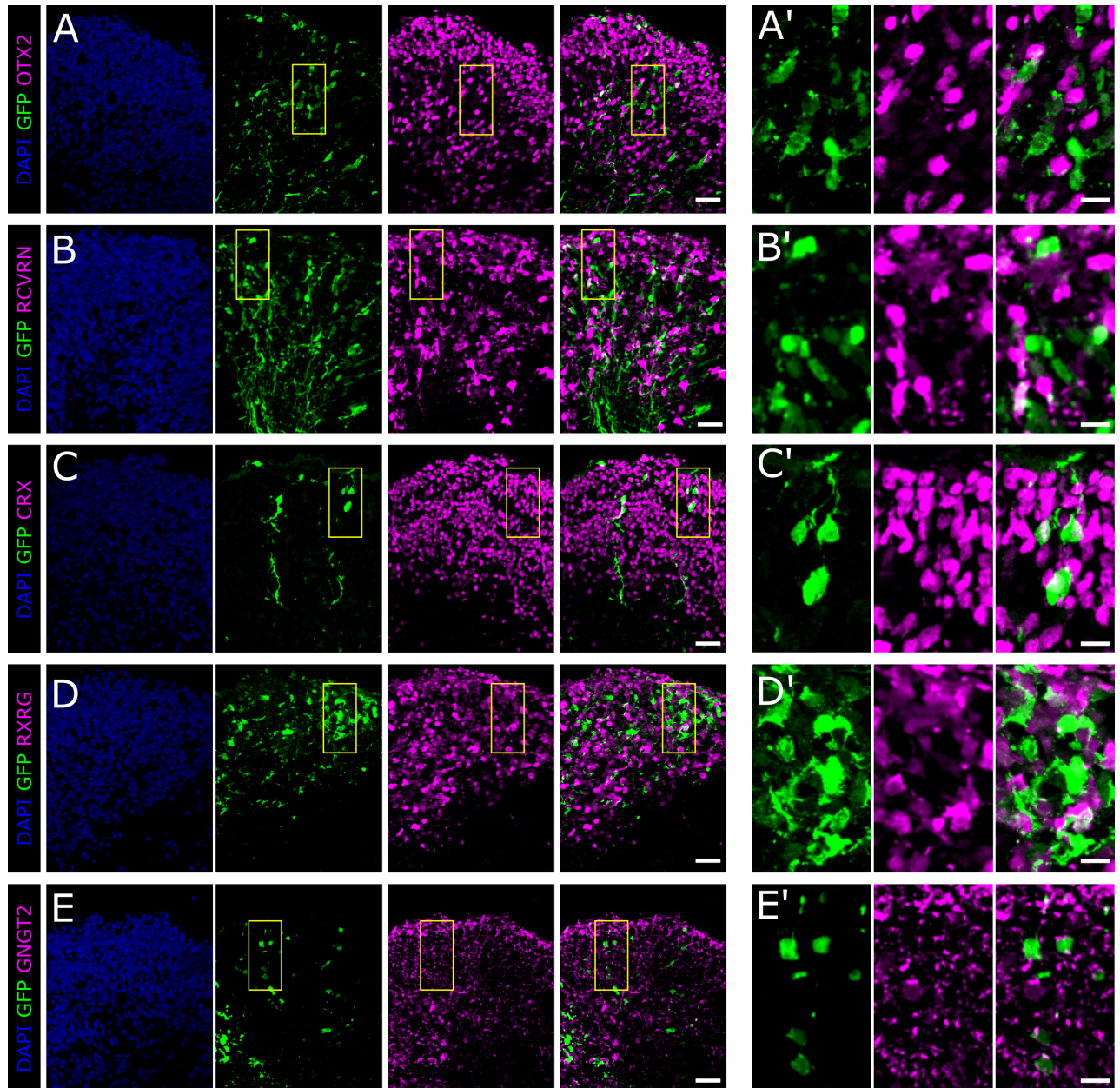


Figure 49: Electroporation test

(A-E) Representative confocal micrographs of electroporated organoids examined at 2WPE (d135). Cells are immunolabelled for different cell population specific markers (magenta), while GFP (green) indicate the electroporated cells. Images were counterstained with DAPI (blue). Yellow rectangles are magnified images on the right (A'-E'). Scale bars= 30 and 10 μ m, respectively.

The radial morphology spanning the whole retinal thickness and the lateral perisynaptic

processes of GFP⁺ population resembled Müller glial cells (MG) *in vivo* (Fig. 50A), although in organoids these cells are normally observed at later stages of differentiation (around d200) [32]. On the one hand staining with CRALBP, a marker of mature MG, revealed minor overlaps with GFP⁺ signal of electroporated cells, mostly confined to the radial process of these Müller cells (Fig. 50B, B'). On the other hand costaining of GFP⁺ cells with SOX9, a marker of both multipotent retinal progenitors (including MG progenitors) and adult MG [213], showed overlap of the two markers, therefore validating previous impressions (Fig. 50C, C'). Overall, these results showed that neuronal populations are a difficult target of *in vitro* electroporation, whilst retinal progenitors and glial cells, e.g., Müller glial cells, are favorably affected by this procedure.

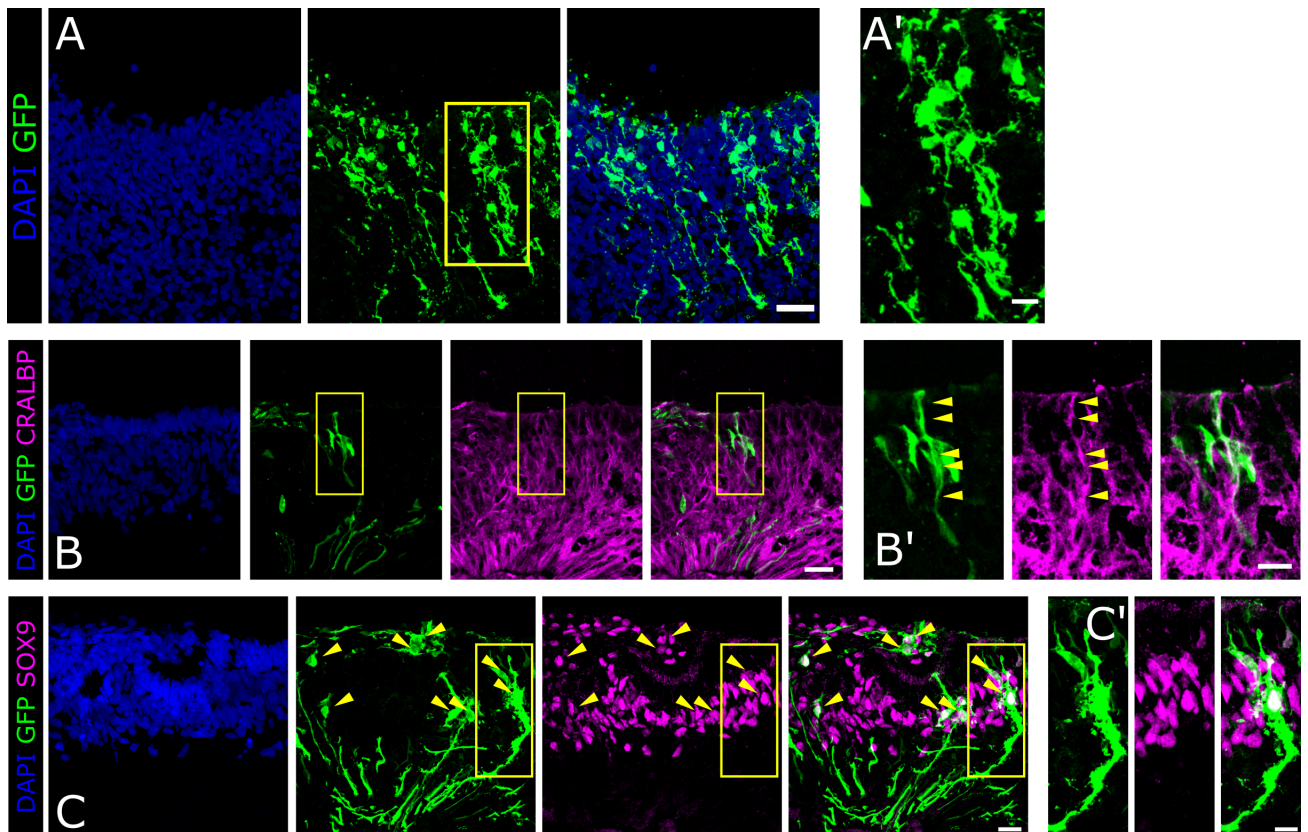


Figure 50: Muller glia morphology in electroporated hROs

(A) Representative confocal micrographs of electroporated organoids examined at 2WPE (d135) showing electroporated cells (green) resembling Müller glia cell morphology. (B) Co-immunolabelling of electroporated cells with CRALBP (magenta) and GFP (green), reveal minor overlap at this stage at Müller glia processes level. (C) Co-staining of GFP (green) and SOX9 (magenta) in electroporated organoids confirmed these cells being MG. Images were counterstained with DAPI (blue). Yellow rectangles are magnified images reported on the right (A'-C'). Scale bars= 30 and 10 μm , respectively.

23.2 *In vitro* electroporation of differentiated hROs with promoter specific GFP constructs.

Considering the scarce selectivity of the ubiquitous promoter (CAG) in driving GFP expression and in general the little overlap of this signal with differentiated cells, the results prompted me to

investigate the targeting efficiency of this method using cell specific promoters, namely ARR3, RG (Red-Green OPSIN), RHO, GFAP, RLBP1 (CRALBP). First, I checked the expression of these selective markers at transcript level and the specificity of expression of related proteins in the desired cell population. At transcript level, the majority of these markers started to be expressed around d70 of differentiation and increased over time, reaching the maximum expression around d150 (Fig. 51A-E). Based on these results, retinal organoids were harvested at d155 and subjected to immunolabeling for the same cell specific markers. The results revealed that retinal organoids can be successfully differentiated *in vitro*, and they contain mature cone photoreceptors, including S- and M-OPSIN subtypes, rod and Müller glia cells (Fig. 51A'-E'). Notably, S-cones in this model appeared with a lower abundance, which reflected the fact that *in vivo* this sub-type is more sparse and less represented compared to the other two (M- and the L-expressing cones) [17]. Additionally, the number of rods appeared to be very low, which could be attributed to the relatively immature age of the differentiated organoids, as rods have been described in organoids at later time points (around d200) [32] [310] [45]. Nevertheless, the expression of the analysed markers in the right cell populations set the basis for the next electroporation experiment.

For this reason, d140 differentiated organoids were injected and electroporated with different constructs, namely: *ARR3*-GFP, *RG*-GFP, *RHO196*-GFP, *RLBP1*-GFP and *GFAP*-GFP (n=1 each) ultimately harvesting the organoids for processing at 2WPE. GFP expression was checked by wide field fluorescence microscopy before fixation (2WPE). Both GFAP and the RLBP1 promoters, driving GFP expression in Müller glial cells (MGs), showed the highest expression in retinal-like structures, and defined radial structures in the electroporated cells resembling MGs processes (Fig. 52A-B). When using RHO, ARR3 and RG promoters, instead, I could detect no expression of GFP in optic vesicle-like structures (Fig. 52C-E). Notably, with ARR3 and, to lesser extent, RG promoters, some GFP was visible among pigmented cells (Fig. 52D-E) suggesting lower specificity of these two constructs in human retinal organoids. Further experimental tests will be necessary to check whether desired cell populations can be targeted via this approach. Taken together, these results corroborate the previous experiment performed using ubiquitous promoter CAG, and further point at glial cells as main target of *in vitro* electroporation in hROs.

24 Strategy for TET3 knock down in human retinal organoids

In the first part of this study, I showed how *Tet3* mutation affects cone photoreceptors and their sub-type specification. In fact, *Tet3* mutant mice resulted in an increase in the number of S-cones and, as a consequence, in the simultaneous expression of both S- and M-opsin in all cones of the mouse retina. For this reason, we wanted to investigate if TET3 influences the sub-type identity of cone photoreceptors in humans. MicroRNA 15b (miR15b) was previously shown

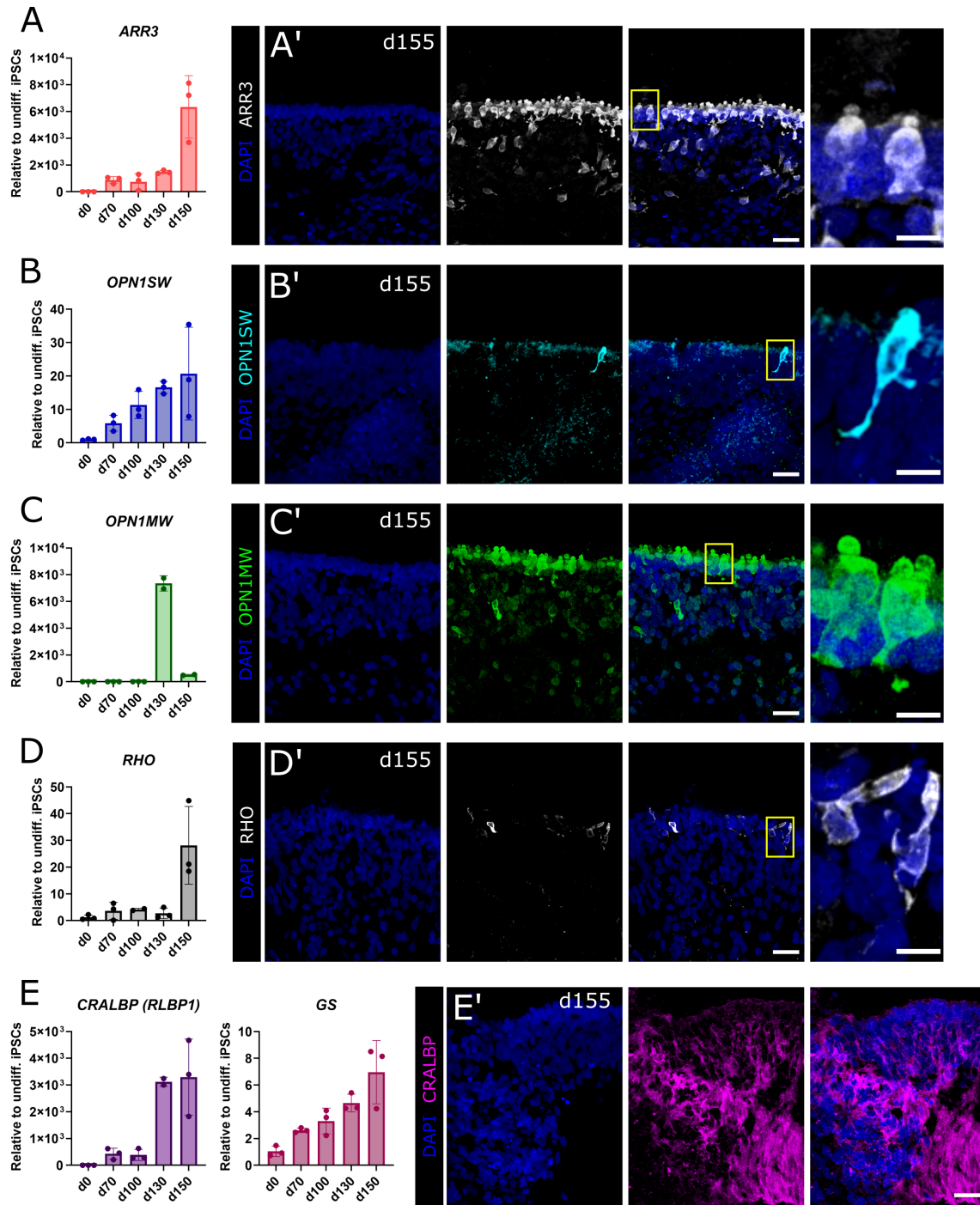


Figure 51: Cellular and molecular characterisation of more mature hROs (A-E) qRT-PCR quantification of specific transcripts for targeted cell populations (cones (A-C), rods (D), Müller glial cells (E) showing expression at later stages of retinal differentiation. Error bars are \pm SD. (A'-E') Confocal micrographs of differentiated retinal organoids at d155 labelled for the same markers as in A-E. Yellow rectangles are magnified images reported on the right. Scale bars= 30 and 10 μ m, respectively.

to effectively mediate knock-down (KD) of Tet3 in the developing mouse cortex [166]. Before electroporating hROs with a construct expressing miR15b (and GFP) for KD of *TET3* *in vitro*, I tested the KD efficiency in HEK293T cells. To this end, HEK293T were transfected

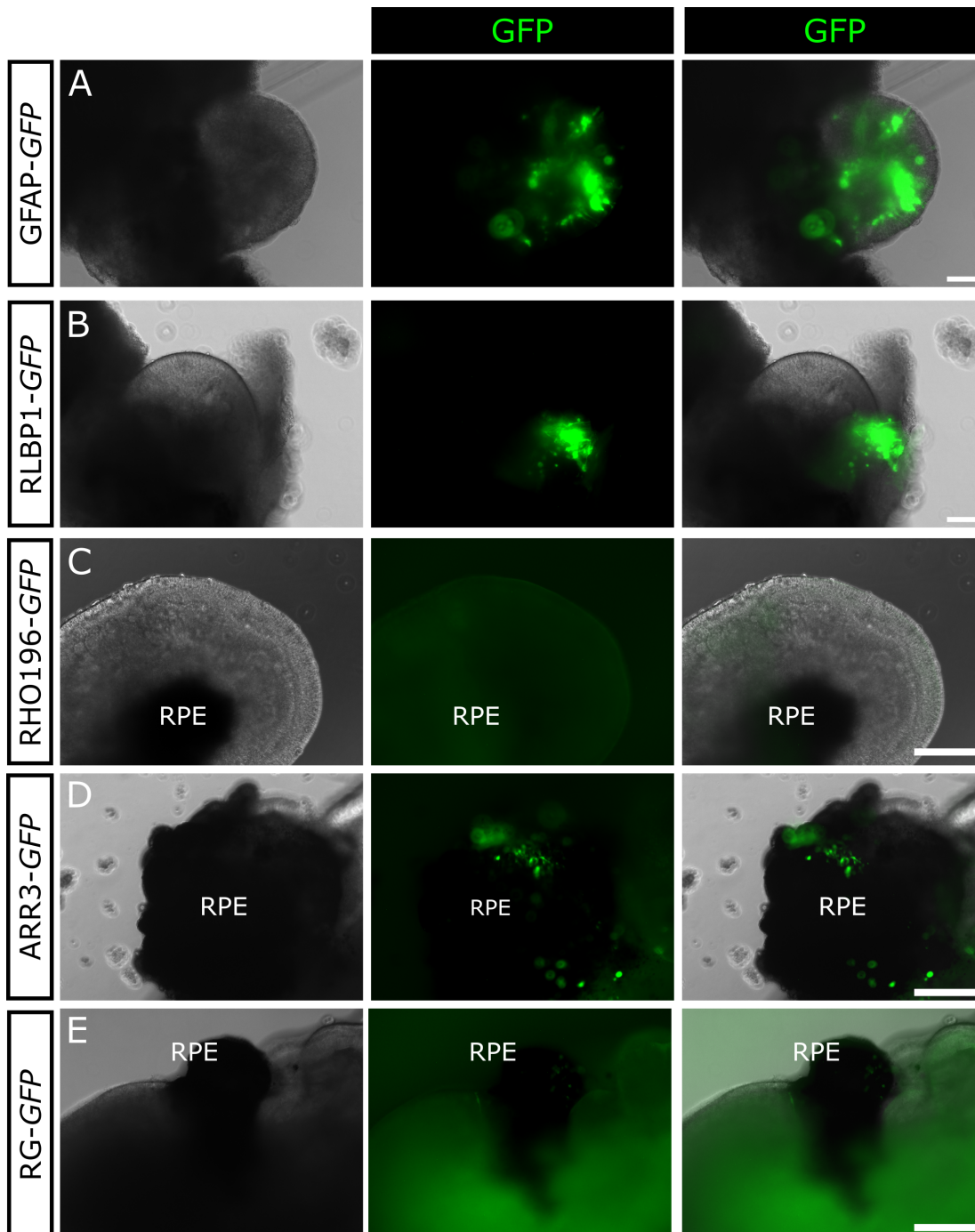


Figure 52: Electroporation of hROs using promoter specific constructs

(A-E) Representative epifluorescent images of electroporated retinal organoids of electroporated organoids at 2WPE, before harvesting. GFP (green) shows electroporated cells that activated the selective promoter. Scale bars are = 100 μ m

RPE= retinal pigmented epithelium

with a miR15b dual reporter sensor (schematically represented in Fig. 53A) consisting of a blue fluorescent protein (eBFP) and a red fluorescent protein (mKATE2), which bears four consecutive and complementary miR15b sequences in the 3'UTR of the mKATE2. In the absence of miR15b, both fluorophores are translated (example 1 and 2 in Fig. 53A), whereas when miR15b

is expressed, it hampers *mKATE2* expression through mRNA decay and its degradation prevents translation (example 3 in Fig. 53A). In a parallel experiment, the reporter construct was administered with either a GFP plasmid or the miR15b-GFP plasmid (Fig. 53A). As expected, the expression of the mature miR15b and the binding to its complementary sequence in the 3'-UTR of *mKATE2*, resulted in the degradation of the *mKATE2* transcript, leaving the blue fluorescent protein intact (Fig. 53B).

Based on TET3 expression levels quantified in Fig. 47B and dynamic changes of hmC (Fig. 47D) in differentiating retinal organoids, electroporation of miR15b for TET3 KD will be performed at d100, when immature photoreceptors including cones start to develop and d130, when outer segments form and cone sub-type are specified *in vitro* [32].

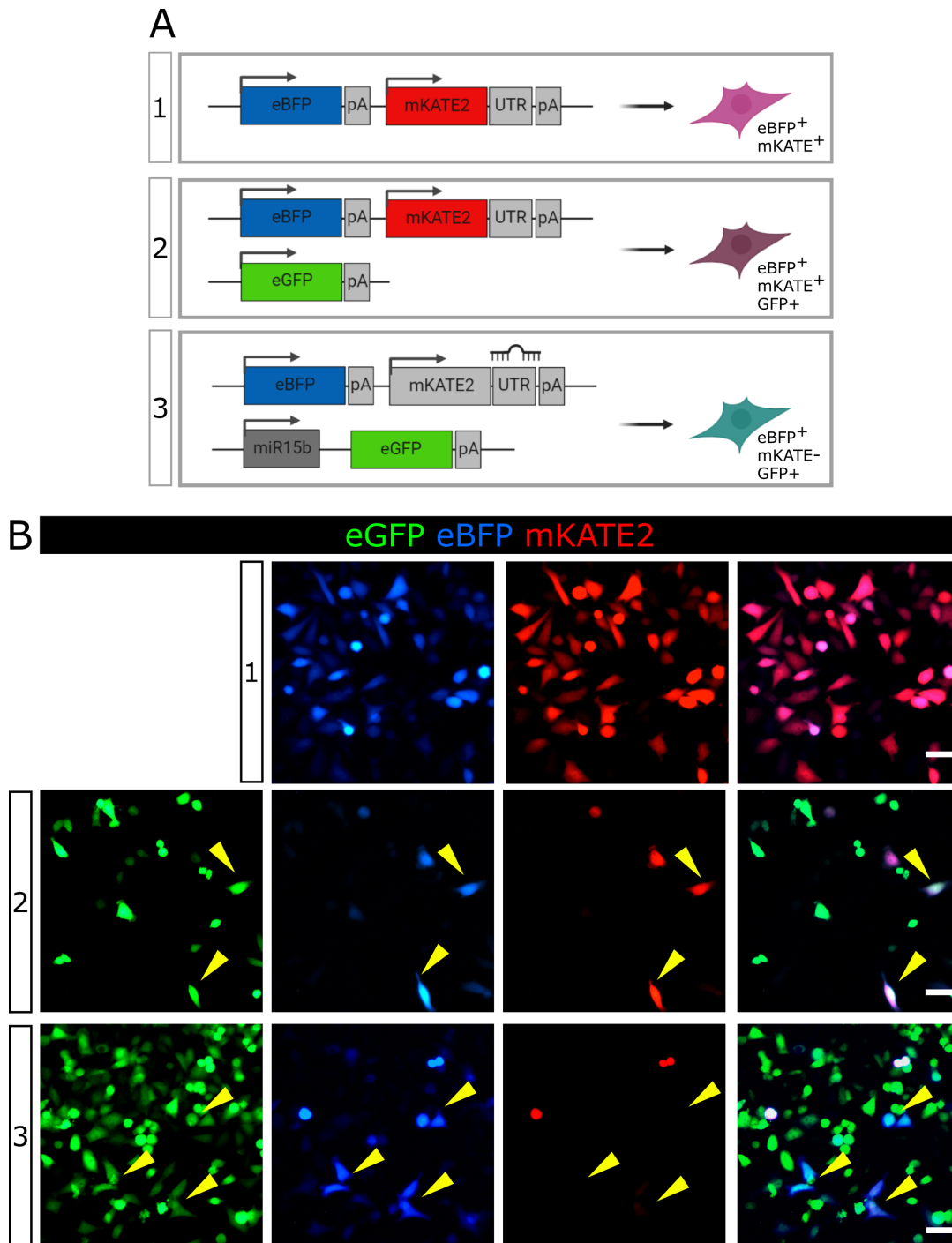


Figure 53: Knock down of mKATE2 by mir15b in HEK293T cells
 (A) Graphics showing the combination of plasmid in the three different conditions. The presence of the miR15b and its binding to the 3'-UTR sequence of the mKATE2 transcript determines the downregulation of its expression. (B) Representative fluorescent images of HEK293T cells transfected with different plasmid condition according to A. Scale bars= 50 μ m

Part V

Discussion

25 Tet3 and the generation of distinct retinal cell populations

Loss of Tet3 catalytical activity in retinal progenitors of Rx-*Tet3* mutant mice resulted in an increase in the number of cone photoreceptors and a reduction in many cell populations of the inner nuclear layer (ACs, HCs, and BPs, but not MGs). This altered cellular composition was not due to perturbations in apoptotic events and cell proliferation. Interestingly, the increase in number of cone photoreceptors matched the amount of reduction in the total number of nuclei in the INL, suggesting a re-direction of some of these retinal progenitors to become cones instead of inner nuclear layer cell types. In this study, I mostly focused on bipolar cells, since their number showed a significant decrease compared to the other two populations, for which only a tendential reduction was observed. Moreover, only some bipolar cell subtypes were affected by Tet3 mutation. In particular, both ON- and OFF-cone bipolar cells showed a slight reduction, while rod bipolar cells remained unchanged. This is also in line with ERG recordings showing only a reduced photopic b-wave, indicative of cone bipolar cells alterations, and leaving the rod pathway unaffected (normal a- and b-waves under scotopic conditions).

25.1 An imbalance in DNA methylation of key genes controlling photoreceptors vs bipolar cell fate commitment suggests a role of Tet3 in this process

Tet3 mutation is expected to cause changes in DNA methylation, which in turn affects gene expression. It is therefore conceivable that differential DNA methylation in key developmental genes underlies the perturbed bipolar-to-cone cell conversion. Among the factors that are known to regulate bipolar vs photoreceptor cell fate are *Otx2*, *Vsx2* and *Prdm1* [118] [28]. On the one hand, *Vsx2*-null retinæ have few, if any, bipolar cells and an excess of photoreceptors [31]. On the other hand, *Prdm1* deletion leads to conversion of almost all photoreceptors into bipolar cells [118]. Deletion of *Otx2* from mouse retina impair photoreceptor and bipolar cell differentiation in favour of amacrine cells suggesting a role of *Otx2* in both photoreceptor and bipolar lineage specification [277]. Notably, all three genes were differentially regulated in *Tet3* mutant mice. Both *Otx2* and *Vsx2* showed significant downregulation, while *Prdm1* was upregulated. Moreover, many genes involved in bipolar sub-type specification were also affected in our bulk RNAseq and/or qRT-PCR experiments, such as genes important for OFF-cone bipolars like *Vsx1*, *Prdm8* and *Bhlhe23* [56], as well as genes essential for ON- and OFF-bipolar cell maturation like *Trpm1*, *Prdm16* and *Cabp4*. All together, these changes in gene expression

support the observations at cellular level of reduced and defective bipolar cells. In mice, the reciprocal inhibitory role of *Vsx2* and *Prdm1* in promoting bipolar vs photoreceptor cell fate has been previously reported [58] [156] [118] [31]. The higher *Prdm1* expression in postmitotic retinal cells (p10 in this study) might be sufficient to suppress the bipolar cell fate in these cells through *Vsx2* inhibition, favoring the differentiation towards photoreceptors. Indeed, Brzezinski et al. demonstrated that there is a temporal window in which even committed *Otx2*⁺ precursor cells exist in a sort of limbo between the two fate choices. The prevalence of one of these factors *in vivo* give the final drive to these cells towards their final fate acquisition. In fact, loss of *Prdm1* in mice results in fate-shift towards *Vsx2*⁺ bipolar cells, even after the cells started to show signs of photoreceptor morphology [29]. On the other hand, *Prdm1* overexpression in specified bipolar cells changes their fate into photoreceptors [76]. Moreover, it has been shown that the decision of bipolar vs photoreceptors is additionally controlled by levels of *Otx2* in the cells. In fact, lower *Otx2* levels preferentially give origin to rod photoreceptors, while higher levels induce bipolar cells. *Otx2* levels are regulated by the same *Prdm1* in a negative feedback mechanism [277]; as such, the reduced expression levels of *Otx2* observed in this study might also be explained by *Prdm1* upregulation. With this in mind, it remains to be elucidated the specific role played by Tet3 in this context. Being a DNA dioxygenase, we hypothesized that Tet3 might regulate the expression of these factors through its signature, namely 5hmC. Thus, we performed an EPIC array with bisulfite and oxidative bisulfite conversion to screen for differential 5mC and 5hmC. A closer look at the methylation status of loci for both *Vsx2* and *Prdm1* genes [198] [18] [181] revealed that on the one hand, *Prdm1* enhancer region [277] lost 5mC signature marks, while in general the locus showed much more gain in 5hmC at several positions, corroborating the general notion that increased 5hmC positively regulate gene expression and further corroborating our expression analysis of *Prdm1* upregulation. On the other hand, *Vsx2* enhancer region, also known as super-enhancer (SE), had an accumulation of 5mC marks. Much more complex is 5mC and 5hmC status in intragenic regions and how this correlates with gene expression. In general, *Vsx2* gene showed higher levels of gained 5mC than 5hmC in the gene body. Previously, gained 5hmC in WT retina has been observed following Tet3 overexpression in mice [209] suggesting a role of Tet3 in regulating the expression levels of *Vsx2* *in vivo*. Moreover, independently from tissue type and species, methylation in the first intron inversely correlates with gene expression, to a higher extent than methylation occurring at promoter regions [6]. The fact that this intronic region is methylated in *Vsx2* gene further speaks for gene silencing and supports the observation of reduced (or delayed) gene expression in *Tet3* mutant mice. This lower abundancy in turn exerts less inhibitory potential on *Prdm1*, leading to the molecular and cellular cascade of events just described.

25.2 More cone photoreceptors generated during postnatal stages suggest late born neurons as source

The other important aspect to be clarified is the temporal window during which this change in cell fate occurs. Of note, cone photoreceptors and bipolar cells are generated during different waves of retinogenesis [268]: cones are specified starting from embryonic day E12.5 and by post-natal day 4 they are already at their final location. Instead, bipolar cells are born mostly in the post-natal period, during the second wave of retinogenesis. If the new cones in *Tet3* mutant mice were specified at the progenitor state, meaning before cell commitment to bipolar or other fates, an increase in their cell number would be observed already at early post-natal stages, when endogenous bipolar cells are born. Notably, even at p10 (considered quite late in the genesis stage), the number of cones did not appear increased, suggesting that these new cones are specified later, not at the progenitor stage. During this time, the number of cone photoreceptors remained stable in control mice, in agreement with the fact that cones are generated earlier during development. In *Tet3* mutant mice, instead, the increase in number of cones was observed at late developmental age (p30 in this study), indicating that the new cones must have been generated postnatally, between p13 and p30. The significant increase only at later postnatal stages might be attributed to the fact that, once born, these cells need time to migrate from the INL to the ONL. Indeed, many *Arr3*⁺ cells were observed with their cell body in the lower half of the ONL at both p10 and p13 (Fig, 34). Notably, bipolar cells showed an opposite trend, as their number increases by p30 in control mice, while in *Tet3* mutant mice the number remained constant over time. This increase between p13 and p30 is in agreement with the fact that bipolar cell markers do not appear until p6 [126], thereby justifying a slight delay between genesis and identity confirmation. All together, these results support a change in cell fate commitment of late born neurons (e.g., bipolar cells) to cone photoreceptors.

Alternatively, this process could occur after the full commitment of bipolar cells, e.g., after the expression of bipolar cell markers and their maturation. Although *Arr3*⁺ cell bodies were found in the INL, I could never observe the co-localisation of mature markers (e.g., *Arr3* and *Vsx2*) in the same cell. Moreover, it has been shown that the sustained expression of *Prdm1* in nascent, but not mature, bipolar cells is able to re-direct the bipolar cell fate towards photoreceptors [76]. The more mature the cells, the less likely the chances that this process occurs, and that the resulting cell survives afterwards. Therefore, it is conceivable that the shift in commitment is specified at the precursor stage, rather than when bipolar cells have achieved full maturation. Further pointing in this direction, and as mentioned before, a temporal window exists in which the already committed precursors (*Otx2*⁺) can be either originate bipolar cells or photoreceptors, depending on which molecular cues prevail [29] [76]. Because the peak of rod genesis overlaps extensively with the production of bipolar cells, many works investigating cell fate choice between bipolar cells and photoreceptors have rather assumed that rods are specifically involved [29] [76] [75], despite the lack of evidence ruling out cones from this scenario. Having found

some $Arr3^+$ cells in the INL at early post-natal days, when normally all cones should localise in the upper half of the ONL, strengthen the possibility that these misplaced cones are actually born within the INL itself.

Recently, two new factors have been identified to be important in cone photoreceptors generation, namely *Pou2f1/2* [112]. In their study, Javed and colleagues observed that overexpressing these two factors in the developing retina expanded the pool of cone photoreceptors. When overexpressed at later stages, the increase in cones was accompanied by a decrease in the number of late born cells (BPs and MGs). This effect was attributed to the ability of *Pou2f2* to bind and repress *Nrl* promoter, and, consequently, also *Nr2e3*, thereby suppressing rod fate in these cells. *Pou2f2* and, to minor extent, *Pou2f1*, additionally retained this ability when ectopically expressed in post-mitotic photoreceptor precursors [112]. Notably, *Vsx2* has been shown to bind and regulate the expression of *Pou2f1*. In fact, in mice where *Vsx2* super-enhancer was deleted (the same showing accumulation of methylation in our study), the expression of *Vsx2* was reduced, in agreement with our observations, while the one of *Pou2f1* was upregulated. As a result, the authors described an increase in the number of cone photoreceptors in their adult retinas [18]. In this study, I proposed a model in which committed post-mitotic bipolar precursors are potentially susceptible to a re-direction of their cell fate towards cone photoreceptors, via an imbalance between *Vsx2* and *Prdm1*. Downregulation of *Vsx2* via epigenetic regulation of its regulatory elements (enhancers) loosen any restraint on *Prdm1* expression, thus pushing cells towards a photoreceptor cell-fate. Moreover, the reduced *Vsx2* availability and its inhibitory action on downstream transcription factors like *Pou2f1/2* seemingly imposes a cone identity preference on photoreceptor precursors, most likely through *Pou2f2* inhibition on *Nrl* and *Nr2e3*. Whether Tet3 normally exerts a direct effect on these additional transcription factors remains to be elucidated.

25.3 The role of Tet3 in cone sub-type specification and cone gradient establishment

In the rodent retina, two different types of cone photoreceptors with distinct chromatic properties exist, whose activity depends on the expression of light absorbing proteins called opsins [103]. Blue cones have S-opsin pigment and absorption maxima at 360 nm (in the blue range, hence the name), whereas green cones express M-opsin chromophore with an absorption at 508 nm [260]. In my model system, I found equal distribution of the S-opsin expressing cones along the dorso-ventral axis of the retina which in turn resulted in the almost complete loss of the typical gradient. S-cones became more abundant dorsally and reached the same amount as M-cones, causing all cones to express both opsins (hybrid cones). These results suggest a role of Tet3 in cone sub-type specification since studies on WT mice have revealed opposite dorso-ventral gradient distribution of the two types of cone photoreceptors [202] [226]. Indeed S-cones are very scarcely represented in the dorsal area and more abundant ventrally whereas M-cones have

the opposite pattern, although less pronounced than S-cones [202]. Moreover, differently from the human retina, mice and other lower vertebrates express more than one opsin within the same cell [8], thus causing the majority of the cones located in the center to be hybrid. Nevertheless, because of the scarce representation of blue cones in the dorsal half, pure green cones (expressing M-opsin only) are more abundant in this part of the retina. Pure S-cones, instead, are a minority residing in the ventral half [202]. Interestingly, the number of pure S-cones in the ventral retina (as well as the few pure S-cones in the dorsal retina) were not affected by *Tet3* mutation.

25.4 *Thrb* has a key role in cones gradient formation

The most described and studied mechanism in the regulation of opsin specification is related to thyroid hormones and their receptor *Thrb* [73] [194] [160]. Therefore, I have based the characterisation of the observed phenotype on the different players of this canonical pathway. *Thrb* exist in two isoforms that differ in their N-termini, generated by an alternative promoter. The isoform $\beta 2$ (*Thrb2*) is selectively expressed in the retina, more specifically in cone photoreceptors, where it plays a pivotal role in opsin specification [141]. Indeed, deletion of this specific isoform from the mouse retina determines the loss of M-cones and a broad expression of S-cones [187]. Although an interaction between *Tet3* and *Thrb* has been described where *Tet3* stabilises *Thrb* association to chromatin [81], *Tet3* does not regulate *Thrb* expression, since its transcript showed comparable levels in control and *Tet3* mutant retinæ. Thyroid hormone receptor activity is achieved by binding of its most active ligand, thyroid hormone T3, to the transactivation domain exerting a positive regulation on gene expression [62] [224]. S-cones are specified first, at a time when T3 concentration does not follow a gradient and is rather low and equally distributed across the retina [224]. In this context, S-cones are uniformly distributed along the dorso-ventral axis. Later on, at the onset of M-cones specification, a non-uniform distribution of T3 has been observed, with an enrichment in the dorsal compared to the ventral side [224]. This mirrors the gradient of green cones, which are also more represented in the dorsal region compared to the ventral. Despite unaltered *Thrb* expression level, we found lower *Dio2* and *Dio3* (the enzymes converting inactive T4 to active T3, and T3 to inactive rT3, respectively) levels in *Tet3* mutant retinæ which prompted a deeper analysis on T4 and T3 direct quantification. Commonly, levels of these molecules can be evaluated via radioimmunoassay (RIA), which can measure the free fraction of T3 and T4, namely FT3 and FT4, and gives a real estimation of their activity. Instead, for our experiment we relied on mass spectrometry (MS), which allows to quantify only the total fractions present in the tissue (free + T3/T4 bound to low-affinity, but highly abundant proteins), but is more sensitive than RIA [230] [21]. Despite that, we were not able to detect differential amounts of available T4 and T3 in our experimental conditions. Being the majority of T3 and T4 bound to these carrier proteins, fluctuations in their free counterparts might be difficult to be appreciated. Moreover, other soluble factors might play a role in the process. In this regard, it is important to mention that other mouse strains (different from BL6J mice used in

this study) do not show a dorso-ventral gradient distribution of S-opsin, e.g., albino mice [202]. Comparison between these strains, at transcript and protein levels, might help to identify new candidates orchestrating this yet-to-be understood process.

Of note, other transcription factors that in previous studies have been implicated in this process, namely *Coup-TFII*, *Bmall*, *Nr2e3*, *Vax2* [72] [232] [231] [165] [180], were not differentially regulated in our RNA sequencing data, as well as in qRT-PCR analysis (data not shown).

25.5 Rxrg helps Thrb in silencing S-opsin and concurs in cone gradient establishment

Retinoid X Receptor Gamma (Rxrg) is a nuclear receptor equally involved in opsin specification process [223]. Loss of function mutations of this receptor show disrupted S-opsin gradient with increased dorsal expression and unaffected M-cone distribution [223]. This suggests that *Rxrg* is important in helping *Thrb* repress *Opn1sw*, without any role in the regulation of *Opn1mw* expression. As for *Thrb*, also *Rxrg* did not show differential expression in *Tet3* mutant retinæ analysed at different time points. At the same time, also the interaction between *Thrb* and *Tet3*, already described in literature [81] [217] and confirmed in this study, was seemingly unaffected by *Tet3* mutation. Based on the expression study of the two opsins, it has been suggested that all cones in the retina initially express S-opsin. Only later, through protein-protein interaction between *Thrb2* and *Rxrg*, S-opsin gene is repressed at the same time M-opsin gene starts to be expressed in cones [172][194]. Considering that neither thyroid hormones, nor receptors, nor the interaction between *Tet3* and *Thrb* seemed to be affected by *Tet3* mutation, only one possible scenario could explain the observed phenotype. In physiological conditions, *Thrb* and/or *Rxrg* recruits *Tet3* for targeted demethylation of selected loci, as it was previously observed for other proteins [209]. In this study, we found that *Thrb* has a synergistic effect on *Tet3* dioxygenase activity *in vitro*, effect not observed when mutations in its catalytic domain impaired correct function. Moreover, further demethylation to 5fC and 5caC, to potentially repress genes, was impaired in mutant mice revealing a key role of *Tet3* in demethylation and gene silencing. In this context, *Tet3* might be directed to *Opn1sw* for targeted demethylation and inactivation in some cone cells for correct gradient establishment. Similarly, direction towards *Opn1mw* might prompt to its correct temporal activation, which would be the first evidence of opsin regulation mediated by *Tet3* at epigenetic level. The delay in the deposition of 5hmC mark might explain why, for instance, we observed a delay in the expression of M-opsin gene, as well as in the detection of its protein, in developing mice (Fig. 30). Similar results have been obtained in other studies, where initial absent/reduced/normal distribution of green cones was accompanied by widespread expression of S- cones. Even if adult mice recovered their M-opsin expression, defects in S-cones remained [72] [160] [232] [229] [231] [165] [153] [184]. The small deviations in the results described in these works could be accounted for by the age at which the expression

of the two opsins was analysed. Nevertheless, these studies seem to point to a similar or common mechanism by which, after the acquisition of the default S-fate, a specific time window exists in which M-opsin needs to be expressed in these cones. Failures or delays in accomplishing this cause a disruption in S-opsin gradient that persists throughout adulthood.

More controversial is, instead, the regulation of *Opn1sw* in monochromat green cones. In these cones, expressing only M-opsin pigment, S-Opsin transcript is still present. In fact, although blue cones have a differential protein expression in the dorso-ventral axis, *Opn1sw* mRNA is homogeneously expressed throughout the whole retina [8]. Therefore, a different kind of regulation, probably at mRNA level, must be in place and prevent translation into protein. miRNAs are suitable candidates for this molecular control, and so far, several were already found to be depleted in *Nrl*-null mice [83] [169], in which almost all photoreceptors are blue cones [169] [300]. Thus, miRNAs are potential candidates for *Opn1sw* suppression in physiological conditions.

25.6 Prediction of loss of opposing opsin gradient on colour vision

Cone photoreceptors are the foundation of colour vision thanks to selective opsin expression responding to specified light wavelengths [260]. Moreover, light components do not only serve as colour discrimination but also luminance detection of shapes, objects and contrast enhancement. Because *Tet3* mutation results in higher number of cone photoreceptors and altered S-cone distribution along the dorso-ventral axis of mouse retina, it is conceivable to expect an effect on colour and luminance detection in these mice. Colour vision starts already at the first synapse in the OPL, where an excited cone transmits its information to the inner retina and receives at the same time negative feedback from an HC, creating opponency in the surround [206] [145] and segregation of the stimulus in two parallel opponent pathways and the basis for colour vision. In mice, blue-green opponency is the equivalent of blue-yellow chromatic opponency in primate retina [208]. As previously mentioned, the murine retina can be divided in three different functional regions based on the opposing gradient distribution of the two opsins: a dorsal region (defining the response in lower visual field) that is enriched in green cones (expressing only M-opsin) interspaced by true blue cones (expressing only S-opsin), a transition or central region where most cones are hybrid (expressing both S- and M-opsin), and a ventral region (upper visual field) similar to the transition zone but more biased towards blue cones [226], since the majority of true blue cones are ventrally located [187]. True blue cones are believed to be the foundation of ventral colour opponency circuit in dichromatic animals, through their selective connectivity to type 9 ON-bipolar cells (BPs) converging the ON-blue pathway on retinal ganglion cells (RGCs) [254] [187]. Their abundance in the ventral retina confers a S-ON sensitive receptive field to these cones, whereas their surround exhibits a strong green shift in the chromatic preference of their receptive field (M-OFF). Differently from other dichromatic animals and primate, in mice the M-OFF inhibition does not seem to arise from HCs negative feedback

[248]. It is not clear whether this opponency in the ventral region is mediated by M-expressing cones (which are still hybrid cones) or rods, at least in mesopic (i.e., activating both rods and cones) conditions, via HCs-mediated lateral inhibition. As a result of this S-ON/M-OFF bipolar activation, a blue-green opponency with a slight shift towards blue sensitivity is established [254]. The blue preference in the upper visual field is believed to help enhance blue contrast and better define an object, to protect the animal from aerial predators [299]. In our model system, despite the increase in number of cone photoreceptors in the ventral half of the retina, the general ratio and distribution of cones (both true S-cones and hybrid cones) did not differ. Therefore, no major alterations are expected in the processing of colour information or luminance perception in this region. Conversely, in the dorsal retina, true S-cones are scarce and the high representation of true M-cones confers a strong, though not unique, response of the circuitry to green stimuli [254]. In this part of the retina, the distribution of M-cones reminds the mosaic representation found in other dichromatic species, suggesting that the mechanism mediating blue-green antagonism in this area is evolutionary conserved. In fact, RGCs showing both S-OFF/M-ON as well as S-ON/M-OFF sensitivity have been described in the dorsal part of the dichromatic retina [61] [241]. The ON component of this circuit, for both S-ON and M-ON counterparts, has been ascribed to ON-BP that receive relative pure inputs from S- and M-cones. The S-OFF input, instead, is provided by the S-selective ON-BP, which in turn contacts amacrine cells and mediates lateral inhibition on activated M-ON bipolar cells [37]. The identification of a type 1 bipolar cell, broadly distributed in the dorsal retina and that accurately avoids S-cone contacts, raised the question of whether the M-OFF component of the S-ON/M-OFF circuitry might arise via selective bipolar cell stimulation by single expressing cones [25]. Unfortunately, such circuitry has not yet been identified in the mouse retina. Since rods absorption maxima fall in a similar range as M-pigment, it is very likely that they participate in the M-OFF component of the circuit through lateral inhibition mediated by HCs, at least in mesopic conditions. Also in this case, at least in the mouse retina, the chemical inhibitory feedback of horizontal cells to cones does not affect the OFF component, therefore excluding rod involvement in determining colour opponency in this region [254]. Therefore, colour opponency is more likely to arise in the inner retina or at the level of the output (RGCs). In fact, the M-OFF input seems to be provided by inhibitory amacrine cells acting on RGCs, since a combination of GABA inhibitors can abolish the opponency in these cells [35]. In our mouse model, the loss of S-opsin gradient determined an equal dorso-ventral expression of this protein and resulted in almost all cones in the lower visual field to be hybrid. This alteration could have a tremendous effect on the circuitry, particularly on colour discrimination in the dorsal region. This newly acquired distribution of dorsal cones resembled more that of the ventral area, where also the majority of cones are hybrid and surrounded by few genuine S-cones, conferring a blue shift in the spectral sensitivity of this region. On the one hand, it is conceivable that the changed arrangement in the dorsal retina determines a shift towards blue range in the chromatic preference of these cones, decreasing or abolishing the green bias conferred by the excess of true M-cones. On the other

hand, it is not certain that to the rearrangement in the outer retina corresponds a remodelling of the circuitry in the inner retina. In favour of the first possibility, studies in mice in which the L-pigment of red cones typical of trichromatic animals was introduced, suggested that retinal circuit can quickly adapt either by creating new circuits or, more likely, rearranging the old ones [108]. In behavioural investigation, I did not detect differences in the performance of mice in the visual acuity test, although *Tet3* mutant mice performed worse in light-dark test, suggesting altered luminance contrast detection which resulted in longer times to identify the opening between the two chambers. Of note, an impairment in anxiety-like behaviour cannot be excluded at this stage, for which deeper investigation will be necessary). However, these results cannot fully address the hypothesis of affected colour discrimination. A more specific tests [51] [109] [298] or electrophysiological recordings of isolated retinæ, like the ones performed by [254], should be employed to better elucidate this particular point. An additional possibility is that the presence of double pigments in cones broadens their sensitivity spectrum [8], potentially offering functional advantages in terms of contrast sensitivity against different spectral backgrounds [298], most likely through induced plasticity and circuitry rearrangement.

25.7 Tet3 is important for correct cone synaptogenesis and synaptic function

Role of Tet3 in rod photoreceptor function and maturation

Tet3 has been previously linked to functional maturation of neurons through active demethylation during the differentiation process [251] [303]. On this line, labelling ON-bipolar cells with *Pcp2* and *PKC α* showed lower axonal arborisation at the inner plexiform layer (IPL) of *Tet3* mutant mice. In this study, I assessed retinal function using *in vivo* electroretinography aimed at investigating the activity of both rod- and cone-initiated responses, under scotopic and photopic conditions, respectively. Scotopic ERG did not reveal alterations in both a- and b-waves, in agreement with the cellular characterisation of unaffected numbers of rods and rod bipolar cells. Surprisingly, many of the genes localised specifically in rod outer segments and important for rod homeostasis and function (including *Rho*, *Pde6a*, *Pde6g*, *Gucal1a*, and *Gucal1b*) appeared downregulated in two of the three time points analysed in bulk RNAseq. Moreover, genes important for ON-bipolar cells (therefore including rod bipolar cells), like *Trpm1*, *Cabp4* and *Cacnals*, were additionally downregulated. Despite the observed changes in genes essential for rod phototransduction cascade, this did not result in functional perturbation of these and their partner cells, as previously mentioned. One possibility is that these changes detected at transcript level are not reflected by similar changes at protein level, as we have sought to perform a proteomic analysis only on cone photoreceptors following the molecular, cellular, and functional defects identified in this study. Therefore, it is possible that cells compensate for the reduction in transcription and counteract it sufficiently to ensure proper functioning, e.g., by

increasing protein stability.

Role of Tet3 in rod photoreceptor function and maturation

Conversely, I observed a different scenario in the propagation of cone-mediated light stimulus. Because cone photoreceptors represent a small minority in the ONL (3-5%) [202], mice stimulated under photopic condition result in a much-reduced inward current amplitude (a-wave) that is difficult to record and quantify. Even in our mouse model, where the number of cone photoreceptors underwent a nearly 25% increase, the photopic a-wave did not show differences (data not shown). However, the same mice showed a strong reduction in the photopic b-wave. Assuming that cone photoreceptors maintain their physiological activity despite their increase, and correctly establish synaptic contacts in the now altered amount ratio with bipolar cells, the b-wave reduction might simply reflect the lower number of ON- and OFF-bipolar cells (both of which are contacted by cone photoreceptors) observed here. Moreover, because of these cellular imbalances resulting in a higher number of synapses, cone stimulation may result in a signaling overload of bipolar cells and, consequently, their malfunction. In line with this, staining with both pre- and post-synaptic markers revealed that contacts are indeed formed between the two neuronal types. However, the OPL appeared thicker, probably due to the higher amount of cone pedicles and their re-arranged distribution in multiple rows. At the same time, when taking into account the cone increase, the number of dendritic spines in ON-bipolar cells, here labelled with Cacna1s, appeared to be reduced, prompting again the number of bipolar cells as the main limiting factor in the altered response. It would be interesting in this context to further investigate the synaptic contacts established between each cone pedicle and the bipolar (and horizontal) dendrites at ultrastructural level.

Cone photoreceptors do not fully integrate in the network by dysregulation of synaptic and junction proteins

Looking, instead, at ribbon synapses [93], the core of synaptic transmission between photoreceptors and the inner retina, with Ctbp2 [234], revealed an additional piece of the puzzle. Of notice, Ctbp2 locus showed differential methylation and hydroxymethylation in our oxidative bisulfite sequencing dataset suggesting that its expression levels might indeed be regulated by Tet3 at DNA level. On the one hand, rod ribbon synapses are arcuate in shape and usually present as a single structure per rod pedicle. On the other hand, cones may contain up to 50 different ribbons each, all of them regulated independently [77]. In *Tet3* mutant mice, some of the cone pedicles were completely deprived of ribbon synapses. Whether these deprived cones are the “endogenous” or the newly generated cones, and whether they integrate and participate to the network activity, remains to be elucidated. In line with these observations, many synaptic proteins (Sv2b, Svop, Syt1, Synj1) were differentially expressed specifically in cone photoreceptors in our proteomics analysis. Notably, synaptojanin1 regulates vesicles release in ribbon and conventional

synapses. Mutations in this protein have been linked to abnormal vesicle maintenance in mice [129] and other species [271] [237] as well as disorganization of ribbon synapses specifically in cone photoreceptors [269] [98]. Although RIBEYE/Ctbp2 ablation affects the formation of ribbon synapses without altering the overall organization and synaptic connectivity in the retina of these mice [171], the absence of this supportive structure may be one explanation for the increase of these proteins involved in the tethering and priming of synaptic vesicles. Moreover, we have found several proteins associated to actin filament and microtubule organization to be significantly downregulated (e.g., Cdc42, Wdr1, Actn1, Tuba1B/C) in *Tet3* mutant mice, which further points to altered assembly of the synaptic machinery in cone pedicles. These same proteins are additionally important for gap junctions, which are observed not only between the same photoreceptor type (rod-rod and cone-cone [265] [266] [53]), but also between rods and cones (the so-called gap junctional coupling). Although the identified proteins have never been observed exclusively in one or the other photoreceptor cell, we speculate that these only affect gap junctions in which at least a cone photoreceptor is involved. Notably, proteins showing differential expression in the proteomic analysis (e.g., Tuba1B/C, Cdc42m Actn1, Ctbp2) also appeared as to be differentially methylated and hydroxymethylated at their loci. Curiously, these loci showed both a gain in 5mC and 5hmC, highlighting the importance of the position at which these modifications occur, and the amount of modified cytosines dictating final expression direction.

Altering the strength of gap junctions is expected to influence the size of photoreceptors receptive field. For instance, cones have larger receptive fields during states in which rods and cones are more strongly electrically coupled [222]. Part of the light response evoked in cones is indeed due to electrical coupling to neighboring rods [100]. In *Tet3* mutant mice, rods appear to function normally and could to some extent compensate and/or contribute to photopic responses. Therefore, the ERG responses we have recorded might even be an underestimation of the real effect. In dim light conditions, where mostly rods are involved, the heterologous junctional coupling (rod-cone) is believed to contribute to lesser extent compared to the homologous type (rod-rod) [149]. In the case of the homologous coupling, instead, the situation might vary depending on the fact that the gap junctions are formed 1) between two integrated and functionally active cones or 2) two both (likely) inactive cones or, even more, 3) between normal and inactive cones. Although the specific contribution of gap junctions and their coupling remains to be elucidated, we have provided additional insight to potential mechanisms underlying reduced photopic responses, as observed in this study. In agreement with previous data [251] [303], we have also shown here that *Tet3* mutation impacts the expression of different proteins involved in synaptogenesis and, consequently, the proper functioning of cone photoreceptors in their light-mediated response.

25.8 The altered metabolic profile of cone photoreceptors in catalytically impaired Tet3 mice – cause or consequence?

Among the differentially expressed proteins in our dataset were proteins involved in metabolic pathways. Photoreceptors are cells that, differently from all other neurons, rely on aerobic glycolysis for their energy requirements in presence of oxygen [195]. This effect is better known as Warburg effect and was first described in cancer cells [280] [281]. The reason for heavily relying on aerobic glycolysis has been linked to very high demand for anabolic metabolites that are required in the daily life of photoreceptor cells. For instance, different lipid and proteins are daily used by RPE cells to digest and reassemble the disks within photoreceptor outer segments [301]. Moreover, neighbouring cells (RPE and MGs) depend on lactate intake, mainly produced by PRs and imported to satisfy their energetic demand [10] [121]. At the same time, RPE cells supplement PRs with ketone bodies, which can be metabolised in the mitochondria via TCA cycle for ATP production [2]. From all these studies a close metabolic relationship between PRs, RPE cells and MGs emerges, based on the exchange of both catabolic and anabolic metabolites. Although the metabolic distinction between rod and cones is not clear yet, cones have a higher metabolic demand than rods. This difference is probably to be attributed to the faster photosensitive kinetics of these cells as well as to the higher number of synaptic contacts established with second order neurons [105]. Many of the proteins found increased in our analysis (e.g., Ogdh, Aco2, Idh3, Ndufa3, Atp6D and Atp5v1) were assigned to TCA cycle and oxidative phosphorylation (OXPHOS), though, as just discussed, PRs do not rely on OXPHOS for their energetic requirements. Notably, mitochondrial oxidative stress caused by increased OXPHOS in these organelles has been linked to RPE degeneration prior to PRs loss in different retinal disorders [82] [199]. In agreement with our proteomics data, pointing at a switch in metabolic pathway in cones, we have observed an increased number of overall smaller mitochondria in cone pedicles. The smaller size and the higher number can be attributed to increased mitochondrial fission (segmentation of a big mitochondrion), whose increased rate has been previously linked to higher OXPHOS levels [311]. Although we have only analysed mitochondria structure in cone pedicles, as a consequence of the altered phototransduction cascade and synapse assembly, we would expect similar results in cone inner segments, in line with our molecular observations.

Recently, we have shown that Tet3 is able to redirect mitochondrial enzymes (Gdh) to the nucleus for local supplement (α KG) supply and Tet-dependent oxidation of 5mC [262]. Curiously, Ogdh, the enzyme responsible for the conversion of α KG in succinyl-CoA, was also found increased. A plausible explanation for this would be that, due to a failure in Tet3 catalytic activity, α KG amounts are elevated, forcing cells to compensate by increasing the levels of the enzyme responsible for its metabolism. An in-depth metabolite analysis is necessary in order to validate this hypothesis. Additionally, the extent to which Tet3 contributes to this altered metabolic landscape, and whether the latter is the primary cause or a mere consequence of all

other affected processes, remains to be elucidated.

26 Human retinal organoids

26.1 Limitations of current models in the study of human retinal development, physiology, and disease

Thus far, human eye research studies have been limited to anatomical and morphological evaluations, due to the scarce availability of foetal and/or adult tissue. Strongly hindering these studies is the preservation of the tissue *ex vivo* and the rapid, tissue-dependent change in gene expression profile post-mortem, which make the investigation of pathophysiological mechanisms of human retinal diseases *in vitro* particularly difficult. Moreover, the different background of donors as well as their pathological state have both raised several constraints on using post-mortem donated retinal specimen. Due to these technical barriers, conventional toxicology, molecular and cellular studies have been and are still carried on alternative model systems, which include rodents as *in vivo* models. At the same time, rodents pose other limitations on human retinal studies. Firstly, they are nocturnal animals, thus extensively relying on rod photoreceptors for their dim vision. Indeed, rods represent 95-7% of all photoreceptors in mouse retina, whereas cones, important for colour vision and visual acuity, are just a minority (3-5%) [202]. As such, their *in vivo* evaluation for pathophysiological studies remains elusive in these specific models. Secondly, in terms of cone research, rodents have only two types of cones, namely the blue and the green [8]. Differently from humans, mice miss the expression of the long wavelength cones (L-cones), or red cones, indeed mice are blind to red light. In the context of this study, where Tet3 seems to have a role in cone sub-type specification in the mouse retina, it would be interesting to evaluate if the phenotypic observations could be recapitulated (completely or in part) in humans and to investigate the effect of human TET3 on M- versus L-cones specification. Lastly, although the gross cellular composition of the retina in rodents and humans is the same, single cell studies have uncovered much deeper differences between the two species in terms of cell complexity [45] [162]. This variability could explain why some disease mechanisms cannot be fully recapitulated in animal models. For all these reasons, there is the need to develop more human-like tools to ensure a better understanding of this tissue in health and disease conditions. The progress made in the field of induced pluripotent stem cells (iPSCs), and their differentiation in 3D organoid structures of several organs, including brain [139], lungs [40], intestine [247] and retina [189], has revolutionised our approach to human studies. Moreover, the flexibility and ease of manipulation of the starting material have opened new doors in several applications, like the identification of new signalling pathway in retinal development [200] [273] and related developmental diseases [273], toxicological studies of drugs and compounds affecting the retina [57], functionality studies [68][178] [?] and potential treatment for retinal diseases [124] [275]. For all these reasons, I sought to establish this 3D model as basis for future studies aiming at

investigating the role of TET3 in cone commitment and opsin specification in a more humanised model.

26.2 Different iPSCs line might react differently to culture conditions

Several protocols have been established since the very first proof of spontaneous optic-like structure formation from mouse embryonic stem cells [?]. These protocols differ in particular in the initial steps of the differentiation procedure, at the stage in which the so-called embryoid body (EB), a spheroid of thousand cells, forms. In the specific case of the three protocols tested in this study [38] [128] and [32], I observed that cells were not able to re-aggregate into single spherical structures when these were dissociated into single cells, even in presence of a rho-associated protein kinase (ROCK) inhibitor, known to improve survival after single cell dissociation [64] [283] [159]. Possibly, the disruption of intercellular interactions for the single cell suspension affects irreversibly the embryoid body formation, at least for the iPSC lines used in this study. Therefore, EBs were generated from colonies (or smaller clumps) dissociation followed by self-assembly. Although resulting in the formation of EBs of different sizes, this method did not alter the final yield or cellular composition.

The second general problem of 3D aggregates is the long-term maintenance of these cultures and their survival. Specifically, it has been described that retinal ganglion cells (RGCs) die around three/four months of *in vitro* differentiation [32], probably due to reduced access to nutrients contained in the media following the increase in organoid size and the absence of a vasculature system ensuring their circulation within the organoid structure. In order to counteract this loss, shaking culture conditions using bioreactors or orbital shakers have been subsequently introduced. For some organoid systems, the continuous agitation has indeed improved both survival and long-term maintenance [304] [139]. Intriguingly, constant shaking revealed to be deleterious for retinal organoids, in particular for photoreceptors cells. Though photoreceptor precursors were present in differentiating retinal organoids, as shown by the presence of OTX2⁺ cells in the outer rim of optic vesicle-like structures, these cells failed to express markers of immature and mature photoreceptors, despite the expression of transcripts encoding some of these proteins. Moreover, these organoids failed to ever form brush-like structures reminiscent of outer and inner segment formations [148] [136]. This suggested that constant agitation might exert a mechanical stress on these structures, which probably resulted in disruption or lack of formation of segments. Indeed, since many photoreceptor proteins are localised in the outer and/or inner segments, the mechanical damage of these might result in enhanced protein degradation due to protein mislocalisation or defective folding [96]. Alternatively, mechanical stress might have an indirect impact on protein translation, through an effect on actin bundles and cytoskeleton integrity [243]. Whether some transcripts and proteins are more susceptible to degradation than others remain to be elucidated, and these 3D aggregates kept in constant agitation might be the perfect model for such investigation.

Once the orbital shaker is removed from the culture conditions, and organoids are grown statically, outer/inner segments are correctly formed and appear on the outer surface of differentiating retinal organoids. Concomitantly, translation and protein localisation are also recovered, revealing a sequential differentiation of these retinal cells reminiscent of *in vivo* retinogenesis with a proper sequential and temporal maturation.

26.3 *In vitro* electroporation is an effective and versatile tool for genetic material transfer in selected retinal cell populations

For several studies in retinal development and disease modelling involving human retinal organoids, original iPSCs lines have been genetically modified to investigate the role of specific genes in these processes. This results in all cells being mutated, limiting the study of the interaction between wild type and mutant cells, which, depending on the disease to be modelled, is a more realistic pathological feature. In this direction of studies, electroporation is a valuable tool for acute *in vitro* manipulation, at the same time allowing to investigate both cell autonomous and non-cell autonomous mechanisms, since the procedure affects only a subset of cells. Electroporation has been extensively used in 2D model of several cell lines, both primary and immortalised [177] [214], as well as in complex model system, such as brain [52] [30] and intestinal [69] organoids, but not retinal organoids. In this study, retinal organoids at different days of maturation have been injected with GFP-encoding plasmids driven either by the ubiquitous promoter CAG, or by cell type-specific promoters (GFAP, RLBP1, ARR3, RG, RHO196) and electroporated using tweezer electrodes. These offer the flexibility to potentially hit different cell populations simply depending on the point of injections and electrode orientation (Fig. 48). Two different paradigms have been followed, consisting of either injection in the internal neuronal retina lumen to hit inner retina cell populations and immature precursors or dispersion of the plasmid solution in the media facing the outer retina for gene transfer to photoreceptors. In both cases electroporation was successful, as shown by fluorescence detection two weeks after performing the procedure. Moreover, cellular characterisation revealed an unexpected scenario, namely that the two most susceptible cell types to this procedure are Müller cells (MGs) and retinal pigmented epithelium-like clusters (RPE), and to lesser extent photoreceptor precursors, but no differentiated neuronal cells. Surprisingly, when using RHO196, targeting mature rods, ARR3 or RG promoter, targeting mature cones, no GFP fluorescence was observed in optic vesicle-like structures at the end of the experiment. The method used in this procedure relies on the same conditions used in both *in vivo* electroporation [48] of new-born mice, and *in vitro* electroporation of neuronal progenitors [30]. In both cases, neuronal precursors or progenitors represented the main target population. Conversely, differentiated neurons have proven to be harder to manipulate, and, when successfully electroporated, higher voltages had to be employed [177]. Therefore, whether changing the setup for this procedure can efficiently target terminally differentiated cells, and to which extent, remains to be evaluated. Nevertheless, the *in vitro* elec-

troporation of complex model systems, like retinal organoids, is a versatile, non-viral option for the genetic transfer in selected cell populations like MGs and RPE-like cells.

26.4 Future directions

In the first part of this study, where the catalytic activity of Tet3 has been impaired by deletion of the first of the two dioxygenase domains, I showed that specifically the cone photoreceptor population was increased in number, and that S-opsin protein was expressed by nearly all cones. This resulted in a loss of dorso-ventral gradient of blue cones and, as a consequence, in almost all cones being hybrid, i.e., expressing simultaneously S- and M-opsin pigments. In humans, in addition to blue and green cones, red cones (expressing the L-opsin pigment) exist [191]. Moreover, the human retina does not have hybrid cones, as each cone has a selective light response caused by the single chromophore it expresses. As in mice, also in human one of the factors playing a role in S- vs M-cone specification is thyroid hormone receptor. Recently, Eldred and colleagues demonstrated that the deletion of THRB2 alone is not sufficient to reproduce the same phenotypic observations as in mice [194] but rather it must be accompanied by THRB1 deletion. These results still underlined the involvement of thyroid hormone, and its receptors, in cone specification [62]. Considering the phenotype observed in our mouse model, the fact that Tet3 and Thrb interact at the chromatin level [81], and that Thrb2 enhances Tet3-dependent hydroxymethylation, there are reasons to believe that TET3 might have a role in the specification of blue vs green cones in humans. In order to investigate TET3 contribution to this process, we are currently working on two separate approaches. On one side, we are genetically engineering our B7 iPSCs line, in order to delete the catalytic domain of TET3 using CRISPR/Cas9 technology. Once the engineered clone will be identified, human retinal organoids will be differentiated, and the expression of the single opsins investigated. On the other side, a milder and more acute effect is being examined, by promoting *TET3* knock-down using a previously described miRNA, specifically miR15b [166]. In case the electroporation method turns out to be unsuitable for terminally differentiated cone photoreceptors, even at higher voltages, miR15b will be delivered by AAVs, already proved to successfully infect both dividing and non-dividing cells (like neurons) [85]. On this line, our new capsid variant AAV2.NN, AAV2.GL and AAV9 outperformed AAV2 WT, 7m8 and AAV9 WT, respectively, in mice, and were showed to effectively transduce retina-like structures *in vitro* [205] [1] [275]. Based on our molecular characterisation of *TET3* expression and cytosine modifications (Fig. 47), viral vectors containing miR15b will be assembled, produced and delivered to differentiated retinal organoids at the time of opsin expression onset (at d100 or d130 to favour the formation of outer segments) and the single opsin expression will be investigated.

Finally, TET3 contribution in M- vs L-cone specification will also be addressed. So far, exploring the role of any factor in this process has proven challenging, due to the difficulty to differentiate between these two transcripts/proteins. In fact, M- and L-opsin genes are in an ar-

ray on the X-chromosome, thus sharing the same DNA regulatory element called locus control region [279]. Moreover, the two sequences share 98% homology at transcript level, with only 20 nucleotides of difference [84]. Recently, a group at the Johns Hopkins University developed an in-situ hybridization approach to discriminate between the two genes at transcript level. Following this method, the group was able to reveal that, in a manner similar to blue vs green cone development, green cones are born before red cones. Moreover, not THRB, but rather retinoic acid (RA) is indispensable for M- vs L-cone expression in a model of human retinal organoids [84]. In a separate context, an interaction between Tet and the Rar/Rxr receptor complex has been described, where RA triggers activation of the complex which in turn recruits Tet/Tdg for targeted DNA demethylation of specific loci [88]. Previously, a role of RA as modulator of TET3 activity has been described, where RA positively regulated TET3 transcript, which in turn increased the DNA demethylation at specific loci [99]. In our model system, *TET3* expression dropped significantly after RA treatment further suggesting an impact of RA on *TET3* regulation. Whether the interaction and recruitment happen also in the context of opsin specification remains to be elucidated and will be addressed in this model upon TET3 KD and KO paradigms.

References

- [1] Kevin Achberger, Madalena Cipriano, Matthias Düchs, Christian Schön, Stefan Michelfelder, Birgit Stierstorfer, Thorsten Lamla, Stefan G. Kauschke, Johanna Chuchuy, Julia Roos, Lena Mesch, Virginia Cora, Selin Pars, Natalia Pashkovskaia, Serena Corti, Alexander Kleger, Sebastian Kreuz, Udo Maier, Stefan Liebau, and Peter Loskill. Human stem cell-based retina-on-chip as new translational model for validation of AAV retinal gene therapy vectors. *bioRxiv*, page 2021.03.02.433550, mar 2021.
- [2] Jeffrey Adijanto, Jianhai Du, Cynthia Moffat, Erin L. Seifert, James B. Hurley, and Nancy J. Philp. The retinal pigment epithelium utilizes fatty acids for ketogenesis. *The Journal of biological chemistry*, 289(30):20570–20582, jul 2014.
- [3] Najate Aït-Ali, Ram Fridlich, Géraldine Millet-Puel, Emmanuelle Clérin, François Delalande, Céline Jaillard, Frédéric Blond, Ludivine Perrocheau, Sacha Reichman, Leah C. Byrne, Anne Olivier-Bandini, Jacques Bellalou, Emmanuel Moyses, Frédéric Bouillaud, Xavier Nicol, Deniz Dalkara, Alain Van Dorsselaer, José Alain Sahel, and Thierry Léveillard. Rod-derived cone viability factor promotes cone survival by stimulating aerobic glycolysis. *Cell*, 161(4):817–832, may 2015.
- [4] Issam Aldiri, Beisi Xu, Lu Wang, Xiang Chen, Daniel Hiler, Lyra Griffiths, Marc Valentine, Abbas Shirinifard, Suresh Thiagarajan, Andras Sablauer, Marie Elizabeth Barabas, Jiakun Zhang, Dianna Johnson, Sharon Frase, Xin Zhou, John Easton, Jinghui Zhang, Elaine R. Mardis, Richard K. Wilson, James R. Downing, and Michael A. Dyer. The Dynamic Epigenetic Landscape of the Retina During Development, Reprogramming, and Tumorigenesis. *Neuron*, 94(3):550–568.e10, may 2017.
- [5] Rachel Amouroux, Buhe Nashun, Kenjiro Shirane, Shoma Nakagawa, Peter W.S. Hill, Zelpha D’Souza, Manabu Nakayama, Masashi Matsuda, Aleksandra Turp, Elodie Ndjetehe, Vesela Encheva, Nobuaki R. Kudo, Haruhiko Koseki, Hiroyuki Sasaki, and Petra Hajkova. De novo DNA methylation drives 5hmC accumulation in mouse zygotes. *Nature Cell Biology* 2016 18:2, 18(2):225–233, jan 2016.
- [6] Dafni Anastasiadi, Anna Esteve-Codina, and Francesc Piferrer. Consistent inverse correlation between DNA methylation of the first intron and gene expression across tissues and species. *Epigenetics and Chromatin*, 11(1):1–17, jun 2018.
- [7] Cláudia Antunes, Jorge D. Da Silva, Sónia Guerra-Gomes, Nuno D. Alves, Fábio Ferreira, Eduardo Loureiro-Campos, Miguel R. Branco, Nuno Sousa, Wolf Reik, Luísa Pinto, and C. Joana Marques. Tet3 ablation in adult brain neurons increases anxiety-like behavior and regulates cognitive function in mice. *Molecular Psychiatry*, 26(5):1445–1457, 2021.

- [8] M. L. Applebury, M. P. Antoch, L. C. Baxter, L. L.Y. Chun, J. D. Falk, F. Farhangfar, K. Kage, M. G. Krzystolik, L. A. Lyass, and J. T. Robbins. The Murine Cone Photoreceptor: A Single Cone Type Expresses Both S and M Opsins with Retinal Spatial Patterning. *Neuron*, 27(3):513–523, sep 2000.
- [9] Yassen Assenov, Fabian Müller, Pavlo Lutsik, Jörn Walter, Thomas Lengauer, and Christoph Bock. Comprehensive analysis of DNA methylation data with RnBeads. *Nature Methods*, 11(11):1138–1140, 2014.
- [10] Gamal A. Badr, Jie Tang, Faramarz Ismail-Beigi, and Timothy S. Kern. Diabetes down-regulates GLUT1 expression in the retina and its microvessels but not in the cerebral cortex or its microvessels. *Diabetes*, 49(6):1016–1021, 2000.
- [11] Madeleine P. Ball, Jin Billy Li, Yuan Gao, Je Hyuk Lee, Emily M. Leproust, In Hyun Park, Bin Xie, George Q. Daley, and George M. Church. Targeted and genome-scale methylomics reveals gene body signatures in human cell lines. *Nature biotechnology*, 27(4):361, apr 2009.
- [12] Christina Bauer, Klaus Göbel, Nagarjuna Nagaraj, Christian Colantuoni, Mengxi Wang, Udo Müller, Elisabeth Kremmer, Andrea Rottach, and Heinrich Leonhardt. Phosphorylation of TET proteins is regulated via O-GlcNAcylation by the O-linked N-acetylglucosamine transferase (OGT). *The Journal of biological chemistry*, 290(8):4801–4812, feb 2015.
- [13] Lisa M Baye and Brian A Link. Nuclear migration during retinal development. *Brain Research*, 1192:29–36, 2008.
- [14] D. A. Baylor, M. G.F. Fuortes, and P. M. O’Bryan. Lateral interaction between vertebrate photoreceptors. *Vision Research*, 11(10):1195–1196, oct 1971.
- [15] D. A. Baylor, B. J. Nunn, and J. L. Schnapf. Spectral sensitivity of cones of the monkey *Macaca fascicularis*. *The Journal of Physiology*, 390(1):145–160, sep 1987.
- [16] Patricia Berber, Sofiia Bondarenko, Lisa Michaelis, and Bernhard Heinrich Friedrich Weber. Transient Retention of Photoreceptor Outer Segments in Matrigel-Embedded Retinal Organoids. *International journal of molecular sciences*, 23(23):14893, nov 2022.
- [17] Alireza Beygi. Lemaître’s law and the spatial distributions of the cone photoreceptors in the retinas of vertebrates. *bioRxiv*, page 2022.01.09.475540, 2022.
- [18] Fuyun Bian, Marwa Daghani, Fangfang Lu, Silvia Liu, Jeffrey M. Gross, and Issam Aldiri. Functional analysis of the *Vsx2* super-enhancer uncovers distinct cis-regulatory circuits controlling *Vsx2* expression during retinogenesis. *Development (Cambridge, England)*, 149(15), aug 2022.

- [19] J C Blanks and L V Johnson. Specific binding of peanut lectin to a class of retinal photoreceptor cells. A species comparison. *Investigative Ophthalmology Visual Science*, 25(5):546–557, may 1984.
- [20] Michael J. Booth, Miguel R. Branco, Gabriella Ficz, David Oxley, Felix Krueger, Wolf Reik, and Shankar Balasubramanian. Quantitative sequencing of 5-methylcytosine and 5-hydroxymethylcytosine at single-base resolution. *Science*, 336(6083):934–937, may 2012.
- [21] Marco Borsò, Patrizia Agretti, Riccardo Zucchi, and Alessandro Saba. Mass spectrometry in the diagnosis of thyroid disease and in the study of thyroid hormone metabolism. *Mass Spectrometry Reviews*, 41(3):443–468, may 2022.
- [22] David H. Brainard. Color and the Cone Mosaic. *Annual Review of Vision Science*, 1(1):519–546, nov 2015.
- [23] Barbara M. Braunger, Cora Demmer, and Ernst R. Tamm. Programmed cell death during retinal development of the mouse eye. *Advances in Experimental Medicine and Biology*, 801:9–13, 2014.
- [24] Gregory A. Brent. Mechanisms of thyroid hormone action. *The Journal of clinical investigation*, 122(9):3035–3043, sep 2012.
- [25] Tobias Breuninger, Christian Puller, Silke Haverkamp, and Thomas Euler. Chromatic Bipolar Cell Pathways in the Mouse Retina. *Journal of Neuroscience*, 31(17):6504–6517, apr 2011.
- [26] Kevin L. Briggman, Moritz Helmstaedter, and Winfried Denk. Wiring specificity in the direction-selectivity circuit of the retina. *Nature*, 471(7337):183–190, 2011.
- [27] Joseph A. Brzezinski, Euseok J. Kim, Jane E. Johnson, and Thomas A. Reh. Ascl1 expression defines a subpopulation of lineage-restricted progenitors in the mammalian retina. *Development (Cambridge, England)*, 138(16):3519–3531, aug 2011.
- [28] Joseph A. Brzezinski and Thomas A. Reh. Photoreceptor cell fate specification in vertebrates, oct 2015.
- [29] Joseph A. Brzezinski, Ko Uoon Park, and Thomas A. Reh. Blimp1 (Prdm1) prevents re-specification of photoreceptors into retinal bipolar cells by restricting competence. *Developmental Biology*, 384(2):194–204, dec 2013.
- [30] Isabel Y Buchsbaum, Pavel Kielkowski, Grazia Giorgio, Adam C O’Neill, Rossella Di Giaimo, Christina Kyrousi, Shahryar Khattak, Stephan A Sieber, Stephen P Robertson, and Silvia Cappello. ECE2 regulates neurogenesis and neuronal migration during human cortical development. *EMBO reports*, 21(5):e48204, may 2020.

- [31] Margit Burmeister, Jakub Novak, Mei-ying Liang, Sharmila Basu, Lynda Ploder, Norman L Hawes, Danka Vidgen, Frank Hoover, Daniel Goldman, Vitauts I Kalnins, Thomas H Roderick, Benjamin A Taylor, Mark H Hankin, and Roderick R McInnes. Ocular retardation mouse caused by Chx10 homeobox null allele: impaired retinal progenitor proliferation and bipolar cell differentiation. *Nature genetics*, 12(April):376–384, 1996.
- [32] Elizabeth E Capowski, Kayvan Samimi, Steven J Mayerl, M Joseph Phillips, Isabel Pinilla, Sara E Howden, Jishnu Saha, Alex D Jansen, Kimberly L Edwards, Lindsey D Jager, Katherine Barlow, Rasa Valiauga, Zachary Erlichman, Anna Hagstrom, Divya Sinha, Valentin M Sluch, Xitiz Chamling, Donald J Zack, Melissa C Skala, and David M Gamm. Reproducibility and staging of 3D human retinal organoids across multiple pluripotent stem cell lines. *Development (Cambridge, England)*, 146(1):dev171686, jan 2019.
- [33] Lázaro Centanin and Joachim Wittbrodt. Retinal neurogenesis. *Development*, 141(2):241–244, jan 2014.
- [34] Constance L. Cepko, Christopher P. Austin, Xianjie Yang, Macrene Alexiades, and Diala Ezzeddine. Cell fate determination in the vertebrate retina. *Proceedings of the National Academy of Sciences*, 93(2):589–595, jan 1996.
- [35] Le Chang, Tobias Breuninger, and Thomas Euler. Chromatic Coding from Cone-type Unselective Circuits in the Mouse Retina. *Neuron*, 77(3):559–571, feb 2013.
- [36] Jichao Chen, Amir Rattner, and Jeremy Nathans. The Rod Photoreceptor-Specific Nuclear Receptor Nr2e3 Represses Transcription of Multiple Cone-Specific Genes. *Journal of Neuroscience*, 25(1):118–129, jan 2005.
- [37] Shan Chen and Wei Li. A color-coding amacrine cell may provide a blue-Off signal in a mammalian retina. *Nature Neuroscience*, 15(7):954–956, 2012.
- [38] Valeria Chichagova, Birthe Dorgau, Majed Felemban, Maria Georgiou, Lyle Armstrong, and Majlinda Lako. Differentiation of Retinal Organoids from Human Pluripotent Stem Cells. *Current Protocols in Stem Cell Biology*, 50(1):1–11, 2019.
- [39] Valeria Chichagova, Gerrit Hilgen, Ali Ghareeb, Maria Georgiou, Madeleine Carter, Evelyn Sernagor, Majlinda Lako, and Lyle Armstrong. Human iPSC differentiation to retinal organoids in response to IGF1 and BMP4 activation is line- and method-dependent. *STEM CELLS*, nov 2019.
- [40] Jinwook Choi, Elhadi Iich, and Joo Hyeon Lee. Organogenesis of adult lung in a dish: Differentiation, disease and therapy. *Developmental biology*, 420(2):278–286, dec 2016.

- [41] Robert L. Chow, Bela Volgyi, Rachel K. Szilard, David Ng, Colin McKerlie, Stewart A. Bloomfield, David G. Birch, and Roderick R. McInnes. Control of late off-center cone bipolar cell differentiation and visual signaling by the homeobox gene *Vsx1*. *Proceedings of the National Academy of Sciences of the United States of America*, 101(6):1754–1759, feb 2004.
- [42] Bradley M. Colquitt, William E. Allen, Gilad Barnea, and Stavros Lomvardas. Alteration of genic 5-hydroxymethylcytosine patterning in olfactory neurons correlates with changes in gene expression and cell identity. *Proceedings of the National Academy of Sciences of the United States of America*, 110(36):14682–14687, sep 2013.
- [43] Joseph C. Corbo and Constance L. Cepko. A Hybrid Photoreceptor Expressing Both Rod and Cone Genes in a Mouse Model of Enhanced S-Cone Syndrome. *PLoS Genetics*, 1(2):0140–0153, 2005.
- [44] Ximena Corso-Díaz, Catherine Jaeger, Vijender Chaitankar, and Anand Swaroop. Epigenetic Control of Gene Regulation during Development and Disease: A View from the Retina. *Progress in retinal and eye research*, 65:1, jul 2018.
- [45] Cameron S. Cowan, Magdalena Renner, Martina De Gennaro, Brigitte Gross-Scherf, David Goldblum, Yanyan Hou, Martin Munz, Tiago M. Rodrigues, Jacek Krol, Tamas Szikra, Rachel Cuttat, Annick Waldt, Panagiotis Papasaikas, Roland Diggelmann, Claudia P. Patino-Alvarez, Patricia Galliker, Stefan E. Spirig, Dinko Pavlinic, Nadine Gerber-Hollbach, Sven Schuierer, Aldin Srdanovic, Marton Balogh, Riccardo Panero, Akos Kusnyerik, Arnold Szabo, Michael B. Stadler, Selim Orgül, Simone Picelli, Pascal W. Hasler, Andreas Hierlemann, Hendrik P.N. Scholl, Guglielmo Roma, Florian Nigsch, and Botond Roska. Cell Types of the Human Retina and Its Organoids at Single-Cell Resolution. *Cell*, 182(6):1623–1640.e34, sep 2020.
- [46] Cameron S Cowan, Magdalena Renner, Brigitte Gross-Scherf, David Goldblum, Martin Munz, Jacek Krol, Tamas Szikra, Panagiotis Papasaikas, Rachel Cuttat, Annick Waldt, Roland Diggelmann, Claudia P Patino-Alvarez, Nadine Gerber-Hollbach, Sven Schuierer, Yanyan Hou, Aldin Srdanovic, Marton Balogh, Riccardo Panero, Pascal W Hasler, Akos Kusnyerik, Arnold Szabo, Michael B Stadler, Selim Orgül, Andreas Hierlemann, Hendrik P N Scholl, Guglielmo Roma, Florian Nigsch, and Botond Roska. Cell types of the human retina and its organoids at single-cell resolution: developmental convergence, transcriptomic identity, and disease map.
- [47] Dennis Dacey, Orin S. Packer, Lisa Diller, David Brainard, Beth Peterson, and Barry Lee. Center surround receptive field structure of cone bipolar cells in primate retina. *Vision Research*, 40(14):1801–1811, jun 2000.

- [48] Jimmy de Melo and Seth Blackshaw. In vivo electroporation of developing mouse retina. *Journal of Visualized Experiments*, (52), 2011.
- [49] Filippo Del Bene, Ann M Wehman, Brian A Link, and Herwig Baier. Regulation of neurogenesis by interkinetic nuclear migration through an apical-basal notch gradient. *Cell*, 134(6):1055–1065, sep 2008.
- [50] Jamie E. DeNizio, Blaine J. Dow, Juan C. Serrano, Uday Ghanty, Alexander C. Drohat, and Rahul M. Kohli. TET-TDG active DNA demethylation at CpG and non-CpG sites. *Journal of molecular biology*, 433(8):166877, apr 2021.
- [51] Daniel J. Denman, Jennifer A. Luviano, Douglas R. Ollerenshaw, Sissy Cross, Derric Williams, Michael A. Buice, Shawn R. Olsen, and R. Clay Reid. Mouse color and wavelength-specific luminance contrast sensitivity are non- uniform across visual space. *eLife*, 7, jan 2018.
- [52] Annina Denoth-Lippuner, Lars N. Royall, Daniel Gonzalez-Bohorquez, Diana Machado, and Sebastian Jessberger. Injection and electroporation of plasmid DNA into human cortical organoids. *STAR Protocols*, 3(1):101129, mar 2022.
- [53] Steven H. DeVries, Xiaofeng Qi, Robert Smith, Walter Makous, and Peter Sterling. Electrical Coupling between Mammalian Cones. *Current Biology*, 12(22):1900–1907, nov 2002.
- [54] Jesse R. Dixon, David U. Gorkin, and Bing Ren. Chromatin Domains: The Unit of Chromosome Organization. *Molecular Cell*, 62(5):668–680, jun 2016.
- [55] Alexander Dobin, Carrie A. Davis, Felix Schlesinger, Jorg Drenkow, Chris Zaleski, Sonali Jha, Philippe Batut, Mark Chaisson, and Thomas R. Gingeras. STAR: ultrafast universal RNA-seq aligner. *Bioinformatics*, 29(1):15–21, jan 2013.
- [56] Xuhui Dong, Hua Yang, Xiangtian Zhou, Xiaoling Xie, Dongliang Yu, Luming Guo, Mei Xu, Wenjun Zhang, Guoqing Liang, and Lin Gan. LIM-Homeodomain Transcription Factor LHX4 Is Required for the Differentiation of Retinal Rod Bipolar Cells and OFF-Cone Bipolar Subtypes. *Cell Reports*, 32(11):108144, sep 2020.
- [57] Birthe Dorgau, Maria Georgiou, Alexander Chaudhary, Marina Moya-Molina, Joseph Collin, Rachel Queen, Gerrit Hilgen, Tracey Davey, Philip Hewitt, Michael Schmitt, Stefan Kustermann, Francois Pognan, David H. Steel, Evelyne Sernagor, Lyle Armstrong, and Majlinda Lako. Human Retinal Organoids Provide a Suitable Tool for Toxicological Investigations: A Comprehensive Validation Using Drugs and Compounds Affecting the Retina. *Stem Cells Translational Medicine*, 11(2):159–177, mar 2022.

- [58] Kimberley M. Dorval, Brian P. Bobechko, Hiroki Fujieda, Shiming Chen, Don J. Zack, and Rod Bremner. CHX10 targets a subset of photoreceptor genes. *Journal of Biological Chemistry*, 281(2):744–751, jan 2006.
- [59] Galina Dvorientchikova, Rajeev J. Seemungal, and Dmitry Ivanov. DNA Methylation Dynamics During the Differentiation of Retinal Progenitor Cells Into Retinal Neurons Reveal a Role for the DNA Demethylation Pathway. *Frontiers in Molecular Neuroscience*, 12:182, jul 2019.
- [60] Mototsugu Eiraku, Nozomu Takata, Hiroki Ishibashi, Masako Kawada, Eriko Sakakura, Satoru Okuda, Kiyotoshi Sekiguchi, Taiji Adachi, and Yoshiki Sasai. Self-organizing optic-cup morphogenesis in three-dimensional culture. *Nature*, 472(7341):51–58, 2011.
- [61] Bjorn Ekesten, Peter Gouras, and Suichi Yamamoto. Cone inputs to murine retinal ganglion cells. *Vision Research*, 40(19):2573–2577, sep 2000.
- [62] Kiara C. Eldred, Sarah E. Hadyniak, Katarzyna A. Hussey, Boris Brenerman, Ping Wu Zhang, Xitiz Chamling, Valentin M. Sluch, Derek S. Welsbie, Samer Hattar, James Taylor, Karl Wahlin, Donald J. Zack, and Robert J. Johnston. Thyroid hormone signaling specifies cone subtypes in human retinal organoids. *Science*, 362(6411), oct 2018.
- [63] Mark M. Emerson, Natalia Surzenko, Jillian J. Goetz, Jeffrey Trimarchi, and Constance L. Cepko. *Otx2* and *Onecut1* promote the fates of cone photoreceptors and horizontal cells and repress rod photoreceptors. *Developmental Cell*, 26(1):59–72, 2013.
- [64] Nil Emre, Jason G. Vidal, Jeanne Elia, Eric D. O’Connor, Rosanto I. Paramban, Michael P. Hefferan, Roman Navarro, Danielle S. Goldberg, Nissi M. Varki, Martin Marsala, and Christian T. Carson. The ROCK Inhibitor Y-27632 Improves Recovery of Human Embryonic Stem Cells after Fluorescence-Activated Cell Sorting with Multiple Cell Surface Markers. *PLOS ONE*, 5(8):e12148, 2010.
- [65] Thomas Euler, Silke Haverkamp, Timm Schubert, and Tom Baden. Retinal bipolar cells: elementary building blocks of vision. *Nature Reviews Neuroscience* 2014 15:8, 15(8):507–519, jul 2014.
- [66] Thomas Euler, Horst Schneider, and Heinz Wässle. Glutamate responses of bipolar cells in a slice preparation of the rat retina. *Journal of Neuroscience*, 16(9):2934–2944, 1996.
- [67] Yana Feodorova, Mirja Koch, Sebastian Bultman, Stylianos Michalakis, and Irina Solovei. Quick and reliable method for retina dissociation and separation of rod photoreceptor perikarya from adult mice. *MethodsX*, 2:39–46, 2015.
- [68] Clarisse M. Fligor, Kirstin B. Langer, Akshayalakshmi Sridhar, Yuan Ren, Priya K. Shields, Michael C. Edler, Sarah K. Ohlemacher, Valentin M. Sluch, Donald J. Zack,

- Chi Zhang, Daniel M. Suter, and Jason S. Meyer. Three-Dimensional Retinal Organoids Facilitate the Investigation of Retinal Ganglion Cell Development, Organization and Neurite Outgrowth from Human Pluripotent Stem Cells. *Scientific Reports*, 8(1):1–14, 2018.
- [69] Masayuki Fujii, Mami Matano, Kosaku Nanki, and Toshiro Sato. Efficient genetic engineering of human intestinal organoids using electroporation. *Nature Protocols*, 10(10):1474–1485, 2015.
- [70] Takahisa Furukawa, Eric M. Morrow, and Constance L. Cepko. Crx, a Novel otx-like Homeobox Gene, Shows Photoreceptor-Specific Expression and Regulates Photoreceptor Differentiation. *Cell*, 91(4):531–541, nov 1997.
- [71] Krishna K Ghosh, Sascha Bujan, Silke Haverkamp, Andreas Feigenspan, and Heinz Wässle. Types of bipolar cells in the mouse retina. *Journal of Comparative Neurology*, 469(1):70–82, 2004.
- [72] Anika Glaschke, Martin Glösmann, and Leo Peichl. Developmental changes of cone opsin expression but not retinal morphology in the hypothyroid Pax8 knockout mouse. *Investigative Ophthalmology and Visual Science*, 51(3):1719–1727, mar 2010.
- [73] Anika Glaschke, Jessica Weiland, Domenico del Turco, Marianne Steiner, Leo Peichl, and Martin Glösmann. Thyroid hormone controls cone opsin expression in the retina of adult rodents. *Journal of Neuroscience*, 31(13):4844–4851, mar 2011.
- [74] Mary Grace Goll and Timothy H. Bestor. Eukaryotic cytosine methyltransferases. *Annual Review of Biochemistry*, 74:481–514, 2005.
- [75] Noah B Goodson, Michael A Kaufman, Ko U Park, and Joseph A Brzezinski. Simultaneous deletion of Prdm1 and Vsx2 enhancers in the retina alters photoreceptor and bipolar cell fate specification, yet differs from deleting both genes. 2020.
- [76] Noah B. Goodson, Ko U. Park, Jason S. Silver, Vince A. Chiodo, William W. Hauswirth, and Joseph A. Brzezinski. Prdm1 overexpression causes a photoreceptor fate-shift in nascent, but not mature, bipolar cells. *Developmental biology*, 464(2):111, aug 2020.
- [77] Justin J. Grassmeyer and Wallace B. Thoreson. Synaptic ribbon active zones in cone photoreceptors operate independently from one another. *Frontiers in Cellular Neuroscience*, 11:198, jul 2017.
- [78] Jochen Graw. Eye Development. *Current Topics in Developmental Biology*, 90(C):343–386, jan 2010.
- [79] Sergei Grebenyuk and Adrian Ranga. Engineering Organoid Vascularization. *Frontiers in Bioengineering and Biotechnology*, 7(MAR):39, 2019.

- [80] Tian Peng Gu, Fan Guo, Hui Yang, Hai Ping Wu, Gui Fang Xu, Wei Liu, Zhi Guo Xie, Linyu Shi, Xinyi He, Seung Gi Jin, Khursheed Iqbal, Yujiang Geno Shi, Zixin Deng, Piroska E. Szabó, Gerd P. Pfeifer, Jinsong Li, and Guo Liang Xu. The role of Tet3 DNA dioxygenase in epigenetic reprogramming by oocytes. *Nature*, 477(7366):606–612, 2011.
- [81] Wenyue Guan, Romain Guyot, Jacques Samarut, Frédéric Flamant, Jiemin Wong, and Karine Cécile Gauthier. Methylcytosine dioxygenase TET3 interacts with thyroid hormone nuclear receptors and stabilizes their association to chromatin. *Proceedings of the National Academy of Sciences of the United States of America*, 114(31):8229–8234, aug 2017.
- [82] Michael H. Guerra, Thangal Yumnamcha, Lalit P. Singh, and Ahmed S. Ibrahim. Relative Contribution of Different Mitochondrial Oxidative Phosphorylation Components to the Retinal Pigment Epithelium Barrier Function: Implications for RPE-Related Retinal Diseases. *International Journal of Molecular Sciences 2021, Vol. 22, Page 8130*, 22(15):8130, jul 2021.
- [83] Laszlo Hackler, Jun Wan, Anand Swaroop, Jiang Qian, and Donald J. Zack. MicroRNA Profile of the Developing Mouse Retina. *Investigative Ophthalmology Visual Science*, 51(4):1823–1831, apr 2010.
- [84] Sarah E. Hadyniak, Kiara C. Eldred, Boris Brenerman, Katarzyna A. Hussey, Joanna F. D. Hagen, Rajiv C. McCoy, Michael E. G. Sauria, James A. Kuchenbecker, Thomas Reh, Ian Glass, Maureen Neitz, Jay Neitz, James Taylor, and Robert J. Johnston. Spatiotemporal specification of green and red cones in human retinas and organoids. *bioRxiv*, page 2021.03.30.437763, dec 2022.
- [85] David L. Haggerty, Gregory G. Grecco, Kaitlin C. Reeves, and Brady Atwood. Adeno-Associated Viral Vectors in Neuroscience Research. *Molecular Therapy - Methods Clinical Development*, 17:69–82, jun 2020.
- [86] Maria A. Hahn, Runxiang Qiu, Xiwei Wu, Arthur X. Li, Heying Zhang, Jun Wang, Jonathan Jui, Seung-Gi Jin, Yong Jiang, Gerd P. Pfeifer, and Qiang Lu. Dynamics of 5-Hydroxymethylcytosine and Chromatin Marks in Mammalian Neurogenesis. *Cell Reports*, 3(2):291–300, feb 2013.
- [87] Dean Hallam, Gerrit Hilgen, Birthe Dorgau, Lili Zhu, Min Yu, Sanja Bojic, Philip Hewitt, Michael Schmitt, Marianne Uteng, Stefan Kustermann, David Steel, Mike Nicholds, Robert Thomas, Achim Treumann, Andrew Porter, Evelyne Sernagor, Lyle Armstrong, and Majlinda Lako. Human-Induced Pluripotent Stem Cells Generate Light Responsive Retinal Organoids with Variable and Nutrient-Dependent Efficiency. *Stem Cells*, 36(10):1535–1551, oct 2018.

- [88] Haider M. Hassan, Bart Kolendowski, Majdina Isovica, Kerstin Bose, Helen J. Dranse, Arthur V. Sampaio, T. Michael Underhill, and Joseph Torchia. Regulation of Active DNA Demethylation through RAR-Mediated Recruitment of a TET/TDG Complex. *Cell Reports*, 19(8):1685–1697, may 2017.
- [89] Silke Haverkamp, Krishna K Ghosh, Arlene A Hirano, and Heinz Wässle. Immunocytochemical description of five bipolar cell types of the mouse retina. *Journal of Comparative Neurology*, 455(4):463–476, 2003.
- [90] Silke Haverkamp, Heinz Wässle, Jens Duebel, Thomas Kuner, George J. Augustine, Guoping Feng, and Thomas Euler. The primordial, blue-cone color system of the mouse retina. *Journal of Neuroscience*, 25(22):5438–5445, jun 2005.
- [91] Yu Fei He, Bin Zhong Li, Zheng Li, Peng Liu, Yang Wang, Qingyu Tang, Jianping Ding, Yingying Jia, Zhangcheng Chen, N. Li, Yan Sun, Xiuxue Li, Qing Dai, Chun Xiao Song, Kangling Zhang, Chuan He, and Guo Liang Xu. Tet-Mediated Formation of 5-Carboxylecytosine and Its Excision by TDG in Mammalian DNA. *Science (New York, N.Y.)*, 333(6047):1303, sep 2011.
- [92] Whitney Heavner and Larysa Pevny. Eye Development and Retinogenesis. *Cold Spring Harbor Perspectives in Biology*, 4(12), dec 2012.
- [93] Ruth Heidelberger, Wallace B. Thoreson, and Paul Witkovsky. Synaptic transmission at retinal ribbon synapses. *Progress in Retinal and Eye Research*, 24(6):682–720, nov 2005.
- [94] Moritz Helmstaedter, Kevin L. Briggman, Srinivas C. Turaga, Viren Jain, H. Sebastian Seung, and Winfried Denk. Connectomic reconstruction of the inner plexiform layer in the mouse retina. *Nature* 2013 500:7461, 500(7461):168–174, aug 2013.
- [95] Andrea Hermann, Rachna Goyal, and Albert Jeltsch. The Dnmt1 DNA-(cytosine-C5)-methyltransferase methylates DNA processively with high preference for hemimethylated target sites. *Journal of Biological Chemistry*, 279(46):48350–48359, nov 2004.
- [96] Jörg Höhfeld, Thomas Benzing, Wilhelm Bloch, Dieter O Fürst, Sebastian Gehlert, Michael Hesse, Bernd Hoffmann, Thorsten Hoppe, Pitter F Huesgen, Maja Köhn, Waldemar Kolanus, Rudolf Merkel, Carien M Niessen, Wojciech Pokrzywa, Markus M Rinschen, Dagmar Wachten, and Bettina Warscheid. Maintaining proteostasis under mechanical stress. *EMBO reports*, 22(8):e52507, aug 2021.
- [97] R. Holliday and J. E. Pugh. DNA Modification Mechanisms and Gene Activity During Development. *Science*, 187(4173):226–232, jan 1975.

- [98] Lars C. Holzhausen, Alaron A. Lewis, Kimberly K. Cheong, and Susan E. Brockerhoff. Differential role for synaptojanin 1 in rod and cone photoreceptors. *Journal of Comparative Neurology*, 517(5):633–644, dec 2009.
- [99] Timothy Alexander Hore, Ferdinand Von Meyenn, Mirunalini Ravichandran, Martin Bachman, Gabriella Ficz, David Oxley, Fátima Santos, Shankar Balasubramanian, Tomasz P. Jurkowski, and Wolf Reik. Retinol and ascorbate drive erasure of Epigenetic memory and enhance reprogramming to naïve pluripotency by complementary mechanisms. *Proceedings of the National Academy of Sciences of the United States of America*, 113(43):12202–12207, oct 2016.
- [100] Eric P. Hornstein, Jan Verweij, Peter H. Li, and Julie L. Schnapf. Gap-Junctional Coupling and Absolute Sensitivity of Photoreceptors in Macaque Retina. *Journal of Neuroscience*, 25(48):11201–11209, nov 2005.
- [101] D Hotchkiss. THE QUANTITATIVE SEPARATION OF PURINES , SND NUCLEOSIDES BY The separation of amino acid mixtures by migration with organic solvents in filter paper has been successfully accomplished by many workers since it was first described by Consden , Gordon , and . (i).
- [102] Shaohui Hu, Jun Wan, Yijing Su, Qifeng Song, Yaxue Zeng, Ha Nam Nguyen, Jaehoon Shin, Eric Cox, Hee Sool Rho, Crystal Woodard, Shuli Xia, Shuang Liu, Huibin Lyu, Guo Li Ming, Herschel Wade, Hongjun Song, Jiang Qian, and Heng Zhu. DNA methylation presents distinct binding sites for human transcription factors. *eLife*, 2013(2), sep 2013.
- [103] David M. Hunt, Livia S. Carvalho, Jill A. Cowing, and Wayne L. Davies. Evolution and spectral tuning of visual pigments in birds and mammals. *Philosophical Transactions of the Royal Society B: Biological Sciences*, 364(1531):2941–2955, oct 2009.
- [104] George A. Hyatt, Ellen A. Schmitt, James M. Fadool, and John E. Dowling. Retinoic acid alters photoreceptor development in vivo. *Proceedings of the National Academy of Sciences of the United States of America*, 93(23):13298, nov 1996.
- [105] Norianne T. Ingram, Gordon L. Fain, and Alapakkam P. Sampath. Elevated energy requirement of cone photoreceptors. *Proceedings of the National Academy of Sciences of the United States of America*, 117(32):19599–19603, aug 2020.
- [106] Shinsuke Ito, Li Shen, Qing Dai, Susan C. Wu, Leonard B. Collins, James A. Swenberg, Chuan He, and Yi Zhang. Tet proteins can convert 5-methylcytosine to 5-formylcytosine and 5-carboxylcytosine. *Science (New York, N.Y.)*, 333(6047):1300, sep 2011.

- [107] Mario Iurlaro, Gabriella Ficz, David Oxley, Eun Ang Raiber, Martin Bachman, Michael J. Booth, Simon Andrews, Shankar Balasubramanian, and Wolf Reik. A screen for hydroxymethylcytosine and formylcytosine binding proteins suggests functions in transcription and chromatin regulation. *Genome Biology*, 14(10):1–11, 2013.
- [108] Gerald H. Jacobs, Gary A. Williams, Hugh Cahill, and Jeremy Nathans. Emergence of novel color vision in mice engineered to express a human cone photopigment. *Science*, 315(5819):1723–1725, mar 2007.
- [109] Gerald H. Jacobs, Gary A. Williams, and John A. Fenwick. Influence of cone pigment coexpression on spectral sensitivity and color vision in the mouse. *Vision Research*, 44(14):1615–1622, jun 2004.
- [110] Rudolf Jaenisch and Adrian Bird. Epigenetic regulation of gene expression: How the genome integrates intrinsic and environmental signals. *Nature Genetics*, 33(3S):245–254, 2003.
- [111] Sylvie Janssens, Michael Schotsaert, Rahul Karnik, Vinod Balasubramanian, Marion Dejosez, Alexander Meissner, Adolfo García-Sastre, and Thomas P. Zwaka. Zika Virus Alters DNA Methylation of Neural Genes in an Organoid Model of the Developing Human Brain. *mSystems*, 3(1), feb 2018.
- [112] Awais Javed, Pierre Mattar, Suying Lu, Kamil Kruczek, Magdalena Kloc, Anai Gonzalez-Cordero, Rod Bremner, Robin R Ali, and Michel Cayouette. Pou2f1 and Pou2f2 cooperate to control the timing of cone photoreceptor production in the developing mouse retina. 2020.
- [113] Seung Gi Jin, Xiwei Wu, Arthur X. Li, and Gerd P. Pfeifer. Genomic mapping of 5-hydroxymethylcytosine in the human brain. *Nucleic Acids Research*, 39(12):5015–5024, jul 2011.
- [114] Seung Gi Jin, Zhi Min Zhang, Thomas L. Dunwell, Matthew R. Harter, Xiwei Wu, Jennifer Johnson, Zheng Li, Jiancheng Liu, Piroska E. Szabó, Qiang Lu, Guo liang Xu, Jikui Song, and Gerd P. Pfeifer. Tet3 reads 5-carboxylcytosine through its CXXC domain and is a potential guardian against neurodegeneration. *Cell reports*, 14(3):493, jan 2016.
- [115] Maximilian Joesch and Markus Meister. A neuronal circuit for colour vision based on rod–cone opponency. *Nature* 2016 532:7598, 532(7598):236–239, apr 2016.
- [116] Jost B. Jonas, Ulrike Schneider, and Gottfried O.H. Naumann. Count and density of human retinal photoreceptors. *Graefe’s Archive for Clinical and Experimental Ophthalmology*, 230(6):505–510, oct 1992.

- [117] Peter A. Jones. Functions of DNA methylation: islands, start sites, gene bodies and beyond. *Nature Reviews Genetics* 2012 13:7, 13(7):484–492, may 2012.
- [118] Joseph A. Brzezinski, Deepak A. Lamba, and Thomas A. Reh. Blimp1 controls photoreceptor versus bipolar cell fate choice during retinal development. 2010.
- [119] Patricia R. Jusuf, Paul R. Martin, and Ulrike Grünert. Synaptic connectivity in the midganglion cell pathway of primate central retina. *Journal of Comparative Neurology*, 494(2):260–274, jan 2006.
- [120] Alyssa Kallman, Elizabeth E. Capowski, Jie Wang, Aniruddha M. Kaushik, Alex D. Jansen, Kimberly L. Edwards, Liben Chen, Cynthia A. Berlinicke, M. Joseph Phillips, Eric A. Pierce, Jiang Qian, Tza Huei Wang, David M. Gamm, and Donald J. Zack. Investigating cone photoreceptor development using patient-derived NRL null retinal organoids. *Communications biology*, 3(1):82, 2020.
- [121] Mark A. Kanow, Michelle M. Giarmarco, Connor S.R. Jankowski, Kristine Tsantilas, Abbi L. Engel, Jianhai Du, Jonathan D. Linton, Christopher C. Farnsworth, Stephanie R. Sloat, Austin Rountree, Ian R. Sweet, Ken J. Lindsay, Edward D. Parker, Susan E. Brockhoff, Martin Sadilek, Jennifer R. Chao, and James B. Hurley. Biochemical adaptations of the retina and retinal pigment epithelium support a metabolic ecosystem in the vertebrate eye. *eLife*, 6, sep 2017.
- [122] Jeremy N Kay, Karin C Finger-Baier, Tobias Roeser, Wendy Staub, and Herwig Baier. Retinal Ganglion Cell Genesis Requires lakritz, a Zebrafish atonal Homolog. *Neuron*, 30(3):725–736, 2001.
- [123] Matthew W. Kellinger, Chun Xiao Song, Jenny Chong, Xing Yu Lu, Chuan He, and Dong Wang. 5-formylcytosine and 5-carboxylcytosine reduce the rate and substrate specificity of RNA polymerase II transcription. *Nature Structural and Molecular Biology*, 19(8):831–833, 2012.
- [124] Hanen Khabou, Marcela Garita-Hernandez, Antoine Chaffiol, Sacha Reichman, Céline Jaillard, Elena Brazhnikova, Stéphane Bertin, Valérie Forster, Mélissa Desrosiers, Céline Winckler, Olivier Goureau, Serge Picaud, Jens Duebel, José Alain Sahel, and Deniz Dalkara. Noninvasive gene delivery to foveal cones for vision restoration. *JCI Insight*, 3(2), jan 2018.
- [125] Tarang Khare, Shraddha Pai, Karolis Koncivicius, Mrinal Pal, Edita Kriukiene, Zita Litukeviciute, Manuel Irimia, Peixin Jia, Carolyn Ptak, Menghang Xia, Raymond Tice, Mamoru Tochigi, Solange Moréra, Anaies Nazarians, Denise Belsham, Albert H.C. Wong, Benjamin J. Blencowe, Sun Chong Wang, Philipp Kapranov, Rafal Kustra, Viviane Labrie, Saulius Klimasauskas, and Arturas Petronis. 5-hmC in the brain is abundant

- in synaptic genes and shows differences at the exon-intron boundary. *Nature Structural and Molecular Biology*, 19(10):1037–1044, 2012.
- [126] Douglas S. Kim, Sarah E. Ross, Jeffrey M. Trimarchi, John Aach, Michael E. Greenberg, and Constance L. Cepko. Identification of molecular markers of bipolar cells in the murine retina. *The Journal of Comparative Neurology*, 507(5):1795, apr 2008.
- [127] Mirang Kim, Young Kyu Park, Tae Wook Kang, Sang Hun Lee, Yong Hee Rhee, Jong Lyul Park, Hee Jin Kim, Daeyoup Lee, Doheon Lee, Seon Young Kim, and Yong Sung Kim. Dynamic changes in DNA methylation and hydroxymethylation when hES cells undergo differentiation toward a neuronal lineage. *Human Molecular Genetics*, 23(3):657–667, feb 2014.
- [128] Sangbae Kim, Albert Lowe, Rachayata Dharmat, Seunghoon Lee, Leah A. Owen, Jun Wang, Akbar Shakoor, Yumei Li, Denise J. Morgan, Andre A. Hejazi, Ales Cvekl, Margaret M. DeAngelis, Z. Jimmy Zhou, Rui Chen, and Wei Liu. Generation, transcriptome profiling, and functional validation of cone-rich human retinal organoids. *Proceedings of the National Academy of Sciences of the United States of America*, 166(22):10824–10833, may 2019.
- [129] Warren T. Kim, Sunghoe Chang, Laurie Daniell, Ottavio Cremona, Gilbert Di Paolo, and Pietro De Camilli. Delayed reentry of recycling vesicles into the fusion-competent synaptic vesicle pool in synaptotagmin 1 knockout mice. *Proceedings of the National Academy of Sciences*, 99(26):17143–17148, dec 2002.
- [130] Lucie Klimova, Jitka Lachova, Ondrej Machon, Radislav Sedlacek, and Zbynek Kozmik. Generation of mRx-Cre Transgenic Mouse Line for Efficient Conditional Gene Deletion in Early Retinal Progenitors. *PLoS ONE*, 8(5):e63029, may 2013.
- [131] Karl Klug, Steve Herr, Ivy Tran Ngo, Peter Sterling, and Stan Schein. Macaque Retina Contains an S-Cone OFF Midget Pathway. *Journal of Neuroscience*, 23(30):9881–9887, oct 2003.
- [132] Chieko Koike, Akihiro Nishida, Shinji Ueno, Hiromitsu Saito, Rikako Sanuki, Shigeru Sato, Akiko Furukawa, Shinichi Aizawa, Isao Matsuo, Noboru Suzuki, Mineo Kondo, and Takahisa Furukawa. Functional Roles of Otx2 Transcription Factor in Postnatal Mouse Retinal Development. *Molecular and Cellular Biology*, 27(23):8318–8329, dec 2007.
- [133] Chieko Koike, Takehisa Obara, Yoshitsugu Uriu, Tomohiro Numata, Rikako Sanuki, Kentarou Miyata, Toshiyuki Koyasu, Shinji Ueno, Kazuo Funabiki, Akiko Tani, Hiroshi Ueda, Mineo Kondo, Yasuo Mori, Masao Tachibana, and Takahisa Furukawa. TRPM1

- is a component of the retinal ON bipolar cell transduction channel in the mGluR6 cascade. *Proceedings of the National Academy of Sciences of the United States of America*, 107(1):332–337, dec 2010.
- [134] Peppi Koivunen and Tuomas Laukka. The TET enzymes. *Cellular and Molecular Life Sciences*, 75(8):1339–1348, apr 2018.
- [135] Friedrich Kretschmer, Viola Kretschmer, Vincent P. Kunze, and Jutta Kretzberg. OMR-Arena: Automated Measurement and Stimulation System to Determine Mouse Visual Thresholds Based on Optomotor Responses. *PLOS ONE*, 8(11):e78058, nov 2013.
- [136] Kamil Kruczek and Anand Swaroop. Pluripotent stem cell-derived retinal organoids for disease modeling and development of therapies. *Stem Cells*, 38(10):1206–1215, oct 2020.
- [137] Methaq Hadi Lafta and Lekshmi Gangadhar. RNBeads 2.0: Comprehensive analysis of DNA methylation data. *Annals of Tropical Medicine and Public Health*, 19(Special Issue):2003–2019, 2019.
- [138] Mounia Lagha, Jacques P. Bothma, and Michael Levine. Mechanisms of transcriptional precision in animal development. *Trends in Genetics*, 28(8):409–416, aug 2012.
- [139] Madeline A. Lancaster, Magdalena Renner, Carol-Anne Martin, Daniel Wenzel, Louise S. Bicknell, Matthew E. Hurles, Tessa Homfray, Josef M. Penninger, Andrew P. Jackson, and Juergen A. Knoblich. Cerebral organoids model human brain development and microcephaly. *Nature*, 501(7467):373–379, sep 2013.
- [140] M F Land and R D Fernald. The Evolution of Eyes. *Annual Review of Neuroscience*, 15(1):1–29, 1992.
- [141] Marie France Langlois, Kerstin Zanger, Tsuyoshi Monden, Joshua D. Safer, Anthony N. Hollenberg, and Fredric E. Wondisford. A unique role of the β -2 thyroid hormone receptor isoform in negative regulation by thyroid hormone: Mapping of a novel amino-terminal domain important for ligand-independent activation. *Journal of Biological Chemistry*, 272(40):24927–24933, oct 1997.
- [142] Thierry Langlois, Barbara Da Costa Reis Monte-Mor, Gaëlle Lenglet, Nathalie Droin, Caroline Marty, Jean Pierre Le Couédic, Carole Almiere, Nathalie Auger, Thomas Mercher, François Delhommeau, Jesper Christensen, Kristian Helin, Najet Debili, François Fuks, Olivier A. Bernard, Eric Solary, William Vainchenker, and Isabelle Plo. TET2 deficiency inhibits mesoderm and hematopoietic differentiation in human embryonic stem cells. *Stem Cells*, 32(8):2084–2097, 2014.

- [143] Tuomas Laukka, Christopher J. Mariani, Tuukka Ihanola, John Z. Cao, Juho Hokkanen, William G. Kaelin, Lucy A. Godley, and Peppi Koivunen. Fumarate and Succinate Regulate Expression of Hypoxia-inducible Genes via TET Enzymes. *The Journal of Biological Chemistry*, 291(8):4256, feb 2016.
- [144] Moyra Lawrence, Sylvain Daujat, and Robert Schneider. Lateral Thinking: How Histone Modifications Regulate Gene Expression. *Trends in Genetics*, 32(1):42–56, jan 2016.
- [145] Barry B. Lee, Dennis M. Dacey, Vivianne C. Smith, and Joel Pokorny. Horizontal cells reveal cone type-specific adaptation in primate retina. *Proceedings of the National Academy of Sciences of the United States of America*, 96(25):14611–14616, dec 1999.
- [146] Bo Li and Colin N. Dewey. RSEM: Accurate transcript quantification from RNA-Seq data with or without a reference genome. *BMC Bioinformatics*, 12(1):1–16, aug 2011.
- [147] En Li and Yi Zhang. DNA Methylation in Mammals. *Cold Spring Harbor Perspectives in Biology*, 6(5):19133–19134, 2014.
- [148] Guilan Li, Bingbing Xie, Liwen He, Tiancheng Zhou, Guanjie Gao, Shengxu Liu, Guangjin Pan, Jian Ge, Fuhua Peng, and Xiufeng Zhong. Generation of retinal organoids with mature rods and cones from urine-derived human induced pluripotent stem cells. *Stem Cells International*, 2018, 2018.
- [149] Peter H. Li, Jan Verweij, James H. Long, and Julie L. Schnapf. Gap-Junctional Coupling of Mammalian Rod Photoreceptors and Its Effect on Visual Detection. *Journal of Neuroscience*, 32(10):3552–3562, mar 2012.
- [150] Xuekun Li, Yujing Li, Chun Xiao Song, Hao Wu, Qing Dai, Hasan Irier, Anup K. Upadhyay, Marla Gearing, Allan I. Levey, Aparna Vasanthakumar, Lucy A. Godley, Qiang Chang, Xiaodong Cheng, Chuan He, and Peng Jin. 5-hmC-mediated epigenetic dynamics during postnatal neurodevelopment and aging. *Nature Neuroscience*, 14(12):1607–1616, 2011.
- [151] Christine Guo Lian, Yufei Xu, Craig Ceol, Feizhen Wu, Allison Larson, Karen Dresser, Wenqi Xu, Li Tan, Yeguang Hu, Qian Zhan, Chung Wei Lee, Di Hu, Bill Q. Lian, Sonja Kleffel, Yijun Yang, James Neiswender, Abraham J. Khorasani, Rui Fang, Cecilia Lezcano, Lyn M. Duncan, Richard A. Scolyer, John F. Thompson, Hojabr Kakavand, Yariv Houvras, Leonard I. Zon, Martin C. Mihm, Ursula B. Kaiser, Tobias Schatton, Bruce A. Woda, George F. Murphy, and Yujiang G. Shi. Loss of 5-hydroxymethylcytosine is an epigenetic hallmark of melanoma. *Cell*, 150(6):1135–1146, sep 2012.
- [152] Arthur Linksz. Outlines of a Theory of the Light Sense. *Archives of Ophthalmology*, 73(4):603–603, apr 1965.

- [153] Hong Liu, Paige Etter, Susan Hayes, Iwan Jones, Branden Nelson, Byron Hartman, Douglas Forrest, and Thomas A. Reh. NeuroD1 regulates expression of thyroid hormone receptor $\beta 2$ and cone opsins in the developing mouse retina. *Journal of Neuroscience*, 28(3):749–756, jan 2008.
- [154] Nan Liu, Mengxi Wang, Wen Deng, Christine S. Schmidt, Weihua Qin, Heinrich Leonhardt, and Fabio Spada. Intrinsic and Extrinsic Connections of Tet3 Dioxygenase with CXXC Zinc Finger Modules. *PLOS ONE*, 8(5):e62755, may 2013.
- [155] F J Livesey and C L Cepko. Vertebrate neural cell-fate determination: Lessons from the retina. *Nature Reviews Neuroscience*, 2(2):109–118, 2001.
- [156] Izzy Livne-Bar, Marek Pacal, Melissa C. Cheung, Mark Hankin, Judy Trogadis, Dorian Chen, Kimberley M. Dorval, and Rod Bremner. Chx10 is required to block photoreceptor differentiation but is dispensable for progenitor proliferation in the postnatal retina. *Proceedings of the National Academy of Sciences of the United States of America*, 103(13):4988–4993, mar 2006.
- [157] Izzy Livne-Bar, Marek Pacal, Melissa C. Cheung, Mark Hankin, Judy Trogadis, Dorian Chen, Kimberley M. Dorval, and Rod Bremner. Chx10 is required to block photoreceptor differentiation but is dispensable for progenitor proliferation in the postnatal retina. *Proceedings of the National Academy of Sciences of the United States of America*, 103(13):4988–4993, mar 2006.
- [158] Michael I. Love, Wolfgang Huber, and Simon Anders. Moderated estimation of fold change and dispersion for RNA-seq data with DESeq2. *Genome Biology*, 15(12):1–21, dec 2014.
- [159] Albert Lowe, Raven Harris, Punita Bhansali, Ales Cvekl, and Wei Liu. Intercellular Adhesion-Dependent Cell Survival and ROCK-Regulated Actomyosin-Driven Forces Mediate Self-Formation of a Retinal Organoid. *Stem Cell Reports*, 6(5):743–756, may 2016.
- [160] Ailing Lu, Lily Ng, Michelle Ma, Benjamin Kefas, Terry F. Davies, Arturo Hernandez, Chi Chao Chan, and Douglas Forrest. Retarded developmental expression and patterning of retinal cone opsins in hypothyroid mice. *Endocrinology*, 150(3):1536–1544, mar 2009.
- [161] Dunja Lukovic, Ana Artero Castro, Koray Dogan Kaya, Daniella Munezero, Linn Gieser, Carlota Davó-Martínez, Marta Corton, Nicolás Cuenca, Anand Swaroop, Visvanathan Ramamurthy, Carmen Ayuso, and Slaven Erceg. Retinal Organoids derived from hiPSCs of an AIPL1-LCA Patient Maintain Cytoarchitecture despite Reduced levels of Mutant AIPL1. *Scientific Reports 2020 10:1*, 10(1):1–13, mar 2020.

- [162] Samuel W Lukowski, Camden Y Lo, Alexei A Sharov, Quan Nguyen, Lyujie Fang, Sandy SC Hung, Ling Zhu, Ting Zhang, Ulrike Grünert, Tu Nguyen, Anne Senabouth, Jafar S Jabbari, Emily Welby, Jane C Sowden, Hayley S Waugh, Adrienne Mackey, Graeme Pollock, Trevor D Lamb, Peng-Yuan Wang, Alex W Hewitt, Mark C Gillies, Joseph E Powell, and Raymond CB Wong. A single-cell transcriptome atlas of the adult human retina. *The EMBO Journal*, pages 1–15, 2019.
- [163] Chongyuan Luo, Madeline A. Lancaster, Rosa Castanon, Joseph R. Nery, Juergen A. Knoblich, and Joseph R. Ecker. Cerebral Organoids Recapitulate Epigenomic Signatures of the Human Fetal Brain. *Cell Reports*, 17(12):3369–3384, dec 2016.
- [164] Ziming Luo, Chaochao Xu, Kaijing Li, Bikun Xian, Yuchun Liu, Kang Li, Ying Liu, Huifeng Rong, Mingjun Tang, Dongpeng Hu, Sijing Yang, Meifang Ye, Xiufeng Zhong, and Jian Ge. Islet1 and Brn3 Expression Pattern Study in Human Retina and hiPSC-Derived Retinal Organoid. *Stem Cells International*, 2019, 2019.
- [165] Giuseppe Lupo, Alessandro Bulfone, Massimiliano Andreazzoli, Margherita Mariani, Françoise Fougère, Gian Giacomo Consalez, Giuseppe Borsani, Jacques S. Beckmann, Giuseppina Barsacchi, Andrea Ballabio, and Sandro Banfi. A homeobox gene, *vax2*, controls the patterning of the eye dorsoventral axis. *Proceedings of the National Academy of Sciences of the United States of America*, 96(19):10729–10734, sep 1999.
- [166] Xiaohui Lv, Huihui Jiang, Yanli Liu, Xuepei Lei, and Jianwei Jiao. MicroRNA-15b promotes neurogenesis and inhibits neural progenitor proliferation by directly repressing TET3 during early neocortical development. *EMBO reports*, 15(12):1305–1314, dec 2014.
- [167] David Mahringer, Pawel Zmarz, Hiroyuki Okuno, Haruhiko Bito, and Georg B. Keller. Functional correlates of immediate early gene expression in mouse visual cortex. *Peer Community Journal*, 2:1–21, 2022.
- [168] Atanu Maiti and Alexander C. Drohat. Thymine DNA Glycosylase Can Rapidly Excise 5-Formylcytosine and 5-Carboxylcytosine: POTENTIAL IMPLICATIONS FOR ACTIVE DEMETHYLATION OF CpG SITES*. *The Journal of Biological Chemistry*, 286(41):35334, oct 2011.
- [169] Takahiko Matsuda and Constance L. Cepko. Electroporation and RNA interference in the rodent retina in vivo and in vitro. *Proceedings of the National Academy of Sciences of the United States of America*, 101(1):16–22, jan 2004.
- [170] Alikea K. Maunakea, Raman P. Nagarajan, Mikhail Bilenky, Tracy J. Ballinger, Cleatus Dsouza, Shaun D. Fouse, Brett E. Johnson, Chibo Hong, Cydney Nielsen, Yongjun

- Zhao, Gustavo Turecki, Allen Delaney, Richard Varhol, Nina Thiessen, Ksenya Shchors, Vivi M. Heine, David H. Rowitch, Xiaoyun Xing, Chris Fiore, Maximiliaan Schillebeeckx, Steven J.M. Jones, David Haussler, Marco A. Marra, Martin Hirst, Ting Wang, and Joseph F. Costello. Conserved role of intragenic DNA methylation in regulating alternative promoters. *Nature*, 466(7303):253–257, 2010.
- [171] Stephan Maxeiner, Fujun Luo, Alison Tan, Frank Schmitz, and Thomas C Südhof. How to make a synaptic ribbon: RIBEYE deletion abolishes ribbons in retinal synapses and disrupts neurotransmitter release. *The EMBO Journal*, 35(10):1098–1114, may 2016.
- [172] Alan J. Mears, Mineo Kondo, Prabodha K. Swain, Yuichiro Takada, Ronald A. Bush, Thomas L. Saunders, Paul A. Sieving, and Anand Swaroop. Nrl is required for rod photoreceptor development. *Nature Genetics* 2001 29:4, 29(4):447–452, nov 2001.
- [173] Philippa Melamed, Yahav Yosefzon, Cfir David, Anna Tsukerman, and Lilach Pnueli. Tet enzymes, variants, and differential effects on function. *Frontiers in Cell and Developmental Biology*, 6(MAR):22, mar 2018.
- [174] Marian Mellén, Pinar Ayata, Scott Dewell, Skirmantas Kriaucionis, and Nathaniel Heintz. MeCP2 binds to 5hmC enriched within active genes and accessible chromatin in the nervous system. *Cell*, 151(7):1417–1430, dec 2012.
- [175] Carla B. Mellough, Joseph Collin, Rachel Queen, Gerrit Hilgen, Birthe Dorgau, Darin Zerti, Majed Felemban, Kathryn White, Evelyne Sernagor, and Majlinda Lako. Systematic Comparison of Retinal Organoid Differentiation from Human Pluripotent Stem Cells Reveals Stage Specific, Cell Line, and Methodological Differences. *STEM CELLS Translational Medicine*, 8(7):694–706, jul 2019.
- [176] Shannath L. Merbs, Miriam A. Khan, Laszlo Hackler, Verity F. Oliver, Jun Wan, Jiang Qian, and Donald J. Zack. Cell-Specific DNA Methylation Patterns of Retina-Specific Genes. *PLOS ONE*, 7(3):e32602, mar 2012.
- [177] Kirsten D Mertz, Gunnar Weisheit, Karl Schilling, and Georg H Lüers. Electroporation of primary neural cultures: a simple method for directed gene transfer in vitro. *Histochemistry and Cell Biology*, 118(6):501–506, 2002.
- [178] Jason S. Meyer, Sara E. Howden, Kyle A. Wallace, Amelia D. Verhoeven, Lynda S. Wright, Elizabeth E. Capowski, Isabel Pinilla, Jessica M. Martin, Shulan Tian, Ron Stewart, Bikash Pattnaik, James A. Thomson, and David M. Gamm. Optic Vesicle-like Structures Derived from Human Pluripotent Stem Cells Facilitate a Customized Approach to Retinal Disease Treatment. *Stem Cells*, 29(8):1206–1218, aug 2011.

- [179] Jason R Meyers, Lily Hu, Ariel Moses, Kavon Kaboli, Annemarie Papandrea, and Pamela A Raymond. β -catenin/Wnt signaling controls progenitor fate in the developing and regenerating zebrafish retina. *Neural Development*, 7(1):30, 2012.
- [180] Ann H. Milam, Linda Rose, Artur V. Cideciyan, Mark R. Barakat, Wai Xing Tang, Nisha Gupta, Tomas S. Aleman, Alan F. Wright, Edwin M. Stone, Val C. Sheffield, and Samuel G. Jacobson. The nuclear receptor NR2e3 plays a role in human retinal photoreceptor differentiation and degeneration. *Proceedings of the National Academy of Sciences of the United States of America*, 99(1):473–478, jan 2002.
- [181] Taylor S. Mills, Tatiana Eliseeva, Stephanie M. Bersie, Grace Randazzo, Jhenya Nahreini, Ko Uoon Park, and Joseph A. Brzezinski. Combinatorial regulation of a Blimp1 (Prdm1) enhancer in the mouse retina. *PLOS ONE*, 12(8):e0176905, aug 2017.
- [182] Robert S. Molday and Orson L. Moritz. Photoreceptors at a glance. *Journal of Cell Science*, 128(22):4039–4045, nov 2015.
- [183] Catherine W. Morgans, Jianmei Zhang, Brett G. Jeffrey, Steve M. Nelson, Neal S. Burke, Robert M. Duvoisin, and R. Lane Brown. TRPM1 is required for the depolarizing light response in retinal ON-bipolar cells. *Proceedings of the National Academy of Sciences of the United States of America*, 106(45):19174–19178, nov 2009.
- [184] Eric M. Morrow, Takahisa Furukawa, Jacqueline E. Lee, and Constance L. Cepko. NeuroD regulates multiple functions in the developing neural retina in rodent. *Development*, 126(1):23–36, jan 1999.
- [185] Fabian Müller, Michael Scherer, Yassen Assenov, Pavlo Lutsik, Jörn Walter, Thomas Lengauer, and Christoph Bock. RnBeads 2.0: Comprehensive analysis of DNA methylation data. *Genome Biology*, 20(1), mar 2019.
- [186] Elisa Murenu, Marina Pavlou, Lisa Richter, Kleopatra Rapti, Sabrina Just, Jasmina Cehajic-Kapetanovic, Neda Tafrishi, Andrew Hayes, Rachel Scholey, Robert Lucas, Hildegard Büning, Dirk Grimm, and Stylianos Michalakis. A universal protocol for isolating retinal ON bipolar cells across species via fluorescence-activated cell sorting. *Molecular Therapy - Methods Clinical Development*, 20:587–600, 2021.
- [187] Francisco M. Nadal-Nicolás, Vincent P. Kunze, John M. Ball, Brian T. Peng, Akshay Krisnan, Gaohui Zhou, Lijin Dong, and Wei Li. True S-cones are concentrated in the ventral mouse retina and wired for color detection in the upper visual field. *eLife*, 9:1–30, 2020.
- [188] Tadashi Nakagawa, Lei Lv, Makiko Nakagawa, Yanbao Yu, Chao Yu, Ana C. D’Alessio, Keiko Nakayama, Heng Yu Fan, Xian Chen, and Yue Xiong. CRL4VprBP E3 Ligase

- Promotes Monoubiquitylation and Chromatin Binding of TET Dioxygenases. *Molecular Cell*, 57(2):247–260, jan 2015.
- [189] Tokushige Nakano, Satoshi Ando, Nozomu Takata, Masako Kawada, Keiko Muguruma, Kiyotoshi Sekiguchi, Koichi Saito, Shigenobu Yonemura, Mototsugu Eiraku, and Yoshiki Sasai. Self-formation of optic cups and storable stratified neural retina from human ESCs. *Cell stem cell*, 10(6):771–785, jun 2012.
- [190] Mathias W. Seeliger Naoyuki Tanimoto, Regine L. Muehlfriedel, M. Dominik Fischer, Edda Fahl, Peter Humphries, Martin Biel. Vision tests in the mouse: Functional phenotyping with electroretinography. *FBL*, 14(7):2730—2737, 2009.
- [191] Jeremy Nathans, Darcy Thomas, and David S. Hogness. Molecular Genetics of Human Color Vision: The Genes Encoding Blue, Green, and Red Pigments. *Science*, 232(4747):196–202, 1986.
- [192] Steve M. Nelson, Leon Park, and Deborah L. Stenkamp. Retinal homeobox 1 is required for retinal neurogenesis and photoreceptor differentiation in embryonic zebrafish. *Developmental biology*, 328(1):24–39, apr 2009.
- [193] Francesco Neri, Danny Incarnato, Anna Krepelova, Stefania Rapelli, Francesca Anselmi, Caterina Parlato, Claudio Medana, Federica DalBello, and Salvatore Oliviero. Single-Base resolution analysis of 5-formyl and 5-carboxyl cytosine reveals promoter DNA Methylation Dynamics. *Cell Reports*, 10(5):674–683, feb 2015.
- [194] Lily Ng, James B. Hurley, Blair Dierks, Maya Srinivas, Carmen Saltó, Björn Vennström, Thomas A. Reh, and Douglas Forrest. A thyroid hormone receptor that is required for the development of green cone photoreceptors. *Nature Genetics* 2001 27:1, 27(1):94–98, 2001.
- [195] Soo Khai Ng, John P.M. Wood, Glyn Chidlow, Guoge Han, Thaksaon Kittipassorn, Daniel J. Peet, and Robert J. Casson. Cancer-like metabolism of the mammalian retina. *Clinical Experimental Ophthalmology*, 43(4):367–376, may 2015.
- [196] Thuy T.M. Ngo, Jejoong Yoo, Qing Dai, Qiucen Zhang, Chuan He, Aleksei Aksimentiev, and Taekjip Ha. Effects of cytosine modifications on DNA flexibility and nucleosome mechanical stability. *Nature Communications*, 7:1–9, 2016.
- [197] Kim Tuyen Nguyen-Ba-Charvet and Alain Chédotal. Development of retinal layers. *Comptes Rendus Biologies*, 337(3):153–159, mar 2014.
- [198] Jackie L. Norrie, Marybeth S. Lupo, Beisi Xu, Issam Al Diri, Marc Valentine, Daniel Putnam, Lyra Griffiths, Jiakun Zhang, Dianna Johnson, John Easton, Ying Shao, Victoria Honnell, Sharon Frase, Shondra Miller, Valerie Stewart, Xin Zhou, Xiang Chen,

- and Michael A. Dyer. Nucleome Dynamics during Retinal Development. *Neuron*, 104(3):512–528.e11, nov 2019.
- [199] Jin Kyun Oh, Jose Ronaldo Lima de Carvalho, Yan Nuzbrokh, Joseph Ryu, Teja Chemudupati, Vinit B. Mahajan, Janet R. Sparrow, and Stephen H. Tsang. Retinal Manifestations of Mitochondrial Oxidative Phosphorylation Disorders. *Investigative Ophthalmology Visual Science*, 61(12):12–12, oct 2020.
- [200] Michelle O’Hara-Wright and Anai Gonzalez-Cordero. Retinal organoids: a window into human retinal development. *Development (Cambridge, England)*, 147(24), dec 2020.
- [201] Yoshihiro Omori, Shun Kubo, Tetsuo Kon, Mayu Furuhashi, Hirotaka Narita, Taro Kom-inami, Akiko Ueno, Ryotaro Tsutsumi, Taro Chaya, Haruka Yamamoto, Isao Suetake, Shinji Ueno, Haruhiko Koseki, Atsushi Nakagawa, and Takahisa Furukawa. Samd7 is a cell type-specific PRC1 component essential for establishing retinal rod photoreceptor identity. *Proceedings of the National Academy of Sciences of the United States of America*, 114(39):E8264–E8273, sep 2017.
- [202] Arturo Ortiñ-Martínez, Francisco M. Nadal-Nicolás, Manuel Jiménez-López, Juan J. Alburquerque-Béjar, Leticia Nieto-López, Diego Garcia-Ayuso, Maria P. Villegas-Pérez, Manuel Vidal-Sanz, and Marta Agudo-Barriuso. Number and distribution of mouse retinal cone photoreceptors: Differences between an albino (Swiss) and a pigmented (C57/BL6) strain. *PLoS ONE*, 9(7), jul 2014.
- [203] Orin S. Packer, Jan Verweij, Peter H. Li, Julie L. Schnapf, and Dennis M. Dacey. Blue-Yellow Opponency in Primate S Cone Photoreceptors. *Journal of Neuroscience*, 30(2):568–572, jan 2010.
- [204] Sara S. Patterson, Maureen Neitz, and Jay Neitz. Reconciling Color Vision Models With Midget Ganglion Cell Receptive Fields. *Frontiers in Neuroscience*, 13(August):1–12, 2019.
- [205] Marina Pavlou, Christian Schön, Laurence M Ocelli, Axel Rossi, Nadja Meumann, Ryan F Boyd, Joshua T Bartoe, Jakob Siedlecki, Maximilian J Gerhardt, Sabrina Babutzka, Jacqueline Bogedein, Johanna E Wagner, Siegfried G Priglinger, Martin Biel, Simon M Petersen-Jones, Hildegard B€ Uning, and Stylianos Michalakis. Novel AAV capsids for intravitreal gene therapy of photoreceptor disorders. *EMBO Molecular Medicine*, 13(4):e13392, apr 2021.
- [206] Leo Peichl and Juncal González-Soriano. Morphological types of horizontal cell in rodent retinae: A comparison of rat, mouse, gerbil, and guinea pig. *Visual Neuroscience*, 11(3):501–517, may 1994.

- [207] Guang Hua Peng and Shiming Chen. Crx activates opsin transcription by recruiting HAT-containing co-activators and promoting histone acetylation. *Human Molecular Genetics*, 16(20):2433–2452, oct 2007.
- [208] Kumiko A. Percival, Patricia R. Jusuf, Paul R. Martin, and Ulrike Grünert. Synaptic inputs onto small bistratified (blue-ON/yellow-OFF) ganglion cells in marmoset retina. *Journal of Comparative Neurology*, 517(5):655–669, dec 2009.
- [209] Arshan Perera, David Eisen, Mirko Wagner, Silvia K. Laube, Andrea F. Künzel, Susanne Koch, Jessica Steinbacher, Elisabeth Schulze, Victoria Splith, Nana Mittermeier, Markus Müller, Martin Biel, Thomas Carell, and Stylianos Michalakis. TET3 is recruited by REST for context-specific hydroxymethylation and induction of gene expression. *Cell Reports*, 11(2):283–294, apr 2015.
- [210] Cristiano N. Pessôa, Leticia A. Santiago, Diana A. Santiago, Danielle S. Machado, Fernando A.F. Rocha, Dora F. Ventura, Jan Nora Hokoç, Carmen C. Pazos-Moura, Fredric E. Wondisford, Patricia F. Gardino, and Tania M. Ortiga-Carvalho. Thyroid Hormone Action Is Required for Normal Cone Opsin Expression during Mouse Retinal Development. *Investigative Ophthalmology Visual Science*, 49(5):2039–2045, may 2008.
- [211] M. Joseph Phillips, Enio T. Perez, Jessica M. Martin, Samantha T. Reshel, Kyle A. Wallace, Elizabeth E. Capowski, Ruchira Singh, Lynda S. Wright, Eric M. Clark, Patrick M. Barney, Ron Stewart, Sarah J. Dickerson, Michael J. Miller, E. Ferda Percin, James A. Thomson, and David M. Gamm. Modeling human retinal development with patient-specific induced pluripotent stem cells reveals multiple roles for visual system homeobox 2. *Stem Cells*, 32(6):1480–1492, 2014.
- [212] Lawrence H. Pinto, Brandon Invergo, Kazuhiro Shimomura, Joseph S. Takahashi, and John B. Troy. Interpretation of the mouse electroretinogram. *Documenta Ophthalmologica*, 115(3):127–136, oct 2007.
- [213] Ross A. Poché, Yasuhide Furuta, Marie Christine Chaboissier, Andreas Schedl, and Richard R. Behringer. Sox9 is expressed in mouse multipotent retinal progenitor cells and functions in Müller Glial cell development. *Journal of Comparative Neurology*, 510(3):237–250, sep 2008.
- [214] Huntington Potter and Richard Heller. Transfection by electroporation. *Current protocols in molecular biology*, Chapter 9(SUPPL. 92), oct 2003.
- [215] Zhao Qin, Ambrose R. Kidd, Jennifer L. Thomas, Kenneth D. Poss, David R. Hyde, Pamela A. Raymond, and Ryan Thummel. FGF signaling regulates rod photoreceptor cell maintenance and regeneration in zebrafish. *Experimental Eye Research*, 93(5):726–734, nov 2011.

- [216] Eun Ang Raiber, Guillem Portella, Sergio Martínez Cuesta, Robyn Hardisty, Pierre Murat, Zhe Li, Mario Iurlaro, Wendy Dean, Julia Spindel, Dario Beraldi, Zheng Liu, Mark A. Dawson, Wolf Reik, and Shankar Balasubramanian. 5-Formylecytosine organizes nucleosomes and forms Schiff base interactions with histones in mouse embryonic stem cells. *Nature Chemistry*, 10(12):1258–1266, 2018.
- [217] Samhitha Raj, Yasuhiro Kyono, Christopher J. Sifuentes, Elvira del Carmen Arellanes-Licea, Arasakumar Subramani, and Robert J. Denver. Thyroid Hormone Induces DNA Demethylation in *Xenopus* Tadpole Brain. *Endocrinology*, 161(11), nov 2020.
- [218] Kasper D. Rasmussen, Ivan Berest, Sandra Keßler, Koutarou Nishimura, Lucía Simón-Carrasco, George S. Vassiliou, Marianne T. Pedersen, Jesper Christensen, Judith B. Zaugg, and Kristian Helin. TET2 binding to enhancers facilitates transcription factor recruitment in hematopoietic cells. *Genome Research*, 29(4):564–575, apr 2019.
- [219] Kasper D. Rasmussen and Kristian Helin. ChIP-Sequencing of TET Proteins. *Methods in Molecular Biology*, 2272:251–262, 2021.
- [220] Metabolic reprogramming during neuronal differentiation from aerobic glycolysis to neuronal oxidative Phosphorylation, Geoffrey P. Lewis, Kenneth A. Linberg, Edward Barawid, and Mark R. Verardo. Cellular Remodeling in Mammalian Retina Induced by Retinal Detachment. *Webvision: The Organization of the Retina and Visual System*, jul 2007.
- [221] K. D. Rhee, J. Yu, C. Y. Zhao, G. Fan, and X. J. Yang. Dnmt1-dependent DNA methylation is essential for photoreceptor terminal differentiation and retinal neuron survival. *Cell Death and Disease*, 3(11):1–8, 2012.
- [222] Christophe Ribelayga, Yu Cao, and Stuart C. Mangel. The Circadian Clock in the Retina Controls Rod-Cone Coupling. *Neuron*, 59(5):790–801, sep 2008.
- [223] Melanie R. Roberts, Anita Hendrickson, Christopher R. McGuire, and Thomas A. Reh. Retinoid X receptor γ is necessary to establish the S-opsin gradient in cone photoreceptors of the developing mouse retina. *Investigative Ophthalmology and Visual Science*, 46(8):2897–2904, aug 2005.
- [224] Melanie R. Roberts, Maya Srinivas, Douglas Forrest, Gabriella Morreale De Escobar, and Thomas A. Reh. Making the gradient: Thyroid hormone regulates cone opsin expression in the developing mouse retina. *Proceedings of the National Academy of Sciences of the United States of America*, 103(16):6218–6223, apr 2006.
- [225] Enrique J. Rodriguez-Boulan, Anand Swaroop, Igor O. Nasonkin, Shannath L. Merbs, Kevin Lazo, Verity F. Oliver, Matthew Brooks, Krushangi Patel, Raymond A. Enke,

- Jacob Nellissery, Milan Jamrich, Yun Z. Le, Kapil Bharti, Robert N. Fariss, Rivka A. Rachel, and Donald J. Zack. Conditional knockdown of DNA methyltransferase 1 reveals a key role of retinal pigment epithelium integrity in photoreceptor outer segment morphogenesis. *Development (Cambridge)*, 140(6):1330–1341, mar 2013.
- [226] P. Röhlich, Th van Veen, and Á Szél. Two different visual pigments in one retinal cone cell. *Neuron*, 13(5):1159–1166, nov 1994.
- [227] Austin Roorda and David R. Williams. The arrangement of the three cone classes in the living human eye. *Nature*, 397(6719):520–522, feb 1999.
- [228] Andrii Rudenko, Meelad M. Dawlaty, Jinsoo Seo, Albert W. Cheng, Jia Meng, Thuc Le, Kym F. Faull, Rudolf Jaenisch, and Li Huei Tsai. Tet1 is critical for neuronal activity-regulated gene expression and memory extinction. *Neuron*, 79(6):1109–1122, sep 2013.
- [229] Kazuma Saito, Kazuhiko Horiguchi, Sayaka Yamada, Battsetseg Buyandalai, Emi Ishida, Shunichi Matsumoto, Satoshi Yoshino, Yasuyo Nakajima, Eijiro Yamada, Tsugumichi Saito, Atsushi Ozawa, Yuki Tajika, Hideo Akiyama, and Masanobu Yamada. Maternal hypothyroidism is associated with M-opsin developmental delay. *Journal of Molecular Endocrinology*, 69(3):391–399, oct 2022.
- [230] Federico Salas-Lucia and Antonio C. Bianco. T3 levels and thyroid hormone signaling. *Frontiers in Endocrinology*, 13:2772, oct 2022.
- [231] Shinya Satoh, Ke Tang, Atsumi Iida, Mariko Inoue, Tatsuhiko Kodama, Sophia Y Tsai, Ming-Jer Tsai, Yasuhide Furuta, and Sumiko Watanabe. Development/Plasticity/Repair The Spatial Patterning of Mouse Cone Opsin Expression Is Regulated by Bone Morphogenetic Protein Signaling through Downstream Effector COUP-TF Nuclear Receptors. 2009.
- [232] Onkar B. Sawant, Amanda M. Horton, Olivia F. Zucaro, Ricky Chan, Vera L. Bonilha, Ivy S. Samuels, and Sujata Rao. The Circadian Clock Gene Bmal1 Controls Thyroid Hormone-Mediated Spectral Identity and Cone Photoreceptor Function. *Cell Reports*, 21(3):692–706, oct 2017.
- [233] Johannes Schindelin, Ignacio Arganda-Carreras, Erwin Frise, Verena Kaynig, Mark Longair, Tobias Pietzsch, Stephan Preibisch, Curtis Rueden, Stephan Saalfeld, Benjamin Schmid, Jean Yves Tinevez, Daniel James White, Volker Hartenstein, Kevin Eliceiri, Pavel Tomancak, and Albert Cardona. Fiji: An open-source platform for biological-image analysis. *Nature Methods*, 9(7):676–682, 2012.
- [234] Frank Schmitz, Andreas Königstorfer, and Thomas C. Südhof. RIBEYE, a component of synaptic ribbons: A protein’s journey through evolution provides insight into synaptic ribbon function. *Neuron*, 28(3):857–872, dec 2000.

- [235] Lars Schomacher and Christof Niehrs. DNA repair and erasure of 5-methylcytosine in vertebrates. *BioEssays*, 39(3), mar 2017.
- [236] Christian Schön, Sabrina Asteriti, Susanne Koch, Vithiyanjali Sothilingam, Marina Garcia Garrido, Naoyuki Tanimoto, Jochen Herms, Mathias W. Seeliger, Lorenzo Cangiano, Martin Biel, and Stylianos Michalakis. Loss of HCN1 enhances disease progression in mouse models of CNG channel-linked retinitis pigmentosa and achromatopsia. *Human Molecular Genetics*, 25(6):1165–1175, mar 2016.
- [237] Kimberly R. Schuske, Janet E. Richmond, Dawn Signor Matthies, Warren S. Davis, Steffen Runz, Daniel A. Rube, Alexander M. Van Der Blik, and Erik M. Jorgensen. Endophilin Is Required for Synaptic Vesicle Endocytosis by Localizing Synaptojanin. *Neuron*, 40(4):749–762, nov 2003.
- [238] Pawat Serittrakul and Jeffrey M. Gross. Tet-mediated DNA hydroxymethylation regulates retinal neurogenesis by modulating cell-extrinsic signaling pathways. *PLOS Genetics*, 13(9):e1006987, sep 2017.
- [239] Karthik Shekhar, Sylvain W. Lapan, Irene E. Whitney, Nicholas M. Tran, Evan Z. Marcenko, Monika Kowalczyk, Xian Adiconis, Joshua Z. Levin, James Nemesh, Melissa Goldman, Steven A. McCarroll, Constance L. Cepko, Aviv Regev, and Joshua R. Sanes. COMPREHENSIVE CLASSIFICATION OF RETINAL BIPOLAR NEURONS BY SINGLE-CELL TRANSCRIPTOMICS. *Cell*, 166(5):1308, aug 2016.
- [240] Li Shen, Hao Wu, Dinh Diep, Shinpei Yamaguchi, Ana C. D’Alessio, Ho Lim Fung, Kun Zhang, and Yi Zhang. Genome-wide analysis reveals TET- and TDG-dependent 5-methylcytosine oxidation dynamics. *Cell*, 153(3):692–706, apr 2013.
- [241] Alexander Sher and Steven H. Devries. A non-canonical pathway for mammalian blue-green color vision. *Nature Neuroscience*, 15(7):952–953, 2012.
- [242] Yoshinori Shichida and Take Matsuyama. Evolution of opsins and phototransduction. *Philosophical Transactions of the Royal Society B: Biological Sciences*, 364(1531):2881–2895, oct 2009.
- [243] Lisa J. Simpson, John S. Reader, and Ellie Tzima. Mechanical Forces and Their Effect on the Ribosome and Protein Translation Machinery. *Cells 2020, Vol. 9, Page 650*, 9(3):650, mar 2020.
- [244] Chun Xiao Song, Keith E. Szulwach, Qing Dai, Ye Fu, Shi Qing Mao, Li Lin, Craig Street, Yujing Li, Mickael Poidevin, Hao Wu, Juan Gao, Peng Liu, Lin Li, Guo Liang Xu, Peng Jin, and Chuan He. Genome-wide profiling of 5-formylcytosine reveals its roles in epigenetic priming. *Cell*, 153(3):678–691, apr 2013.

- [245] Su Jung Song, Keisuke Ito, Ugo Ala, Lev Kats, Kaitlyn Webster, Su Ming Sun, Mojca Jongen-Lavrencic, Katia Manova-Todorova, Julie Teruya-Feldstein, David E. Avigan, Ruud Delwel, and Pier Paolo Pandolfi. The oncogenic microRNA miR-22 targets the TET2 tumor suppressor to promote hematopoietic stem cell self-renewal and transformation. *Cell stem cell*, 13(1):87, jul 2013.
- [246] J R Sparrow, D Hicks, and C P Hamel. The retinal pigment epithelium in health and disease. *Current molecular medicine*, 10(9):802–823, dec 2010.
- [247] Jason R. Spence, Christopher N. Mayhew, Scott A. Rankin, Matthew F. Kuhar, Jefferson E. Vallance, Kathryn Tolle, Elizabeth E. Hoskins, Vladimir V. Kalinichenko, Susanne I. Wells, Aaron M. Zorn, Noah F. Shroyer, and James M. Wells. Directed differentiation of human pluripotent stem cells into intestinal tissue in vitro. *Nature*, 470(7332):105–110, 2011.
- [248] Maureen E. Stabio, Shai Sabbah, Lauren E. Quattrochi, Marissa C. Ilardi, P. Michelle Fogerson, Megan L. Leyrer, Min Tae Kim, Inkyu Kim, Matthew Schiel, Jordan M. Renna, Kevin L. Briggman, and David M. Berson. The M5 Cell: A Color-Opponent Intrinsically Photosensitive Retinal Ganglion Cell. *Neuron*, 97(1):150–163.e4, jan 2018.
- [249] Deborah L. Stenkamp. Development of the Vertebrate Eye and Retina. *Progress in Molecular Biology and Translational Science*, 134:397–414, jan 2015.
- [250] Nat Sternberg and Daniel Hamilton. Bacteriophage P1 site-specific recombination: I. Recombination between loxP sites. *Journal of Molecular Biology*, 150(4):467–486, aug 1981.
- [251] Elitsa Stoyanova, Michael Riad, Anjana Rao, and Nathaniel Heintz. 5-Hydroxymethylcytosine-mediated active demethylation is required for mammalian neuronal differentiation and function. *eLife*, 10:1–23, 2021.
- [252] Sachihiko C. Suzuki, Adam Bleckert, Philip R. Williams, Masaki Takechi, Shoji Kawamura, and Rachel O.L. Wong. Cone photoreceptor types in zebrafish are generated by symmetric terminal divisions of dedicated precursors. *Proceedings of the National Academy of Sciences of the United States of America*, 110(37):15109–15114, sep 2013.
- [253] Anand Swaroop, Douglas Kim, and Douglas Forrest. Transcriptional regulation of photoreceptor development and homeostasis in the mammalian retina. *Nature Reviews Neuroscience 2010 11:8*, 11(8):563–576, aug 2010.
- [254] Klaudia P. Szatko, Maria M. Korympidou, Yanli Ran, Philipp Berens, Deniz Dalkara, Timm Schubert, Thomas Euler, and Katrin Franke. Neural circuits in the mouse retina

- support color vision in the upper visual field. *Nature Communications* 2020 11:1, 11(1):1–14, jul 2020.
- [255] Mamta Tahiliani, Kian Peng Koh, Yinghua Shen, William A. Pastor, Hozefa Bandukwala, Yevgeny Brudno, Suneet Agarwal, Lakshminarayan M. Iyer, David R. Liu, L. Aravind, and Anjana Rao. Conversion of 5-Methylcytosine to 5-Hydroxymethylcytosine in Mammalian DNA by MLL Partner TET1. *Science (New York, N.Y.)*, 324(5929):930, may 2009.
- [256] Keizo Takao and Tsuyoshi Miyakawa. Light/dark Transition Test for Mice. *Journal of Visualized Experiments : JoVE*, (1):104, oct 2006.
- [257] Naoyuki Tanimoto, Vithiyanjali Sothilingam, Mineo Kondo, Martin Biel, Peter Humphries, and Mathias W. Seeliger. Electroretinographic assessment of rod- and cone-mediated bipolar cell pathways using flicker stimuli in mice. *Scientific Reports* 2015 5:1, 5(1):1–7, jun 2015.
- [258] Young Thomas. II. The Bakerian Lecture. On the theory of light and colours. *Philosophical Transactions of the Royal Society of London*, 92:12–48, dec 1802.
- [259] Wallace B. Thoreson, Norbert Babai, and Theodore M. Bartoletti. Feedback from Horizontal Cells to Rod Photoreceptors in Vertebrate Retina. *Journal of Neuroscience*, 28(22):5691–5695, may 2008.
- [260] Wallace B. Thoreson and Dennis M. Dacey. Diverse cell types, circuits, and mechanisms for color vision in the vertebrate retina. *Physiological Reviews*, 99(3):1527–1573, jul 2019.
- [261] Susanne Tom Dieck and Johann Helmut Brandstätter. Ribbon synapses of the retina. *Cell and Tissue Research*, 326(2):339–346, nov 2006.
- [262] Franziska R. Traube, Dilara Özdemir, Hanife Sahin, Constanze Scheel, Andrea F. Glück, Anna S. Geserich, Sabine Oganessian, Sarantos Kostidis, Katharina Iwan, René Rahimoff, Grazia Giorgio, Markus Müller, Fabio Spada, Martin Biel, Jürgen Cox, Martin Giera, Stylianos Michalakis, and Thomas Carell. Redirected nuclear glutamate dehydrogenase supplies Tet3 with α -ketoglutarate in neurons. *Nature Communications*, 12(1):1–13, 2021.
- [263] Franziska R. Traube, Sarah Schiffrers, Katharina Iwan, Stefanie Kellner, Fabio Spada, Markus Müller, and Thomas Carell. Isotope-dilution mass spectrometry for exact quantification of noncanonical DNA nucleosides. *Nature Protocols*, 14(1):283–312, 2019.

- [264] Yu Ichi Tsukada, Tomohiko Akiyama, and Keiichi I. Nakayama. Maternal TET3 is dispensable for embryonic development but is required for neonatal growth. *Scientific Reports*, 5:1–13, 2015.
- [265] Yoshihiko Tsukamoto, Patricia Masarachia, Stanley J. Schein, and Peter Sterling. Gap junctions between the pedicles of macaque foveal cones. *Vision Research*, 32(10):1809–1815, 1992.
- [266] Yoshihiko Tsukamoto, Katsuko Morigiwa, Mika Ueda, and Peter Sterling. Microcircuits for night vision in mouse retina. *The Journal of neuroscience : the official journal of the Society for Neuroscience*, 21(21):8616–8623, nov 2001.
- [267] Yoshihiko Tsukamoto and Naoko Omi. Functional allocation of synaptic contacts in microcircuits from rods via rod bipolar to AII amacrine cells in the mouse retina. *Journal of Comparative Neurology*, 521(15):3541–3555, 2013.
- [268] David L Turner and Constance L Cepko. A common progenitor for neurons and glia persists in rat retina late in development. *Nature*, 328(6126):131–136, 1987.
- [269] Heather A. Van Epps, Mitsuko Hayashi, Louise Lucast, George W. Stearns, James B. Hurley, Pietro De Camilli, and Susan E. Brockerhoff. The Zebrafish nrc Mutant Reveals a Role for the Polyphosphoinositide Phosphatase Synaptojanin 1 in Cone Photoreceptor Ribbon Anchoring. *Journal of Neuroscience*, 24(40):8641–8650, oct 2004.
- [270] Sara J Venters, Takashi Mikawa, and Jeanette Hyer. Early divergence of central and peripheral neural retina precursors during vertebrate eye development. *Developmental dynamics : an official publication of the American Association of Anatomists*, 244(3):266–276, mar 2015.
- [271] Patrik Verstreken, Tong Wey Koh, Karen L. Schulze, R. Grace Zhai, P. Robin Hiesinger, Yi Zhou, Sunil Q. Mehta, Yu Cao, Jack Roos, and Hugo J. Bellen. Synaptojanin Is Recruited by Endophilin to Promote Synaptic Vesicle Uncoating. *Neuron*, 40(4):733–748, nov 2003.
- [272] Filipe O. Viegas and Stephan C.F. Neuhauss. A Metabolic Landscape for Maintaining Retina Integrity and Function. *Frontiers in Molecular Neuroscience*, 14:60, apr 2021.
- [273] Anne Vielle, Yuna K. Park, Conner Secora, and M. Natalia Vergara. Organoids for the Study of Retinal Development and Developmental Abnormalities. *Frontiers in Cellular Neuroscience*, 15:154, may 2021.
- [274] Jozsef Vigh, Evan Vickers, and Henrique von Gersdorff. Light-Evoked Lateral GABAergic Inhibition at Single Bipolar Cell Synaptic Terminals Is Driven by Distinct Retinal Microcircuits. *Journal of Neuroscience*, 31(44):15884–15893, 2011.

- [275] Manuela Völkner, Marina Pavlou, Hildegard Büning, Stylianos Michalakis, and Mike O. Karl. Optimized Adeno-Associated Virus Vectors for Efficient Transduction of Human Retinal Organoids. *https://home.liebertpub.com/hum*, 32(13-14):694–706, jul 2021.
- [276] Waddington. Organisers and Genes (1940), by Conrad Hal Waddington | The Embryo Project Encyclopedia.
- [277] Sui Wang, Cem Sengel, Mark M. Emerson, and Constance L. Cepko. A gene regulatory network controls the binary fate decision of rod and bipolar cells in the vertebrate retina. *Developmental cell*, 30(5):513, sep 2014.
- [278] Sui Wang, Cem Sengel, Mark M Emerson, and Constance L Cepko. Article + A Gene Regulatory Network Controls the Binary Fate Decision of Rod and Bipolar Cells in the Vertebrate Retina. 2014.
- [279] Yanshu Wang, Jennifer P. Macke, Shannath L. Merbs, Donald J. Zack, Brenda Klaunberg, Jean Bennett, John Gearhart, and Jeremy Nathans. A locus control region adjacent to the human red and green visual pigment genes. *Neuron*, 9(3):429–440, 1992.
- [280] Otto Warburg. Über den Stoffwechsel der Carcinomzelle. *Die Naturwissenschaften*, 12(50):1131–1137, dec 1924.
- [281] Otto Warburg. On the origin of cancer cells. *Science*, 123(3191):309–314, feb 1956.
- [282] Heinz Wässle, Christian Puller, Frank Müller, and Silke Haverkamp. Cone Contacts, Mosaics, and Territories of Bipolar Cells in the Mouse Retina. *Journal of Neuroscience*, 29(1):106–117, jan 2009.
- [283] Kiichi Watanabe, Morio Ueno, Daisuke Kamiya, Ayaka Nishiyama, Michiru Matsumura, Takafumi Wataya, Jun B. Takahashi, Satomi Nishikawa, Shin Ichi Nishikawa, Keiko Muguruma, and Yoshiki Sasai. A ROCK inhibitor permits survival of dissociated human embryonic stem cells. *Nature Biotechnology*, 25(6):681–686, 2007.
- [284] Lu Wen, Xianlong Li, Liying Yan, Yuexi Tan, Rong Li, Yangyu Zhao, Yan Wang, Jingcheng Xie, Yan Zhang, Chunxiao Song, Miao Yu, Xiaomeng Liu, Ping Zhu, Xiaoyu Li, Yu Hou, Hongshan Guo, Xinglong Wu, Chuan He, Ruiqiang Li, Fuchou Tang, and Jie Qiao. Whole-genome analysis of 5-hydroxymethylcytosine and 5-methylcytosine at base resolution in the human brain. *Genome Biology*, 15(3), 2014.
- [285] Emma R. West and Constance L. Cepko. Development and diversification of bipolar interneurons in the mammalian retina. *Developmental Biology*, 481:30–42, jan 2022.

- [286] Lee M. Wheldon, Abdulkadir Abakir, Zoltan Ferjentsik, Tatiana Dudnakova, Stephanie Strohbuecker, Denise Christie, Nan Dai, Shengxi Guan, Jeremy M. Foster, Ivan R. Corrêa, Matthew Loose, James E. Dixon, Virginie Sottile, Andrew D. Johnson, and Alexey Ruzov. Transient accumulation of 5-carboxylcytosine indicates involvement of active demethylation in lineage specification of neural stem cells. *Cell Reports*, 7(5):1353–1361, jun 2014.
- [287] Fan Wu, Xiang Li, Mario Looso, Hang Liu, Dong Ding, Stefan Günther, Carsten Kuenne, Shuya Liu, Norbert Weissmann, Thomas Boettger, Ann Atzberger, Saeed Kolahian, Harald Renz, Stefan Offermanns, Ulrich Gärtner, Michael Potente, Yonggang Zhou, Xuejun Yuan, and Thomas Braun. Spurious transcription causing innate immune responses is prevented by 5-hydroxymethylcytosine. *Nature Genetics*, 55(January), 2022.
- [288] Hao Wu, Ana C. D’Alessio, Shinsuke Ito, Kai Xia, Zhibin Wang, Kairong Cui, Keji Zhao, Yi Eve Sun, and Yi Zhang. Dual functions of Tet1 in transcriptional regulation in mouse embryonic stem cells. *Nature*, 473(7347):389–394, 2011.
- [289] Hao Wu and Yi Zhang. Reversing DNA Methylation: Mechanisms, Genomics, and Biological Functions. *Cell*, 156(1):45–68, jan 2014.
- [290] Xiaoji Wu and Yi Zhang. TET-mediated active DNA demethylation: mechanism, function and beyond. *Nature Reviews Genetics* 2017 18:9, 18(9):517–534, may 2017.
- [291] Di Xie, Bernardo Stutz, Feng Li, Fan Chen, Haining Lv, Matija Sestan-Pesa, Jonatas Catarino, Jianlei Gu, Hongyu Zhao, Christopher E. Stoddard, Gordon G. Carmichael, Marya Shanabrough, Hugh S. Taylor, Zhong Wu Liu, Xiao Bing Gao, Tamas L. Horvath, and Yingqun Huang. TET3 epigenetically controls feeding and stress response behaviors via AGRP neurons. *The Journal of Clinical Investigation*, 132(19), oct 2022.
- [292] Yong Juan Xin, Bo Yuan, Bin Yu, Yu Qing Wang, Jia Jia Wu, Wen Hao Zhou, and Zilong Qiu. Tet1-mediated DNA demethylation regulates neuronal cell death induced by oxidative stress. *Scientific Reports*, 5:1–10, 2015.
- [293] Yufei Xu, Feizhen Wu, Li Tan, Lingchun Kong, Lijun Xiong, Jie Deng, Andrew J. Barbera, Lijuan Zheng, Haikuo Zhang, Stephen Huang, Jinrong Min, Thomas Nicholson, Taiping Chen, Guoliang Xu, Yang Shi, Kun Zhang, and Yujiang Geno Shi. Genome-wide Regulation of 5hmC, 5mC, and Gene Expression by Tet1 Hydroxylase in Mouse Embryonic Stem Cells. *Molecular Cell*, 42(4):451–464, may 2011.
- [294] Yufei Xu, Chao Xu, Akiko Kato, Wolfram Tempel, Jose Garcia Abreu, Chuanbing Bian, Yeguang Hu, Di Hu, Bin Zhao, Tanja Cerovina, Jianbo Diao, Feizhen Wu, Housheng Hansen He, Qingyan Cui, Erin Clark, Chun Ma, Andrew Barbara, Gert Jan C.

- Veenstra, Guoliang Xu, Ursula B. Kaiser, X. Shirley Liu, Stephen P. Sugrue, Xi He, Jinrong Min, Yoichi Kato, and Yujiang Geno Shi. Tet3 CXXC domain and dioxygenase activity cooperatively regulate key genes for xenopus eye and neural development. *Cell*, 151(6):1200–1213, dec 2012.
- [295] Haruka Yamamoto, Tetsuo Kon, Yoshihiro Omori, and Takahisa Furukawa. Functional and Evolutionary Diversification of Otx2 and Crx in Vertebrate Retinal Photoreceptor and Bipolar Cell Development. *Cell Reports*, 30(3):658–671.e5, jan 2020.
- [296] Hui Yang, HuaiPeng Lin, Haiyan Xu, Lei Zhang, Lu Cheng, Bo Wen, Jianyong Shou, Kunliang Guan, Yue Xiong, and Dan Ye. TET-catalyzed 5-methylcytosine hydroxylation is dynamically regulated by metabolites. *Cell Research 2014 24:8*, 24(8):1017–1020, jun 2014.
- [297] Xudong Yang, Rüdiger Klein, Xiaolin Tian, Hui Teng Cheng, Raphael Kopan, and Jie Shen. Notch activation induces apoptosis in neural progenitor cells through a p53-dependent pathway. *Developmental Biology*, 269(1):81–94, may 2004.
- [298] Lu Yin, Robert G. Smith, Peter Sterling, and David H. Brainard. Physiology and Morphology of Color-Opponent Ganglion Cells in a Retina Expressing a Dual Gradient of S and M Opsins. *Journal of Neuroscience*, 29(9):2706–2724, mar 2009.
- [299] Qiu Yongrong, Zhao Zhijian, Klindt David, Kautzky Magdalena, Szatko Klaudia, Schaeffel Frank, Rifai Katharina, Franke Katrin, Busse Laura, and Euler Thomas. Natural environment statistics in the upper and lower visual field are reflected in mouse retinal specializations. may 2021.
- [300] Shigeo Yoshida, Alan J Mears, James S Friedman, Todd Carter, Shirley He, Edwin Oh, Yuezhou Jing, Rafal Farjo, Gilles Fleury, Carrolee Barlow, Alfred O Hero, and Anand Swaroop. Expression profiling of the developing and mature Nrl 2/2 mouse retina: identification of retinal disease candidates and transcriptional regulatory targets of Nrl.
- [301] R. W. Young. The renewal of photoreceptor cell outer segments. *The Journal of cell biology*, 33(1):61–72, 1967.
- [302] Richard W. Young. Cell proliferation during postnatal development of the retina in the mouse. *Developmental Brain Research*, 21(2):229–239, aug 1985.
- [303] Huimei Yu, Yijing Su, Jaehoon Shin, Chun Zhong, Junjie U. Guo, Yi Lan Weng, Fuying Gao, Daniel H. Geschwind, Giovanni Coppola, Guo Li Ming, and Hongjun Song. Tet3 regulates synaptic transmission and homeostatic plasticity via DNA oxidation and repair. *Nature Neuroscience*, 18(6):836–843, 2015.

- [304] Alise Zagare, Matthieu Gobin, Anna S. Monzel, and Jens C. Schwamborn. A robust protocol for the generation of human midbrain organoids. *STAR Protocols*, 2(2):100524, jun 2021.
- [305] Juan Zhang, Shuangquan Chen, Dongming Zhang, Zixiao Shi, Hong Li, Tongbiao Zhao, Baoyang Hu, Qi Zhou, and Jianwei Jiao. Tet3-Mediated DNA Demethylation Contributes to the Direct Conversion of Fibroblast to Functional Neuron. *Cell Reports*, 17(9):2326–2339, nov 2016.
- [306] Run Rui Zhang, Qing Yan Cui, Kiyohito Murai, Yen Ching Lim, Zachary D. Smith, Shengnan Jin, Peng Ye, Luis Rosa, Yew Kok Lee, Hai Ping Wu, Wei Liu, Zhi Mei Xu, Lu Yang, Yu Qiang Ding, Fuchou Tang, Alexander Meissner, Chunming Ding, Yanhong Shi, and Guo Liang Xu. Tet1 regulates adult hippocampal neurogenesis and cognition. *Cell Stem Cell*, 13(2):237–245, aug 2013.
- [307] Yanjun Zhang, Zhongxing Sun, Junqi Jia, Tianjiao Du, Nachuan Zhang, Yin Tang, Yuan Fang, and Dong Fang. Overview of Histone Modification. *Advances in Experimental Medicine and Biology*, 1283:1–16, 2021.
- [308] Xinde Zheng, Leah Boyer, Mingji Jin, Jerome Mertens, Yongsung Kim, Li Ma, Li Ma, Michael Hamm, Fred H. Gage, and Tony Hunter. Metabolic reprogramming during neuronal differentiation from aerobic glycolysis to neuronal oxidative phosphorylation. *eLife*, 5(JUN2016), jun 2016.
- [309] Xiufeng Zhong, Christian Gutierrez, Tian Xue, Christopher Hampton, M. Natalia Vergara, Li Hui Cao, Ann Peters, Tea Soon Park, Elias T. Zambidis, Jason S. Meyer, David M. Gamm, King Wai Yau, and M. Valeria Canto-Soler. Generation of three-dimensional retinal tissue with functional photoreceptors from human iPSCs. *Nature Communications*, 5, jun 2014.
- [310] Xiufeng Zhong, Christian Gutierrez, Tian Xue, Christopher Hampton, M. Natalia Vergara, Li Hui Cao, Ann Peters, Tea Soon Park, Elias T. Zambidis, Jason S. Meyer, David M. Gamm, King Wai Yau, and M. Valeria Canto-Soler. Generation of three-dimensional retinal tissue with functional photoreceptors from human iPSCs. *Nature Communications*, 5(May), 2014.
- [311] Yanni Zhou, Dan Long, Ying Zhao, Shengfu Li, Yan Liang, Lin Wan, Jingyao Zhang, Fulai Xue, and Li Feng. Oxidative stress-mediated mitochondrial fission promotes hepatic stellate cell activation via stimulating oxidative phosphorylation. *Cell Death and Disease*, 13(8), 2022.

27 Appendix I

Differentially regulated genes in bulk RNA-seq at postnatal day 4 (p4): comparison Control vs *Tet3* mutant

All downregulated genes in *Tet3* mutant

FoldChange	padj	Gene name	Extended gene name
2.993090456	1.399901328	Rec8	REC8 meiotic recombination protein
2.778473122	1.475502141	Vsx1	visual system homeobox 1
2.24292257	7.00E+00	Krt24	keratin 24
1.771311775	1.468603789	Cfap58	cilia and flagella associated protein 58
1.616078884	3.565146129	Lrrc38	leucine rich repeat containing 38
1.510404366	3.281557857	Cpne6	copine 6
1.439106029	3.565146129	Egr1	early growth response 1
1.42057129	1.617263171	Postn	periostin
1.30322459	1.434578793	Apobec2	apolipoprotein B mRNA editing enzyme catalytic subunit 2
1.268547664	1.475502141	Col3a1	collagen type III alpha 1 chain
1.229474137	4.93E+00	Cfap61	cilia and flagella associated protein 61
1.1081602	1.406740638	Lnx1	ligand of numb-protein X 1
1.059918087	2.732126736	Rnf182	ring finger protein 182
0.939648456	3.127756132	Coro1b	coronin 1B
0.877460532	1.468603789	Psg16	pregnancy specific beta-1-glycoprotein 16

All upregulated genes in *Tet3* mutant

FoldChange	padj	Gene name	Extended gene name
-1.136393234	1.862860192	Gnat1	G protein subunit alpha transducin 1
-1.11453443	1.617263171	Ptges	prostaglandin E synthase
-0.997095685	4.840987482	Klh11	kelch like family member 1
-0.994271527	3.525880106	Moxd1	monooxygenase DBH like 1
-0.96614264	2.016902631	Lman1	lectin, mannose binding 1

28 Appendix II

Differentially regulated genes in bulk RNA-seq at postnatal day 10 (p10): comparison Control vs *Tet3* mutant

Top 50 downregulated genes in *Tet3* mutant

FoldChange	padj	Gene name	Extended gene name
4.156052183	1.65959683	Oasl1	2'-5' oligoadenylate synthetase-like 1
4.071708555	15.41030023	Aqp6	aquaporin 6
3.370699364	11.3831912	Slc6a12	solute carrier family 6 (GABA transporter)
2.696332333	2.175336449	Mgl2	macrophage galactose N-acetyl-galactosamine specific lectin 2
2.608649353	5.861742707	Hepacam	hepatocyte cell adhesion molecule
2.578559567	13.53421194	Tac2	tachykinin 2
2.46552969	3.898069625	Pmfbp1	polyamine modulated factor 1 binding protein 1
2.39161413	77.99915369	Aqp1	aquaporin 1
2.232369401	24.43665667	Dock8	dedicator of cytokinesis 8
2.168123623	4.4432968	Oit3	oncoprotein induced transcript 3
2.152953849	3.30974148	Lct	lactase
2.137619067	2.346269399	Adh6b	alcohol dehydrogenase 6B (class V)
2.122875957	7.149750872	Cfap58	cilia and flagella associated protein 58
1.944248212	7.149750872	Ankrd2	ankyrin repeat domain 2
1.817978021	1.745707153	Rasal1	RAS protein activator like 1 (GAP1 like)
1.778995287	2.908214423	Slc45a3	solute carrier family 45, member 3(
1.731004183	15.08426169	Krt24	keratin 24
1.688739849	36.91667531	Apobec2	apolipoprotein B mRNA editing enzyme, catalytic polypeptide 2
1.597435442	1.383676405	St14	suppression of tumorigenicity 14
1.589920562	2.962351082	Calml4	calmodulin-like 4
1.569863699	17.01391224	Krt18	keratin 18
1.553351378	3.773527935	Tph2	tryptophan hydroxylase 2
1.539708168	1.967732831	Wdr72	WD repeat domain 72
1.497891089	7.275722818	Il9r	interleukin 9 receptor
1.455172391	42.09501211	Cpne6	copine VI
1.454051203	5.843755067	Carns1	carnosine synthase 1

1.442359673	28.63757884	Rbm20	RNA binding motif protein 20
1.430399159	15.11989336	Cfap61	cilia and flagella associated protein 61
1.418477978	7.787693926	Lrrc66	leucine rich repeat containing 66
1.41399388	4.13958427	Col4a4	collagen, type IV, alpha 4
1.391859885	2.649834165	Aldh3b1	aldehyde dehydrogenase 3 family, member B1
1.352811731	1.393686076	Clcf1	cardiotrophin-like cytokine factor 1
1.333179782	20.30389603	Gabbr3	gamma-aminobutyric acid (GABA) receptor
1.309012603	5.027636362	Col4a3	collagen, type IV, alpha 3
1.300964333	5.909015112	Nr1h4	nuclear receptor subfamily 1, group H, member 4
1.287806772	9.768717539	Ppp1r1b	protein phosphatase 1, regulatory (inhibitor) subunit 1B
1.266760636	1.687665383	Cldn2	claudin 2
1.235641683	2.716443608	Lpar1	lysophosphatidic acid receptor 1
1.205453841	8.41160491	Col17a1	collagen, type XVII, alpha 1
1.201123299	9.615677951	Mc1r	melanocortin 1 receptor
1.191885268	8.866608823	Gsg1l2	GSG1-like 2
1.18557432	1.871857905	Kirrel2	kin of IRRE like 2
1.185324203	4.362964353	Syne3	spectrin repeat containing, nuclear envelope family member 3
1.167322656	11.30787504	Vgf	VGF nerve growth factor inducible
1.160722242	2.77612143	Mfrp	membrane frizzled-related protein
1.123013947	16.7535033	Grtp1	GH regulated TBC protein 1
1.118322145	2.06811886	Th	tyrosine hydroxylase
1.104572102	17.40134622	Kcnj14	potassium inwardly-rectifying channel, member 14

Top 50 upregulated genes in *Tet3* mutant

FoldChange	padj	Gene name	Extended gene name
-0.30126819	1.580762941	Mreg	melanoregulin
-0.301377354	2.142925984	Gm9918	predicted gene 9918

-0.303790576	2.27362833	Fam114a2	family with sequence similarity 114, member A2
-0.307621941	1.630163129	Gmcl1	germ cell-less, spermatogenesis associated 1
-0.30848848	1.481118426	Nucb2	nucleobindin 2
-0.30926611	1.689054493	Sox12	SRY (sex determining region Y)-box 12
-0.311139113	2.278163683	Snx6	sorting nexin 6
-0.314072567	1.50693739	Cfl2	cofilin 2, muscle
-0.318878645	2.436020666	Jun	jun proto-oncogene
-0.323974889	3.237680377	Camkk1	calcium/calmodulin-dependent protein kinase kinase 1, alpha
-0.338033397	2.782980119	Hltf	helicase-like transcription factor
-0.338253105	2.207496951	Cngb3	cyclic nucleotide gated channel beta 3
-0.344511091	2.082513536	Rdh13	retinol dehydrogenase 13 (all-trans and 9-cis)
-0.345226199	4.597420978	Tmem237	transmembrane protein 237
-0.345883147	1.49249362	Zfp120	zinc finger protein 120
-0.3480429	5.614872159	Slmap	sarcolemma associated protein
-0.349694244	2.837784056	Kras	Kirsten rat sarcoma viral oncogene homolog
-0.350711429	2.532534194	Synpo2	synaptopodin 2
-0.353226125	1.874440677	Hspa1b	heat shock protein 1B
-0.355416002	1.636547877	Kansl11	KAT8 regulatory NSL complex subunit 1-like
-0.356039229	1.368795824	Dnajc11	DnaJ heat shock protein family (Hsp40) member C11
-0.356979246	2.168804261	Svip	small VCP/p97-interacting protein
-0.360196782	1.381285962	Lsm2	LSM2 homolog, mRNA degradation associated
-0.363551111	1.568310073	Klf10	Kruppel-like factor 10
-0.3650846	1.955196784	Fn3k	fructosamine 3 kinase
-0.371143827	1.482876136	Katna1	katanin p60 (ATPase-containing) subunit A1
-0.372593665	5.397371707	Nnat	neuronatin
-0.37494713	1.380164406	Apex2	apurinic/apurimidinic endonuclease 2
-0.376275089	2.116197582	Nxph4	neurexophilin 4
-0.376304091	5.517087852	Rraga	Ras-related GTP binding A

-0.377309521	1.771852849	Lhpp	phospholysine phosphohistidine inorganic pyrophosphate phosphatase
-0.387858186	5.642435919	Doc2b	double C2, beta
-0.39102027	2.036569408	Vasn	vasorin
-0.396281798	2.447224464	Tmem35a	transmembrane protein 35A
-0.405182723	1.531051909	Gngt2	gamma transducing activity polypeptide 2
-0.410618475	1.427449787	Mtg1	mitochondrial ribosome-associated GTPase 1
-0.413393552	1.332787314	Mlf1	myeloid leukemia factor 1
-0.417954635	5.694341218	Tacc2	transforming, acidic coiled-coil containing protein 2
-0.422728524	2.865179072	Grm7	glutamate receptor, metabotropic 7
-0.426535501	2.269147596	Acat1	acetyl-Coenzyme A acetyltransferase 1
-0.431264755	1.73841165	Tstd2	thiosulfate sulfurtransferase (rhodanese)-like domain containing 2
-0.433288436	1.563173662	Cfap69	cilia and flagella associated protein 69
-0.444734485	7.178036997	Slc26a2	solute carrier family 26 (sulfate transporter), member 2
-0.447164082	3.268805023	Trib1	tribbles pseudokinase 1
-0.457067712	2.007237015	Klhl1	kelch-like 1
-0.460016438	2.639148897	Gpr137c	G protein-coupled receptor 137C
-0.462463988	1.967794678	Camk1g	calcium/calmodulin-dependent protein kinase I gamma
-0.467742537	2.105612492	Abhd3	abhydrolase domain containing 3(Abhd3)
-0.484250862	5.0276363621	Opn1sw	opsin 1 (cone pigments), short-wave-sensitive

29 Appendix III

Differentially regulated genes in bulk RNA-seq at postnatal day 30 (p30): comparison Control vs *Tet3* mutant

Top 50 downregulated genes in *Tet3* mutant

FoldChange	padj	Gene name	Extended gene name
4.747868883	1.488545067	Aqp2	aquaporin 2
3.095713666	6.174385581	Lct	lactase
2.921715634	19.75135901	Dock8	dedicator of cytokinesis 8
2.675465425	4.154171267	Zan	zonadhesin
2.609345725	5.052942957	Alpk2	alpha-kinase 2
2.534954051	1.640102198	Wnt10a	wingless-type MMTV integration site family, member 10A
2.333508997	20.53830733	Klhl3	kelch-like 3
2.287293535	10.08255607	Tph2	tryptophan hydroxylase 2
2.223178371	5.466133133	Bst1	bone marrow stromal cell antigen 1
2.162211779	2.022828697	Aqp6	aquaporin 6
2.151581064	13.59185891	Apobec2	apolipoprotein B mRNA editing enzyme, catalytic polypeptide 2
2.075783166	6.520516389	Abca6	ATP-binding cassette, sub-family A (ABC1), member 6
2.011504446	1.642052712	Cfi	complement component factor i
1.983953284	1.743650254	Cela1	chymotrypsin-like elastase family, member 1
1.933470765	4.002168737	Slc6a12	solute carrier family 6 (GABA), member 12
1.928140366	3.609730418	Dnai1	Dynein Axonemal Intermediate Chain 1
1.552079241	1.766145972	Aldh3b1	aldehyde dehydrogenase 3 family, member B1
1.47118415	11.04806809	Rbm20	RNA binding motif protein 20
1.445307614	10.9385376	Aqp1	aquaporin 1
1.432660921	1.496274671	Th	tyrosine hydroxylase
1.369509792	1.655434219	Cerkl	ceramide kinase-like
1.296041974	2.375791525	Lpar1	lysophosphatidic acid receptor 1
1.275804692	5.781349891	Cfap61	cilia and flagella associated protein 61

1.27404614	2.460851723	Ccdc180	coiled-coil domain containing 180
1.26277603	1.483824114	Ip6k3	inositol hexaphosphate kinase 3
1.234154785	2.657649382	Asic3	acid-sensing (proton-gated) ion channel 3
1.198164802	15.46636903	Thoc5	THO complex 5
1.182420245	4.66633957	Cpm	carboxypeptidase M
1.170089279	7.494431109	Krt18	keratin 18
1.139486289	4.46550879	Cabp4	calcium binding protein 4
1.139381655	2.220557557	Cfap126	cilia and flagella associated protein 126
1.128837342	5.663765011	Faim	Fas apoptotic inhibitory molecule
1.022772691	8.998034456	Coro1b	coronin, actin binding protein 1B
1.015389043	2.791825333	Stk17b	serine/threonine kinase 17b (apoptosis-inducing)
1.002480808	3.009710319	Plekha8	pleckstrin homology domain containing, family A member 8
0.997203442	2.378229395	Gabrr3	gamma-aminobutyric acid (GABA) receptor
0.991779338	5.997134588	Gpr152	G protein-coupled receptor 152
0.946181628	5.781349891	Pgap3	post-GPI attachment to proteins 3
0.941124908	3.419370127	Zfpm1	zinc finger protein, multitype 1
0.891524995	4.543253269	Gas7	growth arrest specific 7
0.884540106	1.450464939	Taf4b	TATA-box binding protein associated factor 4b
0.877321074	1.607093613	Rab3il1	RAB3A interacting protein (rabin3)-like 1
0.812454266	1.655434219	Guca1a	guanylate cyclase activator 1a (retina)
0.79791972	2.294982461	Aip	aryl-hydrocarbon receptor-interacting protein
0.780126124	3.014826337	Thrsp	thyroid hormone responsive
0.765732436	2.016019068	Agpat3	1-acylglycerol-3-phosphate O-acyltransferase 3
0.757798056	2.005540036	Tmem134	transmembrane protein 134
0.731883947	2.894922022	Kifc3	kinesin family member C3
0.714954289	2.24569264	Gsg1	germ cell associated 1

All upregulated genes in *Tet3* mutant

FoldChange	padj	Gene name	Extended gene name
-2.19969424	15.61165532	Glb1l3	galactosidase, beta 1 like 3
-2.163956042	16.49456717	Tmem26	transmembrane protein 26
-1.885117904	4.660503865	Shisa12b	Family With Sequence Similarity 159 Member B
-1.7173928	1.337276073	Lad1	ladinin
-1.703321443	3.003835385	Slco1a5	solute carrier organic anion transporter family, member 1a5
-1.443125236	3.516543058	Tecta	tectorin alpha
-1.217319241	1.363099692	Fcrls	Fc receptor-like S, scavenger receptor
-1.143239616	1.523588107	A2m	alpha-2-macroglobulin
-1.126415733	5.234851444	Tnfrsf8	tumor necrosis factor receptor superfamily, member 8
-1.004236363	2.016019068	Sardh	sarcosine dehydrogenase
-1.003523323	4.360460257	St6galnac5	ST6 (alpha-N-acetyl-neuraminyl-2,3-beta-galactosyl-1,3)-N-acetylgalactosaminide alpha-2,6-sialyltransferase 5
-0.94559091	2.016019068	Chrn4	cholinergic receptor, nicotinic, beta polypeptide 4
-0.929597944	2.294982461	Gfap	glial fibrillary acidic protein
-0.878615558	1.598119619	Cryz12	crystallin zeta like 2
-0.852062802	2.606625178	Aldh1a7	aldehyde dehydrogenase family 1, subfamily A7
-0.738993323	1.327458348	C1qb	complement component 1, q subcomponent, beta polypeptide
-0.738760802	3.231624292	Rtn4r12	reticulon 4 receptor-like 2
-0.730897973	4.81321783	Lman1	lectin, mannose-binding, 1
-0.722249182	2.109294942	Id3	inhibitor of DNA binding 3
-0.691539036	3.780159761	Rax	retina and anterior neural fold homeobox
-0.678081471	3.78523534	Ptprn	protein tyrosine phosphatase, receptor type, N
-0.644049026	1.718589325	Ctss	cathepsin S
-0.618197051	4.656970405	Ssbp4	single stranded DNA binding protein 4
-0.570260044	1.821125443	Crym	crystallin, mu
-0.590319443	1.629951584	Metrn	meteorin, glial cell differentiation regulator

30 Appendix IV

Differentially regulated proteins from proteomics analysis: comparison *Tet3* mutant vs Control

Top 50 downregulated proteins in *Tet3* mutant

FoldChange	padj	Gene name	Extended protein name
-6.956944466	4.078290943	Mapre1	Microtubule-associated protein RP/EB family member 1
-6.270785332	2.091451745	Rpl15	60S ribosomal protein L15;Ribosomal protein L15
-6.120715459	3.300751919	Ola1	Obg-like ATPase 1
-6.052179972	3.149567246	Sfn	14-3-3 protein sigma
-6.030607541	2.655670715	Csde1	Cold shock domain-containing protein E1
-5.792498906	4.928596662	Cep250	Centrosome-associated protein CEP250
-5.737416585	3.564854631	Rpn2	Dolichyl-diphosphooligosaccharide--protein glycosyltransferase subunit 2
-5.00352033	2.332479643	Cdc42	Cell division control protein 42 homolog
-4.656514486	2.519297452	P4ha1	Prolyl 4-hydroxylase subunit alpha-1
-4.546254476	2.002928815	Rpl12	60S ribosomal protein L12
-4.263374964	3.177098175	Ube2k	Ubiquitin-conjugating enzyme E2 K
-4.037867864	4.49593195	Copb2	Coatomer subunit beta
-3.819948196	2.195259744	Gdi1	Rab GDP dissociation inhibitor alpha
-3.784254074	2.095210784	Wdr1	WD repeat-containing protein 1
-3.771923701	1.534777108	Copa	Coatomer subunit alpha;Xenin;Proxenin;Coatomer subunit alpha
-3.607570648	2.73137638	Kpna2	Importin subunit alpha-1
-3.228011449	2.623516018	Capns1	Calpain small subunit 1
-3.018409411	2.652958518	Stom	Erythrocyte band 7 integral membrane protein
-3.017217	1.985892331	Usp5	Ubiquitin carboxyl-terminal hydrolase 5
-2.743184408	1.966314356	Cops4	COP9 signalosome complex subunit 4
-2.737924576	2.474865801	Rab11	Ras-related protein Rab-11
-2.526572545	2.060011457	Prps2	Ribose-phosphate pyrophosphokinase 2
-2.494639715	2.490416174	Mcm2	DNA replication licensing factor MCM2

-2.265967051	1.768712809	Eif5a	Eukaryotic translation initiation factor 5A
-2.24911499	1.454287488	Nup155	Nuclear pore complex protein Nup155
-2.228030205	2.916067305	P3h1	Prolyl 3-hydroxylase 1
-1.986965815	1.594109106	Atp2a2	Sarcoplasmic/endoplasmic reticulum calcium ATPase 2
-1.85139974	1.878759983	Eef2	Elongation factor 2
-1.846099536	2.262423603	Srp68	Signal recognition particle subunit SRP68
-1.82190005	1.994327366	Rpl35a	60S ribosomal protein L35a
-1.798445702	1.682416964	Pabpc4	Polyadenylate-binding protein
-1.760173798	1.963890606	Sept11	Septin-11
-1.671000799	1.61022123	Rps27	40S ribosomal protein S27
-1.629166285	1.321041296	Tmsb10	Thymosin beta-10
-1.473466237	1.48691658	Pdcd6	Programmed cell death protein 6
-1.354233424	1.38848955	Actn1	Alpha-actinin-1
-1.270499547	1.378344546	Ldhb	L-lactate dehydrogenase;L-lactate dehydrogenase B chain
-1.266994476	1.390881191	Copa	Coatomer subunit alpha;Xenin;Proxenin;Coatomer subunit alpha
-1.208901087	1.405761587	Cct8	T-complex protein 1 subunit theta
-1.201367696	2.733354294	Prdx1	Peroxiredoxin-1
-1.180998484	1.876306116	Tuba1b,1c,8	Tubulin alpha-1B chain;Tubulin alpha-1C chain;Tubulin alpha-8 chain
-1.12629954	1.353890348	Phb2	Prohibitin-2
-1.119600296	2.352027122	Myl6	Myosin light polypeptide 6
-1.098300298	1.371398304	Rpl7a	60S ribosomal protein L7a
-1.094866435	1.963133269	Hspb1	Heat shock protein beta-1
-1.081199646	1.526648834	Pgam1	Phosphoglycerate mutase 1
-0.956348419	2.902830709	Ctnnd1	Catenin delta-1
-0.676566442	1.550118341	Stat1	Signal transducer and activator of transcription

Top 50 upregulated proteins in *Tet3* mutant

FoldChange	-padj	Gene name	Extended protein name
------------	-------	-----------	-----------------------

6.053644816	1.591873254	Mif	Macrophage migration inhibitory factor
5.672786077	3.059775923	Hnrnpd	Heterogeneous nuclear ribonucleoprotein D0
5.343052546	2.200748397	Epb4.113	Band 4.1-like protein 3;Band 4.1-like protein 3, N-terminally processed
4.957687378	2.667222419	Guk1	Guanylate kinase
4.931486766	1.583464068	Acot7	Cytosolic acyl coenzyme A thioester hydrolase
4.789199829	1.495290806	Hnrmpa3	Heterogeneous nuclear ribonucleoprotein A3
4.752545039	3.073170305	Sv2b	Synaptic vesicle glycoprotein 2B
4.751407623	4.25169447	Myeov2	Myeloma-overexpressed gene 2 protein homolog
4.697452863	2.950039673	Ppp1r1a	Protein phosphatase 1 regulatory subunit 1A
4.638671239	4.169816062	Ndufb8	NADH dehydrogenase [ubiquinone] 1 beta subcomplex subunit 8, mitochondrial
4.609422048	1.579052316	Aco2	Aconitate hydratase, mitochondrial
4.534033457	1.590414613	Hba	Hemoglobin subunit alpha
4.436417262	1.74886433	Pcp2	Purkinje cell protein 2
4.297092438	4.384959858	Dnajc5	DnaJ homolog subfamily C member 5
4.282480558	5.168946324	Chmp4b	Charged multivesicular body protein 4b
4.262980143	3.476224118	Slc16a1	Monocarboxylate transporter 1
4.237166723	2.518303545	Fkbp1a	Peptidyl-prolyl cis-trans isomerase FKBP1A;Peptidyl-prolyl cis-trans isomerase
4.18102169	2.161803992	Hebp1	Heme-binding protein 1
4.030941963	1.781072062	Tceal5	Transcription elongation factor A protein-like 5
3.985548019	1.95137767	Fam136a	Protein FAM136A
3.985281944	2.949948214	Cabp5	Calcium-binding protein 5
3.983976364	4.379286925	Anp32e	Acidic leucine-rich nuclear phosphoprotein 32 family member E
3.969370524	3.860185872	Hmg20a	High mobility group protein 20A
3.951968193	1.42684706	Lsm4	U6 snRNA-associated Sm-like protein LSm4

3.936992645	3.431128833	Nfu1	NFU1 iron-sulfur cluster scaffold homolog, mitochondrial
3.934983253	1.351415544	Snrpc	U1 small nuclear ribonucleoprotein C
3.911133448	1.38498399	Rbmx	RNA binding motif protein, X-linked-like-1
3.866841634	2.238368116	Arhgdib	Rho GDP-dissociation inhibitor 2
3.838566462	2.315022005	Mcee	Methylmalonyl-CoA epimerase, mitochondrial
3.79057312	2.351335953	Snca,b	Alpha-synuclein;Beta-synuclein
3.742593765	1.330390976	Ttn	Titin
3.669320107	1.802715145	Ehmt2	Histone-lysine N-methyltransferase EHMT2
3.666599909	1.489059645	Atp5d	ATP synthase subunit delta, mitochondrial
3.645899455	2.677871531	Polr2i	DNA-directed RNA polymerase II subunit RPB9;DNA-directed RNA polymerase subunit
3.6215264	2.755445246	Tom1l2	TOM1-like protein 2
3.604910851	2.446732873	Synj1	Synaptojanin-1
3.597357432	1.838188864	Idh3a	Isocitrate dehydrogenase [NAD] subunit alpha, mitochondrial
3.585625331	2.337491813	Map4	Microtubule-associated protein;Microtubule-associated protein 4
3.576640129	1.399522122	Atox1	Copper transport protein ATOX1
3.538334529	1.814237192	Son	Protein SON
3.534123739	2.595302951	Lsm5	U6 snRNA-associated Sm-like protein LSm5
3.505589167	2.772762331	Diablo	Diablo homolog, mitochondrial
3.429122925	2.853645682	Cetn2	Centrin-2
3.408425649	2.019569343	Yif1b	Protein YIF1B
3.403566996	1.330071541	Txndc12	Thioredoxin domain-containing protein 12
3.385240237	2.20467651	Ensa	Alpha-endosulfine
3.289478938	1.859681752	Timm10b	Mitochondrial import inner membrane translocase subunit Tim10 B
3.278022766	2.122011026	Ndufa3	NADH dehydrogenase 1 alpha subcomplex subunit 3
3.200860659	4.018837469	Amph	Amphiphysin

31 Appendix V

Top 50 gene hits showing differentially methylated sites (DMSs) in combined rank analysis

Bisulfite conversion (true methylation (5mC))

Gene	Frequency of DMSs	Fisher.p.fdr
Golgb1	3	0.000882204
Slc6a6	4	0.000882204
Fryl	5	0.001482017
Kcnv2	3	0.00165384
A330023F24Rik	3	0.006301668
Ip6k2	3	0.007817341
Epm2aip1	2	0.011319976
Coro1c	3	0.011319976
Erc2	4	0.012751054
Etv6	4	0.012831405
A930006I01Rik	2	0.012831405
Prrc2a	3	0.022187032
Ppp1r15a	2	0.022957057
Cdh26	2	0.023735368
Gm31784	2	0.023735368
Pde6b	2	0.023735368
Prph2	2	0.023735368
Exoc8	2	0.027382238
Stk35	2	0.027382238
Aqp1	2	0.031022211
Zfp65	2	0.031022211
Rho	2	0.036158029
Gm4258	2	0.039798005
Rufy1	2	0.039798005
Itm2b	2	0.043683163
Tbc1d16	3	0.043683163
r1Cabp1	2	0.045452102

Fam3c	2	0.045452102
Vezf1	2	0.045452102
Lrrc75a	2	0.050599988
Ankrd33b	2	0.057699644
Camsap1	2	0.057699644
Csrp2	2	0.057699644
Umad1	2	0.057699644
Wscd1	2	0.075566114
Zc3h4	2	0.075566114
Bptf	2	0.081077975
Arid3b	2	0.0946038
Nol4	2	0.107148817
Arid1b	3	0.107148817
Agpat3	2	0.107148817
Dpf3	2	0.107148817
chr11-50376899-50378597	1	0.107148817
chr15-25364175-25364865	1	0.107148817
chr2-18800079-18800510	1	0.107148817
chr4-148951660-148952711	1	0.107148817
chr7-38106954-38108064	1	0.107148817
chr7-6172892-6173097	1	0.107148817
Gm26752	1	0.107148817
Gm30525	1	0.107148817

Oxidative bisulfite conversion (true hydroxymethylation (5hmC))

Gene	Frequency of DMSs	Fisher.p.fdr
Zranb1	5	1.44E-06

Epb41	5	0.000461853
Igsf11	4	0.000461853
Anp32a	4	0.001424388
Prom1	4	0.002560576
Rd3	3	0.003624316
Epc1	3	0.004307399
Tapt1	3	0.004307399
Cnga1	3	0.006639969
Nadk2	3	0.010883533
Casz1	4	0.017678391
Rprd1a	2	0.031288967
Rtbdn	2	0.031288967
Kat6b	3	0.033394303
Josd1	2	0.034987766
Pik3r1	3	0.034987766
2510009E07Rik	2	0.034987766
Ddhd1	2	0.034987766
Guk1	2	0.034987766
Ncoa2	3	0.035528112
Ipmk	2	0.035528112
Otud7b	2	0.035528112
Vat11	2	0.035528112
Mbnl1	3	0.035615802
Cnot6	2	0.037782295
Ptbp2	2	0.037782295
Glis2	2	0.038772968
Ky	2	0.038772968
Tmem243	2	0.038772968
Ubap11	2	0.038772968
Mgat1	2	0.041119431
Mtfr1	2	0.041119431
Pitpnm3	2	0.041119431
Gm30149	2	0.043467151
Gm34338	2	0.043467151
Mdc1	2	0.043467151
Atp9b	2	0.046987216
Tnpo1	2	0.046987216

Zmynd8	3	0.048153018
Kirrel	2	0.048153018
Pcbp2	2	0.048153018
Tspan14	2	0.048153018
Map4k3	2	0.051608645
Slc25a22	2	0.051608645
Tspan9	3	0.053309397
Ccser2	2	0.05391249
Fam169a	2	0.05391249
Abhd14a	2	0.058503725
B4galt1	2	0.060748273
Hp1bp3	2	0.060748273

List of publications

- Traube FR, Stern M, Tölke AJ, Rudelius M, Mejías-Pérez E, Raddaoui N, Kümmerer BM, Douat C, Streshnev F, Albanese M, Wrátil PR, Gärtner YV, Nainytė M, **Giorgio G**, Michalakis S, Schneider S, Streeck H, Müller M, Keppler OT, Carell T. Suppression of SARS-CoV-2 Replication with Stabilized and Click-Chemistry Modified siRNAs. *Angew Chem Int Ed Engl.* 2022 Sep 19;61(38):e202204556. doi: 10.1002/anie.202204556. Epub 2022 Aug 12. PMID: 35802496; PMCID: PMC9350007.
- Traube FR, Özdemir D, Sahin H, Scheel C, Glück AF, Geserich AS, Oganessian S, Kostidis S, Iwan K, Rahimoff R, **Giorgio G**, Müller M, Spada F, Biel M, Cox J, Giera M, Michalakis S, Carell T. Redirected nuclear glutamate dehydrogenase supplies Tet3 with α -ketoglutarate in neurons. *Nat Commun.* 2021 Jul 2;12(1):4100. doi: 10.1038/s41467-021-24353-9. PMID: 34215750; PMCID: PMC8253819.
- Buchsbaum IY, Kielkowski P, **Giorgio G**, O'Neill AC, Di Giaimo R, Kyrousi C, Khattak S, Sieber SA, Robertson SP, Cappello S. ECE2 regulates neurogenesis and neuronal migration during human cortical development. *EMBO Rep.* 2020 May 6;21(5):e48204. doi: 10.15252/embr.201948204. Epub 2020 Mar 24. PMID: 32207244; PMCID: PMC7202216.
- **Giorgio G**, Gasparoni G, Moïnfar A, Evangelista L, Traube FR, Bertolini A, Kielkowski P, Haverkamp S, Saba A, Biel M, Theis F, Walter J, Murenu E, Michalakis S. The DNA dioxygenase Tet3 regulates retinal lineage specification, maturation and function. (Manuscript in preparation)
- Traube F, Gasparoni G, Geserich A, Sepulveda H, Splith V, Scheel C, Winkler A, **Giorgio G**, Murenu M, Özdemir D, Sahin H, Salhab A, Yue X, Angel C, Rao A, Carell T, Walter J, Michalakis S. MECP2 binds and regulates TET3 activity in neurons (Manuscript in preparation)
- Murenu E, **Giorgio G**, Chen H, Reschigna A, Yang Z, Pavlou M, Li Y, Kielkowski P, Michalakis S. Unlocking retinal microglia studies with a reproducible and durable in vitro system. (Manuscript in preparation)

Declaration of author contributions

Giorgio G, Gasparoni G, Moinfar A, Evangelista L, Traube FR, Bertolini A, Kielkowski P, Haverkamp S, Saba A, Biel M, Theis F, Walter J, Murenu E, Michalakis S. The DNA dioxygenase Tet3 regulates retinal lineage specification, maturation and function. (Manuscript in preparation)

G.Ga. performed RNA-sequencing as well as EPIC array and bisulfite and oxidative bisulfite conversion on provided RNA and gDNA from control and Tet3 mutant retinæ under the supervision of J.W. L.E. contributed to the mouse line characterization. T.F. performed quantification of cytosine modifications. A.B performed thyroid hormones quantification and analysis in dorsal and ventral retinæ of control and mutant mice under the supervision of S.A. Proteomics analysis was performed by P.K. on provided sorted cone photoreceptors. Ultrastructural image acquisition on provided dorsal and ventral retinal tissue has been performed by S.H. A.M. and F.T. are analyzing 10x single cell data not included in the current thesis. M.B. provided critical comments on the manuscript draft. E.M. and S.M. designed experiments, contributed to the interpretation of the data and coordinated drafting and writing of the manuscript.

My contribution to this work in detail:

For this study, I prepared and provided the collaborators with the material for their individual contribution, including sorting of cone photoreceptors for proteomics. I performed *in vivo* ERG and OCT evaluations and behavioral experiments and the characterization of the mouse line. I performed *in vitro* experiments including cloning of all plasmids used in the study. Additionally, I designed the experiments, analyzed and interpreted the data. Finally, I prepared the figures and manuscript draft.

Munich,

Supervisor (Prof. Dr. Michalakis)

Grazia Giorgio

Acknowledgements

First of all, I would like to thank my Supervisor Prof. Michalakis for granting me the opportunity of pursuing my PhD in his lab, for the scientific support and discussions during these years. To Prof. Biel, my gratitude for his feedbacks on my projects. Special thanks to my TAC members Prof. Cappello, Dr. Murenu and Dr. Spada, for their scientific inputs, constant support and guide through this journey. To all my collaborators, thank you for your valuable contribution to the Tet3 story, your professionalism and hard work.

To the entire AK Biel, thanks for making working days easier and funny, for the laughs and the parties. Big thanks to the AG Michalakis current and past, in particular my room-ladies, who shared with me all the ups and downs of this journey, who -literally- boosted my health with treats and goodies these last months, thanks for always sharing a word of comfort. I wish all of you to reach your goals successfully.

My acknowledgements go to my graduate school GSN for accepting me in their program that has brought me so much on both professional and personal level and for all the brilliant colleagues and friends I met. On this line, thank you Alessio, Olga and Ioanna for having lightened my (weekend) days with hiking adventures, skiing trips, dinners and much more.

To my magic duo Elisa and Marina, I am so glad my path crossed with yours, I could have not wished for better companions and brilliant minds. Elisa, words will never be enough to express my gratitude for everything you thought me, for all the times you made the point(s) together with me and pushed me over my limits (and not out of the window). Marina, in you I found a true friend and soul, always ready to cheer me up and find the bright side in all situations. To both, grazie forever <3. A special and sincere thanks goes to Manja, my brave Robin Hood (a buon intenditore poche parole).

Ai miei amici tanto lontani quanto vicini, Francesca, Giulia, Paolo, Lorenzo, per esserci sempre stati anche tramite uno schermo o un telefono, grazie.. per le cene, le chiacchierate, le passeggiate, le sciare e i concerti che verranno. A Francy L., che mi accompagna da lontano in tutti i traguardi importanti, grazie. A tutti i membri delle famiglie Marotta, Scandurra, Barrella e Panorano per la costante presenza e per aver sempre creduto in me, grazie!

Alle Antonelle del mio cuore, Elisa, Laura e Cecilia, un immenso grazie per i sorrisi che mi strappate sempre durante le nostre zoomate da mezza Europa.

Un sincero grazie a Lisa, la miglior master student, non solo per il prezioso aiuto e contributo al mio progetto principale, ma soprattutto per aver assecondato le mie idee folli (incluso girovagare tra le campagne e fattorie bavaresi). Un grande in bocca al lupo per il tuo dottorato.

A tutta la mia famiglia allargata Giorgio-Gaudino un enorme grazie. Ma in particolare grazie a te, mamma, che mi dai da sempre la carica per affrontare le situazioni, belle o brutte, e a te, papà, che mi aiuti sempre a focalizzarmi sulle cose importanti. Ad entrambi, infinitamente

grazie per il supporto che ogni giorno ricevo. A voi dedico questo lavoro svolto che racchiude tanta passione quanti sacrifici. Al mio fratellone, che in più occasioni mi ha aiutata ad affrontare questo dottorato con più spensieratezza, grazie!

E Marco, che dire, probabilmente ti toccherà supportarmi (o sopportarmi), spronarmi e bacchettarmi *a vita* ormai. Intanto, grazie grazie grazie <3.